Science

15 August 2008 | $10

AAAS

CONTENTS

Volume 321, Issue 5891

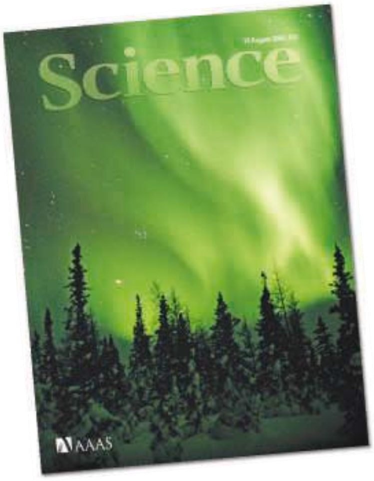

COVER

A dynamic aurora borealis during a storm over Canada. Energy from the Sun's extended atmosphere is stored at Earth's magnetic field and is released explosively, powering the aurorae. Previously stable aurorae brighten, filament, expand poleward, and cover the sky within 1 to 2 minutes. The energy release starts at an altitude of 130,000 kilometers, at the magnetic equator, near local midnight. See page 931.

Image: Norbert Rosing/National Geographic/Getty Images

DEPARTMENTS

887 *Science* Online
888 This Week in *Science*
892 Editors' Choice
894 Contact *Science*
895 Random Samples
897 Newsmakers
981 New Products
982 *Science* Careers

EDITORIAL

891 Dying for Science?
by M. R. C. Greenwood, Gordon Ringold, and Doug Kellogg

NEWS OF THE WEEK

Full-Genome Sequencing Paved the Way From Spores to a Suspect 898
Seasonal-Climate Forecasts Improving Ever So Slowly 900
Bizarre 'Metamaterials' for Visible Light in Sight? 900
>> Brevia p. 930
SCIENCESCOPE 901
Treatment and Prevention Exchange Vows at International Conference 902

NEWS FOCUS

Going Deeper Into the Grotte Chauvet 904
>> Science *Podcast*
Olivera Finn: Directing a Life in Science 906
Science Scholarships Go Begging 908
Climate Change Hot Spots Mapped Across the United States 909

904

LETTERS

Reservations About Dam Findings *D. J. Bain* et al. 910
What to Do About Those Dammed Streams *P. Wilcock*
Response *R. C. Walter and D. J. Merritts*
Looking for Familiar Faces *L. Shamir*
Response *R. Jenkins and A. M. Burton*
CORRECTIONS AND CLARIFICATIONS 912

BOOKS *ET AL.*

Lost Land of the Dodo 913
A. Cheke and J. Hume, reviewed by S. L. Olson
On Deep History and the Brain 914
D. L. Smail, reviewed by A. A. Ghazanfar

POLICY FORUM

Research Alone Is Not Enough 915
L. M. Branscomb

PERSPECTIVES

Neutrophil Soldiers or Trojan Horses? 917
B. John and C. A. Hunter *>> Report p. 970*
Halogen Versus Hydrogen 918
P. Metrangolo and G. Resnati
Directing Self-Assembly Toward Perfection 919
R. A. Segalman *>> Reports pp. 936 and 939*
The Elusive Onset of Geomagnetic Substorms 920
A. A. Petrukovich *>> Research Article p. 931*
Secret Weapon 922
R. F. Young III *>> Report p. 960*
Ironing Out Ocean Chemistry at the Dawn of Animal Life 923
T. W. Lyons *>> Report p. 949*
Retrospective: Victor A. McKusick (1921–2008) 925
F. S. Collins

913

CONTENTS continued >>

SCIENCE EXPRESS

www.sciencexpress.org

COMPUTER SCIENCE

reCAPTCHA: Human-Based Character Recognition via Web Security Measures

L. von Ahn, B. Maurer, C. McMillen, D. Abraham, M. Blum

A security system that relies on the superior performance of humans in comparison to computers in reading distorted text can be harnessed for digitized scanned documents.

10.1126/science.1160379

MATERIALS SCIENCE

Polymer Pen Lithography

F. Huo et al.

An array that can support millions of thin, flexible polymer pens can be used to deposit tiny molecular ink dots of variable size over large areas.

10.1126/science.1162193

PHYSICS

Transient Electronic Structure and Melting of a Charge Density Wave in $TbTe_3$

F. Schmitt et al.

Photoemission spectroscopy is extended to reveal the dynamics of correlated electronic phase transitions, showing how ordered electrons "melt" upon heating of $TbTe_3$.

10.1126/science.1160778

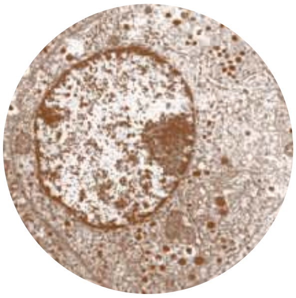

CELL BIOLOGY

Conformational Switch of Syntaxin-1 Controls Synaptic Vesicle Fusion

S. H. Gerber et al.

The synaptic vesicle protein that mediates membrane fusion during exocytosis also regulates the rate and extent of this process by controlling vesicle tethering.

10.1126/science.1163174

MEDICINE

Germline Allele-Specific Expression of *TGFBR1* Confers an Increased Risk of Colorectal Cancer

L. Valle et al.

In patients with colorectal cancer, one allele of the transforming growth factor–β gene produces less messenger RNA and thus less protein, a likely contributor to disease risk.

10.1126/science.1159397

TECHNICAL COMMENT ABSTRACTS

COMPUTER SCIENCE

Comment on "100% Accuracy in Automatic Face Recognition" 912

W. Deng, J. Guo, J. Hu, H. Zhang

full text at www.sciencemag.org/cgi/content/full/321/5891/912c

Response to Comment on "100% Accuracy in Automatic Face Recognition"

R. Jenkins and A. M. Burton

full text at www.sciencemag.org/cgi/content/full/321/5891/912d

REVIEW

ECOLOGY

Spreading Dead Zones and Consequences for Marine Ecosystems 926

R. J. Diaz and R. Rosenberg

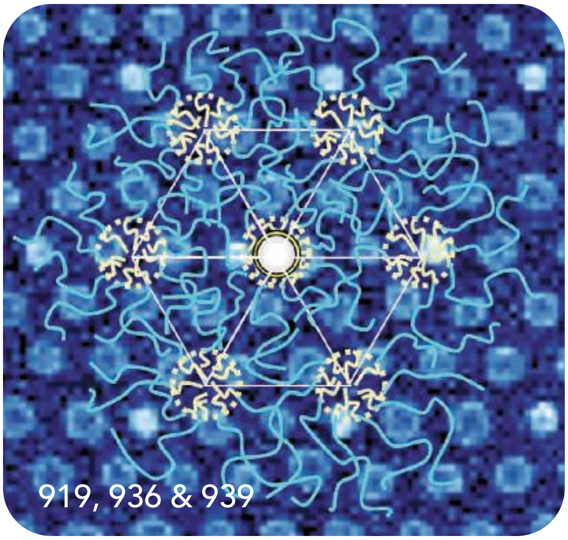

919, 936 & 939

BREVIA

APPLIED PHYSICS

Optical Negative Refraction in Bulk Metamaterials 930

J. Yao et al.

An array of silver nanowires placed in a porous alumina matrix forms a three-dimensional material that negatively refracts visible light.

>> News story p. 900

RESEARCH ARTICLE

ATMOSPHERIC SCIENCE

Tail Reconnection Triggering Substorm Onset 931

V. Angelopoulos et al.

Satellite and ground-based data show that reconnection of magnetic field lines in Earth's magnetotail precedes dramatic aurora displays and is the source of magnetic substorms. *>> Perspective p. 920*

REPORTS

MATERIALS SCIENCE

Density Multiplication and Improved Lithography by Directed Block Copolymer Assembly 936

R. Ruiz et al.

An appropriate substrate pattern can direct an even finer pattern of a block copolymer, improving the resolution for lithography by a factor of four, beyond the usual limits.

>> Perspective p. 919

MATERIALS SCIENCE

Graphoepitaxy of Self-Assembled Block Copolymers on Two-Dimensional Periodic Patterned Templates 939

I. Bita et al.

A substrate patterned with a sparse array of nanoscale posts can direct the self-assembly of block copolymers to create a finely ordered lithographic array, even over a large area.

>> Perspective p. 919

CONTENTS continued >>

REPORTS *CONTINUED...*

CHEMISTRY

X-ray Diffraction and Computation Yield the Structure of Alkanethiols on Gold(111) 943

A. Cossaro et al.

The structure of monolayers of alkyl thiols on gold—widely useful in nanotechnology—depends on the packing of the alkyl chains; long chains disorder the gold surface.

ATMOSPHERIC SCIENCE

Smoke Invigoration Versus Inhibition of Clouds Over the Amazon 946

I. Koren, J. V. Martins, L. A. Remer, H. Afargan

Modeling and satellite data show how absorption of light by aerosols can affect cloud properties and growth, linking these particles' opposing radiative and physical effects.

GEOCHEMISTRY

Ferruginous Conditions Dominated Later Neoproterozoic Deep-Water Chemistry 949

D. E. Canfield et al.

Low sulfur input caused the deeper ocean to become anoxic and rich in ferrous iron 750 million years ago, a reversal from the more oxidizing conditions of the previous 1 billion years. *>> Perspective p. 923*

PLANT SCIENCE

Plant Immunity Requires Conformational Charges of NPR1 via S-Nitrosylation and Thioredoxins 952

Y. Tada et al.

After a pathogen invades a plant, a protein, usually kept in a multimeric state by S-nitrosylation, is dissociated by thioredoxin, freeing the monomers for defense responses.

MOLECULAR BIOLOGY

A Global View of Gene Activity and Alternative Splicing by Deep Sequencing of the Human Transcriptome 956

M. Sultan et al.

Shotgun sequencing of 27–base pair segments of messenger RNA from human kidney and immune cells identifies previously undescribed transcriptional units and splice functions.

MOLECULAR BIOLOGY

Small CRISPR RNAs Guide Antiviral Defense in Prokaryotes 960

S. J. J. Brouns et al.

Some bacterial genomes contain remnant sequences from previous viral infections, which are transcribed into RNA to guide inactivation of the virus in subsequent infections. *>> Perspective p. 922*

MOLECULAR BIOLOGY

Suppression of the MicroRNA Pathway by Bacterial Effector Proteins 964

L. Navarro, F. Jay, K. Nomura, S. Y. He, O. Voinnet

Upon bacterial infection, *Arabidopsis* mounts a microRNA-mediated innate immune defense, which is inhibited by proteins of the bacteria, allowing other infections.

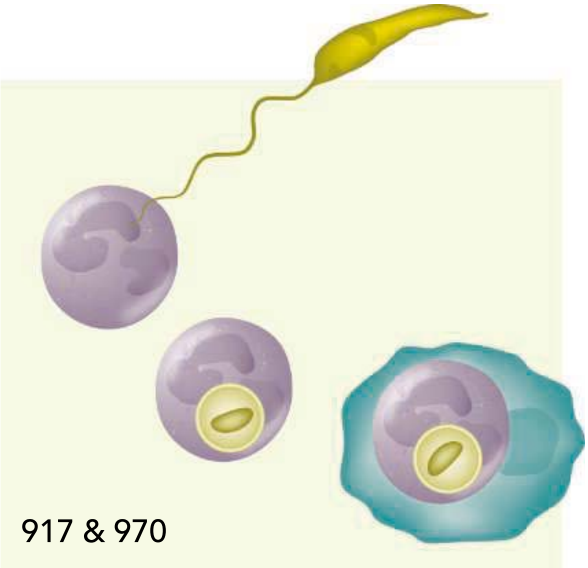

MICROBIOLOGY

Arsenic(III) Fuels Anoxygenic Photosynthesis in Hot Spring Biofilms from Mono Lake, California 967

T. R. Kulp et al.

A primitive form of photosynthesis in which arsenic is the electron donor occurs in purple bacteria in a California lake, perhaps a relic of early life forms.

IMMUNOLOGY

In Vivo Imaging Reveals an Essential Role for Neutrophils in Leishmaniasis Transmitted by Sand Flies 970

N. C. Peters et al.

Visualization of the area around a bite from a parasite-infected sand fly shows that the first immune cells to arrive engulf and unexpectedly protect the invading parasite. *>> Perspective p. 917*

MEDICINE

Tumor Regression in Cancer Patients by Very Low Doses of a T Cell–Engaging Antibody 974

R. Bargou et al.

Tested in a small group of patients, a therapeutic antibody binds to both tumor cells and immune cells, increasing the local concentration and effectiveness of the immune cells.

NEUROSCIENCE

The Contribution of Single Synapses to Sensory Representation in Vivo 977

A. Arenz, R. A. Silver, A. T. Schaefer, T. W. Margrie

Only 100 synapses are required to accurately code for the animals' velocity in the mouse cerebellum; the charge transfer into neurons is linearly related to acceleration.

SCIENCE (ISSN 0036-8075) is published weekly on Friday, except the last week in December, by the American Association for the Advancement of Science, 1200 New York Avenue, NW, Washington, DC 20005. Periodicals Mail postage (publication No. 484460) paid at Washington, DC, and additional mailing offices. Copyright © 2008 by the American Association for the Advancement of Science. The title SCIENCE is a registered trademark of the AAAS. Domestic individual membership and subscription (51 issues): $144 ($74 allocated to subscription). Domestic institutional subscription (51 issues): $770; Foreign postage extra: Mexico, Caribbean (surface mail) $55; other countries (air assist delivery) $85. First class, airmail, student, and emeritus rates on request. Canadian rates with GST available upon request, GST #1254 88122. Publications Mail Agreement Number 1069624. SCIENCE is printed on 30 percent post-consumer recycled paper. **Printed in the U.S.A.**

Change of address: Allow 4 weeks, giving old and new addresses and 8-digit account number. **Postmaster:** Send change of address to AAAS, P.O. Box 96178, Washington, DC 20090–6178. **Single-copy sales:** $10.00 current issue, $15.00 back issue prepaid includes surface postage; bulk rates on request. **Authorization to photocopy** material for internal or personal use under circumstances not falling within the fair use provisions of the Copyright Act is granted by AAAS to libraries and other users registered with the Copyright Clearance Center (CCC) Transactional Reporting Service, provided that $20.00 per article is paid directly to CCC, 222 Rosewood Drive, Danvers, MA 01923. The identification code for *Science* is 0036-8075. *Science* is indexed in the *Reader's Guide to Periodical Literature* and in several specialized indexes.

Printed on
30% post-consumer
recycled paper.

CONTENTS continued **>>**

Science ONLINE

www.sciencemag.org

Water walker.

SCIENCE**NOW**

www.sciencenow.org

HIGHLIGHTS FROM OUR DAILY NEWS COVERAGE

Water Striders Put Best Foot Forward
New calculation shows water-walking bugs have evolved feet of optimal length.

Threading Light Through the Opaque
Experiment confirms that light can be passed through disordered materials.

They Smell Like Twins
Sweaty study reveals that genetics determines body odor.

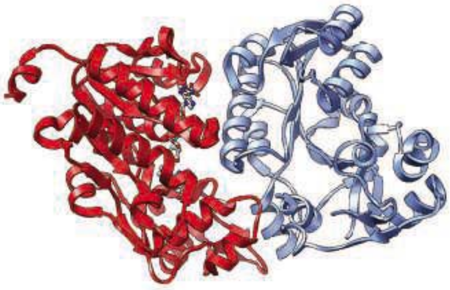

NADP-binding produces an asymmetric dimer.

SCIENCE **SIGNALING**

www.sciencesignaling.org

THE SIGNAL TRANSDUCTION KNOWLEDGE ENVIRONMENT

PERSPECTIVE: Dinucleotide-Sensing Proteins—Linking Signaling Networks and Regulating Transcription
H. K. Lamb, D. K. Stammers, A. R. Hawkins
Proteins that bind NAD(H) or NADP(H) may couple cellular redox state to transcription or other signaling pathways.

PERSPECTIVE: Great Times for Small Molecules—c-di-AMP, a Second Messenger Candidate in Bacteria and Archaea
U. Römling
The bacterial checkpoint protein DisA has diadenylate cyclase activity, suggesting that c-di-cAMP acts as a second messenger.

The basics of peer review.

SCIENCE **CAREERS**

www.sciencecareers.org/career_development

FREE CAREER RESOURCES FOR SCIENTISTS

Learning the Ropes of Peer Reviewing
E. Pain
Peer review demands a blend of critical skills, honesty, and empathy.

If at First You Don't Succeed, Cool Off, Revise, and Submit Again
L. Laursen
Rejection can be a constructive part of the publication process, really.

The *Science* Careers Web Log
Science *Careers Staff*
Here's where to find information from around the Web on careers in science.

SCIENCE**PODCAST**

www.sciencemag.org/multimedia/podcast

FREE WEEKLY SHOW

Download the 15 August *Science* Podcast to hear about ancient paintings inside France's Chauvet Cave, T cell-based cancer immunotherapy, modeling aerosols in the Amazon, and more.

Separate individual or institutional subscriptions to these products may be required for full-text access.

CREDITS: (*SCIENCE NOW*) ROSALIE LARUE/YELLOWSTONE NATIONAL PARK/NPS; (*SCIENCE CAREERS*) VAIKUNDA RAJA/CREATIVE COMMONS; (*SCIENCE SIGNALING*) CHRIS BICKEL

EDITED BY STELLA HURTLEY

Cloud Transitions

Aerosols can produce changes in the number, size, and size distribution of cloud drops, thereby impacting climate by affecting how clouds change the distributions and fluxes of energy and water. There are two major pathways by which aerosols act on clouds, the microphysical and the radiative, and (depending on the conditions) the net result can be either warming or cooling. **Koren *et al.*** (p. 946) focus on the Amazon to show that there exists a smooth transition between these two opposing effects and that a feedback between the optical properties of aerosols and cloud fraction can change the distribution of energy within the atmosphere.

Suffocating the Oceans

In many coastal regions of the world during the past 60 years, the concentration of dissolved oxygen has declined to levels anathema to life and the number and extent of listed hypoxic areas has increased from 46 in 1995 to more than 400. Loss of dissolved oxygen is linked to the release of nutrients when organic waste or fertilizer runs off into river outflows. Hypoxia poses a grave threat to the viability of coastal marine and estuarine ecosystems and can quickly lead to the elimination of the sea bed organisms and fish. **Diaz and Rosenberg** (p. 926) review how the issue of dissolved oxygen may become the most important factor controlling man's use of the sea.

From Storm to Aurora

Where do explosive auroral displays and their space-counterpart, magnetospheric substorms, which release energy from the solar wind stored in Earth's magnetosphere, originate? **Angelopoulos *et al.*** (p. 931, published online 24 July; cover; see the Perspective by **Petrukovich**) have used a series of satellites and ground networks to time the development of a substorm in detail and identify its source. Magnetic reconnection in Earth's magnetotail started the event, triggering an aurora display 1.5 minutes later.

Small Pillars and Blocks

Block copolymers, which are made from chemically dissimilar polymers covalently bonded together, will phase-segregate into a range of ordered patterns, and provide valuable tools for making lithographic patterns at the nanometer scale through a self-assembly process. However, a significant challenge is to make patterns over large distances owing to the formation of boundary regions or defects where the ordering is defective (see the Perspective by **Segalman**). **Ruiz *et al.*** (p. 936), through a judicious choice of substrate pattern, could multiply the resolution of the resulting block copolymer by a factor of four, allowing for patterning over large areas without substantial numbers of defects. **Bita *et al.*** (p. 939) created a sparse array of pillars that chemically mimicked the minority component of their block copolymer. The pillars disrupt the uniformity of the substrate and act as nucleation sites for the self-assembly, thus aiding in the creation of large-area-patterned templates.

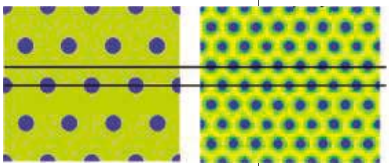

Ironing Out Ancient Ocean Chemistry

The Neoproterozoic Era, which lasted from approximately 1 billion to 540 million years ago, was distinguished by a phenomenal diversification of organisms and a transition from an anoxic to an oxic atmosphere. How did ocean chemistry change during that time? **Canfield *et al.*** (p. 949; published online 17 July; see the Perspective by **Lyons**) report that for most of the mid- and upper Neoproterozoic, the deep ocean was enriched in ferrous iron (ferruginous), sometimes sulfidic, and finally oxic. The observed return of ocean chemical conditions to the ferruginous ones not seen for more than 1 billion years probably was because of the long preceding interval of a sulfidic marine environment.

CRISPR Virus Defenses

Like eukaryotes, bacteria must defend themselves against viruses and transposons. A system has evolved in prokaryotes where fragments of these pathogenic species are collected into special genomic regions known as clusters of regularly interspaced short palindromic repeats (CRISPRs). CRISPRs provide a heritable memory of previous infections and a means to fend off subsequent infections. **Brouns *et al.*** (p. 960; see the Perspective by **Young**) show that the CRISPR region in *Escherichia coli* is transcribed and the CRISPR-associated (*cas*) gene *casE* is required for cleavage of the transcript into small, ~57-nucleotide CRISPR-RNAs (crRNAs). A complex of *cas* genes, including *casE*, form the Cascade complex, which uses the crRNAs to target the DNA of invading species and prevent infection.

Arsenic and Old Organisms

Mat-forming purple bacteria and cyanobacteria that couple arsenite oxidation to the reduction of carbon dioxide in the absence of oxygen have been found in hot brine springs of Mono Lake, California. The advent of photosynthesis was a key moment in the evolution of the Earth because the

CREDITS (TOP TO BOTTOM): ISTOCKPHOTO.COM; RUIZ ET AL.

reaction split water to release oxygen and promoted the diversification of life and our planet's characteristic geochemistry. But photosynthesis evolved under anoxic conditions, and one alternative route is that light-driven carbon fixation was based on arsenic as an electron donor. In a series of biochemical investigations on the Mono Lake organisms, **Kulp *et al.*** (p. 967) have confirmed the phylogenetic hints that this scenario was indeed the case. Increasingly, arsenic is implicated in a complex round of redox transformations mediated by microorganisms, to the extent that examples have been discovered of entire microbial communities supported by a metalloid that is toxic to most other forms of life.

RNA Interference and Plant Defenses

RNA interference plays an important role in innate immunity in plants and in animals. Specific microRNAs have also been implicated in pathways that sense pathogen-associated molecular patterns (PAMPs). Now **Navarro *et al.*** (p. 964) examine in more detail the role of microRNAs in innate immunity in *Arabidopsis*. MicroRNAs were found to be more broadly required for PAMP sensing. Pathogenic bacteria appear to have evolved various effectors that are secreted into the host that suppress the microRNA pathway at various points. Infection with Turnip Mosaic virus, which produces a suppressor of both the small interfering RNA and microRNA pathways, promotes infection by nonpathogenic bacteria, which may explain the observed synergy between viral and bacterial pathogens seen in the field.

Unwitting Accomplices

Many parasitic diseases are transmitted via the bite of an infected insect vector. The host response at the early subsequent stages is likely to influence the course of disease. **Peters *et al.*** (p. 970; see the Perspective by **John and Hunter**) use intravital imaging to visualize the dynamics of the initial events in mice following transmission of the intracellular parasite *Leishmania*, which normally infects macrophages. Unexpectedly, neutrophils were among the first major arrivals at the site of the insect bite and were seen to engulf parasites, which remained viable and infective. Rather than helping the host deal with the parasite, this behavior made these innate immune cells unwitting accomplices in the ongoing process of infection.

Tethering Therapeutic T Cells

Considerable effort has been made in cancer immunotherapy in elaborating robust T cell responses to tumors. However, focusing a T cell's attention on its tumor target is difficult, often because tumor cells do not present sufficient distinguishing features from normal human cells for the immune system to detect. **Bargou *et al.*** (p. 974) overcome this by using a modified bi-specific antibody that simultaneously binds two different cell surface proteins: one on a killer T cell and one on the target tumor cells—in this case, non–Hodgkin's lymphoma B cells. By tethering the T cell to its intended target, the modified antibody forces direct killing of the lymphoma cells and, even at very low doses, could achieve measurable, or even complete, regression of cancer in a small number of patients who had proven refractory to existing therapies. Although the durability of this treatment needs careful follow-up, it offers further patient-based evidence that T cell–based immunotherapy may yet offer a viable means of treating cancer in the clinic.

Synaptic Coding Capacity

What is the contribution of single excitatory synaptic events to the representation of sensory stimuli? In vitro preparations have provided theoretical limits on single-input coding. However, analysis of stimulus-evoked unitary synaptic activity with physiologically relevant stimuli in vivo has been hampered by compound synaptic responses and poor stimulus control. Taking advantage of cerebellar granule cells as a model system with very few synaptic inputs and a well-controlled quantifiable vestibular stimulus, **Arenz *et al.*** (p. 977) explored sensory encoding at single synapses in vivo in real time over a broad range of stimuli. Unitary, direction-sensitive synapses report motion velocity by using a frequency code that is modulated around a tonic rate. The reliability of the synaptic signal ensures that velocity is represented linearly by charge transfer. Only 100 synapses were required for realistic velocity resolution, well within the number of inputs received by many neurons in dedicated sensory processing brain regions. Single-cell computation can thus easily achieve fine-scale reconstruction of sensory stimulus features.

CREDIT: NAVARRO *ET AL.*

M. R. C. Greenwood is chancellor emerita at the University of California, Santa Cruz; a professor of nutrition at the University of California, Davis; and past-president of the American Association for the Advancement of Science.

Gordon Ringold is the president of the University of California, Santa Cruz Foundation.

Doug Kellogg is chair of the Department of Molecular, Cell and Developmental Biology at the University of California, Santa Cruz.

Dying for Science?

MOST SCIENTISTS ARE DEVOTED TO THEIR WORK AND ARE PASSIONATE ABOUT THE POTENTIAL benefits their research brings to society. But are they and their families prepared to die for their work? Should this even be a consideration when these individuals are working under carefully legislated and legal research conditions? For 13 University of California, Santa Cruz (UCSC), researchers, some of whom work with mice and others with fruit flies, this became a sudden reality.

Two weeks ago, a UCSC neurobiologist at home with his wife and children was awakened before dawn by a firebomb and found his home filled with smoke. Fortunately, the family climbed out of their second-story rooms to safety. Another scientist's car was destroyed by a similar firebomb at about the same time. This is only the latest episode in a string of violence, with five firebombs targeting UC research faculty over the past 3 months. A spokesperson for the Animal Liberation Front press office, credited in press reports for these firebombing attacks, said, "This is historically what happens whenever revolutionaries begin to take the oppression and suffering of their fellow beings seriously, whether human or nonhuman. It is regrettable that certain scientists are willing to put their families at risk…."

These are criminal acts, being investigated as an attempted homicide by local, state, and federal authorities. It is of serious concern that these acts of terrorism and their associated incendiary statements were not immediately condemned by our political leaders. There have been no high-profile or unified statements about the incidents, and days afterward, California's governor had still declined to comment.

Those responsible must be prosecuted to the full extent of the law. Those who oppose animal research, even when conducted under strict federal and state laws, are free to express those beliefs. They are also free to reject the medicines—the fruits of animal research—that now allow us to treat disease and lead healthier lives. But they are not free to conduct a terror campaign. Scientists and their colleagues, from all disciplines, should speak out to galvanize support for expanded efforts to apprehend and prosecute these types of criminals. This may involve new laws and resources at both state and federal levels. Federal laws, including the Animal Enterprise Protection Act of 1992 and its subsequent 2006 modification, the Animal Enterprise Terrorism Act, provide some protections that could be further strengthened. In addition, because of jurisdictional issues, these laws are not always applicable to acts in individual states, and they do not provide for state prosecution.

State laws that reinforce these protections need to be enacted. A proposed bill in the California Legislature (AB2296), which would extend protection to "animal enterprise workers" similar to that provided for politicians and reproductive health workers, has been much weakened from its original intent. In its original form, it would have prevented the posting of personal information on Web sites with the intent to incite acts of violence or threaten researchers and their families. If passed, the current form of the bill only enacts a misdemeanor trespass law. This is potentially useful in investigating offenders, but does not have stringent penalties. Perhaps we can learn from laws elsewhere, such as the United Kingdom's Serious Organised Crime and Police Act of 2005, which has much stronger antiharassment clauses and penalties for interfering with contractual relations. Its enforcement has been credited with a reduction in such crimes in the UK.

In a 2008 national poll (conducted by Research!America), Americans overwhelmingly supported scientific research (83%). Nearly 70% are more likely to support a presidential candidate who supports research, 75% believe that it is important that the United States remains a leader in medical research, and 90% want the U.S. to train more scientists. Our scientific enterprise lies at the core of our economic success, national security, and our very well-being. This is why all concerned citizens should rally to the call to stop antiscience violence. Our political leaders must reject these criminal acts as forcefully as they reject all other forms of terrorism.

– M. R. C. Greenwood, Gordon Ringold, Doug Kellogg

10.1126/science.1164337

CREDIT: AP

EDITORS' CHOICE

EDITED BY GILBERT CHIN AND JAKE YESTON

MOLECULAR BIOLOGY

Variety from Repetitive DNA

Ionizing radiation is harmful to living creatures because it scythes through both strands of genomic DNA, leading to potentially lethal chromosome aberrations. To identify the origin of these aberrations, Argueso *et al.* have used x-rays to shred the genomes of diploid yeast cells and introduced a staggering ~250 DNA breaks per cell; within 3 hours, most of the shattered chromosomes had been stitched together, with half of the analyzed surviving cells harboring at least one chromosome aberration. A molecular autopsy revealed that most aberrations were associated with a repetitive sequence, the Ty retrotransposon, a selfish DNA element scattered throughout the yeast genome, and that the aberrations appeared to have arisen via failed DNA repair attempts. Normally, homologous chromosomes in a diploid cell allow one chromosome to act as a template for the repair of the other. For breaks that occur in or near Ty elements, rather than the homologous element being used, any of the Ty elements in the yeast genome might be selected, mixing chromosomal material and making repetitive DNA a driving force for genomic variation. — GR

Proc. Natl. Acad. Sci. U.S.A. **105**, 10.1073/pnas.0804529105 (2008).

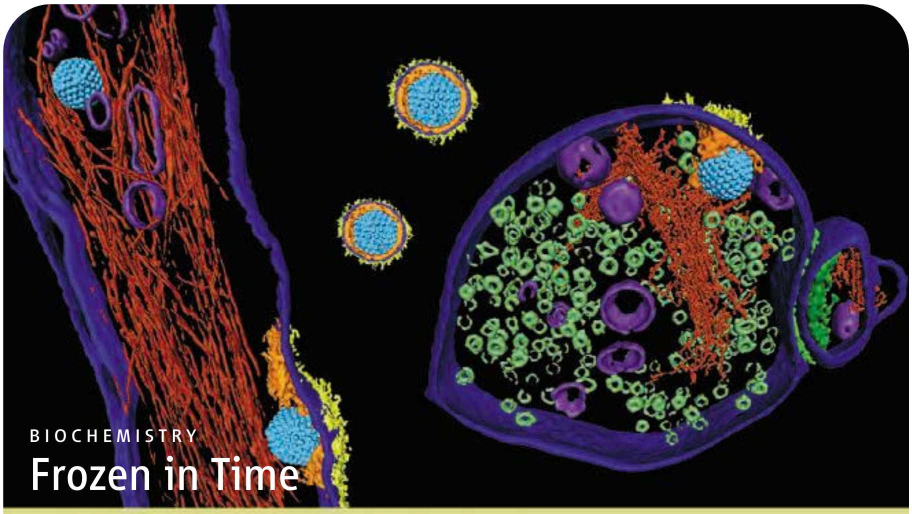

BIOCHEMISTRY

Frozen in Time

Insights into how an enveloped virus fuses with a cellular membrane have come primarily from high-resolution structures of individual virus proteins and from real-time, low-resolution fluorescence microscopy trajectories of virus particles during entry. Maurer *et al.* have used cryoelectron tomography to reconstruct three-dimensional images of herpes simplex virus type 1 (HSV-1) particles frozen in the process of entering kidney cells and synaptic nerve endings. HSV-1 particles consist of a glycoprotein-rich outer membrane surrounding an amorphous protein layer (the tegument) and an icosahedral capsid housing the DNA genome. Capsids (cyan in the figure) released into the cytoplasm left their clustered envelope glycoproteins (yellow) and tegument proteins (orange) at the site of entry and had entered the actin network (red) apparently without local actin depolymerization. Among the virus particles found docked at target cells were two whose envelopes had already been pulled into contact with the target membrane; one of these contained an open fusion pore of 25-nm diameter, indicating that the pore had already started expanding. In both cases, neighboring the region of membrane contact were hints of V-shaped densities connecting the membranes that could represent viral fusion proteins. — NM*

Proc. Natl. Acad. Sci. U.S.A. **105**, 10559 (2008).

PSYCHOLOGY

The Cost of Equal Opportunity

Lotteries have become a widespread means of generating billions of dollars for state treasuries in the United States. The low chances of winning life-style–altering prizes are prominently posted, yet many people, especially those in low-income brackets, pay $1 in order to receive only 50¢ in return, on average. What motivates such financially maladaptive behavior? Haisley *et al.* suggest that one contributory factor is the psychological desire to improve one's standing in a social hierarchy defined by one's friends and neighbors. When bus passengers earning $20,000 annually were subjected to a subtle manipulation (in the form of answering a survey), those induced to feel that their income was below average purchased twice as many scratch-off tickets as those placed at the midpoint of an income ladder. One reason why playing the lottery holds a differential appeal for lower-income individuals (and why they buy into this dream) is implicit in the winning chances, which though small, apply equally to all players, regardless of socioeconomic status. In a second field experiment, priming subjects with considerations of opportunity in the context of employment, elections, or gambling was also sufficient to induce them to purchase a greater number of lottery tickets. — GJC

J. Behav. Dec. Making **21**, 283 (2008).

GEOLOGY

Colder than Expected

Extensive glaciations on Earth have been rare since the Cambrian explosion of life, about 550 million years ago. Earth's recent Ice Age spans only the last 2.5 million years when extensive continental ice sheets grew in the Northern Hemisphere. A comparable glaciation seems to have occurred during the Late Carboniferous and Early Permian Periods, about 300 million years ago, when ice sheets covered regions toward the South Pole of a large single supercontinent (across what is now southern Africa, Australia, Antarctica, South America, and India). Soreghan *et al.* discuss evidence that some glaciation may have occurred even at tropical latitudes during this time. An exhumed low-elevation valley in the western United States has a "U" shape consistent with glacial formation and contains sediments that date to

---

*Nilah Monnier is a summer intern in *Science*'s editorial department.

CREDITS (TOP TO BOTTOM): MAURER ET AL., PROC. NATL. ACAD. SCI. U.S.A. 105, 10559 (2008); LENSCAP/ALAMY

this time and are consistent with glacial deposition. Thick windblown dust deposits derived from basement rocks, common around the large Pleistocene ice sheets, are common in rocks in southwestern North America. These observations, if indicative of persistent ice at low latitudes, pose a challenge to climate models even if atmospheric CO_2 levels were low at this time, as is thought. — BH

Geology **36**, 659 (2008).

MOLECULAR BIOLOGY

Silencing miRNAs

In embryonic stem cells, the genes that specify differentiated cells are silenced. The extent of regulation of microRNAs (miRNAs), which also contribute to tissue differentiation, has been unclear because of the difficulty in locating their promoters. Marson *et al.* have identified the promoters, using a tell-tale trimethylated histone, on the human and mouse genomes in embryonic stem cells and also in precursor neurons and embryonic fibroblasts. In stem cells, some miRNA promoters were occupied by the four transcription factors (Oct4/Sox2/Nanog/Tcf2) that confer embryonic cell pluripotency, and many of the miRNAs were actively transcribed. In contrast, a subset of these miRNA promoters was occupied by Polycomb group proteins, which are known to silence expression, and these Polycomb-bound miRNA genes were specifically induced in the neural precursors and the fibroblast cells. Therefore, like protein-encoding genes, miRNA genes that drive differentiation are repressed in embryonic stem cells. — KK

Cell **134**, 521 (2008).

CLIMATE SCIENCE

Cause of Death

During the mass extinction event that occurred 200 million years ago, at the end of the Triassic Period, around half of all extant species vanished. In the marine realm, about 20% of all families and more than 90% of the genera in some groups of organisms disappeared. What caused that catastrophe? One hypothesis is that elevated atmospheric CO_2 was the culprit, but evidence of that cause has been elusive. Hautmann *et al.* present data indicating that ocean acidification, possibly caused by high rates of magmatic CO_2 degassing and thermal dissociation of marine gas hydrates, was responsible for the burst of marine extinctions. They show that carbonate sedimentation was interrupted globally, and that organisms that had skeletons of aragonite or high-Mg calcite were preferentially affected. Thus, it seems that high concentrations of atmospheric CO_2 were in fact the proximal cause of the Triassic-Jurassic extinction event, a conclusion that has direct bearing on efforts to understand what may be the consequences of the buildup of atmospheric CO_2 that now is underway. — HJS

Neues Jahrb. Geol. Palaeontol. Abh. **249**, 119 (2008).

Science Signaling

AAAS

<<Two Pathways Are Better than One

Glutamate mediates functions such as synaptic plasticity, proliferation, and survival via metabotropic receptors (mGluRs) on neurons and glial cells. Sitcheran *et al*. demonstrate that glutamate promotes the binding of the p65 and p50 subunits of the transcription factor NF-κB to DNA. Glutamate activation of NF-κB was comparable to that produced by epidermal growth factor (EGF) binding to its receptor EGFR, which is found on astrocytes. Glutamate also induced the phosphorylation and activation of inhibitor of κB kinase α and β (IKKα and IKKβ) and of p65. In canonical NF-κB signaling, IKKβ phosphorylates IκBα, which leads to its degradation and the release of active NF-κB subunits, but glutamate did not increase phosphorylation or degradation of IκBα, although it did dissociate IκBα and p65. Knockdown of EGFR blocked mGluR5-stimulated phosphorylation of p65; conversely, mGluR5 stimulation led to the phosphorylation of tyrosine residues in EGFR and to its association with mGluR5. A Ca^{2+} chelator blocked mGluR5-mediated NF-κB activation, and an inhibitor of EGFR activity reduced mGluR5-stimulated Ca^{2+} signaling. Together, these data suggest that EGFR signaling is critical for the activation of NF-κB by glutamate. — JFF

Mol. Cell. Biol. **28**, 5061 (2008).

CREDIT: G. S. SOREGHAN

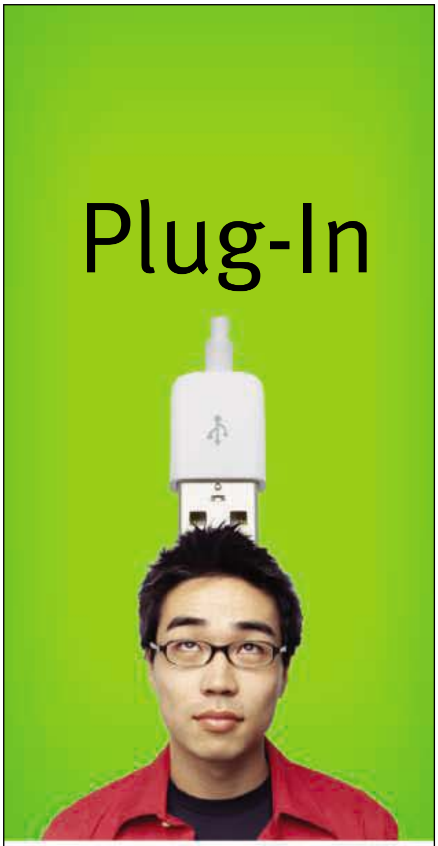

www.sciencemag.org

Science

1200 New York Avenue, NW
Washington, DC 20005
Editorial: 202-326-6550, FAX 202-289-7562
News: 202-326-6581, FAX 202-371-9227
Bateman House, 82-88 Hills Road
Cambridge, UK CB2 1LQ
+44 (0) 1223 326500, FAX +44 (0) 1223 326501

Subscription Services For change of address, missing issues, new orders and renewals, and payment questions: 866-434-AAAS (2227) or 202-326-6417, FAX 202-842-1065. Mailing addresses: AAAS, P.O. Box 96178, Washington, DC 20090-6178 or AAAS Member Services, 1200 New York Avenue, NW, Washington, DC 20005

Institutional Site Licenses please call 202-326-6755 for any questions or information

Reprints: Author Inquiries 800-635-7181
Commercial Inquiries 803-359-4578

Permissions 202-326-7074, FAX 202-682-0816

Member Benefits AAAS/Barnes&Noble.com bookstore www.aaas.org/bn; AAAS Online Store http://www.apisource.com/aaas/ code MKB6; AAAS Travels: Betchart Expeditions 800-252-4910; Apple Store www.apple/eppstore/aaas; Bank of America MasterCard 1-800-833-6262 priority code FAA3YU; Cold Spring Harbor Laboratory Press Publications www.cshlpress.com/affiliates/aaas.htm; GEICO Auto Insurance www.geico.com/landingpage/go51.htm?logo=17624; Hertz 800-654-2200 CDP#343457; Office Depot https://bsd.officedepot.com/portalLogin.do; Seabury & Smith Life Insurance 800-424-9883; Subaru VIP Program 202-326-6417; VIP Moving Services http://www.vipmayflower.com/domestic/index.html; Other Benefits: AAAS Member Services 202-326-6417 or www.aaasmember.org.

science_editors@aaas.org	(for general editorial queries)
science_letters@aaas.org	(for queries about letters)
science_reviews@aaas.org	(for returning manuscript reviews)
science_bookrevs@aaas.org	(for book review queries)

Published by the American Association for the Advancement of Science (AAAS), *Science* serves its readers as a forum for the presentation and discussion of important issues related to the advancement of science, including the presentation of minority or conflicting points of view, rather than by publishing only material on which a consensus has been reached. Accordingly, all articles published in *Science*—including editorials, news and comment, and book reviews—are signed and reflect the individual views of the authors and not official points of view adopted by AAAS or the institutions with which the authors are affiliated.

AAAS was founded in 1848 and incorporated in 1874. Its mission is to advance science, engineering, and innovation throughout the world for the benefit of all people. The goals of the association are to: enhance communication among scientists, engineers, and the public; promote and defend the integrity of science and its use; strengthen support for the science and technology enterprise; provide a voice for science on societal issues; promote the responsible use of science in public policy; strengthen and diversify the science and technology workforce; foster education in science and technology for everyone; increase public engagement with science and technology; and advance international cooperation in science.

Information for Authors

See pages 634 and 635 of the 1 February 2008 issue or access www.sciencemag.org/about/authors

EDITOR-IN-CHIEF **Bruce Alberts**
EXECUTIVE EDITOR **Monica M. Bradford**
DEPUTY EDITORS **R. Brooks Hanson, Barbara R. Jasny, Katrina L. Kelner**
NEWS EDITOR **Colin Norman**

Editorial supervisory senior editor Phillip D. Szuromi; **senior editor/perspectives** Lisa D. Chong; **senior editors** Gilbert J. Chin, Pamela J. Hines, Paula A. Kiberstis (Boston), Marc S. Lavine (Toronto), Beverly A. Purnell, L. Bryan Ray, Guy Riddihough, H. Jesse Smith, Valda Vinson; **associate editors** Jake S. Yeston, Laura M. Zahn; **online editor** Stewart Wills; **associate online editors** Robert Frederick, Tara S. Marathe; **web content developer** Martyn Green; **book review editor** Sherman J. Suter; **associate letters editor** Jennifer Sills; **editorial manager** Cara Tate; **senior copy editors** Jeffrey E. Cook, Cynthia Howe, Harry Jach, Barbara P. Ordway, Trista Wagoner; **copy editors** Chris Filiatreau, Lauren Kmec, Peter Mooreside; **editorial coordinators** Carolyn Kyle, Beverly Shields; **publications assistants** Ramatoulaye Diop, Joi S. Granger, Jeffrey Hearn, Lisa Johnson, Scott Miller, Jerry Richardson, Jennifer A. Seibert, Brian White, Anita Wynn; **editorial assistants** Carlos L. Durham, Emily Guise, Patricia M. Moore; **executive assistant** Sylvia S. Kihara; **administrative support** Maryrose Madrid

News deputy news editors Robert Coontz, Eliot Marshall, Jeffrey Mervis, Leslie Roberts; **contributing editors** Elizabeth Culotta, Polly Shulman; **news writers** Yudhijit Bhattacharjee, Adrian Cho, Jennifer Couzin, David Grimm, Constance Holden, Jocelyn Kaiser, Richard A. Kerr, Eli Kintisch, Andrew Lawler (New England), Greg Miller, Elizabeth Pennisi, Robert F. Service (Pacific NW), Erik Stokstad; **interns** Rachel Zelkowitz, Andrea Lu, Fayana Richards; **contributing correspondents** Jon Cohen (San Diego, CA), Daniel Ferber, Ann Gibbons, Mitch Leslie, Charles C. Mann, Virginia Morell, Evelyn Strauss, Gary Taubes; **copy editors** Linda B. Felaco, Melvin Gatling; **administrative support** Scherraine Mack, Fannie Groom; **bureaus** New England: 207-549-7755, San Diego, CA: 760-942-3252, FAX 760-942-4979, Pacific Northwest: 503-963-1940

Production director James Landry; **senior manager** Wendy K. Shank; **assistant manager** Rebecca Doshi; **senior specialists** Steve Forrester, Chris Redwood; **specialist** Anthony Rosen; **Preflight director** David M. Tompkins; **manager** Marcus Spiegler; **specialist** Jessie Mudjitaba

Art director Yael Kats; **associate art director** Aaron Morales; **illustrators** Chris Bickel, Katharine Sutliff; **senior art associates** Holly Bishop, Laura Creveling, Preston Huey, Nayomi Kevitiyagala; **associate** Jessica Newfield; **photo editor** Leslie Blizard

***Science* International**

Europe (science@science-int.co.uk) **editorial: international managing editor** Andrew M. Sugden; **senior editor/perspectives** Julia Fahrenkamp-Uppenbrink; **senior editors** Caroline Ash, Stella M. Hurtley, Ian S. Osborne, Peter Stern; **editorial support** Deborah Dennison, Rachel Roberts, Alice Whaley; **administrative support** John Cannell, Janet Clements, Louise Smith; **news: europe news editor** John Travis; **deputy news editor** Daniel Clery; **contributing correspondents** Michael Balter (Paris), John Bohannon (Vienna), Martin Enserink (Amsterdam and Paris), Gretchen Vogel (Berlin); **intern** Lauren Cahoon

Asia Japan Office: Asca Corporation, Eiko Ishioka, Fusako Tamura, 1-8-13, Hirano-cho, Chuo-ku, Osaka-shi, Osaka, 541-0046 Japan; +81 (0) 6 6202 6272, FAX +81 (0) 6 6202 6271; asca@os.gulf.or.jp; **asia news editor** Richard Stone (Beijing: rstone@aaas.org); **contributing correspondents** Dennis Normile (Japan: +81 (0) 3 3391 0630, FAX +81 (0) 3 5936 3531; dnormile@gol.com); Hao Xin (China: +86 (0) 10 6307 4439 or 6307 3676, FAX +86 (0) 10 6307 4358; cindyhao@gmail.com); Pallava Bagla (South Asia: +91 (0) 11 2271 2896; pbagla@vsnl.com)

Africa Robert Koenig (contributing correspondent, rob.koenig@gmail.com)

EXECUTIVE PUBLISHER **Alan I. Leshner**
PUBLISHER **Beth Rosner**

Fulfillment Systems and Operations (membership@aaas.org); **director** Waylon Butler; **senior systems analyst** Jonny Blaker; **customer service supervisor** Pat Butler; **specialists** Latoya Casteel, LaVonda Crawford, Vicki Linton; **data entry supervisor** Cynthia Johnson; **specialist** Tarrika Hill

Business Operations and Administration director Deborah Rivera-Wienhold; **assistant director, business operations** Randy Yi; **manager, business analysis** Michael LoBue; **manager, business operations** Jessica Tierney; **financial analysts** Benjamin Aronin, Priti Pamnani; **rights and permissions: administrator** Emilie David; **associate** Elizabeth Sandler; **marketing director** John Meyers; **marketing manager** Allison Pritchard; **marketing associates** Aimee Aponte, Alison Chandler, Mary Ellen Crowley, Marcia Leach, Julianne Wielga, Wendy Wise; **international marketing manager** Wendy Sturley; **marketing executive** Jennifer Reeves; **marketing/member services executive** Linda Rusk; **site license sales director** Tom Ryan; **sales manager** Russ Edra; **sales and customer service** Iquo Edim, Kiki Forsythe, Catherine Holland, Ilese Ominsky, Phillip Smith, Philip Tsolakidis; **electronic media: manager** Lizabeth Harman; **project manager** Trista Snyder; **assistant manager** Lisa Stanford; **senior production specialists** Christopher Coleman, Walter Jones; **production specialists** Nichele Johnston, Kimberly Oster

Advertising director, worldwide ad sales Bill Moran

Product (science_advertising@aaas.org); **midwest** Rick Bongiovanni: 330-405-7080, FAX 330-405-7081; **west coast/w. canada** Teola Young: 650-964-2266; **east coast/e. canada** Laurie Faraday: 508-747-9395, FAX 617-507-8189; **uk/europe/asia** Tracy Holmes: +44 (0) 1223 326525, FAX +44 (0) 1223 326532; **japan** Mashy Yoshikawa: +81 (0) 3 3235 5961, FAX +81 (0) 3 3235 5852; **senior traffic associate** Deiandra Simms

Commercial Editor Sean Sanders: 202-326-6430

Project Director, Outreach Brianna Blaser

Classified (advertise@sciencecareers.org); **us: recruitment sales manager** Ian King: 202-326-6528, FAX 202-289-6742; **inside sales manager: midwest/canada** Daryl Anderson: 202-326-6543; **inside sales representative** Karen Foote: 202-326-6740; **key account manager** Joribah Able; **northeast** Alexis Fleming: 202-326-6578; **southeast** Tina Burks: 202-326-6577; **west** Nicholas Hintibidze: 202-326-6533; **sales coordinators** Erika Foard, Rohan Edmonson, Shirley Young; **international: sales manager** Tracy Holmes: +44 (0) 1223 326525, FAX +44 (0) 1223 326532; **sales** Marium Hudda, Alex Palmer, Alessandra Sorgente; **sales assistant** Louise Moore; **japan** Mashy Yoshikawa: +81 (0) 3 3235 5961, FAX +81 (0) 3 3235 5852; **advertising production operations manager** Deborah Tompkins; **senior production specialists** Robert Buck, Amy Hardcastle; **senior traffic associate** Christine Hall; **publications assistant** Mary Lagnaoui

AAAS Board of Directors retiring president, chair David Baltimore; **president** James J. McCarthy; **president-elect** Peter C. Agre; **treasurer** David E. Shaw; **chief executive officer** Alan I. Leshner; **board** Lynn W. Enquist, Susan M. Fitzpatrick, Alice Gast, Linda P. B. Katehi, Nancy Knowlton, Cherry A. Murray, Thomas D. Pollard, Thomas A. Woolsey

AAAS
ADVANCING SCIENCE, SERVING SOCIETY

Wired Up

Deep brain stimulation (DBS) is looking ever more promising for people with persistent severe depression that resists drugs, therapy, and shock treatments.

A team at the University of Toronto in Canada and Emory University in Atlanta, Georgia, has treated 20 patients for a year or more with DBS—a technique also tried for Parkinson's disease and severe obsessive-compulsive disorder. The researchers, led by Toronto neurosurgeon Andres Lozano, targeted an area called the subcallosal cingulate gyrus, which brain imaging has shown to be hyperactive in severe depression. They surgically inserted electrodes into each side of a patient's brain, ran wires under the skin down the neck, and attached them to a low-voltage pulse generator embedded under a collarbone. Patients then came in regularly for monitoring and tune-ups. Sixty percent of them improved significantly, and about one-third achieved remission.

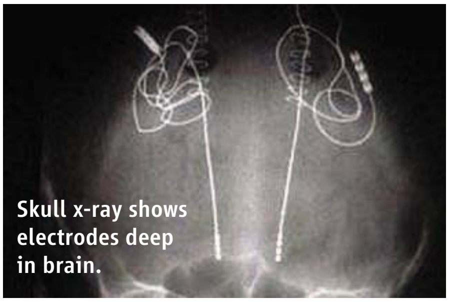

Skull x-ray shows electrodes deep in brain.

Psychiatrist Helen Mayberg, a co-author, says it's still unclear why DBS works. It may stimulate some neurocircuitry, stop abnormal firing in other circuits, or cause the release of neurotransmitters affected by antidepressants, the team reported online last month in *Biological Psychiatry*.

"The results are encouraging," says Wayne Goodman, a psychiatrist at the National Institute of Mental Health in Bethesda, Maryland. But DBS is still brain surgery, so it's a last resort.

STEM CELL STRUGGLES

"Between the opposition and lack of funding, it's been a battle to survive for the last 10 years. … This is at least the sixth time we've had the telephones turned off."

—Robert Lanza, chief scientist at Advanced Cell Technology, pioneering company in research on human embryonic stem cells that has been reported to be in a financial crisis.

Ant Traffic Solutions

How do ants avoid gridlock when their trails narrow into one-way paths? Vincent Fourcassié, a biologist at Paul Sabatier University in Toulouse, France, decided the question needed answering, so he and colleagues set up experiments in which ants had to cross a narrow bridge to get from nest to foraging site and back.

It turned out that different species follow different rules to determine who goes first. The black garden ant, *Lasius niger*, which feeds on sugary excretions from aphids, won't enter the bridge if another ant is crossing from the opposite direction. In contrast, the leaf-cutter ant, *Atta colombica*, which farms fungi for food on beds of shredded leaves, will make way for ants carrying leaves back to the colony. Fourcassié reported the results last month at the European Conference on Behavioural Biology in Dijon, France.

Guy Théraulaz, a biologist at Paul Sabatier University who studies traffic in animals and humans, says this kind of research shows how simple algorithms followed by individuals lead to complex behaviors—in this case, smoothly flowing two-way traffic on a single-lane track.

Get Back, Get Back

Yesterday, all your troubles seemed so far away. But what about your memories? Scientists in the United Kingdom are launching the Magical Memory Tour, a study that uses people's recollections of the Beatles as a lens to look at what they have retained about their lives.

The project, an online survey devised by psychologists Martin Conway and Catriona Morrison at the University of Leeds, U.K., asks people to describe the first memory that comes to mind related to the Fab Four—such as a movie, a news item, or a pot-addled night listening to *Sgt. Pepper*.

"We are interested in what types of information are mentioned with what frequency," says Conway, as well as the emotions associated with those memories. The researchers are particularly interested in the respondent's age at the time the memory was encoded. Although scientists have studied "flashbulb" events such as the J.F.K. assassination, the researchers believe that with the Beatles' impact spanning generations and cultures, they can gain a broad perspective on how our personal memories develop and change. From the 3000 responses received so far, Conway says, it's clear there is "a strong reminiscence bump" in data from the over-30 population, consisting of memories from when they were about 15 to 25. Some events—such as John Lennon's murder—may be "immune to the reminiscence bump," Conway adds.

The results will be unveiled at the British Association for the Advancement of Science's Festival of Science, to be held 6 to 11 September in Liverpool.

CREDITS (TOP TO BOTTOM): AUDREY DUSSUTOUR, U. SYDNEY; HELEN MAYBERG/EMORY UNIVERSITY; DEA/A. DAGLI ORTI/GETTY IMAGES

Science ONLINE

www.sciencemag.org

Water walker.

SCIENCE**NOW**

www.sciencenow.org

HIGHLIGHTS FROM OUR DAILY NEWS COVERAGE

Water Striders Put Best Foot Forward
New calculation shows water-walking bugs have evolved feet of optimal length.

Threading Light Through the Opaque
Experiment confirms that light can be passed through disordered materials.

They Smell Like Twins
Sweaty study reveals that genetics determines body odor.

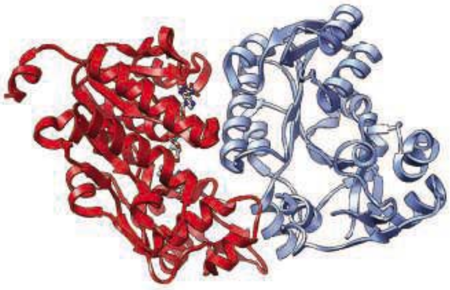

NADP-binding produces an asymmetric dimer.

SCIENCE **SIGNALING**

www.sciencesignaling.org

THE SIGNAL TRANSDUCTION KNOWLEDGE ENVIRONMENT

PERSPECTIVE: Dinucleotide-Sensing Proteins—Linking Signaling Networks and Regulating Transcription
H. K. Lamb, D. K. Stammers, A. R. Hawkins
Proteins that bind NAD(H) or NADP(H) may couple cellular redox state to transcription or other signaling pathways.

PERSPECTIVE: Great Times for Small Molecules—c-di-AMP, a Second Messenger Candidate in Bacteria and Archaea
U. Römling
The bacterial checkpoint protein DisA has diadenylate cyclase activity, suggesting that c-di-cAMP acts as a second messenger.

The basics of peer review.

SCIENCE **CAREERS**

www.sciencecareers.org/career_development

FREE CAREER RESOURCES FOR SCIENTISTS

Learning the Ropes of Peer Reviewing
E. Pain
Peer review demands a blend of critical skills, honesty, and empathy.

If at First You Don't Succeed, Cool Off, Revise, and Submit Again
L. Laursen
Rejection can be a constructive part of the publication process, really.

The *Science* Careers Web Log
Science *Careers Staff*
Here's where to find information from around the Web on careers in science.

SCIENCE**PODCAST**

www.sciencemag.org/multimedia/podcast

FREE WEEKLY SHOW

Download the 15 August *Science* Podcast to hear about ancient paintings inside France's Chauvet Cave, T cell-based cancer immunotherapy, modeling aerosols in the Amazon, and more.

Separate individual or institutional subscriptions to these products may be required for full-text access.

CREDITS: (SCIENCE NOW) ROSALIE LARUE/YELLOWSTONE NATIONAL PARK/NPS; (SCIENCE CAREERS) VAIKUNDA RAJA/CREATIVE COMMONS; (SCIENCE SIGNALING) CHRIS BICKEL

Seasonal forecasts improve 900

HIV/AIDS summit short on science 902

Full circle. The 2001 anthrax attacks originated in a lab that helped investigate the attacks, the FBI says.

CREDIT: REUTERS/CORBIS

ANTHRAX INVESTIGATION

Full-Genome Sequencing Paved the Way From Spores to a Suspect

The scientific evidence against Bruce Ivins, the 62-year-old Army scientist who killed himself while about to be indicted for the anthrax murders, is finally emerging. Last week, the Federal Bureau of Investigation (FBI) laid some of its cards on the table. One key document, scientists say, now enables a reconstruction of the trail that led the FBI from the deadly letters back to Ivins's lab at the U.S. Army Medical Research Institute of Infectious Diseases (USAMRIID) in Fort Detrick, Maryland.

The investigation relied heavily on outside labs such as The Institute for Genomic Research (TIGR) in Rockville, Maryland, which sequenced a large number of anthrax samples; it also required the development of new genetic tests. Although none of the steps was revolutionary or particularly inventive, researchers say, combining them to solve a criminal case was. Surprisingly, many past speculations on the forensic science were wrong on one point: Sophisticated fingerprinting techniques for *Bacillus anthracis* developed at Northern Arizona University (NAU) in Flagstaff, widely rumored to be crucial, didn't play a significant role.

Scientists say they need many more details to decide the merits of the case against Ivins. But despite the bureau's widely ridiculed mistakes—including an early focus on Ivins's former colleague Steven Hatfill—"the scientific evidence is probably really strong," says Steven Salzberg, a former TIGR researcher now at the University of Maryland (UMD), College Park. "They've got some very good people," Salzberg says. "The impression that they're not good may just come from their style. They never tell you anything."

The main document unsealed last week is an October 2007 affidavit by Thomas Dellafera, a postal inspector. Filed in support of a warrant to search Ivins's home, cars, and a safety box, the 25 pages of text didn't spell out the details of the evidence. But a close reading of the four paragraphs about the FBI's genetic analysis helps clarify how the bureau approached the problem, says microbiologist Jeffrey Miller of the University of California, Los Angeles.

The key to understanding the investigation is that the anthrax used in the attacks didn't have a single, uniform genetic makeup, a source close to the investigation says. Each of the envelopes likely contained many billions of spores; within such a population, there are always subpopulations of cells bearing mutations that set them apart from the majority. The same minorities would presumably have been present in the "mother stock" of anthrax from which the spores were prepared.

However, standard sequencing—which would require the DNA from thousands of spores—would have resulted in a "consensus sequence" for the spores, in which such rare mutations were simply drowned out. To find them, researchers used a different technique: They grew spores from the envelopes on petri dishes, generating hundreds or even thousands of colonies per dish, each the progeny of a single spore. They then searched for colonies that looked different from the majority; the affidavit mentions variations in "shape, color, texture." (Those colonies might have been rough instead of smooth, or much smaller than most, Miller says.) Next, they set out to find the mutations that made those colonies different.

To do that, the FBI used a brute-force approach: It had the entire genomes of the bacteria in the minority sequenced. TIGR—which merged into the J. Craig Venter Institute in 2006—sequenced "probably somewhere between 10 and 20" such genomes in the years after the attacks, Salzberg says. TIGR could not handle live anthrax cells itself; the FBI gave the lab purified DNA produced by Paul Keim's lab at NAU, Salzberg says. Claire Fraser-Liggett, who led TIGR at the time and is now also at UMD, declines to discuss details of the investigation. But two other sources confirm TIGR's role.

Comparing the sequence of the variant colonies to an original *B. anthracis* strain called Ames, widely used in research, identified a number of mutations, says Salzberg; they included single-nucleotide polymorphisms, a change of a single base pair, and tandem repeats, in which a short piece of DNA is repeated a variable number of times.

The FBI then had scientists at other labs develop tests that allowed them to screen any anthrax sample for four of these mutations. Such assays "are very easy to design," for instance, using a polymerase chain reaction–based strategy, says evolutionary biologist Richard Lenski of Michigan State University in East Lansing; molecular biology labs do it all the time.

Armed with the four tests, the FBI examined more than 1000 anthrax isolates, col-

lected from 16 labs that had the Ames strain in the United States and several more in Canada, Sweden, and the United Kingdom. In only eight of those samples, they found all four mutations seen in the envelope samples; and each of these eight, the affidavit says, was "directly related" to a "large flask" of spores, identified as RMR-1029, which Ivins had created in 1997 and of which he was the "sole custodian."

That still leaves many questions open, researchers say. One thing that needs to be explained, says Miller, is whether the eight isolates that were "directly related" to RMR-1029 were all found at USAMRIID, or whether some came from other laboratories. In the latter case, it's unclear why the FBI ruled out those labs as the potential origin. (One clue that the affidavit offers is that USAMRIID is the only lab in Maryland or Virginia, the states where the particular envelopes used in the attacks were sold.)

It's also unclear how many of the 1000 samples had fewer than four, but more than zero, of the mutations. "If a whole bunch of them had two or three," that would increase the odds that the perfect match at USAMRIID was just a false positive, Lenski says. Another key question, he adds: Where in the anthrax genome did the four mutations occur? If they were in hypervariable regions, that would also probably make the case against Ivins weaker.

Whether the analysis would hold up in court seemed to be front and center in the FBI's thinking, says Salzberg. For instance, when researchers from TIGR and NAU published a comparison of two anthrax strains in *Science* in 2002 (14 June 2002, p. 2028), a top FBI researcher named Bruce Budowle encouraged them to include a statistical analysis to estimate the data's accuracy, Salzberg says. "Budowle felt it would be useful to have it all go through peer review, in case it went to court," he says.

The FBI has invested heavily in microbial forensic expertise since 2001, and Budowle has co-authored many papers on the topic. But the bureau farmed out much of the scientific bench work, in part because the Marine Corps doesn't allow bioweapons agents at its base in Quantico, Virginia, where the FBI Laboratory is located. The work was "highly compartmentalized," says a source close to the investigation: Most labs didn't know exactly what the others were doing.

The affidavit is very unclear about whether the spore preparations might have undergone physical or chemical treatments to make them disperse more easily—still a point of major confusion, says Barbara Hatch Rosenberg, a bioweapons specialist at Purchase College in New York. Scientists at the Armed Forces Institute of Pathology reported in October 2001 that the spores sent to U.S. Senator Tom Daschle's office had been mixed with silica to make them more easily dispersible. However, in congressional briefings and in a paper published in the August 2006 issue of *Applied and Environmental Microbiology*, FBI officials described the powder as a simple spore preparation without additives.

Anthrax: From Spores to Source

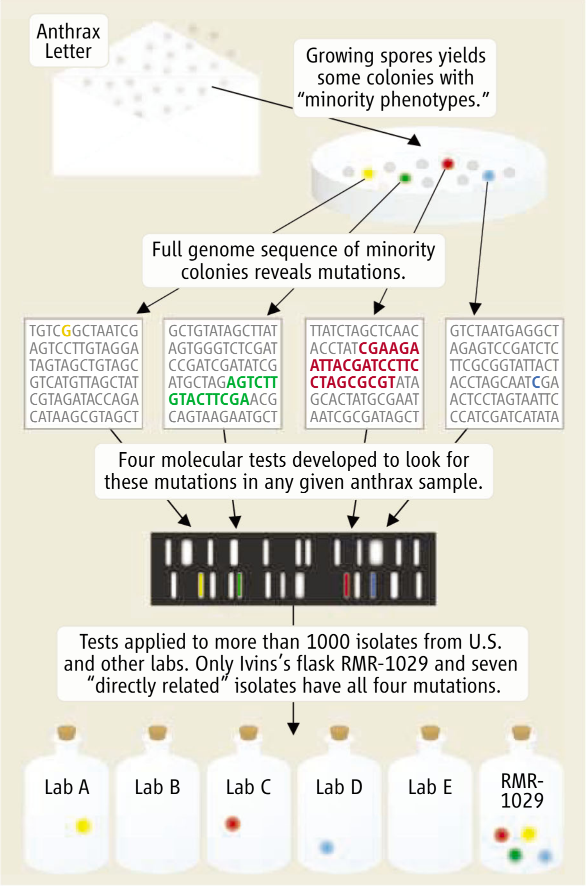

CREDIT: J. NEWFIELD/SCIENCE

The affidavit reports that there was "an elemental signature of Silicon within the spores" in all four letters that were recovered. This silicon signature is later cited as part of the evidence linking the mailed anthrax to the flask of spores that Ivins had access to. But what the silicon was for, or whether other samples were tested for the signature, remains unclear.

Science aside, the affidavit relies heavily on circumstantial evidence. For instance, it notes unexplained spikes in Ivins's nighttime lab activity right before the two waves of letters were sent. It also claims that he tried to mislead investigators to hide his involvement. In April 2002, he submitted samples from his lab that tested negative for the four mutations, according to the affidavit; but on 7 April 2004, an FBI agent seized the RMR-1029 flask, which tested positive for all four. Ivins insisted he had given agents RMR-1029 the first time around, however.

One of the weak points in the affidavit is Ivins's motive, says Gregory Koblentz, a biodefense specialist at George Mason University in Fairfax, Virginia. The FBI suggests that Ivins was afraid of losing his job if the government ended a project he was working on that was trying to solve regulatory issues around the so-called AVA anthrax vaccine. It "seems a bit of a stretch" that Ivins would have thought his job hinged on that project, says Koblentz. His group "would have had plenty of other anthrax vaccine–related work to keep them busy." A glaring omission, meanwhile, is any evidence placing Ivins in Princeton, New Jersey, on any of the days the envelopes could have been mailed from there.

A spokesperson for the FBI's laboratory declined a request to interview Budowle and referred scientific questions to the FBI's Washington, D.C., field office. "In the near future the FBI will determine the best way to address the science involved in the anthrax case," the spokesperson e-mailed *Science*. Many suspect that with so many burning questions, a full account of the evidence—including the scientific details—is now just a matter of time.

–MARTIN ENSERINK

With reporting by Yudhijit Bhattacharjee.

CLIMATE PREDICTION

Seasonal-Climate Forecasts Improving Ever So Slowly

Farmers, ski-resort operators, and heating-oil suppliers would very much like to know what the coming winter will be like. If a strong El Niño were brewing in the tropical Pacific, at least some of them would be in luck. The official United States winter forecast could warn them, with considerable reliability, that the Southeast and the Gulf Coast will be cooler and wetter than normal. But without an El Niño or its counterpart, La Niña, next winter's weather is pretty much anybody's guess.

Of the dozens of forecasting techniques proffered by government, academic, and private-sector climatologists, all but two are virtually worthless, according to a new study. "There are seasons, places, and situations in which skill is very, very good," says climatologist and study co-author Robert Livezey, recently retired from the National Weather Service (NWS). But even many people in the field "don't appreciate how little there is to work with. There is really no evidence here that there are any other silver bullets" waiting to be found.

Since 1946, NWS forecasters have been trying to forecast the average temperature and precipitation across the lower 48 states a month ahead, and more recently season by season up to a year ahead. At NWS's Climate Prediction Center (CPC) in Camp Springs, Maryland, where Livezey oversaw seasonal forecasting in the late 1990s, the trick has generally been to identify some element of recent or current climate—say, the presence of El Niño—that can influence future climate. If they couldn't find one, researchers could fashion a forecast "tool"—such as a collection of past time periods when the climate system resembled the current situation—that when tested on past seasons gave some inkling of future seasons. They would then subjectively choose which techniques to combine and how to combine them in order to predict whether temperature and precipitation would be above, near, or below normal in some 3-month period in a particular region.

The CPC approach has shown very modest though increasing skill at CPC, Livezey and climatologist Marina Timofeyeva of NWS in Silver Spring, Maryland, report in the June issue of the *Bulletin of the American Meteorological Society*. They worked up a scorecard for CPC forecasts made from 1994 to 2004, comparing the success rates for different seasons, regions, and periods when a strong El Niño or La Niña was present or absent.

About the only time forecasters had any success predicting precipitation was for winters with an El Niño or a La Niña, Livezey and Timofeyeva found. Using a scale in which mere chance is 0% and perfection is 100%, in those winters they estimate "unprecedented" skill—50% to more than 85%—along the southern tier states and up the West Coast about half a year into the future. Even so, the overall skill score for precipitation was just 3%.

Temperature forecasts fared better, with an overall skill score of 13%, up from a score of 8% for the previous decade. El Niño and La Niña helped out again during winter, raising skill to more than 85% across much of the eastern United States out to more than 8 months. But CPC also had substantial success predicting temperature out to a year in the American

APPLIED PHYSICS

Bizarre 'Metamaterials' for Visible Light in Sight?

When, in 2000, physicists unveiled the first "left-handed metamaterial"—an assemblage of metallic rods and rings that interacted with and bent microwaves in strange ways—physicists immediately knew they had a grand goal to shoot for: miniaturized metamaterials that would bend visible light in the same way. If such things could be made, they could result in wild devices, such as a "superlens" that would focus light tighter than any conventional lens. Metamaterials might be used to make invisibility cloaks, too, researchers have since shown. Now, metamaterials for visible light may be within reach, thanks to advances reported this week online in *Nature* and on page 930 of this issue of *Science*.

Both results come from the lab of Xiang Zhang, an applied physicist at the University of California, Berkeley. In *Nature*, Zhang's team describes a metamaterial that works for near-infrared light and, unlike previous materials, is three-dimensional. In *Science*, the team presents a different three-dimensional metamaterial that bends visible red light in the desired way.

Opinions vary as to how substantial the advances are. "With the *Science* paper, we are really very, very close" to applications with visible light, says Costas Soukoulis, a physicist at Iowa State University in Ames and the Department of Energy's Ames Laboratory. But Henri Lezec, an electrical engineer at the National Institute of Standards and Technology (NIST) in Gaithersburg, Maryland, says "the claims are misstated and overhyped."

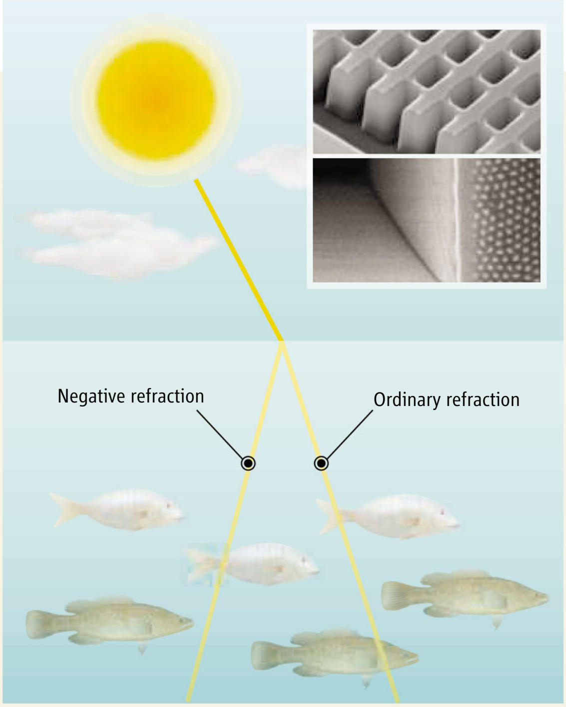

Kinky. A metamaterial full of holes (top inset) bends infrared light in an unusual way. Another full of silver nanowires (bottom inset) works in the visible.

CREDIT: N. KEVITIYAGALA/*SCIENCE*, INSETS: J. VALENTINE *ET AL*./*NATURE*; J. YAO/UC BERKELEY

Metamaterials put a kink in the way light usually passes from one medium into another. Suppose light from the setting sun

Spot on. Forecasters nailed California's 1997–'98 winter forecast thanks to El Niño.

West outside of El Niño–La Niña years, thanks to the long-term greenhouse warming trend picked up by one of the forecast tools.

Because a strong El Niño or La Niña shows up only every few years, his results paint "a kind of discouraging picture" of seasonal forecasting, Livezey says: "You can probably find dozens of forecast [techniques] people use to give themselves an edge. Almost all of that is mumbo jumbo." CPC forecasters have done well to make their forecasts more objective in recent years, Livezey and Timofeyeva write; CPC should weed out remaining weak forecast tools and focus future research on computer model forecasting of climate months ahead.

"This is a very tough business," agrees CPC's head of forecast operations, climatologist Edward O'Lenic. But he says Livezey and Timofeyeva's analysis of past skill "does have some flaws" that make it underrate CPC's performance, and he thinks some of the forecast tools they dismiss may still prove useful in ways researchers don't yet understand.

Climatologist Anthony Barnston of Columbia University's International Research Institute for Climate and Society in Palisades, New York, leans toward what he calls O'Lenic's "philosophical" preference for being more inclusive of forecasting tools. But Barnston agrees with Livezey that modeling holds the greatest promise for improving seasonal forecasting. **–RICHARD A. KERR**

shines on a pond. As light waves strike the surface, their direction will change so that they flow more directly down into the water. (See diagram.) Such "refraction" arises because the light travels more slowly in water than in air, giving water a higher "index of refraction." Still, the light continues to flow from west to east. Were water a left-handed metamaterial, however, "negative refractions" would bend the light back toward the west.

To produce the effect for near-infrared light, Zhang, Jason Valentine, and colleagues created a material that looks like a miniature waffle. They laid down 21 alternating layers of conducting silver and insulating magnesium fluoride on a quartz substrate and drilled holes in the stack using an ion beam. They cut the stack at an angle to make a prism and showed that it bent light the "wrong" way compared with an ordinary prism. To achieve negative refraction in the visible range, Zhang, Jie Yao, and the team used a standard electrochemical technique to make a sample of aluminum oxide filled with a regular array of nanometer-sized holes, which they filled with silver. When they shined red light onto the sample at an angle, it underwent negative refraction.

That might seem to seal the deal, but not everyone is convinced. Lezec argues that the infrared metamaterial isn't truly three-dimensional because it works for light coming from only a narrow range of directions. The metamaterial that bends visible light works for light of only a single polarization, he notes. And all agree that, strictly speaking, it does not have a key property—a negative index of refraction—although the infrared metamaterial does.

That's nitpicking, says Vladimir Shalaev, a physicist at Purdue University in West Lafayette, Indiana. "What's wrong with [using] a particular polarization?" he says. "As a first step, it's not so bad." The real advance in the *Science* paper may be a new self-organizing approach to fashioning the materials, Shalaev says. Soukoulis warns that researchers must confront a basic problem: At shorter wavelengths, metamaterials absorb far too much light. For now, however, the future for metamaterials looks particularly bright.

–ADRIAN CHO

CREDIT: GEORGE NIKITIN/AP PHOTO

The Stars Are Out in China

BEIJING—China is building a new set of ears tuned to our nearest star. Last month, the government of Inner Mongolia provided land to the National Astronomical Observatories of the Chinese Academy of Sciences for the Chinese Spectral Radioheliograph (CSRH), one of two major ground-based solar instruments that China's scientific community plans for the coming decade. Construction will begin later this month on the $7.3 million facility, which will listen in on radio bursts that could presage coronal mass ejections and solar flares. When directed at Earth, these ionic tidal waves can trigger geomagnetic storms that disable satellites and knock out power grids. Set to open in 2010, CSRH will consist of 40 radio dishes, each 4.5 meters wide. They will be clustered on the steppe in a zone devoid of earthly radio waves—apart from stray cell phone signals—260 kilometers northwest of Beijing.

Meanwhile, there's work on a complementary facility, the Frequency-Agile Solar Radiotelescope (FASR). In June, the National Radio Astronomy Observatory (NRAO) and several university partners asked the U.S. National Science Foundation for $25 million to build FASR at Owens Valley Radio Observatory in California. If they receive the funds, the consortium wants to begin building a prototype array at Owens Valley next year, says NRAO's Tim Bastian. **–RICHARD STONE**

Changes to Species Law Draw Fire

The U.S. Department of the Interior has proposed loosening rules controlling how the government follows the Endangered Species Act in building and permitting highways, dams, and other projects. Currently, federal officials must consult scientists in the U.S. Fish and Wildlife Service or National Oceanic and Atmospheric Administration if the proposed projects "may" affect endangered species. Under the changes, officials would ask for consultations only if they "anticipated" impacts on threatened species. The Administration says the changes will reduce paperwork so that "more time and resources can be devoted to the protection of the most vulnerable species." But former U.S. Forest Service ecologist Robert Mrowka, now with the Tucson, Arizona–based Center for Biological Diversity, says the rules are "like the fox guarding the hen house" and remove independent scientists from the review process. **–ELI KINTISCH**

Dead reckoning. Protesters urged Abbott to lower its price of the anti-HIV drug Kaletra in Mexico.

HIV/AIDS

Treatment and Prevention Exchange Vows at International Conference

MEXICO CITY—AIDS researchers have long argued that HIV prevention and treatment efforts should go hand in hand, but they rarely do. Their fickle relationship received intense scrutiny at the XVII International AIDS Conference held here last week. "They keep going to the altar," said Myron "Mike" Cohen of the University of North Carolina (UNC), Chapel Hill, in a plenary presentation. "They never get married. They have to get married today."

More than 20,000 researchers, health care workers, representatives from hard-hit communities, and activists attended the conference, which had never been held in Latin America before. The meeting ran 3 to 8 August, and about one-fourth of the participants came from the region.

As usual at these gatherings, science shared the limelight with diverse issues such as scaling up access to anti-HIV drugs, the increasing criminal prosecution of people who infect others, and the need for countries to address their epidemics in ostracized groups. Protests were more muted than in past years, although several added a novel Latin American spice to this conference staple.

New research findings were fewer and farther between than ever, creating the sense that the meeting has evolved into a giant review paper rather than a place for colleagues to share their latest data. "This is more a world AIDS summit, where every 2 years we reexamine everything we know," said Julio Montaner, the new president of the International AIDS Society (IAS), the meeting's organizer.

Cohen was one of several presenters who stressed that the great gains in treatment have overshadowed prevention needs. Today, 3 million people in low- and middle-income countries receive anti-HIV drugs, but an estimated five people become infected for every two on treatment. "There has not been that push for prevention as there's been for treatment," said Peter Piot, head of the Joint United Nations Programme on HIV/AIDS. "If we thought the first phase was hard, we have to prepare for even tougher times."

Piot also noted that the characteristics of the epidemic keep changing in different locales, urging countries to "know their epidemics" and target prevention to the most vulnerable groups. In Thailand, where the epidemic has been concentrated among injecting drug users and sex workers, married women now account for more new infections than any other group. In parts of sub-Saharan Africa, where epidemics have been primarily driven by heterosexual sex, injecting drug use is an increasingly important mode of spread. China, which has a large number of infected injecting drug users, today has a growing epidemic in men who have sex with men. In the United States, infections of whites peaked in the mid-1980s; blacks now account for 45% of the new infections and have an eight times higher risk of becoming infected, according to new estimates published by the U.S. Centers for Disease Control and Prevention (CDC). "The end of AIDS is nowhere in sight," said Piot.

Efficacy Trials of Biomedical Prevention

Intervention	Completed	Effective
Male circumcision	3	3
HSV-2 suppression	2	0
Bacterial STI treatment	5	1
Cervical barriers	1	0
Microbicides	9	0
Vaccines	4	0
Total	**24**	**4**

Little success. This prevention scorecard shows a stark bottom line for pills, shots, gels, and diaphragms.

The success with combinations of potent anti-HIV drugs, which reduce the amount of virus people carry and make them less infectious, has led to the increasing awareness that treatment *is* prevention, both for individuals and populations. But the degree to which the drugs can prevent infections has proved highly contentious.

A statement issued by the Swiss Federal Commission for HIV/AIDS in January on this topic served as a lightning rod. After reviewing the scientific literature, the Swiss commission concluded that a heterosexual person faced virtually no risk of becoming infected by having unprotected sex with an HIV-infected person on continued treatment, provided that person had undetectable levels of virus in the blood for 6 months and no sexually transmitted infections. The statement stopped short of explicitly discounting the value of condoms, but many thought that was its implicit message.

"There's condom absolutism, and everyone who questions it is put into controversy," said Bernard Hirschel, who heads the HIV/AIDS program at the University Hospital, Geneva. The main aims of the statement, he said, were to tell "discordant" couples—in which one is infected and the other isn't—who met these criteria that they could safely try to have children and also to combat a Swiss law that says an HIV-infected person who has sex without a condom can be held criminally liable, even in the absence of infecting a consenting partner.

Kevin De Cock, head of HIV/AIDS for the World Health Organization, and others

CREDIT: J. COHEN/*SCIENCE*; SOURCE: JUDITH WASSERHEIT/UW, NANCY PADIAN/UCSF

blasted the statement as irresponsible. “It just doesn’t seem like a cautious public health recommendation,” said De Cock. “I don’t think anyone’s shown the threshold below which people cannot transmit.”

A model published in the 26 July issue of *The Lancet* by David Wilson and colleagues at the University of New South Wales in Sydney, Australia, further emphasized the dangers. The study devised a mathematical model to compare 10,000 discordant couples that had unprotected sex for 10 years with the same number of couples who used condoms 80% of the time. The risk of transmission increased four times in the unprotected group because of occasional viral rebounds that happen to people on effective treatment.

Also hotly contested was the degree to which ongoing treatment can prevent transmission on the population scale. IAS President Montaner, a researcher at the University of British Columbia, co-authored an article in the 1 July issue of the *Canadian Medical Association Journal* that contends that potent treatment led to a decrease in HIV’s spread in British Columbia. Specifically, their study notes that new HIV infections dropped about 50% in British Columbia from 1995 to 1998, the years when highly potent anti-HIV drugs first became available. During the same years, syphilis infections increased, suggesting that the drop was not due to condom use or other behavioral changes. “Antiviral therapy greatly lowers infectiousness,” contended Montaner.

Got condoms? Jorge Saavedra, the openly gay and HIV-infected head of Mexico’s national HIV/AIDS program, promotes safe sex and denounces homophobia wherever he goes.

CREDIT: INTERNATIONAL AIDS SOCIETY/MONDAPHOTO

But epidemiologist Geoffrey Garnett of Imperial College London countered that antiretroviral drugs are unlikely to make a large impact on transmission on a global scale. Roughly 80% of infected people do not even know their status. Of those who do, most are not eligible for free treatment until their immune systems have been substantially damaged—which means most transmissions occur long before people are taking the drugs.

Garnett and others encouraged their colleagues to embrace the notion of “combination prevention.” No currently available intervention can by itself turn an epidemic around, but by combining treatment with preventive measures such as condoms and circumcision, it may be possible to create “a natural synergy,” Garnett said. “Rather than arguing for a single magic bullet, we really need to be trying to focus everything that we can on what works to realize these natural synergies.”

The growing enthusiasm for combination prevention in part reflects the dispiriting fact that the vast majority of biomedical prevention studies, from large human vaccine trials to microbicides to treatment of sexually transmitted diseases, have failed (see table). Still, many investigators have high hopes for what could be something of a magic bullet: pre-exposure prophylaxis (PrEP), which gives anti-HIV drugs to *un*infected people. The idea is that people at high risk of infection will take the drugs shortly before having sex, much in the way that people take antimalarial drugs before visiting countries where that disease is prevalent. Studies around the world are now enrolling more than 18,000 people to test this concept—more than the number of people in AIDS vaccine trials, noted Mitchell Warren, head of the AIDS Vaccine Advocacy Coalition in New York City. UNC’s Cohen predicted that PrEP, similar to the successful strategy used to prevent transmission of HIV from an infected, pregnant woman to her baby, “is almost certain to work.”

The approach has had remarkable success in monkeys. Walid Heneine of CDC in Atlanta, Georgia, described experiments in which he and his colleagues inserted anti-HIV drugs into the vaginas of six monkeys and then 30 minutes later tried to infect the animals with vaginal infusions of an engineered AIDS virus. None of the animals became infected after 20 such “challenges,” whereas seven of eight untreated control animals did.

Anthony Fauci, head of the U.S. National Institute of Allergy and Infectious Diseases in Bethesda, Maryland, said PrEP may lead to protection in more ways than one: The drugs prevent infections by killing or weakening the AIDS virus, which could trigger immune responses that subsequently derail infections. “That may be the first vaccine,” said Fauci.

–JON COHEN

SCIENCESCOPE

Report: Think Simple on Cars

The hype over hydrogen or hybrid cars may be blinding policymakers from taking steps to improve the fuel efficiency of gasoline-powered cars, suggests a new report by scientists at the Massachusetts Institute of Technology (MIT) in Cambridge. The researchers concluded that fully electric cars or hydrogen-powered vehicles will require major technical improvements if they hope to become cost-competitive in the next 20 years. And although plug-in hybrid cars may offer greenhouse gas emissions reductions sooner than those technologies, the study says, more efficient or lighter gasoline-powered cars may offer reductions more cheaply. “It’s an eye-opening report,” says John DeCicco of the Environmental Defense Fund, who applauds the report’s “rigorous” analysis. Report author John Heywood of MIT says fuel-efficiency production standards, which Congress tightened last year, should be supported by incentives such as fuel taxes. **–ELI KINTISCH**

British Scientists Seek Altered Trees

Scientists in the United Kingdom are hoping to launch the first field trial of genetically modified (GM) trees in that country in a decade. Gail Taylor of the University of Southampton and her colleagues have asked the U.K. Forestry Commission to provide land for a small-scale trial of poplar trees with reduced lignin, which could make them a more efficient source of ethanol for biofuel. The trial has reignited a debate over GM trees in the United Kingdom. Trees would be harvested after 3 years, says Taylor, before they release pollen. But Ricarda Steinbrecher, a molecular geneticist with EcoNexus in Oxford, U.K., says that because trees are so long-lived and relatively undomesticated, “we need to learn much more about poplars before we can dream about a proper risk assessment.” **–GRETCHEN VOGEL**

Physicists Feel the Spotlight

Physicists will attempt to load beams into the Large Hadron Collider, the most energetic particle smasher ever built, on 10 September, the European particle physics lab, CERN, announced last week. Researchers had better be ready for their close-up, as officials have invited the press to the lab near Geneva, Switzerland, to watch. “We’re petrified,” says Paul Collier, head of accelerator operations at CERN. “When we turn the tap and the beam goes down [the beam pipe], there will be a lot of fingers crossed.” **–ADRIAN CHO**

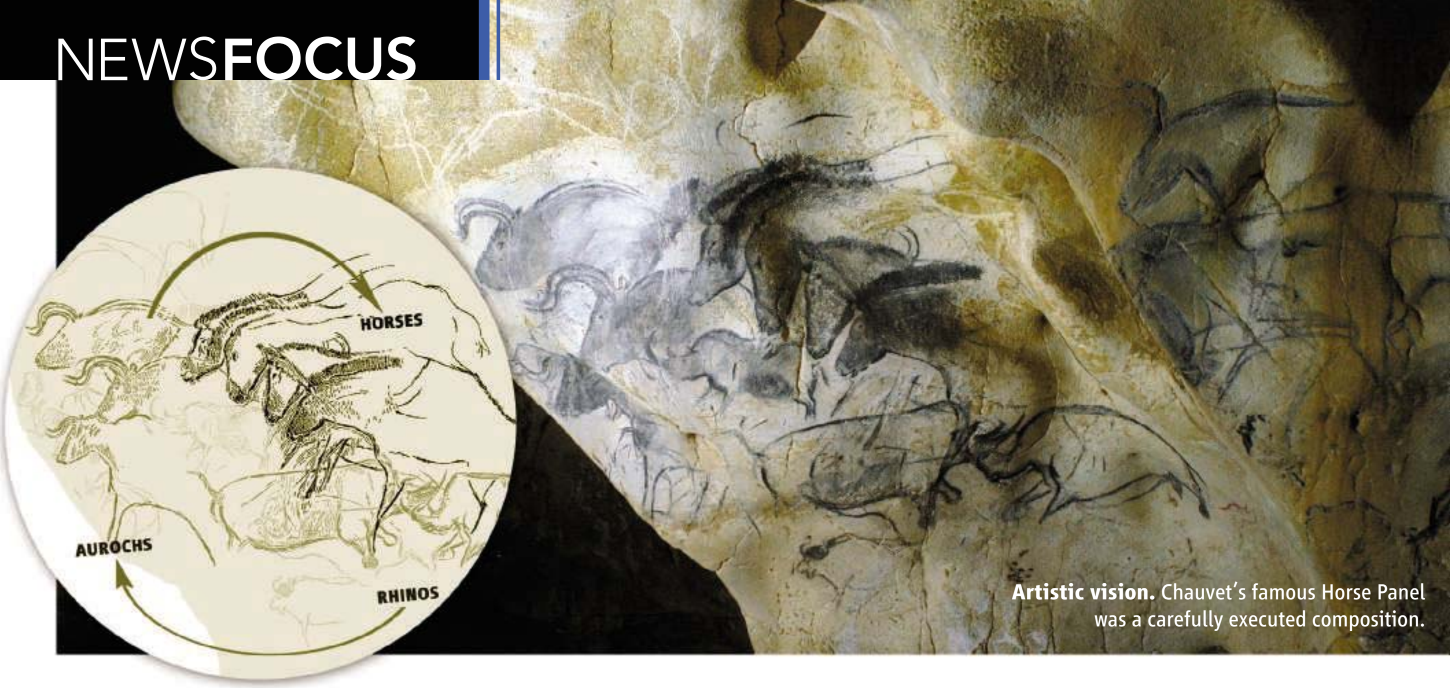

Artistic vision. Chauvet's famous Horse Panel was a carefully executed composition.

Going Deeper Into the Grotte Chauvet

Ten years of research have yielded detailed new insights into the stunning images considered the world's oldest cave art. But questions about their age are resurfacing

Sometime during the last ice age, artists entered a cave in southern France, lit torches and fires, and began work on a masterpiece. Squatting on the cave floor and wielding pieces of charcoal, the artists first drew the outlines of two rhinoceroses locking horns. Then, standing up and moving to the left, they sketched the heads and upper bodies of three wild cattle. Finally, a lone artist stepped forward to execute the pièce de résistance: four horses' heads, drawn with exquisite shading and perspective in the center of the tableau, each horse displaying its own expression and personality.

Online
sciencemag.org
Podcast interview with the author of this article.

This, at least, is how researchers studying the Chauvet Cave in the Ardèche region of southern France envision the creation of the famous Horse Panel. According to direct radiocarbon dating of the two rhinos and one of the cattle, they were drawn between 32,000 and 30,000 radiocarbon years ago, making them the oldest known cave art in the world. (The exact calendar age is uncertain because there is no accepted radiocarbon calibration for this period; see *Science*, 15 September 2006, p. 1560.) These early dates, announced soon after the cave's discovery in December 1994, struck a blow to conventional assumptions that such sophisticated artworks did not appear until up to 15,000 years later.

In the decade since researchers began working in the Grotte Chauvet (*Science*, 12 February 1999, p. 920), they have photographed and redrawn many of the more than 400 animals depicted, identified signs of human activity such as footprints and hearths, deciphered the cave's geology, and analyzed thousands of bones left by cave bears that shared the cave with humans. And archaeologists have begun to propose hypotheses about what the art might have symbolized to those who created it.

But as the team continues its work, a small but persistent group of archaeologists continues to question the age of the paintings. "Chauvet is the world's most problematically dated cave art site," says archaeologist Paul Pettitt of the University of Sheffield, U.K., whose most recent challenge was published online this month in the *Journal of Human Evolution* (*JHE*). That contention—which the team vigorously rejects—has critical implications for our understanding of the origins of art. "The fundamental importance of Chauvet is to show that the capacity of *Homo sapiens* to engage in artistic expression did not go through a linear evolution over many thousands of years," says cave art expert Gilles Tosello of the University of Toulouse (UT), France. "It was there from the beginning."

Lions, and horses, and bears, oh my!

Since resolving lawsuits and beginning scientific study a decade ago, researchers have reconstructed how the artists worked, analyzing each stroke of charcoal, red ochre, and engraving. Tosello and his wife, UT cave art expert Carole Fritz, have spent hundreds of hours perched in front of the 6-square-meter Horse Panel, photographing it in sections and drawing the artworks onto tracing paper. Working in this meticulous fashion, and noting the superposition of charcoal lines as well as slight thickenings at the beginning and end of each stroke, the pair was able to reconstruct the order and direction in which each line was drawn.

"The detailed nature of their observations is extraordinary," says archaeologist Iain Davidson of the University of New England in Armidale, Australia. Tosello and Fritz found that the artists who drew the two rhinos began with the horns and muzzles, then drew the front legs and bellies, and finally the rest of the bodies, making corrections and filling in details as they went. As the artists worked around the panel from the edges to the middle (see diagram above), they reserved a space in the center for the four horses, whose heads and necks are slightly superimposed over the backs of the cattle and arranged in a tight, diagonal orientation. This suggests to Tosello and Fritz that they were drawn by one artist. To make the horses' heads even more vivid, the artist used a tool to etch the cave wall around their muzzles so that they stand out in a prehistoric version of bas-relief.

"The entire composition is very homoge-

CREDITS (TOP TO BOTTOM): CAROLE FRITZ; GILLES TOSELLO AND CAROLE FRITZ

neous and has a very strong coherence," Tosello says, making it likely that the artwork was drawn by a small number of artists over a fairly short period of time. He adds that the Horse Panel, along with other compositions in the cave—such as a troop of lions apparently chasing a herd of bison—seems to be telling a story. "The animals appear on the wall in a certain order, like characters coming on stage during a play," he says. He speculates that prehistoric humans, who hunted bison, might have identified with the lions and wished to emulate their hunting prowess.

Humans probably kept their distance from lions, but the artists of Chauvet shared their cave with at least one dangerous animal: the cave bear. The team has found about 4000 cave bear bones, representing nearly 200 animals, on the cave floor, including a skull that was apparently placed deliberately atop a limestone block. Archaeologists have long debated whether humans hunted cave bears, worshipped them, or had some other relationship with these now-extinct animals. The artists clearly saw them from time to time: Chauvet's menagerie includes 15 drawings of cave bears.

Cavemates. Thousands of bear bones were found on Chauvet's floors.

Radiocarbon dates on 18 bear bones put them between 28,850 and 30,700 radiocarbon years ago, "slightly younger" than the dates for the paintings, according to evolutionary biologist Hervé Bocherens of the University of Tübingen in Germany. One other bone exposed by erosion of the cave floor was dated to 37,000 years ago, indicating, Bocherens's team concluded in a 2006 paper in *JHE*, that bears were already using the cave when prehistoric artists first entered.

"Imagine the terror of entering the cave with flickering lights, knowing that there might be bears in there," says Davidson. But bears and humans might have visited the caves in different seasons—winter hibernation for the bears, spring for the humans, points out paleogeneticist Jean-Marc Elalouf of the French Atomic Energy Commission in Saclay.

How old is old?

The dates for both the bears and the art correspond to the Aurignacian period, the first culture associated with the modern humans who colonized Europe beginning about 40,000 years ago. Yet some researchers have argued that the art more closely resembles much later cultures, possibly even the Magdalenian, which stretched from about 17,000 to 12,000 years ago and to which the great paintings at Lascaux in France and Altamira in Spain are attributed. But most experts accepted the dates, which were produced by the Laboratory of the Sciences of Climate and the Environment (LSCE) in Gif-sur-Yvette, France, a lab that pioneered the direct dating of cave paintings.

In 2003, however, Sheffield's Pettitt, along with British archaeology writer Paul Bahn, threw down the gauntlet again, arguing in *Antiquity* that the dates were not reliable because they had not been replicated by other labs; the Chauvet team defended its results in the same issue. "Chauvet is the best dated rock art site in the world," says French rock art expert Jean Clottes, former leader of the Chauvet team. Randall White, an archaeologist at New York University, agrees: "There are more dates from Chauvet than from most other caves combined."

In his new *JHE* paper, Pettitt launches the most detailed onslaught yet, saying that the drawings are simply too magnificent for that time. "Chauvet stands out in terms of overall technical sophistication whatever one compares it to," Pettitt told *Science*. He insists that the seven direct dates from paintings are unreliable because of the small sample sizes and the possibility of contamination from the cave wall.

Pettitt also discounts radiocarbon dates from more than 40 charcoal samples from the cave floor, which range between about 27,000 and 32,000 years ago, as well as recent redating of charcoal samples from a chamber rich with art. Those samples, split between six radiocarbon labs, gave consistent results of about 32,000 years before the present. Pettitt says these charcoal dates are irrelevant to the age of the art. "Could I not enter the cave today, pick out a piece of this well-preserved charcoal from a hearth on the floor, and write 'Paul Pettitt was here' on the cave wall?"

Some archaeologists take Pettitt's argument seriously. "People might have picked up old charcoal from the Aurignacian period during the Magdalenian," says William Davies, an Aurignacian expert at the University of Southampton, U.K. Pettitt's Sheffield colleague, archaeologist Robin Dennell, goes further: "Chauvet should be removed from assessments of early modern humans in Europe. Including it leads to a gross distortion of their cognitive abilities."

But the Chauvet team is having none of it. "This is ridiculous," Clottes says. "There were heaps of charcoal right in front of the paintings." Tosello agrees: "Who can believe that the Aurignacians came into the cave, left behind piles of charcoal without making any drawings, and then thousands of years later the Magdalenians entered and used the charcoal kindly left by their ancestors to draw on the walls?" Team members insist that the close agreement of dates from the paintings, the charcoal, and the bear bones argues that the cave was frequented by humans and bears during the Aurignacian, not the Magdalenian. Clottes also cites uranium/thorium dating that suggests that the cave entrance was blocked to entry by a landslide about 19,000 years ago—before the Magdalenian period. As for replicating the direct dating of the paintings, Hélène Valladas, leader of the LSCE team that carried out this work, says it is not possible to take more samples without "visibly altering the [art] traces."

Some archaeologists also find Pettitt's stylistic arguments unpersuasive. Even Davies, who hesitates to call the art Aurignacian, says, "I am not convinced the paintings are Magdalenian. … Some of the techniques are unique to the site and not found in the Magdalenian period." White adds that there is plenty of other evidence for sophisticated symbolism in the Aurignacian, including thousands of personal ornaments made from shell and bone. "It's all part of the Aurignacian package," White says.

In any case, the significance of Chauvet goes beyond the "oldest art" debate, says anthropologist Margaret Conkey of the University of California, Berkeley. "Chauvet was an expression of the sensibilities, beliefs, and social relations of anatomically modern humans in this part of the world," she says. "What was it about their lives that made imagemaking in caves meaningful?"

–MICHAEL BALTER

CREDIT: JEAN CLOTTES/FRENCH MINISTRY OF CULTURE

PROFILE: OLIVERA FINN

Directing a Life in Science

After forgoing theater ambitions, and despite early marriage and motherhood, Olivera Finn has risen through immunology's ranks thanks to her work on cancer vaccines

Take a look at Olivera "Olja" Finn's life, and you can tick off the actions women are supposed to avoid if they want to advance in science. Get married fresh out of high school. Check. Interrupt your education for your husband's sake. Check. Allow his career to take precedence over yours. Check. Have children before you have a job and give birth at what seem like inopportune times, such as shortly before you start graduate school. Check.

Yet Finn has, with great success, pursued career and family goals simultaneously. She celebrated her 40th wedding anniversary last month, has raised a daughter and a son, and, at the age of 59, already has grandchildren. Professionally, Finn has prospered. Nearly 20 years ago, she discovered the first cancer antigen, a tumor molecule that elicits a reaction from immune cells. And despite spending her youth in Communist-run Yugoslavia, Finn has climbed the academic ladder in the United States—she is chair of immunology at the University of Pittsburgh in Pennsylvania and has served as president of the American Association of Immunologists. She argues that interweaving career and family is essential. "I don't think we live long enough to do things sequentially."

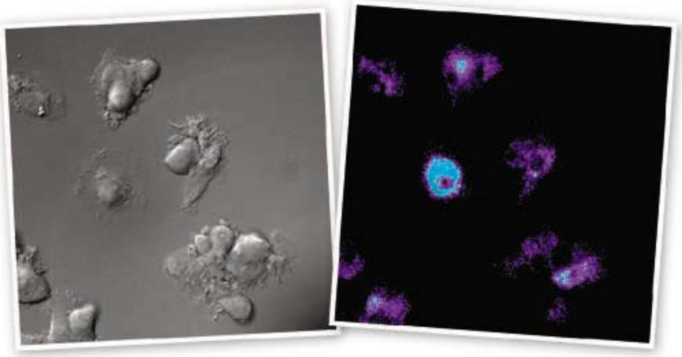

Ready to rumble. Activated dendritic cells light up after exposure to the cancer antigen MUC1.

Colleagues laud her work in cancer immunotherapy, the goal of which is to enlist the immune system to combat tumors. In an extension of her tumor antigen discovery, Finn's group is gearing up to test a vaccine to prevent benign colon growths from spawning deadly cancers. Her effort is rare in that most cancer "vaccines" are not preventive; they're designed to treat serious tumors. The few preventive cancer vaccines approved for use target tumor-causing pathogens such as the hepatitis B and human papilloma viruses rather than growths themselves, as Finn's vaccine does.

"The field has advanced faster because of her," says Martin Cheever, a medical oncologist at the Fred Hutchinson Cancer Research Center in Seattle, Washington. Finn deserves credit not only for her scientific insights, he adds, but also for her devotion to nurturing other scientists' research and fostering cross-disciplinary collaborations. Without such prompting, "cancer biologists and immunologists [usually] sit on their own sides of the fence," notes immunologist Ralph Steinman of Rockefeller University in New York City.

The courage, tenacity, and independent-mindedness Finn needed to start anew in a strange country also characterize her science, says Paola Castagnoli, scientific director of the Singapore Immunology Network and Finn's friend since the late 1970s. Finn is currently exploring the provocative idea that infections throughout life, including chickenpox and other childhood diseases, prime our defenses against cancer. "She is a very good scientist because scientists should not be conformists," says Castagnoli.

The accidental scientist

Growing up in what was then Yugoslavia, Finn aspired to direct plays. But she strayed from the script once she met Seth Finn, an American college student on a foreign exchange program. Over her parents' objections, the couple married and moved to the United States. She'd been studying English since age 7, so language wasn't a barrier. What shocked her, she says, was Americans' ignorance of foreign affairs, obsession with money, and willingness to make long-haul commutes.

After briefly attending college in California and Indiana, she ended up in Puerto Rico, where her husband was serving in the Coast Guard. At the urging of her father, a theater manager with geology and biology degrees, Finn had followed the technical track at her Yugoslavian high school. In Puerto Rico, her scientific ambition blossomed. For an undergraduate project at the Interamerican University in San Juan, where she completed her bachelor's degree in biology, Finn figured out missing steps in the life cycle of a hookworm that circulates among humans, birds, rats, and cockroaches. The work involved poking around seedy areas of downtown San Juan and picking up roaches as big as a tablespoon, but she loved it. "The life of research—getting data and making hypotheses—consumed me," she says.

After finishing a Ph.D. and a postdoc at Stanford University in Palo Alto, California, Finn set up her own lab at Duke University in Durham, North Carolina. She chose Duke because Seth, who

CREDITS (TOP TO BOTTOM): RON FONTANA; OLJA FINN

by that point had earned a Ph.D. in communications from Stanford, had landed a position at the nearby University of North Carolina, Chapel Hill. When she arrived at Duke in 1982, it was a hotbed of transplant immunology research, and she focused on identifying what triggers the rejection of donated organs. Her group reared T cells extracted from patients who'd received kidney transplants and nailed down which of the donor's antigens, or molecular markers, provoked the cells to attack. Although hundreds of molecules could potentially prompt a rejection response, typically only one or two antigens did, her team discovered.

That success spurred Finn to ask whether the same techniques might shed light on cancer–immune system interactions. Scientists had known since the 1950s that cancer cells can rouse the immune system. In fact, a debate has raged since then about whether the immune system thwarts many incipient cancers, or whether the immune response is too feeble to curb most abnormal growths. However, in the early days of this debate, scientists didn't even know what antigens on tumors trigger an alarm.

In the mid-1980s, Finn decided to track down these telltale tags. Looking back, the decision to shift to tumor immunology was naïve, Finn says. The lab's skill in identifying rejection antigens "gave us a confidence that was exaggerated." Finding cancer antigens turned out to be much tougher. For one thing, whereas a transplanted organ riles the immune system, tumor cells elicit a much weaker response.

Weak, yes, but not undetectable, and by 1989 Finn's lab had nabbed the first cancer antigen, a protein called MUC1 that protrudes from pancreatic and breast tumor cells. Human T cells keyed on this antigen, her team reported.

MUC1 also decorates normal cells in several organs, so why don't T cells pounce on those tissues? The answer came in work Finn continued after moving to the University of Pittsburgh in 1991. Normal MUC1 is festooned with carbohydrate chains, which are nearly absent from the protein fashioned by cancer cells. The pattern is clear, Finn says. Tumor antigens usually differ from their normal counterparts in some way, such as structure, quantity, or cellular location. For cyclin B1, which helps propel cells through mitosis, quantity explains why it can act as a tumor antigen. In normal cells, the amount of cyclin B1 remains low except for a spike at the beginning of mitosis. Yet cancer cells churn out the protein nonstop. MUC1, cyclin B1, and the like are not "self" antigens but "abnormal self" antigens, Finn says.

Family time

As Finn talks about her life, you don't hear any regrets—she clearly doesn't regard her early marriage and motherhood as youthful indiscretions. Finn, who started graduate school at Stanford with a 7-month-old son to tend, encourages women at the same stage of their careers to have children. If you think you'll have more time for parenting later in life, you are wrong, she says.

Carrie Miceli, who was Finn's first graduate student and is now an immunologist at the University of California, Los Angeles, says she followed Finn's example, although she waited until starting her own lab to have a child. "It was great to see a woman with kids and a family who was not talking about what a compromise it was," says Miceli.

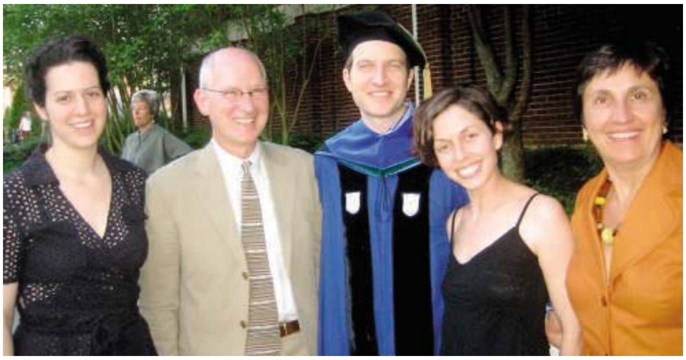

The next generation. Finn with her daughter Sonja (*left*), husband, Seth, son Sasha, and daughter-in-law Carey Storan.

CREDIT: COURTESY OF OLJA FINN

Finn and her husband took turns going for advancement. After Seth's job led them to North Carolina, the choice to move to Pittsburgh was hers. For 4 years, Seth commuted every week between Pennsylvania and North Carolina before being hired by Robert Morris University in Pittsburgh.

The cancer shot

For more than a decade, Finn has worked to package the tumor antigen she discovered into a vaccine that would prevent cancer. Her group conducted initial safety trials of a MUC1-containing vaccine, using patients with advanced pancreatic cancer. In 2005, for instance, the researchers reported that the vaccine produced no obvious side effects—and also seemed to promote an immune response to MUC1 in some recipients. Yet the U.S. Food and Drug Administration (FDA) balked at her proposal to test the vaccine in healthy people, she says, partly because of the fear that it would trigger autoimmunity, an immune assault on normal tissue.

Now she's finally getting a chance. This summer, her group will launch a 5-year trial to determine whether injections containing abnormal MUC1 can prevent recurrence of intestinal adenomas. Surgeons usually remove these benign growths because they can morph into colon tumors. However, adenomas often sprout again after the operation. The study's control group will be historical: past patients who were operated on by the same doctors. Finn concedes that even this trial isn't ideal. The researchers are testing the vaccine's ability to prevent adenoma regrowth, not its ability to fend off cancer in healthy people. Moreover, the patients will be elderly, and the response to vaccines dwindles with age.

Age's affect on immunity also figures into an idea that has captured Finn's interest. Work by her group and other labs suggests that many of us receive "natural" vaccinations against cancer from an unexpected source: pathogens. A variety of body invaders, including those that cause childhood diseases, spur the production of the same abnormal self antigens as cancer cells. The chickenpox virus, for instance, sparks an explosion in cyclin B1. The mumps virus prompts cells to display denuded MUC1. Getting sick in our youth, when our immune systems are primed to make the memory cells that can confer lifelong immunity, might spare us from cancer later on, Finn proposes.

To test the idea, Finn teamed up with epidemiologist Daniel Cramer of Brigham and Women's Hospital in Boston and colleagues. They found that women who'd undergone events that can lead to infections or inflammation—including intrauterine device use, pelvic surgery, and broken bones—were more likely to carry antibodies to MUC1, a sign of an immune response. These women also had a lower risk of developing ovarian cancer, the researchers reported in 2005.

In a life full of challenging career moves, Finn is pondering her next and last. She says she would like to work at FDA to help pave the way for preventive cancer vaccines. "People used to say it would take 10 years to evaluate [these] vaccines, but it's been 10 years and we are still discussing how it will take 10 years." As in her family life, Finn is not inclined to wait.

–MITCH LESLIE

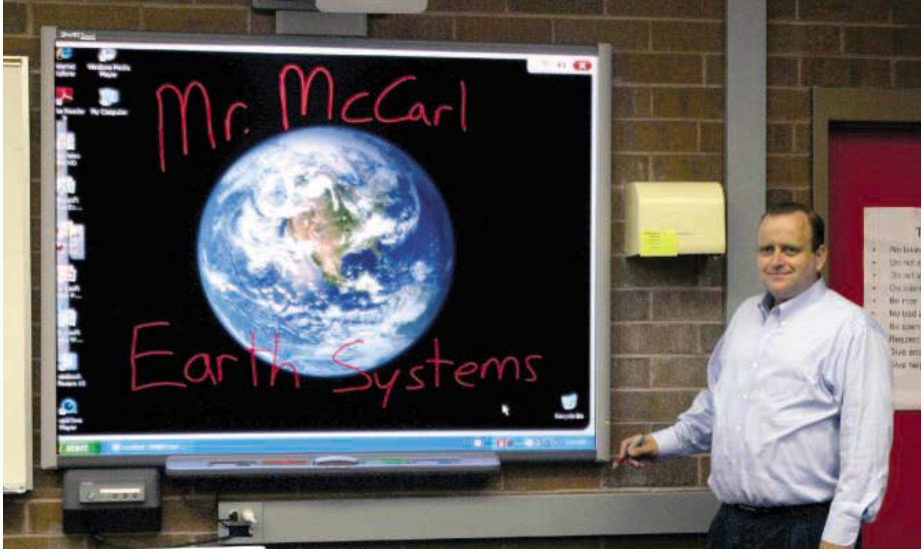

OutSMARTed. New science teacher Paul McCarl, shown setting up his high school classroom, couldn't get federal aid to return to college.

CREDIT: PAUL MCCARL

U.S. HIGHER EDUCATION

Science Scholarships Go Begging

Despite ever-rising college costs, a $4.5 billion federal aid program to lure students into science is vastly undersubscribed

Paul McCarl dropped out of Brigham Young University (BYU) in 1991 and rode the dot-com boom and bust writing entertainment software before moving into retail management. But when his son told him that his eighth-grade teacher had said the phases of the moon are caused by Earth's shadow falling on the lunar surface, McCarl decided he was needed in the classroom. So 2 years ago, at the age of 38, the former computer science major returned to BYU's Provo campus and enrolled in its physical science teacher program. And this week, he began his new career in the science department at Whitehorse High School, a tiny school on the Navajo reservation in southeastern Utah.

McCarl would seem like the perfect candidate for a fledgling federal scholarship designed to attract more U.S. students into scientific fields. But he was excluded because the BYU courses he was taking didn't meet its stringent eligibility requirements. In fact, the bar is so high that the Department of Education is spending money at only half the rate Congress envisioned in 2006 when it created the 5-year, $4.5 billion National Science and Mathematics Access to Retain Talent (SMART) and the Academic Competitiveness (AC) grant programs.

Secretary of Education Margaret Spellings says the reason so few college students are eligible for the largest federal aid program of its kind is that they haven't taken the necessary courses in high school. But university financial aid directors point to the many requirements, a break from the traditional practice of awarding aid according to financial need. "The AC and SMART grants are the most administratively burdensome programs that I have ever seen," says Katy Maloney, director of financial aid at the University of California, Davis. "It's pretty much a nightmare because they have so many rules."

The grants were created in response to a flood of reports on the woeful condition of U.S. math and science education and the need for a more technically trained workforce. To be eligible for the AC grant, worth $750 in the first year and $1300 in the second year, students must qualify for the government's major needs-based scholarship, called a Pell grant, and have graduated from "a rigorous secondary school program." That means 3 years each of higher level math and science and at least 1 year of a foreign language. Once in college, they also need to maintain a 3.0 or higher grade point average. The SMART grant pays $4000 a year to third- and fourth-year students with good grades who are pursuing majors in the sciences, mathematics, engineering, and technology.

With seven children and a wife to support, McCarl was counting on SMART grants to complete his college education. But he got tripped up by the provision that a student's major must be on a list approved by the department. Although his degree will be awarded by the College of Physical and Mathematical Sciences, whose programs are eligible, his course of study falls under the category of secondary education, which doesn't qualify.

Such requirements are one reason why, despite the ever-rising cost of college, the money for AC and SMART grants isn't flying out the door. The department spent barely half of its $850 million allocation in 2006–07, awarding grants to 360,000 students. That shortfall caused Congress to cut the 2007–08 allocation to $397 million. It's also elicited a promise from Spellings to double the number of grant recipients by its final year (2010–11).

That's 2 years after she and her boss, President George W. Bush, leave office, of course. In the meantime, Spellings blames the underutilization on the sorry state of elementary and secondary education and argues that the best way to raise participation rates is to reauthorize the president's signature education initiative, No Child Left Behind.

But financial aid directors question whether the prospect of a small scholarship is likely to induce students to take more math and science courses before they enter college. "Let's be realistic," says Anna Griswold, who oversees student aid programs at Pennsylvania State University in State College. "Is a high school sophomore going to take a tougher schedule because he might get $750 more as a college freshman?" She and other student aid officials agree that the SMART grant might be more of a lure for some upper-level students, but they say its impact would be very difficult to measure.

The chair of the House Committee on Education and Labor, Representative George Miller (D–CA), declined to speculate on the fate of the scholarship program in the next Congress. "Let's give it some time and see what happens," Miller said last month after chairing a hearing on corporate efforts to improve STEM education. A spokesperson for the Republican minority on the committee predicted that legislators won't take a hard look at funding levels for the programs until it's time to refill the pot.

Even so, Congress this year passed two bills that are expected to goose participation rates. In May, it decided that half-time students and permanent residents were eligible for both programs. And last month, in a long-overdue higher education bill awaiting the president's signature, it gave state education officials the authority to certify a rigorous course of study, a power that previously had rested with the education secretary.

Neither will affect McCarl, who this month moved his entire family to the reservation. But he's okay with that. "I'm getting the chance to become a teacher," he says. "And I plan to stay here for the rest of my life."

–JEFFREY MERVIS

With reporting by Fayana Richards.

GLOBAL WARMING

Climate Change Hot Spots Mapped Across the United States

Taking some of the fuzziness out of climate models is revealing the uneven U.S. impact of future global warming; the most severely affected region may be emerging already

Now that almost everyone expects a certain amount of global warming by the end of the century, attention can turn to more local climate change. What's going to happen in our own backyards? Researchers can't go that far yet, but in an effort to squeeze the maximum detail out of notoriously fuzzy climate models, they are pooling results from some of the most sophisticated simulations available.

The latest regional climate effort points up the uneven burden climate change will place on the United States. "It highlights that there are regions where climate changes will be bigger than others," says climate modeler Gerald Meehl of the National Center for Atmospheric Research (NCAR) in Boulder, Colorado. The American Southwest looks to be hardest hit by far, but the work also highlights a dramatic increase in year-to-year climate variability contributing to hot spots.

The new work is in press in *Geophysical Research Letters* (*GRL*). As climate modeler Noah Diffenbaugh of Purdue University in West Lafayette, Indiana, and his colleagues lay out in the paper, regional climate modeling in the wake of last year's report from the Intergovernmental Panel on Climate Change has come a long way since the previous IPCC report in 2001. For that report, researchers divided the contiguous 48 states into 1300-kilometer-wide west, central, and east regions, including a good bit of Canada in the west. Drawing on IPCC simulations of future greenhouse climate generated by nine then–state-of-the-art global climate models, they concluded that each broad region could expect slightly more warming and in the winter slightly more precipitation than the global average.

In the *GRL* paper, Diffenbaugh and his colleagues offer a much sharper picture of climate change. They combine forecasts from 15 new, state-of-the-art global models run for last year's IPCC report. These models individually paint a more detailed picture than their predecessors did and have more realistic renditions of the physical processes in the climate system. The group also formulates a new gauge of climate change—climate responsiveness—by combining projected changes in temperature and precipitation as well as changes in variability of those climate properties from year to year. High values of this climate responsiveness mark "hot spots" where the models say climate will be changing the most.

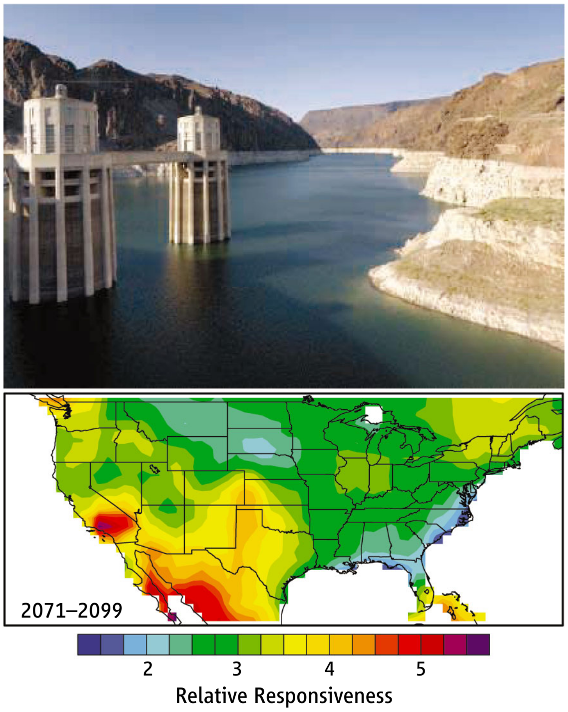

More of the same? Models predict that the U.S. Southwest and northern Mexico will be most responsive (reds and yellows) to the strengthening greenhouse; Lake Mead (*top*) may have responded already.

CREDITS (TOP TO BOTTOM): CHRISTOPHER MORRIS/CORBIS; ORIGINAL AUTHOR ADAPTATION FROM N. DIFFENBAUGH ET AL., *GEOPHYS. RES. LETT.* (AUGUST 2008)

According to the 15-model consensus, the strongest U.S. hot spot by far stretches across the Southwest from southern California to west Texas and intensifies even more over northern Mexico. By another statistical analysis technique, the American Southwest hot spot extends northward into Nevada, Utah, and Colorado. By either technique, the U.S. Southeast is a distinct "cool spot," a region relatively less responsive in changing temperature and precipitation, although Diffenbaugh cautions that "we need to be careful to not overinterpret these areas as 'safe' or 'immune.' " Other studies have suggested that these less responsive regions may be at risk of other sorts of greenhouse changes, such as increased severe weather in the Southeast.

Two higher resolution models not included in the consensus—one global, the other an extremely high-resolution model of the continental United States—suggest a similar pattern but also identify a milder climate change hot spot in the Midwest.

Most surprising to Diffenbaugh, the better part of a hot spot's strength came not from progressive warming or a long-term rise or fall in precipitation but from increased variability from one year to the next, especially in precipitation. Models have predicted that a strengthening greenhouse would make the climate more variable, but "I'm not sure what that means," says regional climate modeler Linda Mearns of NCAR. "More attention should be given to how variability is going to change."

"Needless to say, this work is only the beginning of a possible new avenue … towards a clearer picture of where regional climate change matters," regional modeler Jens Christensen of the Danish Meteorological Institute in Copenhagen writes in an e-mail. It was good that the group checked the combined global models against the higher resolution models, he explains. But the work points up the need for combining results from multiple regional models, not just the global models. Such an approach might help address concerns that the models still aren't very good at replicating climate change across the United States during the past 50 years, as meteorologist Kevin Trenberth of NCAR notes in an e-mail. That may be in part because the models have trouble simulating natural climate changes induced by slow changes like El Niño, he says.

Shortcomings or not, the IPCC models may have found a hot spot that is already developing. The predicted Southwest hot spot of climatic change looks much the same during the next 30 years as at the end of this century. And that future hot spot bears a strong resemblance to the drying and warming of the Southwest during the past decade or so. Says Diffenbaugh: "We may already be seeing some emerging hot spot patterns."

–RICHARD A. KERR

Mascarene extinctions 913
Parasite depot 917

LETTERS

edited by Jennifer Sills

Reservations About Dam Findings

IN THE RESEARCH ARTICLE "NATURAL STREAMS AND THE LEGACY OF WATER-POWERED MILLS" (18 January, p. 299), R. C. Walter and D. J. Merritts observe that milldam density is regionally more important than previously recognized (*1*–*7*). We have several reservations: (i) Local observations cannot necessarily be generalized to wider settings, (ii) pre-Colonial forms were inconsistently documented, and (iii) implications for contemporary watershed management are unclear.

The detailed observations in the Research Article are from southeastern Pennsylvania, a famously fertile portion of the eastern U.S. Piedmont with high historic milldam density. Most portions of the Piedmont could not support this milling density, yet no detailed comparison of mill deposits with deposits in relatively dam-free basins was provided. More evidence is needed to justify broad application of these findings elsewhere.

Enhanced understanding of historic valley conditions can offer useful guidance for parts of stream rehabilitation design, but the characteristics of the valley's streams in pre-Colonial times remains undetermined. Walter and Merritts provide some evidence—such as organic-rich, hydric (i.e., consistently saturated) soils, interpreted to indicate channel bottoms with multiple low-flow channels—to question previous work on Piedmont channel processes. However, contrary evidence from one cited source was ignored (*7*), and three of four sources cited do not support the "typical" alluvial profile. None, other than (*3*), describe prominent buried hydric soils or wetlands, and several, including (*3*), mention buried gravel bars, uncharacteristic of interpreted conditions. Wide variation in reported ^{14}C data is not addressed. Pennsylvania ^{14}C ages (median 450 years ago) are used to indicate presettlement surfaces, but Maryland samples from similar deposits are much older (median 3410 years ago). Given the importance of such details to describing the pre-Colonial channel form, more detailed documentation is necessary.

A milldam near Bloomville, New York.

CREDIT: GREG NAGLE

Streams in the mid-Atlantic have responded to boundary conditions, including base-level adjustments, water and sediment supply fluctuations, and varying beaver populations (*8*), throughout the Holocene. Before European colonization, valley conditions likely reflected the activities of Native Americans rather than a natural regime. Perturbations increased in frequency and magnitude after colonization, and they continue to this day. Accordingly, the milldam observations do not justify the inference that historic fluvial forms can address contemporary riparian management issues, as pre-Colonial forms evolved from historic boundary conditions.

The strategy resulting from these observations, which is already practiced, is to dredge valley bottom sediment and realign channels in a semblance of pre-Colonial morphology. This strategy has risks. Recreating these forms without addressing contemporary upland sediment supplies could result in partial refilling of dredged valleys. Lowering floodplains in meandering reaches also permits straighter down-valley paths for a wider range of flows, which can destabilize riparian corridors (*9*). In either scenario, the constructed morphology would require maintenance such as periodic dredging or structural controls, both arguably no closer to "natural" than current conditions.

For watershed managers, suggesting that pre-Colonial river valley forms represent an updated "ideal" condition resembles the misuse of generic stream "types" for restoration design over a decade ago (*10*). The current demand to mitigate adverse impacts to wetlands and waterways is high, but watershed managers need to consider both contemporary and historical causes of stream impairment before deciding how to respond.

DANIEL J. BAIN,[1] SEAN M. C. SMITH,[2,3]
GREGORY N. NAGLE[4]

[1]Department of Geology and Planetary Science, University of Pittsburgh, Pittsburgh, PA 15260, USA. [2]Maryland Department of Natural Resources, Annapolis, MD 21401, USA. [3]Department of Geography and Environmental Engineering, The Johns Hopkins University, Baltimore, MD 21218, USA. [4]Department of Biological and Environmental Engineering, Cornell University, Ithaca, NY 14853, USA.

References

1. N. E. Allmendinger, J. E. Pizzuto, G. E. Moglen, M. Lewicki, *J. Am. Water Resources Assoc.* **43**, 1483 (2007).
2. D. J. Bain, G. S. Brush, *Am. J. Sci.* **305**, 957 (2005).
3. R. B. Jacobson, D. J. Coleman, *Am. J. Sci.* **286**, 617 (1986).
4. S. W. Trimble, *Science* **285**, 1244 (1999).
5. L. B. Leopold, R. Huppman, A. Miller, *Proc. Am. Philos. Soc.* **149**, 349 (2005).
6. J. E. Pizzuto, *Sedimentology* **34**, 301 (1987).
7. J. E. Costa, *Geol. Soc. Am. Bull.* **86**, 1281 (1975).
8. R. Ruedemann, W. J. Schoonmaker, *Science* **88**, 523 (1938).
9. S. M. Smith, K. L. Prestegaard, *Water Resources Res.* **41**, (2005).
10. D. Malakoff, *Science* **305**, 937 (2004).

What to Do About Those Dammed Streams

IN THE RESEARCH ARTICLE "NATURAL STREAMS and the legacy of water-powered mills" (18 January, p. 299), R. C. Walter and D. J. Merritts contribute to the evolving story of human impact on streams in the U.S. mid-Atlantic Piedmont. Historical forest removal,

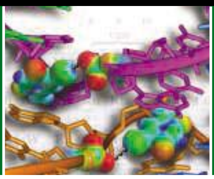

Halogen bonding

918

What triggers aurorae?

920

farming, and soil erosion produced widespread valley-bottom sedimentation, followed by modern stream incision into these deposits, termed "legacy sediment." This raises the question of what, if anything, should be done. Should we dig up legacy deposits to reduce sediment loading to Chesapeake Bay? Should streams be restored to their pre-Colonial condition? The legacy sediment debate is decades old (*1*, *2*), but its social context has evolved. The emergence of a stream restoration industry and long-running struggles to reduce sediment loading to the Chesapeake Bay provide a constituency and pressure for large-scale remediation, action apparently advocated by Walter and Merritts (*3*).

"Hot spots" of stream bank erosion can be found, although the longevity of sediment still in valley bottoms supports observations of small erosion rates in most places. Eroded sediment can be redeposited before leaving the watershed (*4*), indicating that local reductions in sediment loading from bank protection will correspond to a proportionally smaller reduction in loading to the Chesapeake Bay. Current practice is not effective at identifying "hot spots" or establishing their connection to receiving waters. We need to demonstrate that these actions are worthwhile before undertaking widespread and expensive earth-moving.

Walter and Merritts reinforce earlier work indicating that today's streams differ from their pre-Colonial condition. A pristine stream is an unlikely template for restoration because the drivers of stream dynamics (water and sediment runoff and riparian vegetation) have all changed. Combined with the elimination of beavers, there is little prospect of returning mid-Atlantic Piedmont streams to their presettlement form, a restoration target that Montgomery appears to advocate in an accompanying Perspective (*5*).

PETER WILCOCK

Department of Geography and Environmental Engineering, The Johns Hopkins University, Baltimore, MD 21218–2686, USA.

References

1. R. B. Jacobson, D. J. Coleman, *Am. J. Sci*. **286**, 617 (1986).
2. J. E. Costa, *Geol. Soc. Am. Bull.* **86**, 1281 (1975).
3. *Science* Podcast, 18 January 2008.
4. N. E. Allmendinger, J. E. Pizzuto, G. E. Moglen, M. Lewicki, *J. Am. Water Resources Assoc*. **43**, 1483 (2007).
5. D. R. Montgomery, *Science* **319**, 291 (2008).

Response

BAIN *ET AL.* QUESTION OUR HYPOTHESIS THAT milldams were primary factors in historical sedimentation in mid-Atlantic valleys. Hillslope gullying and sheetwash erosion undoubtedly occurred during postsettlement land clearing and farming, but the trapping of immense volumes of fine-grained sediment along valley bottoms is a process that we attribute to those factors coupled with raised base level and backwater effects of damming. Whereas previous workers focused on increased sediment supply and stormwater runoff from upland land-use change, we maintain that changes in stream velocity and sediment-transport capacity due to widespread damming were overlooked. As all agree that soil erosion rates were high during early settlement and that the valley floors filled with sediment, the central question—which our work addresses—is, how abundant were milldams and millponds on U.S. streams, and what was their cumulative impact on sedimentation?

Bain *et al*. suggest that southeastern Pennsylvania had anomalously high mill densities because of its fertile soil. However, a wealth of historical evidence shows that water-powered milling was associated with nearly all manufacturing processes of the 17th to 20th centuries, including logging, mining, forging, textiles and paper production, and machining (*1*, *2*). Mill densities, irrespective of soil fertility, increased throughout the eastern United States with time and settlement, but the upstream extent of impact from milldams varied with stream gradient and dam spacing.

The "wide variation" in radiocarbon ages of the presettlement hydric soil that we report is consistent with our interpretation that widespread wetlands were stable for thousands of years, since mid-Holocene climatic and ecological conditions became established. It is inappropriate to calculate a median radiocarbon age that combines the analyses of separate samples from different locations and stratigraphic intervals within the presettlement hydric soil.

Bain *et al*. disagree with our characterization of presettlement mid-Atlantic Piedmont valley bottomlands as containing multiple branches of smaller streams, with pervasive wetlands and hydric soils. Our conclusion was based on hundreds of study sites in 20 midsize watersheds throughout the mid-Atlantic Piedmont. We described the stratigraphic evidence of buried dark, organic-rich soils with near planar surfaces spanning valley bottoms and noted that this same association was observed elsewhere by earlier workers. The dark buried soils that we describe in the mid-Atlantic piedmont contain seeds of presettlement obligate and facultative wetland plants. We propose that the construction of numerous beaver dams helped to create anabranching stream networks in the mid-Atlantic region during presettlement times, and beavers were an important factor in creating the pervasive wetlands that are now buried beneath thick stacks of postsettlement mud (*3*).

Wilcock and Bain *et al*. argue that elevated supplies of stormwater runoff and sediment from uplands at present are a much more serious problem than stream bank erosion or impacts of historic milldams, but they provide no data or references to support these claims or to indicate that modern upland erosion rates actually are high. Our measured values of eroded sediment from stream banks at multiple sites are high and contradict these concerns (*4*). Other research, in fact, indicates that upland erosion rates diminished substantially in the past century (*5*). Wilcock contends that eroded stream bank sediment can be redeposited downstream and might not degrade waterways. We counter that silts and clays eroded from upland farm slopes and construction sites are no more likely to be carried downstream than suspended sediments eroded from stream banks, yet policy-makers do not consider efforts to minimize upland soil erosion to be futile.

We did not discuss specific stream restoration practices in our paper, and we consider Wilcock's statement that we "advocate" large-scale remediation to be grossly misleading. We hope our research will inform the science of future stream and wetland rehabilitation in the mid-Atlantic region, and we advocate scientific investigations to evaluate new approaches.

Recognizing the importance of wetlands, state and federal agencies spend millions of dollars attempting to restore existing wetlands or to create wetlands where none ever existed. Through our discovery of extensive presettlement hydric soils buried along Piedmont valley bottoms, with potentially viable seed banks, a new opportunity emerges to rehabilitate previously unrecognized valley-bottom wetlands. In response to Bain *et al.*, we assert that it would be bad policy to ignore these presettlement conditions and to assume that all stream impairments are modern.

ROBERT C. WALTER* AND DOROTHY J. MERRITTS

Department of Earth and Environment, Franklin and Marshall College, Lancaster, PA 17604–3003, USA.

*To whom correspondence should be addressed. E-mail: robert.walter@fandm.edu

References

1. T. S. Reynolds, *Stronger Than a Hundred Men: A History of the Vertical Water Wheel* (Johns Hopkins University Press, Baltimore, 1983).
2. M. Dopp, *Bull. Am. Geogr. Soc.* **45**, 902 (1913).
3. R. C. Walter, D. J. Merritts, *Science* (www.sciencemag.org/cgi/eletters/319/5861/299).
4. R. C. Walter, D. J. Merritts, M. Rahnis, "Estimating volume, nutrient content, and rates of stream bank erosion of legacy sediment in the Piedmont and Valley and Ridge Physiographic provinces, southeastern and central Pennsylvania" (Report to Pennsylvania Department of Environmental Protection, 2007); www.depweb.state.pa.us/chesapeake/lib/chesapeake/pdfs/padeplegacysedimentreport2007waltermerrittsrahnisfinal.pdf.
5. S. W. Trimble, P. Crosson, *Science* **289**, 248 (2000).

CORRECTIONS AND CLARIFICATIONS

Reports: "Efficient inhibition of the Alzheimer's disease β-secretase by membrane targeting" by L. Rajendran *et al.* (25 April, p. 520). The mice were misidentified as APPsw/PSΔE9 mice. The correct nomenclature is APPPS1 mice, according to R. Radde *et al.*, *EMBO Rep*. **7**, 940 (2006).

TECHNICAL COMMENT ABSTRACTS

COMMENT ON "100% Accuracy in Automatic Face Recognition"

Weihong Deng, Jun Guo, Jiani Hu, Honggang Zhang

Jenkins and Burton (Brevia, 25 January 2008, p. 435) reported that image averaging increased the accuracy of the automatic face recognition to 100% and thus could be applied to photo-identification documents. We argue that the feasibility of image averaging on identification documents is not fully supported by the presented evidence.

Full text at www.sciencemag.org/cgi/content/full/321/5891/912c

RESPONSE TO COMMENT ON "100% Accuracy in Automatic Face Recognition"

R. Jenkins and A. M. Burton

Contrary to the suggestion of Deng *et al.*, image registration reduced face-recognition accuracy when divorced from the averaging procedure. Average-to-photo mapping generalizes beyond specific photographs, and averaging either gallery images or probe images can improve the match. The alternative protocol suggested by the authors is unsuitable because it evaluates face-matching algorithms, not face representations, and relies on standard image sets.

Full text at www.sciencemag.org/cgi/content/full/321/5891/912d

Looking for Familiar Faces

IN THE BREVIA "100% ACCURACY IN AUTOmatic face recognition" (25 January, p. 435), R. Jenkins and A. M. Burton proposed a simple method to "elevate machine performance to the standard of familiar face recognition in humans." However, these statements seem overoptimistic.

Only one experiment resulted in perfect accuracy, and only 25 (averaged) face images were used. To meet the standards of human face recognition, a program would have to perform accurately on a sample much larger than 25.

Because the authors did not provide performance figures based on the standard methodology [i.e., FERET (*1*) or Face Recognition Grand Challenge (FRGC)], readers could not assess the efficacy of their method in comparison to existing algorithms.

Finally, My Heritage is a for-profit organization, which is not expected to share its intellectual property with the public. Therefore, the mechanism that achieved "100% accuracy" is unknown to the scientific community (including the authors). Given that the data and software of My Heritage online services change regularly, the reported experiment is practically unrepeatable.

LIOR SHAMIR

Image Informatics Unit, National Institute on Aging, Baltimore, MD 21224, USA.

Reference

1. P. J. Phillips, H. Moon, P. J. Rauss, S. Rizvi, *IEEE Trans. Pattern Anal. Mach. Intell*. **22**, 1090 (2000).

Letters to the Editor

Letters (~300 words) discuss material published in *Science* in the previous 3 months or issues of general interest. They can be submitted through the Web (www.submit2science.org) or by regular mail (1200 New York Ave., NW, Washington, DC 20005, USA). Letters are not acknowledged upon receipt, nor are authors generally consulted before publication. Whether published in full or in part, letters are subject to editing for clarity and space.

Response

WE CERTAINLY DO NOT CLAIM THAT OUR PROcedure delivers 100% accuracy in all cases. Our main message is that whatever the level of accuracy achieved when photos are used, image averaging raises the bar. This approach focuses on the representation of the face instead of the matching algorithm. As such, it complements existing systems rather than competing with them.

Shamir compares automatic recognition with a putative human viewer. However, there is no general human viewer when it comes to face recognition. Humans are extremely good at recognizing familiar faces, but very poor at recognizing unfamiliar faces (*1*, *2*). Ignoring this distinction impedes our understanding of face recognition ability and leads to unrealistic ambitions on the part of those building automatic systems. By requiring systems to match pairs of photographs, they are creating a problem that humans find extremely difficult. We proposed matching a photograph to an average image in an attempt to integrate our psychological theory of face familiarity (*3*) with an automatic system.

Finally, our decision not to use the FERET/Face Recognition Vendor Test (FRVT) database was deliberate. That database does not contain enough photos of each face to generate average images, nor does it contain the level of variation required. The My Heritage gallery contains many thousands of real-world images encompassing the kind of variability encountered in everyday life (for example, photos taken with many different cameras). Similarly, our probe database was gathered by means of Google Image search. This natural variability presents a far more realistic and demanding challenge. It has already been established that FaceVACS performs well on the FERET/FRVT database; indeed, it was the overall winner of the most recent evaluations (*4*). We showed that it also works well on images over which the experimenter has no control, provided one feeds it averages rather than snapshots.

ROB JENKINS AND A. MIKE BURTON

Department of Psychology, University of Glasgow, Glasgow G12 8QQ, UK.

References

1. A. M. Burton, S. Wilson, M. Cowan, V. Bruce, *Psych. Sci.* **10**, 243 (1999).
2. R. Clutterbuck, R. A. Johnston, *Visual Cognit.* **11**, 857 (2004).
3. A. M. Burton, R. Jenkins, P. J. B. Hancock, D. White, *Cognit. Psych.* **51**, 256 (2005).
4. P. J. Phillips *et al.*, "FRVT 2006 and ICE 2006 large-scale results" (National Institute of Standards and Technology, NISTIR 7408, 2007); http://face.nist.gov.

ECOLOGY

Biohistory of the Mascarenes

Storrs L. Olson

The dodo of Mauritius, *Raphus cucullatus*, (last unequivocally recorded in 1662) is an icon of human-caused extinctions on islands. On the neighboring island of Rodrigues, the related solitaire, *Pezophaps solitaria*, soon followed the dodo into extinction. Modern studies of DNA extracted from their remains suggest that these large, flightless birds were derived independently from the nomadic Nicobar pigeon, *Caloenas nicobarica*, of Australasia. Only a decade ago it was realized from newly discovered bones that the supposed dodolike "Réunion solitaire" (now *Threskiornis solitarius*) was actually derived from the sacred ibis, *T. aethiopicus*, and that the misinterpreted accounts of 17th-century voyagers applied much better to an ibis than to a dodo. Réunion may possibly have had a dodolike bird, but geologists now understand that the island underwent a cataclysmic volcanic upheaval about 200,000 years ago that probably wiped out many terrestrial organisms, so that much of the biota must be younger than that of the other two Mascarene islands.

These are just a few examples of the advances in knowledge of the Mascarene biota brought together in *Lost Land of the Dodo*, which is both timely and an indispensable reference. Anthony Cheke has over three decades' experience in research and conservation in the Mascarenes and is responsible for the bulk of the volume. Julian Hume, who has long been interested in extinction on islands, has conducted recent paleontological research in the Mascarenes and contributes an appendix on that subject, boxed accounts of the different groups of Mascarene vertebrates, and illustrations.

The book's principal focus is on terrestrial vertebrates, with emphasis also on botany, ecology, and conservation. Unlike Pacific islands, for example, where recent discoveries of past biodiversity have come entirely from the fossil record, the Mascarenes had no period of prehistoric human occupation and were essentially in pristine condition when discovered in the 16th century. Thus the accounts of early European explorers and settlers take on greater importance than on islands subjected to centuries of prehistoric human intervention. Much new material has emerged in the past few years through the combing of old archives and through new paleontological discoveries. The systematic relationships of Mascarene organisms have now been augmented by recent DNA studies, and modern conservation techniques have met with both successes and disappointments in attempts to save the remnants of fauna and flora that have survived over 500 years of human devastation and neglect.

Lost Land of the Dodo

by Anthony Cheke and Julian Hume

Yale University Press,
New Haven, CT, 2008.
480 pp. $55.
ISBN 9780300141863.
T & AD Poyser (A&C Black),
London. £45.
ISBN 9780713665444.

The three Mascarene islands have very different geological, biological, and human histories. This disparity is part of what contributes to the book's organizational problems. The chapters are arranged more or less as a chronological progression, with each chapter having separate sections devoted to the individual islands. Information on particular topics, such as bats or lizards, is scattered among the various chapters without any final syntheses. The abundant illustrations include color plates with 39 of Hume's always-evocative paintings of extinct organisms as they may have looked in life.

The volume's utility is severely compromised by the gross overuse of endnotes in an attempt to produce a "text unencumbered by endless 'Harvard references' and explanatory byways." Some of the notes simply provide an author and year so that one must then turn to the bibliography, but most are extensive discourses that cannot very well be read outside the context of the main text. All but 3 of the 15 appendices have their own sets of endnotes. After flipping back and forth through the first two chapters, I became exasperated, cut the book apart, and removed the 90 pages of endnotes so they could be more easily consulted. The book is sturdily bound, however, and the separate parts have held together well. As examples of excess, a little over three columns of text concerning dodos shipped alive from Mauritius is accompanied by five columns of endnotes in smaller type; chapters on the Mascarenes in the 19th and 20th centuries have 389 and 498 endnotes, respectively. To make matters worse, the endnotes are not indexed.

Not so dodolike. Réunion ibises (last recorded circa 1710) on the slopes of the Piton des Neiges volcano.

CREDIT: JULIAN HUME/FROM *LOST LAND OF THE DODO*

Many of the topics that I attempted to find were not included in the index. Maps are not indexed as such and can only be located by flipping pages. (Mauritius and Réunion are shown in many different maps, but I only found one of Rodrigues.) The extinct fruitbat (*Pteropus subniger*) referred to as "rougette," a name revived for the book, is indexed under that "long vanished" vernacular, which is of no help whatsoever as the species is not listed at all under "bat." The absence of a comprehensive index is a great impediment in a work so crammed with widely scattered facts.

Despite the mistaken attempt to make the book read like something else,

---

The reviewer is in the Division of Birds, National Museum of Natural History, Smithsonian Institution, Washington, DC 20013–7012, USA. E-mail: olsons@si.edu

Lost Land of the Dodo is a scientific reference work that will long be essential to anyone studying evolution and conservation of insular organisms. Unfortunately, it also serves as a model for how such volumes should not be organized, and it will prove very difficult to use unless eventually made available as a searchable electronic text.

10.1126/science.1162110

CULTURAL EVOLUTION

Bridging the Big Gap

Asif A. Ghazanfar

Histories are full of gaps. Whether these are apparent (reflecting a lack of data) or real (nothing of import actually occurred) is often an open question. Nevertheless, there is a tendency to develop theories that suggest the latter and thereby explain away our lack of knowledge. For example, the classic historical paradigm of a period of intellectual stasis between the philosophical contributions of the ancient Greeks and their rediscovery in the Middle Ages ignores seminal works of Arab-Muslim scholars (*1*). But perhaps the most important gap in human history is actually more an abyss—our "prehistory." It is into this abyss that Daniel Lord Smail, a historian at Harvard University, journeys in hopes of finding links between Stone Age and Modern people.

On Deep History and the Brain maps his voyage. In it, Smail shows where we are with respect to understanding humanity's history, how we got here, and the general direction toward which we should move. He offers two key lines of argument. One illustrates how past and current ways of thinking about human history are based on misguided notions of what counts as history. The second provides a unifying framework for a cultural history that incorporates evolutionary biology and neuroscience.

In essence, "prehistory" refers to the thousands of years before civilization, when history supposedly did not move. Historians came to such an idea through a mixture of ignorance and practicality. Into the 19th century, European historians turned to the Book of Genesis; later scholars, forced to reckon with deep geological time and evolution by natural selection, were more creative. The spirit of their arguments for ignoring deep history is reflected in a sentence Smail quotes from the historian Mott Green: "At some point a leap took place, a mutation, an explosion of creative power—the 'discovery of mind,' or the 'birth of self-consciousness'—interposing a barrier between us and our previous brute, merely biological existence" (*2*). The essential idea is that history in the proper sense began when cultural evolution eclipsed biological evolution. Furthermore, cultural evolution is Lamarckian (directed progress toward a goal) and thus obviates the need to incorporate Darwinian explanations and lessens the importance of our biological history.

The idea that recent history follows an accelerating Lamarckian pattern is pervasive among historians and even endorsed by the late paleontologist Stephen Jay Gould: "Cultural evolution has progressed at rates that Darwinian processes cannot begin to approach…. Human cultural evolution … is Lamarckian in character" (*3*). Smail tempers this idea by demonstrating that often apparent directed and accelerated progress is actually an illusion of teleology. First, many cultural paradigms are the result of trial and error or the inadvertent consequence of a sequence of actions. Second, the accelerated nature of cultural evolution does not preclude Darwinian mechanisms (selection based on random events); in fact, the short generation time (sharing an idea with other people multiples it within a short period) creates the illusion of directed progress. Smail concludes that humanity's deep history has no particular beginning and is driving toward no particular end.

On Deep History and the Brain

by Daniel Lord Smail

University of California Press, Berkeley, 2008. 286 pp. $21.95, £12.95. ISBN 9780520252899. Paper, $15.95, £9.50. ISBN 9780520258129.

For Smail's unifying framework, the crux of his synthesis is that culture is made possible by the plasticity of human neurobiology. Civilization—with its attendant agriculture, animal domestication, abandonment of migration, and increasing density of human settlements—Smail holds, did not bring an end to the role of biology in human history. Rather, civilization brought rapid changes in human behaviors and created new neurophysiological ecosystems in which different brain-body states could evolve (molded by different cultures). These brain-body states have their roots in our primate and other vertebrate ancestors. Thus, in essence, any culture represents the dynamic interactions between the brain, body, and environment of humans within a particular group. Smail presents an embodied and situated view of human history.

How do culture and neurophysiology influence each other? One example that Smail elaborates, and that has a direct link to our primate ancestors, is the dominance hierarchy. The social emotions associated with dominance hierarchies (e.g., anger, fear, contempt, and pity) are in large part mediated by the autonomic nervous system and often revealed involuntarily by our facial expressions. These have deep phylogenetic roots. Although the neural responses may not have changed much across time, the means by, and contexts in, which dominance and submission are felt and exploited by people in a society are culturally specific. More generally (and without our being aware of it), emotional and physiological ups and downs are exploited in different ways in different cultures—for pleasure, for inflicting harm, etc.—through different associations. Smail dubs the varying forms of culturally specific instruments that drive brain-body responses "psychotropic mechanisms." These include mood-altering practices, behaviors and institutions generated by human culture, foods like coffee and chocolate, our interactions with others through social hierarchies or religions, and self-stimulation through novels or roller coasters. Importantly, the exploitation of brain-body states by cultures is not intentional nor does it have a goal.

On Deep History and the Brain is a small book with big ideas: that human history is linked in deep time by the physiological mechanisms that we share with our vertebrate ancestors and that the historical "progress" and "acceleration" we detect are in fact directionless series of ongoing culturally specific experiments with psychotropic mechanisms. Smail deftly and impressively pulls together information from the disparate fields of cultural history, evolutionary biology, and neuroscience. His knowledge and sophistication are most evident when he avoids the traps and numerous inadequacies of evolutionary psychology; he cogently adopts a developmental systems–embodied cognition view of behavioral biology for his historical framework. A creative and compelling synthesis of ideas, Smail's book provides an engaging and invigorating analysis of our history.

References

1. S. M. Ghazanfar, *Diogenes* **154**, 117 (1991).
2. M. T. Greene, *Natural Knowledge in Preclassical Antiquity* (Johns Hopkins Univ. Press, Baltimore, MD, 1992).
3. S. J. Gould, *The Panda's Thumb: More Reflections in Natural History* (Norton, New York, 1992).

10.1126/science.1162481

The reviewer is in the Neuroscience Institute and Department of Psychology, Princeton University, Princeton, NJ 08540, USA. E-mail: asifg@princeton.edu

SCIENCE AND INDUSTRY

Research Alone Is Not Enough

Powerful forms of business innovation represent a challenge to U.S. efforts in technology development.

Lewis M. Branscomb

In election year 2008, the economy has overtaken the war in Iraq as the primary concern of voters. Even before the mortgage and credit crisis emerged last summer, rising national debt, unbalanced budgets, and increased competition in the global economy have engendered a debate over U.S. competitiveness. There is no agreement, however, on the right policies to restore the health of American commercial innovation. One group focuses on the lagging support for basic research and the need to reform science and engineering education. Others emphasize the processes that turn research and talent into innovations, which, in turn, create new industries and job growth. Both groups are half right, for both processes are essential to ultimate economic growth. U.S. preeminence is threatened, not only because emergent economies are catching up but also because they are exploiting new business models based on global networks of specialized firms (*1*). The good news: We too can leverage the entrepreneurship of our specialized small- to medium-sized enterprises and the research base that drives their innovative capability. Public policy must begin to foster these opportunities.

The United States does still lead the world in the number of researchers (1.3 million), but the European Union is close behind (1.1 million), and China is coming up fast (0.93 million) (*2*). The trends are discouraging. The U.S. global share of new doctorates in science and engineering slipped from 52% in 1986 to 22% in 2003; the U.S. share of scientific publications declined from 38% in 1988 to 30% in 2003 (*2*). Although the United States led the world in magnitude of total research and development (R&D) investment in 2007 ($353 billion), with about a third of the total, China led the world in the growth rate of its R&D, by 2007, and was expected to pass Japan for second place (*3*).

The Administration has given vocal support to the National Academies' report *Rising Above the Gathering Storm* (*4*) and the need for more basic research. However, the government continues to believe, wrongly, that market forces are sufficient to bridge the "valley of death" between basic research and commercial innovations without public policy support (*5*). Even if these recommendations are funded by Congress, they will not address global changes in business models.

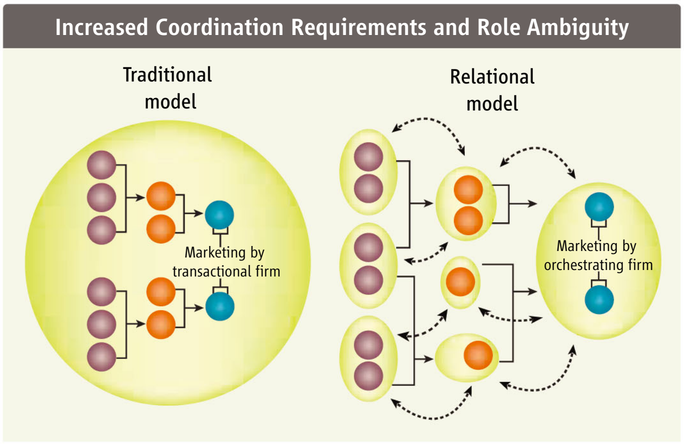
Increased Coordination Requirements and Role Ambiguity

Models of traditional and relational company structures. Dotted arrows indicate dynamic links based on trust and orchestration. [Adapted from (*16*)]

When global corporations are polled and asked what are the most attractive country locations for new R&D facilities, China ranks higher than the United States by 61% to 41%, with India in third place with 29% (*2*). All other countries come in at or behind Japan, at 14%. The share of value-added in China's domestic output of all industries that derive from the high-technology segment of the economy, quadrupled over 8 years, to 16% in 2005 (*6*). At that value, China's world share of value-added exceeded both the United Kingdom and Germany's and is just shy of Japan's. Between 1998 and 2003, the share of R&D investment by U.S. firms and affiliates grew twice as fast overseas (52%) as it did domestically (26%) (*7*). Thus, foreign markets and climates for investment appear to be outpacing us.

Christopher Hill, in a recent essay, notes that U.S. policy must pay more attention to the risks and barriers associated with the later stages in the innovation process (*8*). This trend can be illustrated by the strategy that helped IBM to recover from a serious profitability problem in the late 1980s. Customer value was increasingly migrating from hardware assembled from commodity components to the associated software and services that embody the functions customers most need and want. The information technology services portion of IBM's global revenues swelled as IBM extended its information technology services, reaching beyond the traditional bounds of software and operational help to provide all of the elements customers need, to satisfy its own customers (*9*). From a start in 1989, this service revenue swelled to $12.7 billion in 1995. By 2007, it reached 54.8%t of IBM's total worldwide revenue (*10*). At the same time, IBM adopted a new approach to the way it does business internationally.

The old model was the traditional multinational assembly of wholly-owned subsidiaries, each producing for local markets. IBM's CEO, Samuel J. Palmisano, described IBM's change from "multinational" to "global network enterprise" this way: "Just as hub-and-spoke architecture for communications networks gave way to the peer-to-peer structure of the Internet, so too global businesses are relying less on decisions made by management from corporate headquarters and more on the initiatives of partner firms around the world" (*11*). The global enterprise is, increasingly, a flexible assembly of firms around the world, with skills that can provide the most efficient combination of business processes for a global market.

Hagel and Brown (*12*) argue that process networks are no longer transactional (i.e., contract), but instead relational (i.e., cooperative agreement). In transactional relationships, decisions are made centrally and are executed by negotiated arrangements with subordinate partners. Relational relationships are based more heavily on cooperation and trust, with both parties accepting the responsibility for creativity and the need for realizing agreed-upon goals. Once formed, such relational networks persist over time and withstand changes in the business envi-

---

School of International Relations and Pacific Studies, Scripps Institution of Oceanography, University of California–San Diego, San Diego, CA 92093–0519, USA, lbranscomb@ucsd.edu; and J. F. Kennedy School of Government, Harvard University, Cambridge, MA 02138, USA.

ronment. "Relational nets," Hagel and Brown point out, "are used for (or produce) all kinds of innovation; transaction-based nets almost never produce any real innovation." This, they note "is the difference between Toyota (which tends to use tightly coupled relational nets) and GM (which is solely transactional, no matter what claims they may make to the contrary)."

Hagel and Brown have documented several examples of these relational nets. They describe Cisco Systems as a U.S.–based example. Cisco prides itself on business model and process innovations. It built a sophisticated process network in 1996 called Cisco Connection Online (CCO), open to all of the firms to whom Cisco customers look for their solutions. Already in 2003, some 80% of all products were built and shipped without Cisco's ever taking ownership (*13*). Thus, Cisco shares with thousands of customers, suppliers, and competitors a peer-to-peer "e-learning" platform (*12*). Cisco introduced perhaps its biggest innovation of 2006, the Cisco Telepresence, a new technology solution that provides brand new in-person experiences between people, places, and events, whether they are across town or across the world, making CCO even more productive. With Cisco's acquisition of WebEx in March 2007, Telepresence is already halfway to being the quickest Cisco product to reach $1 billion in annual sales. Cisco is passionate about innovations, but far from "not invented here," Cisco's most important innovation is its partnership with both customers and competitors, making it a true networked enterprise.

A Chinese apparel manufacturer, Li & Fung, addressed their low-margin problem with an approach they describe as "process orchestrator" (*12*, *14*). "They own nothing; they do the logistics. They define and customize the production process," Brown says. Li & Fung work with some 10,000 suppliers in more than 40 countries, yet they have only about 5000 employees of their own. Their relationship with partner firms is based on the "30/30" principle: Li & Fung will purchase at least 30% from a supplier but will not exceed 70% of the capacity of that firm. This ensures that no one in the network is captive and that learning and trust permeate the network. Every participating firm must also go outside the network to survive. Thus, each firm is specialized and must be able to innovate—to take on new ideas, new varieties of skills, and new products. The asset productivity of this arrangement for Li & Fung is a surprising 30 to 50% return on equity; people productivity is $1 million per employee per year, and scalable; sales reached $11 billion in 2004.

What is Li & Fung's innovation? They maximize the collective innovative capacity of dozens of partners needed for a specific product by orchestrating them into a remarkably flexible, agile, and skilled collaborative supply chain. They mix and match the special technical skills of the partners, creating a network enterprise. Does U.S. economic policy recognize and encourage such a trend? Unfortunately, government policy in the last decade has been marked by sustained complacency regarding the assets on which productivity growth must be based. The one piece of recent legislation that seeks to address innovation issues, the America COMPETES bill of 2007 (*15*), only weakens the capability of the U.S. Commerce Department to support innovation-enhancing policies. The Administration abolished its Technology Administration, which was the source of the department's innovation policy research. It fought for years to abolish the National Institute of Standards and Technology's Advanced Technology Program (ATP). A pale shadow of ATP now survives as the Technology Innovation Program (TIP), with a budget smaller than any between 1998 and 2004.

Candidates for the presidency in 2008 have said very little about innovation policy in their campaigns. They say good things about the need for more basic science and better education, and even about the merits of innovation. Traditional domestic-oriented policies, however, may not compete with the emerging globally networked business models. For networked enterprises to flourish, nations will have to adopt compatible principles for regulation of intellectual property, flows of information and technically skilled people, technical standards, and new forms of business relationships globally. Thus, the new U.S. policies should give much more attention to international issues and relationships and should feature the role of innovation by highly specialized, middle-sized, and smaller firms through creative arrangements of networked enterprises. Supply chains are becoming supply networks; markets are becoming multidimensional, geographically and culturally. Competitive advantage is, more and more, coming down to talent and imagination in business organization and service, going beyond traditional emphasis on science- and engineering-based product innovations. Scientists and engineers should be steeped in the realities of how the global system for creating, exploiting, and rewarding innovations works most effectively. So too must those heading for careers in finance, law, government, and international relations.

We must have new leadership that recognizes that a broad range of government policies directly affect the nation's power to innovate: new technology investments, economic policy, trade strategy, government procurement, intellectual property, and standards policy. A major recalibration of private-sector thinking and government policies and priorities is in order. The way we think about networks of talent, the tools we have for building institutional skills and trust, the approach we take to competition in a world of process networks—all must be addressed. The temptation to revert to protectionism must be resisted. The growing importance of technically sophisticated, middle-sized firms that know how to cooperate and compete in a new world of peer-networked enterprises must be recognized and encouraged.

References and Notes

1. P. E. Auerswald, L. M. Branscomb, *Technol. Soc.* **30**, 339 (2008).
2. Council on Competitiveness, *Competitiveness Index: Where America Stands* (Council on Competitiveness, Washington, DC, May, 2007), p. 74.
3. American Association for the Advancement of Science, *R&D Budget and Policy Program: Guide to R&D Funding Data—International Comparisons 2007* (AAAS, Washington, DC, 2007); www.aaas.org/spp/rd/guiintl.htm.
4. Committee on Prospering in the Global Economy of the 21st Century, *Rising Above the Gathering Storm* (National Academies Press, Washington, DC, 2007).
5. P. Auerswald, L. M. Branscomb, *J. Technol. Transfer* **28**, 227 (2003).
6. U.S. National Science Board*, Science and Engineering Indicators 2006* (National Science Foundation, Washington, DC, 2006), pp. 6–12.
7. R. Atkinson, H. Wial, *Boosting Productivity, Innovation, and Growth Through a National Innovation Foundation* (Brookings Institution, Washington, DC, 2008), p. 8.
8. C. Hill, *Issues Sci. Technol.* **24**, 78 (2007).
9. IBM Global Services, http://en.wikipedia.org/wiki/IBM_Global_Services.
10. *IBM Annual Report 2007* (IBM, Armonk, NY, 2007); www.ibm.com/annualreport/2007/md_4rco.shtm
11. S. J. Palmisano, *Foreign Affairs* **85** (3), 127 (2006).
12. J. Hagel, J. S. Brown, presentation at the Workshop on High Tech Regions 2.0, Stanford University, Palo Alto, CA, 13 to 14 November 2006.
13. W. F. Achtmeyer, "E-business innovation at Cisco," Tuck School of Business at Dartmouth, Center for Global Leadership, case 1-0001 (2003).
14. J. Hagel, J. S. Brown, *The Only Sustainable Edge: Why Business Strategy Depends on Productive Friction and Dynamic Specialization* (Harvard Business School Press, Boston, 2005), pp. 87–90, 134–135.
15. Bill S.761.ES, an amendment to Publ. Law 110–69.
16. G. Britan, *MIT Sloan Manag. Rev.* **48**, (3), 30 (Spring 2007); http://sloanreview.mit.edu.
17. This Policy Forum is based on the author's William Carey Lecture at the AAAS Forum on Science and Technology Policy, Washington, DC, 8 May 2008.

10.1126/science.1160496

IMMUNOLOGY

Neutrophil Soldiers or Trojan Horses?

Leishmania parasites convert the toxic environment within a neutrophil into a safe haven during infection.

Beena John and Christopher A. Hunter

Biting insects transmit numerous viral, bacterial, and parasitic infections of human and veterinary importance. However, the initial events that occur as pathogens are introduced by these vectors at sites of local feeding (wounds) are poorly understood. On page 970 in this issue, Peters *et al.* (*1*) report that early events in vector-mediated injury influence the outcome of infection with the sand fly–transmitted parasite *Leishmania major*.

Wounds are the points of entry for multiple pathogens, and neutrophils are the first of a wave of inflammatory cells that migrate into these sites. These highly phagocytic cells have been regarded as foot soldiers, armed with toxic oxygen radicals, lytic enzymes, and cationic proteins to destroy the microorganisms they ingest. Indeed, their vital role in efficiently mounting an immune response to pathogens is emphasized by the susceptibility of neutropenic patients to bacterial infections (*2*). However, in current models, neutrophils are short-lived and undergo programmed cell death (apoptosis). Their corpses, when phagocytosed by macrophages (part of the wound-healing response), have an anti-inflammatory effect. In a twist on this model, van Zandbergen *et al.* (*3*) showed that neutrophils internalize *L. major* and, as these infected cells die, they are engulfed by other immune cells—macrophages. Thus, this allows silent entry of the parasites into their host immune cell of preference.

The availability of transgenic mice in which neutrophils have been engineered to express green fluorescent protein, combined with advances in deep-tissue imaging, allowed Peters *et al.* to visualize in real time the rapid egress, migration, and accumulation of neutrophils at a sand fly bite, as well as their interaction with macrophages, during infection with *L. major*. Infected neutrophils form a dense plug across the epidermal and dermal layers marking the region where the sand fly proboscis penetrates the skin. Although some reports suggest a role for parasite-induced factors in neutrophil recruitment, such as *Leishmania* chemotactic factor (*4*), Peters *et al.* found that the initial response was independent of the presence of parasites, because injection of latex beads or simple wounding induced a similar accumulation of neutrophils. Although tissue damage was proposed to override any effect of parasite-derived factors on neutrophil recruitment, sustained recruitment was observed in response to the sand fly bite, compared to needle stick injury. Sand fly saliva has been linked to numerous immunomodulatory properties (*5*, *6*), but whether those contribute to the differential recruitment and/or enhanced survival of neutrophils at sites of infection is uncertain.

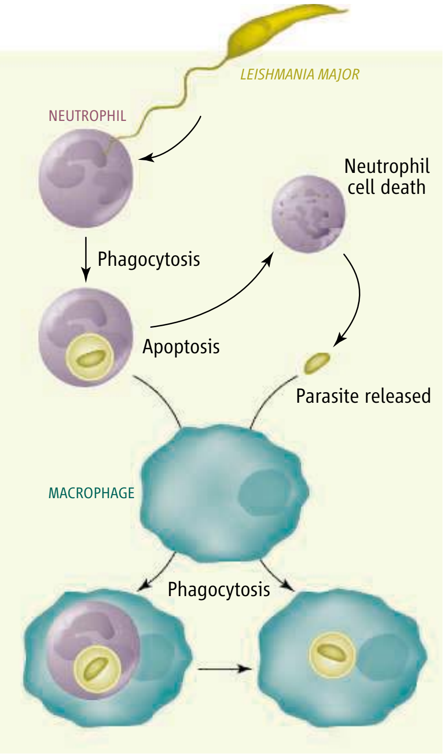

Trojan horse needed? Response to a sand fly bite in the mouse includes a rapid influx of neutrophils to the wound site, which phagocytose *L. major* parasites. In one scenario (**left**), as the neutrophils undergo apoptosis, they are phagocytosed by macrophages and send an anti-inflammatory signal as part of this process. This results in silent entry of the parasites into the ultimate host cell, the macrophage. In the alternative scenario (**right**), the antiinflammatory environment created by the uptake of apoptotic neutrophils antagonizes the antimicrobial activities of the macrophage. Parasites egress from dying neutrophils and are engulfed, but not killed, by macrophages.

The study by Peters *et al.* raises questions about the general nature of host-pathogen interactions. Consistent with the Trojan horse hypothesis (*7*), the majority of cells containing viable parasites early after a sand fly bite (18 hours) were neutrophils. Furthermore, depletion of neutrophils from mice led to a decrease in parasite burden and reduced capacity to establish infection. However, 6 to 7 days after a sand fly bite, the infected cells consisted predominantly of macrophages. Unexpectedly, instead of engulfing dying infected neutrophils, macrophages appeared to acquire parasites that had been released from neutrophils undergoing apoptosis. Paradoxically, even early after sand fly bite, macrophages and neutrophils were present in similar numbers at the site of infection, but macrophages were not the predominant cell type involved in phagocytosis of these pathogens. Peters *et al.* suggest that this could be due to compromised activity of the macrophages that are involved in clearing apoptotic neutrophils. Thus, depletion of neutrophils is associated with increased expression of proinflammatory molecules such as interleukin-1α and -1β. Moreover, the authors observed that in the absence of neutrophils, macrophages were recruited to the wound site and did phagocytose parasites, but the ability of *L. major* to establish infection was compromised. The results of Peters *et al.* lead to an alternative hypothesis that the parasites released from apoptotic neutrophils are better adapted to survive in macrophages, although no direct evidence exists in the current data sets for this mechanism.

A complex network of immune cells within the skin—dendritic cells and Langerhans cells—also has a prominent role in cutaneous leishmaniasis (*8*, *9*). Peters *et al.* show that the number of activated dendritic cells increases at the site of infection. Because neutrophils have a short half-life and macrophages are not thought to leave the local wound site, dendritic cells likely transport parasites and parasite-derived products to lymph nodes, where T cell responses are developed to control infection. Imaging the dynamics of the dendritic cell response and the role of local neutrophils in modulating this response will be key to understanding the complex

CREDIT: P. HUEY/SCIENCE

School of Veterinary Medicine, University of Pennsylvania, PA 19108, USA. E-mail: chunter@vet.upenn.edu

interplay of events occurring at the bite site.

There are in vitro results both for and against a role for neutrophils in promoting entry of *L. major* into macrophages. However, in vivo imaging has highlighted the question of whether these parasites have exploited the host response against tissue injury and evolved mechanisms to benefit from the early neutrophil influx. Most organisms that are ingested by neutrophils are readily killed within the phagocytic compartments, but *L. major* can block the oxidative burst within the neutrophils and evade elimination (*10*). For leishmaniasis, the study of Peters *et al.* favors a modification of the Trojan horse model, whereby neutrophils serve as depots for the parasites until their definitive host cells, the macrophages, arrive at the site (see the figure).

There are other vector-borne diseases in which neutrophils are vital, and it seems likely that the same types of neutrophil behavior reported by Peters *et al.* for *L. major* would be relevant to mosquito, tick, and flea bites and the diseases they transmit. Several other vector-borne pathogens, such as *Ehrlichia* and *Francisella tularensis*, can survive within neutrophils (*7*), suggesting that this mechanism is probably not restricted to *Leishmania* infection.

References

1. N. C. Peters *et al.*, *Science* **321**, 970 (2008).
2. C. Nathan, *Nat. Rev. Immunol.* **6**, 173 (2006).
3. G. van Zandbergen *et al.*, *J. Immunol.* **173**, 6521 (2004).
4. G. van Zandbergen, N. Hermann, H. Laufs, W. Solbach, T. Laskay, *Infect. Immun.* **70**, 4177 (2002).
5. S. Kamhawi, *Microbes Infect.* **2**, 1765 (2000).
6. R. Zer, I. Yaroslavski, L. Rosen, A. Warburg, *Int. J. Parasitol.* **31**, 810 (2001).
7. T. Laskay, G. van Zandbergen, W. Solbach, *Immunobiology* **213**, 183 (2008).
8. M. P. Lemos, F. Esquivel, P. Scott, T. M. Laufer, *J. Exp. Med.* **199**, 725 (2004).
9. M. C. Udey, E. von Stebut, S. Mendez, D. L. Sacks, Y. Belkaid, *Immunobiology* **204**, 590 (2001).
10. H. Laufs *et al.*, *Infect. Immun.* **70**, 826 (2002).

10.1126/science.1162914

CHEMISTRY

Halogen Versus Hydrogen

Use of noncovalent interactions involving halogen atoms opens up new ways to manipulate molecular recognition processes.

P. Metrangolo and G. Resnati

In his Nobel lecture in 1970, Hassel unequivocally demonstrated the importance of halogen atoms in directing molecular self-assembly phenomena (*1*). Yet, the ability of halogen atoms to function as reliable sites for directing molecular recognition processes long remained underappreciated. In the past decade, numerous papers describing supramolecular architectures formed by iodo- and bromoperfluorocarbons have drawn attention to the ability of these halocarbons to function as versatile building blocks in crystal engineering (*2*). Others have begun to study the possible use of halogen bonding in biological assays (*3*–*5*).

The term "halogen bonding" is used in analogy with the better-known hydrogen bonding, with which halogen bonding shares numerous properties. It describes the vast class of noncovalent interactions found mostly in halogenated organic molecules. In biological systems, high-resolution structures of complexes of halogenated ligands are rare, making it difficult to ascertain the active role of halogen bonding in the binding of biological molecules. Incorporation of halogen atoms into drug candidates increases their lipophylicity, which improves penetration through lipid membranes and tissues, thus favoring the intracellular delivery of the drug. By some estimates, 50% of compounds in high-throughput drug screens are halogenated (*6*). A better understanding of how halogenated molecules bind to biological substrates could open the door to more effective approaches to drug development and could help to rationalize the adverse effects of some chemicals to which humans are commonly exposed (such as polyhalogenated molecules).

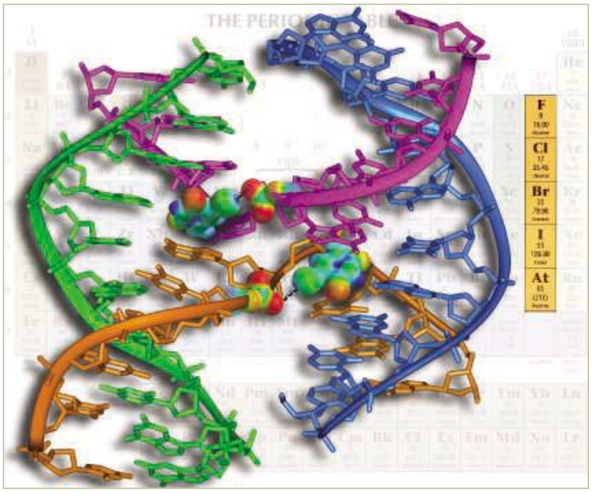

Halogen-bonded Holliday junction. The unusually short bond between the Br atom of a brominated uracil residue and the phosphate oxygens in a four-stranded DNA junction is an example of noncovalent halogen bonding.

CREDIT: P. S. HO/COLORADO STATE UNIVERSITY

In some recent studies, Ho and co-workers have investigated Holliday junctions (four-stranded DNA junctions that are believed to be key structural intermediates during homologous recombination of DNA). When thymine is replaced by 5-bromouracil (BrUra) in a base sequence, the stacked-X form of a Holliday junction is stabilized as a result of short Br···O contacts (*4*). In these contacts, the bromine atoms function as electrophilic sites. The stacked-X form of the Holliday junction can be used as a simple, well-controlled biomolecular assay, which can isomerize between two nearly isoenergetic and structurally similar conformers (*5*).

In this assay, isomerization involves restacking of the arms and migration of the junction, placing either a hydrogen bond or a halogen bond at the junction crossover. A bromine atom at the inside crossover strand indicates formation of the halogen-bonded isomer; a bromine atom at the outside strand is indicative of the hydrogen-bonded isomer. This assay proved halogen bonding to be stronger than the analogous hydrogen bonding in the same environment. This elegant method helps to establish halogen bonding as a potential new tool for the rational construction of molecular materials based on DNA and other biological macromolecules.

Many other groups have explored the competition between hydrogen bonding and halogen bonding in the cocrystallization of small molecular building blocks. For example, Corradi *et al.* reported that, when a bipyridine derivative (an electron donor) is mixed with a solution containing equimolar amounts of a halogen bonding and a hydrogen bonding donor (*7*), the halogen

---

The authors are at the Department of Chemistry, Materials, and Chemical Engineering "Giulio Natta," Politecnico di Milano, Milan, 20131, Italy. E-mail: pierangelo.metrangolo@polimi.it; giuseppe.resnati@polimi.it

bonding donor forms the corresponding cocrystal with the bipyridine derivative, while the hydrogen bonding donor remains in solution (*8*). More recently, Aakeröy *et al*. have used the competition between hydrogen bonding and halogen bonding in the cocrystallization of small aromatic building blocks. Their structural study will undoubtedly assist in developing versatile strategies for the assembly of heteromeric molecular architectures comprising both types of bonds (*9*).

Furthermore, Legon noted a striking similarity between the properties of halogen-bonded complexes of the type B···XY and their hydrogen-bonded analogs B···HX (where XY is a generalized dihalogen molecule, HX a hydrogen halide, and B a Lewis base). The rules for predicting angular geometries of hydrogen-bonded complexes (and other generalizations) can thus be extended to the halogen-bonded series, with the caveat that halogen bonds tend to remain closer to linearity (*10*).

The use of halogen bonding as a complement, or alternative, to hydrogen bonding in the assembly of functional molecular materials is only in its infancy (*11*). In the examples described above, either hydrogen bonding or halogen bonding drives the molecular recognition process, but the two interactions could also coexist and cooperate in building more complex and functional supramolecular structures (*12*, *13*). DNA provides a beautiful example of orthogonal multivalency: Every pair of matching single strands is orthogonal to other pairs (*14*). Similarly, the design of multivalent building blocks with orthogonal halogen bonding and hydrogen bonding motifs may lead to increased specificity and complexity compared with architectures using a single interaction motif.

References and Notes

1. O. Hassel, *Science* **17**, 497 (1970).
2. P. Metrangolo, F. Meyer, T. Pilati, G. Resnati, G. Terraneo, *Angew. Chem. Int. Ed.* **47**, 6114 (2008).
3. F. A. Hays, J. M. Vargason, P. S. Ho, *Biochemistry* **42**, 9586 (2003).
4. P. Auffinger, F. A. Hays, E. Westhof, P. S. Ho, *Proc. Natl. Acad. Sci. U.S.A.* **101**, 16789 (2004).
5. A. R. Voth, F. A. Hays, P. S. Ho, *Proc. Natl. Acad. Sci. U.S.A.* **104**, 6188 (2007).
6. A. R. Voth, Ph.D. dissertation, Oregon State University, see https://ir.library.oregonstate.edu/dspace/handle/1957/6696.
7. A halogen bonding donor is a species that contains an electrophilic halogen that can become a member of a halogen bond. In the literature on halogen bonding, the reader should be alert to how the words "donor" and "acceptor" are used. In a complex RX···B, RX is the halogen bond donor but the electron acceptor (Lewis acid); B is the electron donor and halogen bond acceptor (Lewis base).
8. E. Corradi, S. V. Meille, M. T. Messina, P. Metrangolo, G. Resnati, *Angew. Chem. Int. Ed*. **39**, 1782 (2000).
9. C. B. Aakeröy *et al.*, *J. Am. Chem. Soc.* **129**, 13772 (2007).
10. A. C. Legon, *Struct. Bond*. **126**, 17 (2008).
11. A. Sun, J. W. Lauher, N. S. Goroff, *Science* **312**, 1030 (2006).
12. C. B. Aakeröy *et al.*, *Chem. Commun*. 4236 (2007).
13. B. K. Saha, A. Nangia, M. Jaskólski, *Cryst. Eng. Comm.* **7**, 355 (2005).
14. C. W. Lim *et al.*, *Proc. Natl. Acad. Sci. U.S.A.* **104**, 6986 (2007).

10.1126/science.1162215

MATERIALS SCIENCE

Directing Self-Assembly Toward Perfection

A combination of self-assembled block copolymers with templated substrates can be used for precision lithographic applications.

Rachel A. Segalman

The self-assembly of block copolymers into nanoscale features is potentially attractive as a means for patterning media in microelectronic applications. This new route to nanopatterning is gaining interest as optical lithography, the current engine of the semiconductor industry, begins to approach intrinsic technological limits while demand for higher-density features for improved data storage and computing speed continues to grow (*1*). These applications require not only regularly sized nanoscale features but also a degree of perfection of order and registry relative to other components, which have so far been elusive in self-assembled systems. On pages 939 and 936 of this issue, block copolymers in conjunction with coarse templates are used to create nanoscale structures with an unprecedented level of control and long-range order (*2*, *3*).

Block copolymers consist of chemically distinct polymer chains (blocks) joined by a covalent bond. The immiscibility of the blocks drives their segregation, but their connectivity prevents complete separation, resulting in pattern formation on the length scale of the blocks (~10 nm). Spheres, cylinders, bicontinuous, or lamellar structures can form depending on the volumetric ratio of the two blocks (*4*). The chemical structure of the blocks, block lengths, and block sequence can be independently selected for a desired set of attributes, including length scale and physical properties, particularly etch contrast. Lithographic masks can then be fabricated by selectively removing one component of block copolymer (*5*).

During the self-assembly process, regularly sized and shaped nanodomains form quickly but generally assemble into defective polycrystalline arrays even after long annealing times. A wide range of techniques has emerged to control block copolymer order to create single-crystalline structures (*6*). For example, graphoepitaxial techniques use topographic features much greater in length scale than the nanodomains to induce single crystallinity (*7*, *8*). These arrays, however, possess only the quasi–long-range positional order inherent in two-dimensional crystals (*9*). Surface epitaxial

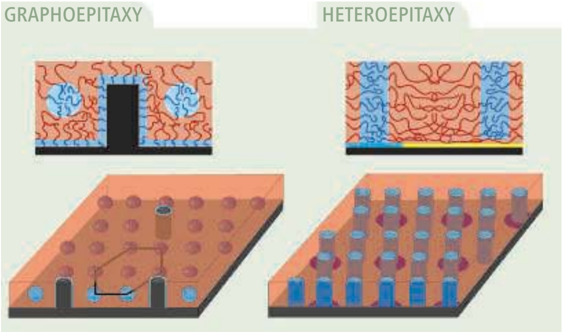

Self-assembly. Block copolymers self-assemble into regularly sized and spaced nanodomains such as hexagonal lattices of spheres or cylinders that are normally polycrystalline and contain defects. Graphoepitaxy (**left**) and heteroepitaxy (**right**) create long-range order with templates prepatterned on a length scale greater than the natural lattice of the block copolymer.

The Department of Chemical Engineering, University of California, Berkeley, and Lawrence Berkeley National Laboratory, Berkeley, CA 94720, USA. E-mail: segalman@berkeley.edu

techniques induce higher degrees of ordering perfection by patterning the substrate surface with chemical features on the same length scale as the blocks but require sophisticated processing (*10*–*12*). The work now reported uses sparse templates to direct block copolymer order.

Bita *et al.* describe the use of sparse arrays of "posts" (see the figure, left) to graphoepitaxially induce long-range order on a block copolymer sphere array forming hexagonal patterns on a ~20-nm length scale. The posts are carefully designed in both size and surface chemistry to substitute for a few of the blue, spherical nanodomains, effectively pinning positional order during self-assembly. When the spatial frequency of the posts is commensurate with the block copolymer lattice, unprecedented degrees of long-range positional and orientational order are achieved. The elastic nature of the block copolymer suggests that stretching and compression of individual chains may be an intriguing response to mismatches between the templated lattice and that of the self-assembling structure. The chain shape is driven by a combination of entropy and enthalpic repulsion of the opposite block, and deformations of the lattice are translated directly to the chains. Thus, it is possible to calculate the response of the block copolymer chains to strain on the lattice relative to universal parameters quantifying block copolymer self-assembly and chain shape. The ability of this model to capture the tolerance of the block copolymer to a given template lattice suggests that it may be possible to design a template for block copolymers of arbitrary chain lengths and chemistries, allowing for easy translation of this technique to any system of polymers and substrates.

Earlier work on the use of a nanopatterned substrate to direct the long-range order in a block copolymer thin film still required lithography on the same length scale as the block copolymer. Ruiz *et al.* demonstrate that block copolymers can now be used to multiply the feature density and improve the quality of the original surface pattern. An electron beam is used to write a pattern of round spots onto a surface layer, and then the polymer is self-assembled on top of the chemically prepatterned substrate (see the figure, right). The chains making up the blue cylinders are preferentially attracted to the blue spots on the surface. When the spot size is the same as the cylinder diameter and its spacing is an integer multiple of the natural block copolymer spacing, self-assembly interpolates additional cylinders between the prepatterned spots, thereby amplifying the feature density while maintaining a perfect lattice. More intriguing is the fact that if the spot size is even twice the cylinder diameter, the block copolymer also rectifies the pattern to form regularly sized and perfectly patterned spots on its natural lattice. This is surprising because this surface pattern forces additional unfavorable surface interactions between the red matrix and the dark blue patterned surface spots.

The results of Ruiz *et al.* and Bita *et al.* suggest exciting routes toward nanopatterns with perfected long-range positional order that are suitable for microelectronic applications. Clearly, the challenge ahead for block copolymer lithography is to stretch these sparse templating approaches away from expensive, difficult to scale electron beam patterned substrates toward less expensive, scalable options such as optical lithography or other routes that allow the electron beam template to be reused.

References

1. International Technology Roadmap for Semiconductors, 2007 (www.itrs.net).
2. I. Bita *et al.*, *Science* **321**, 939 (2008).
3. R. Ruiz *et al.*, *Science* **321**, 936 (2008).
4. F. S. Bates, G. H. Fredrickson, *Annu. Rev. Phys. Chem.* **41**, 525 (1990).
5. M. Park, C. Harrison, P. M. Chaikin, R. A. Register, D. H. Adamson, *Science* **276**, 1401 (1997).
6. R. A. Segalman, *Mater. Sci. Eng. R* **48**, 191 (2005).
7. J. Y. Cheng, C. A. Ross, E. L. Thomas, H. I. Smith, G. J. Vancso, *Appl. Phys. Lett.* **81**, 3657 (2002).
8. R. A. Segalman, H. Yokoyama, E. J. Kramer, *Adv. Mater.* **13**, 1152 (2001).
9. D. E. Angelescu *et al.*, *Phys. Rev. Lett.* **95**, 025702 (2005).
10. L. Rockford *et al.*, *Phys. Rev. Lett.* **82**, 2602 (1999).
11. S. O. Kim *et al.*, *Nature* **424**, 411 (2003).
12. M. P. Stoykovich *et al.*, *Science* **308**, 1442 (2005).

10.1126/science.1162907

PLANETARY SCIENCE

The Elusive Onset of Geomagnetic Substorms

The triggers of geomagnetic substorms, and their connection to auroral displays, have been sought in data from a satellite fleet and ground-based observations.

A. A. Petrukovich

In Earth's magnetosphere, the geomagnetic field interacts with the solar magnetic field carried by the solar wind (the interplanetary magnetic field). When the two fields are aligned appropriately, the interplanetary magnetic field can deposit 10^{14} to 10^{15} J of energy during several tens of minutes into Earth's magnetosphere. At the subsequent onset of a geomagnetic substorm, this energy is explosively released and leads to the colorful auroral lights often seen at high latitudes. Onset events are essentially unpredictable, and onset models suggesting different scenarios of substorm development are hotly debated in magnetospheric physics. On page 931 of this issue, Angelopoulos *et al.* (*1*) use data from a fleet of satellites, as well as ground observations of an auroral event, to elucidate what triggers substorm onset.

The term "substorm" originates in some of the earliest geophysical observations (*2*, *3*). In the mid-19th century, global variations in the geomagnetic field were named "magnetic storms." Similar variations that occurred only at high latitudes in association with auroras were discovered later, and because they were supposed to be a part of storms, were termed "substorms." The two events differ, however, in that storms are a global reaction to extreme interplanetary conditions, mostly after solar eruptive events such as coronal mass ejections. Storms and substorms are major constituents of geomagnetic activity and space weather (*4*).

Earth's magnetosphere is shaped by the flow of the solar wind, but direct transfer of energy by impinging solar-wind particles is relatively ineffective, in comparison with the effects of the interplanetary magnetic field. With no collisions and almost no dissipation, ion and electron trajectories trace spirals around magnetic field lines. We can use their paths to help visualize field lines as continuous physical objects.

When oppositely directed field lines converge, the magnetic field vanishes locally. The field line picture is smeared in this zone, and parts of formerly different field lines can reemerge ("reconnect") as a new line if the new state has lower energy. In his classic reconnection scheme, Dungey (*5*) suggested

---

Space Research Institute, Moscow, Russia. E-mail: apetruko@iki.rssi.ru

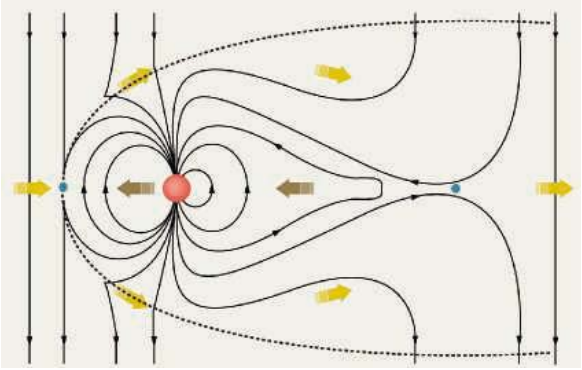

Magnetic convection in the magnetosphere. Interplanetary field lines (yellow) reconnect with geomagnetic ones (brown) at the day side (left center), form the magnetotail (right center), and finally exit (right) in the downstream solar wind.

that when the interplanetary magnetic field and the dayside geomagnetic field are antiparallel (as occurs with variations in the interplanetary magnetic field), the magnetosphere is "open." Magnetic field lines are disconnected on the day side and transported by the solar wind flow to the night side, where an elongated magnetotail forms and antiparallel stretched field lines may again reconnect and return to Earth (see the first figure). When the interplanetary magnetic field and the geomagnetic field are parallel, the magnetosphere is "closed." Substorms occur in the open configuration if the nightside reconnection is not fast enough and magnetic energy accumulates in the magnetotail. After substorm onset, excess magnetic flux is rapidly disposed in the newly forming reconnection region.

This general picture is relatively well established, but many important details are missing. An onset is driven by an explosive instability, and plasma theory offers a rich choice of candidates, depending in particular on onset location. However, the mechanism in question operates for only a few minutes in a rather localized region, so its direct observation with a spacecraft that measures only local plasma properties (such as plasma density, flows, and magnetic and electric fields) is almost impossible. However, an array of several spacecraft detecting plasma flows and other features on different sides of an onset (reconnection site) could effectively probe its location and reconstruct a cause-and-effect scheme (*6*, *7*).

On the other hand, ground observations of aurora development (*8*)—such as the data in the movies that accompany the report by Angelopoulos *et al.*—can help. Auroral lights are produced when electrons precipitating from magnetosphere excite neutral atoms and molecules in the ionosphere; this partially ionized layer extends from 100 to 500 km. In contrast, the overlying magnetosphere is made up of a much more dilute, fully ionized gas. Every point in the ionosphere is connected with some point in the magnetotail by a field line. During onsets, auroras brighten suddenly under the effect of increased electron precipitation and fill up the sky poleward from this first enhancement. However, the auroral display does not provide an ultimate answer on onset location because its connection with the ionosphere varies substantially when the magnetotail elongates and contracts. In addition, the ionosphere-magnetosphere link is not passive; some magnetospheric signals are amplified en route to the ionosphere and others are damped.

Unfortunately, the approaches described above do not converge to any unified picture of onset development. The satellite data indicate that reconnection occurs on the order of 120,000 to 200,000 km from Earth, whereas onsets in auroral display point to a much closer location around 60,000 km. Two counterposed scenarios have been suggested to explain these different results. The "outside-in" model advocates a reconnection impulse as the primary onset (*9*). Subsequent plasma flows, ejected from the reconnection site toward Earth, may then generate auroral features. Alternatively, the "inside-out" models place primary onset (or "current disruption") with aurora observations (*10*). Reconnection is then a secondary effect that initiates later and further downtail.

In 2007, NASA launched five spacecraft as part of the THEMIS project specially targeted to elucidate substorm onset (*11*). Their orbits were properly synchronized so that all of the satellites periodically lined up above the extensive ground-observing network in Canada (see the second figure). Such a setup is believed to increase significantly the probability of catching onsets and to test these two opposing scenarios. Angelopoulos *et al.* present one of the first results of the project. In their particular observation, the reconnection is the first sign of onset, starting at 120,000 km. More statistically substantiated conclusions are awaited soon with larger observational time.

Actually, substorms are likely to be a combination of many elementary processes occurring concurrently, and scenarios might differ from case to case. This mosaic of possibilities might fit into a clear picture only during selected "perfect" events. An even more ambitious project with about 100 small satellites spread across the magnetotail is being planned in the nearest decades as a further step to understand substorms in more detail.

References

1. V. Angelopoulos *et al.*, *Science* **321**, 931 (2008); published online 24 July 2008 (10.1126/science.1160495).
2. D. P. Stern, *Rev. Geophys.* **27**, 103 (1989).
3. D. P. Stern, *Rev. Geophys*. **34**, 1 (1996).
4. J. W. Freeman, *Storms in Space* (Cambridge Univ. Press, Cambridge, UK, 2001).
5. J. W. Dungey, *Phys. Rev. Lett.* **6**, 47 (1961).
6. A. A. Petrukovich, A. G. Yahnin, *Space Sci. Rev*. **122**, 81 (2006).
7. A. Nishida, *Magnetic Reconnection*, in *Handbook of the Solar-Terrestrial Environment*, Y. Kamide, A. C.-L. Chian, Eds. (Springer, Berlin, 2007).
8 S.-I. Akasofu, *Planet. Space Sci*. **12**, 273, (1964).
9. D. N. Baker *et al.*, *J. Geophys. Res.* **101**, 12975 (1996).
10. A. T. Y. Lui, *J. Geophys. Res*. **101**, 13067 (1996).
11. V. Angelopoulos, *Space Sci. Rev.* 10.1007/s11214-008-9336-1 (2008).

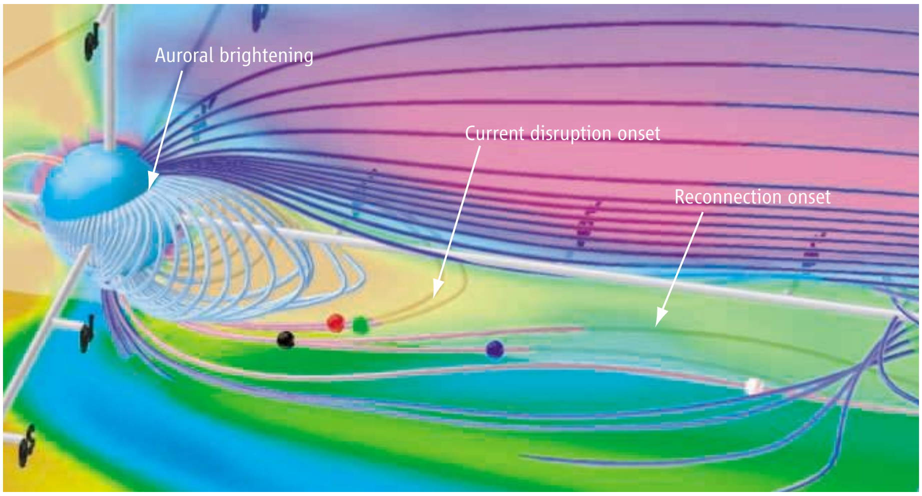

Sampling a substorm. The positions of the five THEMIS satellites were synchronized radially so that the onset location could be judged. Associated events that were monitored at different positions in the magnetosphere and ionosphere are shown.

CREDIT: (BOTTOM) JIMMY RAEDER/UNIVERSITY OF NEW HAMPSHIRE

MOLECULAR BIOLOGY

Secret Weapon

Ryland F. Young III

A mechanism that generates small RNAs in bacteria provides protection against bacteriophage.

The battle between bacteria and their viruses (bacteriophages) is, quantitatively, the dominant predator-prey relation in the biosphere, with an estimated 10^{30} infections per day. It is an unequal contest in many ways. Phages replicate prodigiously. Within 2 hours of the addition of a single T7 bacteriophage particle to a culture of 10 billion *Escherichia coli* cells, more than 99.9% of the bacteria are destroyed and 10 trillion virus particles are generated. And although, in an evolutionary sense, bacteria can "run" by generating receptor mutations that prevent phage binding, they cannot "hide"—phage mutate at such high frequency that every mutational evasion tried by bacteria is soon overcome by phages with altered specificity (*1*). Moreover, phages undergo unparalleled degrees of genomic recombination, so new specificities and other virulence features can spread rapidly to brethren and even unrelated phages. On page 960 in this issue, Brouns *et al*. (*2*) characterize a new kind of bacterial defense based on small RNA molecules that match short sequences in the phage DNA.

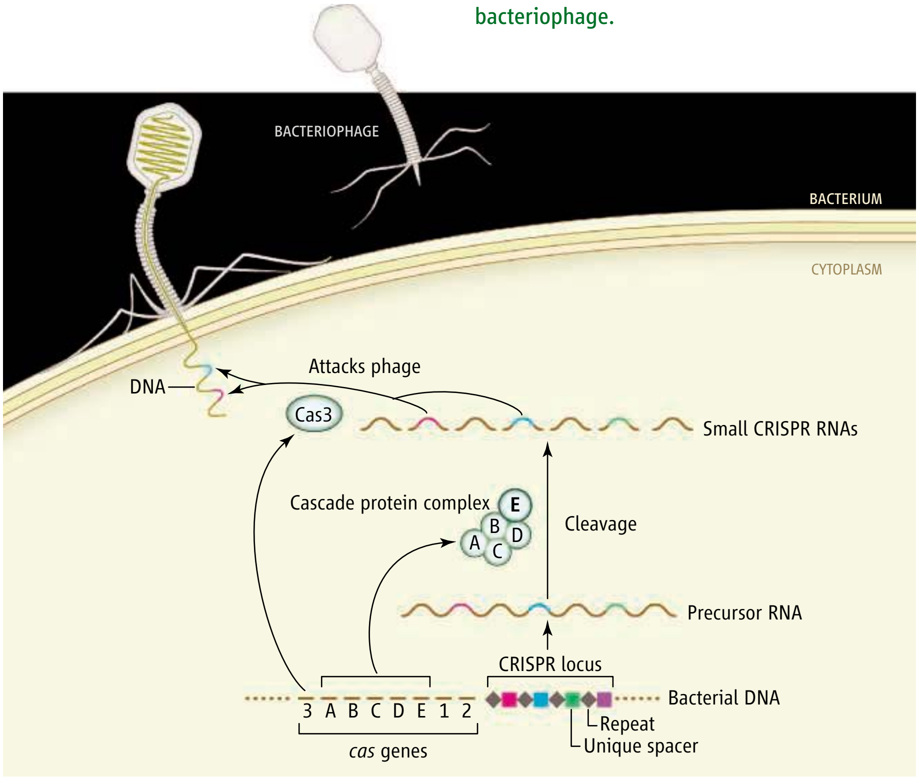

A CRISPR defense. The CRISPR locus in *E. coli* is transcribed into a large precursor RNA, which is processed by the Cascade protein complex into short fragments that contain unique spacers identical to sequences in the phage DNA. Assisted by the protein Cas3, these small CRISPR RNAs block the phage infection cycle.

CREDIT: ADAPTED BY P. HUEY/SCIENCE

After binding to a receptor, a phage injects its genetic material into the bacterium, whereupon viral DNA and proteins are synthesized and new virions are assembled. A system called restriction-modification is a well-known bacterial defense against phage infection, in which a bacterium chemically modifies its own DNA at every occurrence of a particular restriction site, usually a short palindromic sequence. Wherever the sequence occurs in the newly injected phage DNA, it will not be modified and consequently, it will be cleaved by a corresponding restriction endonuclease, stopping the virus in its tracks. But occasionally the system fails, and if the DNA of even one virus becomes modified, all of its subsequent progeny will encounter no barrier in further infection cycles. Moreover, some phages use altered DNA bases that confound restriction enzymes, whereas others inject proteins that inhibit the restriction enzymes. Even more cleverly, phages may use a two-step injection process, in which only a small portion of phage DNA first enters the bacterium. This DNA encodes proteins that antagonize restriction enzymes. Cells also have suicide defenses, in which infections by certain phages leads to premature cell death, squelching the infection cycle before virus particles assemble.

Recently, a new kind of phage defense was discovered, based on loci called clusters of regularly interspaced short palindromic repeats (CRISPR) that are widespread in the DNA of bacteria and archaea (*3*–*5*). CRISPR loci consist of multiple short nucleotide repeats separated by unique spacer sequences and flanked by a characteristic set of *CRISPR-associated* (*cas*) genes (see the figure) (*6*, *7*). The discovery that the spacers were often identical to short sequences in phage DNA, and that they seem to be constantly changing in bacteria, suggested that they were a kind of "memory of past genetic aggressions" (*8*) and might underlie some kind of defense against foreign DNA (*9*–*11*). This was confirmed in an elegant study by Barrangou *et al*. (*3*), in which a culture of *Streptococcus thermophilus* was challenged with phage. Rare phage-resistant bacteria were isolated that had acquired at least one new CRISPR spacer identical to a sequence in the phage DNA. By replacing the entire CRISPR repeat array in *S. thermophilus* with the new CRISPR spacers, phage resistance was conferred. Moreover, phage overcame resistant bacteria by mutating just 1 base pair within the sequence corresponding to the new spacer.

More recently, metagenomic analysis of archaea has indicated that CRISPR loci are extremely dynamic, with sequence changes occurring on a time scale of months, and that new spacers appear corresponding to phages coexisting in archaeal communities (biofilms) (*12*). An interesting twist from this analysis was that, at least for the phages in these biofilms, overcoming the CRISPR defense appeared to be primarily a matter of intense recombinational shuffling down to a scale of the size of CRISPR spacers, rather than mutations.

Although these genetic and genomic analyses (*3*, *12*) clearly showed that the CRISPR defense is a fundamental aspect of bacterial and archaeal evolution, mechanistic insight was completely lacking. In a major step forward, Brouns *et al*. have reconstituted the CRISPR phenomenon in laboratory strains of *E. coli*, which, although it has CRISPR sequences, had not been shown to use the

Department of Biochemistry and Biophysics, Texas A&M University, College Station, TX 77843–2128, USA. E-mail: ryland@tamu.edu

CRISPR defense against any known phages. The authors identify a multiprotein complex called CRISPR-associated complex for antiviral defense (Cascade), consisting of five Cas proteins (CasA to CasE), and show that it processes a long primary CRISPR transcript to 57-nucleotide fragments, each containing a unique spacer and bits of the flanking repeat sequences (see the figure). By cloning all five *cas* genes in different combinations into an *E. coli* strain lacking CRISPR sequences entirely, Brouns *et al*. show that only CasE is required for cleavage of the primary CRISPR transcript. Cascade processed primary CRISPR RNA, but not CRISPR RNA (with a different CRISPR repeat) from a different *E. coli* species, and could be copurified with the 57-nucleotide RNAs, indicating the formation of a ribonucleoprotein complex. Importantly, the authors could also construct a CRISPR defense against the bacteriophage lambda by engineering new spacers into the *E. coli* CRISPR locus, chosen from sites throughout the lambda genome. The artificial CRISPR array was efficient, reducing the ability of phage lambda to grow by a factor of 10,000,000. This effect depended on the presence of functional Cascade and expression of the *cas3* gene. In each case, the spacer sequences could be chosen from either the template or noncoding DNA strand of the phage genes, suggesting that the target of CRISPR is the phage DNA. This seems to be fundamentally different from the small inhibitory RNA strategy of eukaryotes, which suppresses viral gene expression by destroying corresponding messenger RNA.

The work by Brouns *et al*. has put at least the active defense aspect of the CRISPR system on track for thorough mechanistic and structural analysis. The ability to genetically and biochemically manipulate *E. coli* is far superior to other biological systems, and bacteriophage lambda is arguably the only biological entity for which we have nearly predictive understanding. It can be expected that rapid advances will be made in elucidating the molecular details for CRISPR gene expression, RNA processing, and the attack on the target phage.

Still obscure is how a bacterium acquires new spacer sequences. No one has reported a system for achieving this naturally, at efficiencies conducive to biochemical analysis. Moreover, we should anticipate that phages have developed clever evasions of the CRISPR system just as they have done for restriction enzymes. Considering that the origin of modern molecular biology is grounded in the study of bacteriophage, it is puzzling that this particular weapon in the phage-bacteria war remained a secret for so long.

References

1. U. Qimron, B. Marintcheva, S. Tabor, C. C. Richardson, *Proc. Natl. Acad. Sci. U.S.A.* **103**, 19039 (2006).
2. S. J. J. Brouns *et al.*, *Science* **321**, 960 (2008).
3. R. Barrangou *et al.*, *Science* **315**, 1709 (2007).
4. H. Deveau *et al.*, *J. Bacteriol.* **190**, 1390 (2008).
5. P. Horvath *et al.*, *J. Bacteriol.* **190**, 1401 (2008).
6. R. Jansen, J. D. Embden, W. Gaastra, L. M. Schouls, *Mol. Microbiol.* **43**, 1565 (2002).
7. D. H. Haft, J. Selengut, E. F. Mongodin, K. E. Nelson, *PLoS Comput. Biol.* **1**, e60 (2005).
8. C. Pourcel, G. Salvignol, G. Vergnaud, *Microbiology* **151**, 653 (2005).
9. A. Bolotin, B. Quinquis, A. Sorokin, S. D. Ehrlich, *Microbiology* **151**, 2551 (2005).
10. F. J. Mojica, C. Diez-Villasenor, J. Garcia-Martinez, E. Soria, *J. Mol. Evol.* **60**, 174 (2005).
11. K. S. Makarova, N. V. Grishin, S. A. Shabalina, Y. I. Wolf, E. V. Koonin, *Biol. Direct* **1**, 7 (2006).
12. A. F. Andersson, J. F. Banfield, *Science* **320**, 1047 (2008).

10.1126/science.1162910

OCEAN SCIENCE

Ironing Out Ocean Chemistry at the Dawn of Animal Life

New data change the picture of how the iron, oxygen, and sulfur contents of the ocean evolved.

Timothy W. Lyons

Few who study the evolution of Earth's early ocean and atmosphere would quibble with models that point to vanishingly low amounts of oxygen before the first major step in oxygenation about 2.4 billion years ago. Because iron is insoluble in O_2-containing waters, scientists have long linked this first step to the eventual disappearance of iron-rich oceans by 1.8 billion years ago; according to this model, iron-rich oceans only reappeared for brief curtain calls more than a billion years later, during the "snowball Earth" glaciations (see the figure). On page 949 of this issue, Canfield *et al.* (*1*) argue instead for a full repeat performance, with a global, long-lived return to dominantly iron-rich (ferruginous) conditions about 700 million years ago (see the figure). This surprising reappearance, with its implications for past and coeval ocean chemistry, climate, and biological evolution, seems to have persisted to 540 million years ago and perhaps a little longer, overlapping with the second major step in atmospheric oxygenation and the concomitant rise of animals (*2–4*).

A decade ago, Canfield (*5*) challenged the prevailing paradigm for oxygenation of the ocean and the disappearance of banded iron formations (BIFs)—the layered, rusty, sulfur-poor smoking guns of the early, iron-rich ocean. The classic argument links the demise of BIFs to wholesale oxygenation of the deep ocean about 1.8 billion years ago, which overwhelmed the iron sources from that point forward and kept the ocean free of all but the tiniest amounts of iron. Canfield suggested instead that the deep ocean remained oxygen-free for another billion years or more. During that long period of deep-ocean anoxia, it was high concentrations of dissolved hydrogen sulfide (H_2S) that eventually drove out the iron, because H_2S and oxygen have a similarly debilitating effect on iron solubility.

As the story goes, the still-small amounts of oxygen in the atmosphere after 2.4 billion years ago were consumed through decay of settling organic matter produced in the surface ocean, leaving the deep ocean oxygen-poor (*5*). But even a small increase of oxygen in the atmosphere meant greater oxidation of sulfur-containing minerals exposed on the continents. With that weathering came delivery of sulfate (SO_4^{2-}) to the ocean by rivers. Increasing sulfate in seawater and the underlying sediments resulted in ubiquitous production of H_2S by bacteria that reduce sulfate in the absence of oxygen, and this H_2S reacted with the dissolved iron to form pyrite (FeS_2) (see the figure).

Today, large reservoirs of anoxic, H_2S-containing seawater are rare; the most voluminous is the Black Sea. In contrast, as sulfate began to accumulate in the still oxygen-poor earlier deep ocean (*6*), it is likely that H_2S-rich waters were far more common over the billion

---

Department of Earth Sciences, University of California, Riverside, CA 92521, USA. E-mail: timothy.lyons@ucr.edu

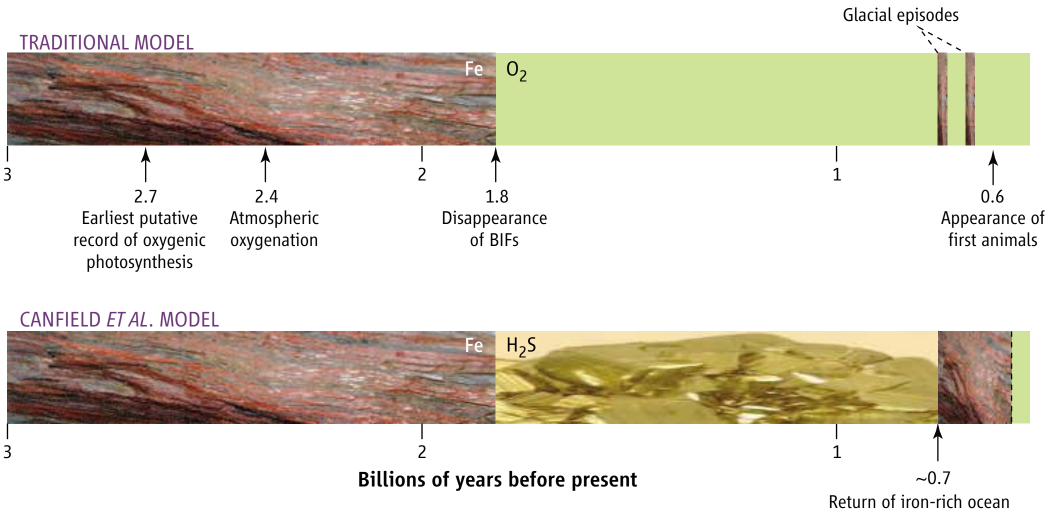

The evolving deep ocean. In the traditional model, oxygenation of the ocean occurred 1.8 billion years ago, with only brief recurrence of ferruginous conditions during later global glaciations (*11*). Canfield *et al.* now suggest that widespread deep-ocean anoxia lasted to 540 million years ago and perhaps a little longer. Instead of early oxygenation, after 1.8 billion years ago the deep ocean was dominated by H_2S, followed by a repeat of widespread iron conditions (*1*).

years following the disappearance of the BIFs about 1.8 billion years ago, before the reprise of ferruginous conditions around 700 million years ago (*4*, *7*–*10*). Evidence for anything like a global Black Sea during this interval remains patchy, often indirect, and difficult to reconcile with the full range of data now available (*4*, *11*), but H_2S must have been common in the deep waters and/or in the underlying sediments. And the capacity to form and bury pyrite in these oxygen-lean deep settings and thus remove sulfate from seawater was also sufficient to consume dissolved iron for millions of years. Canfield *et al.* now suggest that this delicate balance may have set the stage for the iron rebound 700 million years ago: A sudden dearth of sulfate overwhelmed the ocean's ability to lock up iron in pyrite, leaving more of the metal floating free once more.

The authors found evidence for this dramatic, long-lived return to iron-rich conditions by analyzing sediments from around the world, spanning from 760 to 530 million years in age. Their well-tested method delineates iron present as pyrite and as oxide and carbonate phases that form pyrite on geologically short time scales if exposed to H_2S. Broad temporal compilations often blur important details, but here the authors find that a clear first-order trend prevails: enrichments in iron minerals, with oxides and carbonates typically swamping the pyrite. Much of the unpyritized iron occurs as the same minerals that dominate BIFs deposited before 1.8 billion years ago, when the ocean was anoxic and iron-rich. These findings suggest that the deep sea was similarly oxygen-free and iron-rich starting 700 million years ago—which also implies that it was severely lacking in both H_2S and sulfate.

This lack of sulfate is surprising, considering that by then the atmosphere contained more than enough oxygen to foster sulfate delivery to the ocean by oxidative weathering on the continents. Part of the explanation stems from a global deep freeze that started about that same time. In most models for this snowball Earth event, during which ice shrouded much if not most of the continents and oceans, lower extents of chemical weathering on icy continents would have limited sulfate delivery to the ocean, and loss of sulfate would be exacerbated by its bacterial conversion to H_2S and subsequent pyrite formation in an oxygen-free, ice-covered ocean (*12*).

But what is most striking about the data of Canfield *et al.* is that both anoxia and high-iron, low-H_2S conditions seem to dominate for many millions of years beyond the known effects of the snowball glaciations. The most important factor in the dearth of sulfate may thus be a long history of pyrite formation in the deep ocean and underlying sediments. Its burial and the eventual subduction of the pyrite-bearing seafloor below overriding tectonic plates utterly stripped the ocean of sulfate by shutting down its potential return by weathering (*13*). Independent of ice cover, oxygen in the atmosphere (and thus in seawater) was still too low to overcome the compensating effects of respiratory consumption in the ocean. In short, pyrite may have driven the ocean to anemia 1.8 billion years ago, but a billion years of pyrite burial may have shifted the balance back to iron.

Sulfur isotope data from similarly aged rocks in Oman capture the same extremes in sulfate deficiency (*2*), yet other sulfur isotope data spanning roughly the same time suggest bacterial cycling under higher sulfate concentrations (*2*, *14*). Consistent with the latter, gypsum—a calcium sulfate mineral—is known to have formed from evaporation of seawater of the same age (*15*).

Other vexing inconsistencies and gaps remain. We still do not know much about H_2S and iron in the deep sea during the billion years that preceded the hypothesized iron ocean, although Canfield *et al.* give us a reason to look harder. Snowball Earth proponents may have to remove a ferruginous ocean from their supporting arguments. Given that iron is a bioessential metal, evolutionary scientists (*16*) will have to reexplore eukaryotic evolution in light of a deep ocean that was persistently oxygen-poor but may have transitioned from iron-rich to iron-poor back to iron-rich. And, as always, global-scale extrapolations from local environments should be viewed with a squint. But once all this is ironed out, Canfield *et al.* will have guided many of the emerging views on biospheric oxygenation.

References

1. D. E. Canfield *et al.*, *Science* **321**, 949 (2008); published online 17 July 2008 (10.1126/science.1154499).
2. D. A. Fike, J. P. Grotzinger, L. M. Pratt, R. E. Summons, *Nature* **444**, 744 (2006).
3. D. E. Canfield, S. W. Poulton, G. M. Narbonne, *Science* **315**, 92 (2007); published online 6 December 2006 (10.1126/science.1135013).
4. C. Scott *et al.*, *Nature* **452**, 456 (2008).
5. D. E. Canfield, *Nature* **396**, 450 (1998).
6. L. C. Kah, T. W. Lyons, T. D. Frank, *Nature* **431**, 834 (2004).
7. Y. Shen, A. H. Knoll, M. R. Walter, *Nature* **423**, 632 (2003).
8. G. L. Arnold, A. D. Anbar, J. Barling, T. W. Lyons, *Science* **304**, 87 (2004); published online 4 March 2004 (10.1126/science.1091785).
9. J. J. Brocks *et al.*, *Nature* **437**, 866 (2005).
10. S. W. Poulton, P. W. Fralick, D. E. Canfield, *Nature* **431**, 173 (2004).
11. H. D. Holland, *Philos. Trans. R. Soc. London Ser. B* **361**, 903 (2006).
12. M. T. Hurtgen, M. A. Arthur, N. Suits, A. J. Kaufman, *Earth Planet. Sci. Lett.* **203**, 413 (2002).
13. D. E. Canfield, *Am. J. Sci.* **304**, 839 (2004).
14. D. E. Canfield, A. Teske, *Nature* **382**, 127 (1996).
15. D. A. Fike, J. P. Grotzinger, *Geochim. Cosmochim. Acta* **72**, 2636 (2008).
16. A. D. Anbar, A. H. Knoll, *Science* **297**, 1137 (2002).

10.1126/science.1162870

RETROSPECTIVE

Victor A. McKusick (1921–2008)

The founder of medical genetics was a driving force behind current progress in applying genetic information to medicine.

Francis S. Collins

It is the rare scientist who is universally recognized as the founder of a field. Even rarer is the one who witnesses his vision evolve from a solitary pursuit into a major discipline. But such was the life of the father of medical genetics, Victor Almon McKusick, who died 22 July after more than a half-century of pioneering research, mentorship, and leadership.

McKusick was the driving force for moving genetics beyond the tidy realm of flies and mice in the research lab into the messier realm of the medical clinic. In 1957, he established a medical genetics clinic at Johns Hopkins, the model for what would become more than 100 such clinics nationwide, and unleashed a flood of discoveries that demonstrated connections between genes and disease. Today, thanks largely to McKusick's creative and tireless contributions, the field of medical genetics is at the center of medicine.

While the influence of some scientific leaders wanes with their passing, McKusick's will only grow with time. His work created a dynamic legacy that lives on in the thousands of physician-researchers he mentored, and the marvelous, updatable resources he created. Nearly every medical geneticist, including myself, can trace his or her scientific lineage back to McKusick.

The first of my many sips from McKusick's seemingly bottomless well of knowledge came in 1981. As a medical genetics fellow at Yale, I was confronted with a puzzling infant with a congenital intestinal obstruction. The child had a sibling with an identical condition. I was stumped about the diagnosis, as was my attending physician, Uta Francke. So, we consulted McKusick's landmark text, *Mendelian Inheritance in Man*, and came upon entry "*243600, Familial apple peel jejunal atresia," a perfect description of the child's condition. Whereupon, Uta said, "This is wonderful. Victor should win the Nobel Prize!"

Scientific prizes probably were not on anyone's mind when McKusick and his identical twin, Vincent, were born 21 October 1921 on a dairy farm in Parkman, Maine. In fact, McKusick considered becoming a minister until age 15, when he developed a serious streptococcal infection and came away inspired by the physicians who saved his life. After spending 3 years as an undergraduate at Tufts, McKusick enrolled in 1943 in the Johns Hopkins School of Medicine, from which he graduated in 1946 and where he held a series of distinguished professorships up until his death.

While he authored many seminal papers and books on genetics, McKusick also delighted in sharing the story of his first encounter with the world of scientific publishing. As a medical student, he and his brother Robert (who became a dairy farmer) wrote a paper on the inheritance pattern of coat color in Jersey cattle, describing how the apparently dominant fawn color was actually a recessive trait. They eagerly sent their genetics paper off to the *Journal of Heredity*, but never got a response. Fortunately, both for McKusick and the scientific community, future journal editors would display better judgment.

CREDIT: TORU YAMANAKA/AFP/GETTY IMAGES

Among his key publications was a 1966 paper describing the first mapping of a human autosomal gene, the Duffy blood group locus. He also clinically defined a series of connective tissue disorders, the most famous of which is the Marfan syndrome. The tour de force of McKusick's publications, however, remains his constantly updated *Mendelian Inheritance in Man*, a catalog of human genes and genetic disorders. This classic reference first appeared in print in 1966 and contained about 1500 entries. Today, an electronic version features nearly 19,000 entries.

No description of McKusick's impact on science is complete without mentioning his prescient call for mapping the human genome. In August 1969, at the International Conference on Birth Defects in The Hague, McKusick proposed that mapping all human genes would be useful for understanding basic derangements in birth defects. "The proposal reflected the exuberant mindset that followed the first Moon landing by Apollo 11," he recalled in a 2006 article. But the idea met with perplexed silence, in part because no one—not even McKusick—was clear on what methods could be used to achieve such an ambitious goal. Thankfully, McKusick was not one to give up easily, and was a strong advocate for The Human Genome Project, stepping forward in the mid-1980s to serve as the founding president of the Human Genome Organisation.

During a career that spanned an impressive 60 years, McKusick received many accolades, including election to the National Academy of Sciences in 1973, the Albert Lasker Award for Special Achievement in Medical Science in 1997, the National Medal of Science in 2001, and the Japan Prize in Medical Genetics and Genomics in 2008.

Medals and proclamations aside, I suspect that one achievement that McKusick would most want to be remembered for is his role in establishing the legendary "Short Course in Medical and Experimental Mammalian Genetics." This 2-week event, held each summer at The Jackson Laboratory in Bar Harbor, Maine, has had a profound influence on medical genetics. Since it began in 1960, more than 5000 clinical specialists, educators, and others have had the privilege of learning about the latest advances from some of the best minds in the field. In fact, according to Anne, McKusick's physician wife of 59 years, hours before her husband died peacefully of cancer at their home outside Baltimore, Maryland, he had enjoyed watching the live streaming video of this summer's "Short Course."

More than a century ago, the father of modern medicine, Sir William Osler, wrote: "To wrest from nature the secrets which have perplexed philosophers in all ages, to track to their sources the causes of disease, to correlate the vast stores of knowledge, that they may be quickly available for the prevention and cure of disease—these are our ambitions." Victor McKusick, who appropriately held the Osler Professorship for many years at Johns Hopkins, lived that vision better than any other physician of the last half-century.

10.1126/science.1163901

National Human Genome Research Institute, National Institutes of Health, Bethesda, MD 20892, USA. E-mail: 4rancis@mail.nih.gov

Spreading Dead Zones and Consequences for Marine Ecosystems

Robert J. Diaz[1]* and Rutger Rosenberg[2]

Dead zones in the coastal oceans have spread exponentially since the 1960s and have serious consequences for ecosystem functioning. The formation of dead zones has been exacerbated by the increase in primary production and consequent worldwide coastal eutrophication fueled by riverine runoff of fertilizers and the burning of fossil fuels. Enhanced primary production results in an accumulation of particulate organic matter, which encourages microbial activity and the consumption of dissolved oxygen in bottom waters. Dead zones have now been reported from more than 400 systems, affecting a total area of more than 245,000 square kilometers, and are probably a key stressor on marine ecosystems.

The visible ecosystem response to eutrophication is the greening of the water column as the algae and vegetation in coastal areas grow in direct response to nutrient enrichment. The most serious threat from eutrophication is the unseen decrease in dissolved oxygen (DO) levels in bottom waters, created as planktonic algae die and add to the flow of organic matter to the seabed to fuel microbial respiration (*1*). Hypoxia occurs when DO falls below ≤ 2 ml of O_2/liter, at which point benthic fauna show aberrant behavior—for example, abandoning burrows for exposure at the sediment-water interface, culminating in mass mortality when DO declines below 0.5 ml of O_2/liter (*2*). In most cases, hypoxia is associated with a semi-enclosed hydrogeomorphology that, combined with water-column stratification, restricts water exchange. More recently, dead zones have developed in continental seas, such as the Baltic, Kattegat, Black Sea, Gulf of Mexico, and East China Sea, all of which are major fishery areas.

Although the anthropogenic fertilization of marine systems by excess nitrogen has been linked to many ecosystem-level changes, there are natural processes that can lead to nutrient enrichment along continental margins that produce similar ecosystem responses. Coastal upwelling zones associated with the western boundary of continental landmasses are highly productive but are associated with severe hypoxia (<0.5 ml O_2/liter). These oxygen minimum zones (OMZs) occur primarily in the eastern Pacific Ocean, south Atlantic west of Africa, Arabian Sea, and Bay of Bengal, and are persistent oceanic features occurring in the water column at intermediate depths (typically 200 to 1000 m) (*3*). Where they extend to the bottom, the benthic fauna is adapted to DO concentrations as low as 0.1 ml of O_2/liter. This is in stark contrast to the faunal responses seen during recent eutrophication-induced hypoxic events in coastal and estuarine areas where DO concentrations this low led to mass mortality and major changes in community structure (*2*).

Global Nature of Eutrophication-Induced Hypoxia

The worldwide distribution of coastal oxygen depletion is associated with major population centers and watersheds that deliver large quantities of nutrients (Fig. 1 and table S1). Most of these systems were not hypoxic when first studied, but it appears that from the middle of the past century, the DO concentrations of many coastal ecosystems have been adversely affected by eutrophication. The observed declines in DO have lagged about 10 years behind the increased use of industrially produced nitrogen fertilizer that began in the late 1940s, with explosive growth in the 1960s to 1970s (*4*). For marine systems with data from the first half of the 20th century, declines in oxygen concentrations were first observed in the 1950s in the northern Adriatic Sea (*5*), between the 1940s and 1960s in the northwestern continental shelf of the Black Sea (*6*), and in the 1980s in the Kattegat (*7*). Localized declines of DO levels were noted in the Baltic Sea as early as the 1930s, but it wasn't until the 1960s that hypoxia became widespread (*7*). Localized hypoxia had also been observed since the 1930s in the Chesapeake Bay (*8*) and since the 1970s in the northern Gulf of Mexico (*9*) and many Scandinavian coastal systems (*7*). Paleoindicators (foraminifera ratios and organic and inorganic compounds) show that hypoxia had not been a naturally recurring event in these ecosystems (*10*, *8*). The number of dead zones has approximately doubled each decade since the 1960s (fig. S1 and table S1).

Hypoxia tends to be overlooked until higher-level ecosystem effects are manifested. For example, hypoxia did not become a prominent environmental issue in the Kattegat until several years after hypoxic bottom waters were first reported and fish mortality and the collapse of the Norway lobster fishery attracted attention (*11*). Although hypoxia in the northern Gulf of Mexico has affected benthic communities over the past several decades, there is no clear signal of hypoxia in fishery landings statistics (*9*).

Ecosystem-level change is rarely the result of a single factor, and several forms of stress typically act in concert to cause change. The shallow northwest continental shelf of the Black Sea provides an example of a system stressed by eutrophication-driven hypoxia in combination with other stressors, including overfishing and the introduction of invasive species, all of which led to drastic reductions in demersal fisheries. Nutrient inputs declined in the 1990s, hypoxia disappeared, and ecosystem services recovered; however, nutrient inputs are again rising as agriculture expands and a return to hypoxic conditions may be imminent (*12*). The key to reducing dead zones will be to keep fertilizers on the land and out of the sea. For agricultural systems in general, methods need to be developed that close the nutrient cycle from soil to crop and back to agricultural soil (*13*).

Degrees of Hypoxia

The most common form of eutrophication-induced hypoxia, responsible for about half the known dead zones, generally occurs once per year, in the summer after spring blooms—when the water is warmest and stratification is strongest—and lasts until autumn (table S1). The usual ecosystem response to seasonal oxygen depletion is mortality of benthic organisms followed by some level of recolonization with the return of normal oxygen conditions. Higher-level trophic transfer from the benthos is limited by seasonal hypoxia and can occur only when normal DO conditions prevail (*2*).

Periodic oxygen depletion has been observed in about a quarter of systems reported as hypoxic and may occur more often than seasonally, but this tends to be less severe, lasting from days to weeks. Many smaller systems, such as the York River in the Chesapeake Bay (*2*), are vulnerable to periodic hypoxia because local weather events and spring neap-tidal cycles influence stratification intensity. Diel cycles that influence production and respiration can also cause hypoxia that lasts only hours but has a daily reoccurrence (*14*). The margins of seasonal dead zones may also experience periodic hypoxic events influenced by wind and tides (*15*).

Another 17% of the systems reported as hypoxic experience infrequent episodic oxygen depletion, with less than one event per year, sometimes with years elapsing between events. Episodic oxygen depletion is the first signal that a system has reached a critical point of eutrophication, which, in combination with physical processes that stratify the water column, tips the system into hypoxia. In 1976, a single hypoxic event in the New York Bight that covered about 1000 km^2 caused mass mortality of demersal fishes and benthos and blocked the northward migration of bluefish (*Pomatomus saltatrix*) (*16*). Many systems experience episodic hypoxia be-

---

[1] Virginia Institute of Marine Science, College of William and Mary, Gloucester Point, VA 23062, USA. [2] Department of Marine Ecology, University of Gothenburg, Kristineberg 566, 450 34 Fiskebäckskil, Sweden.

*To whom correspondence should be addressed. E-mail: diaz@vims.edu

fore the onset of seasonal hypoxia, such as in the northern Adriatic, Pomeranian Bay, and the German Bight. Paleoindicators and models from the northern Gulf of Mexico also support this pattern of occurrence.

Because eutrophication increases the volume of organic matter that reaches the sediments, there is a tendency for hypoxia to increase in time and space. In systems prone to persistent stratification, oxygen depletion may also persist. This type of persistent hypoxia accounts for 8% of dead zones, including the Baltic Sea, the largest dead zone in the world, as well as many fjordic systems.

Progression of Hypoxia

Coastal hypoxia seems to follow a predictable pattern of eutrophication first enhancing the deposition of organic matter, which in turn promotes microbial growth and respiration and produces a greater demand for oxygen. DO levels become depleted if the water column stratifies. In the second phase, hypoxia occurs transiently, accompanied by mass mortalities of benthic animals. With time and further buildup of nutrients and organic matter in the sediments, a third phase is initiated, and hypoxia becomes seasonal or periodic, characterized by boom-and-bust cycles of animal populations. If hypoxia persists for years and organic matter and nutrients accumulate in the sediments, a fourth phase is entered, during which the hypoxic zone expands, and as the concentration of DO continues to fall, anoxia is established and microbially generated H_2S is released. This type of threshold response has been documented in the Gulf of Mexico (*17*), Chesapeake Bay (*8*), and Danish waters (*18*).

The critical point in the response trajectory of an ecosystem to eutrophication is the appearance of severe seasonal hypoxia. Although some level of nutrient enrichment is a positive force in enhancing an ecosystem's secondary productivity and, to a point, fishery yields (*19*), eutrophication and seasonal hypoxia favor only benthic species with opportunistic life histories, shorter life spans, and smaller body sizes (*2*).

Ecosystem Responses

The effect of seasonal hypoxia on biomass and annual secondary production is well documented (*2*, *9*). What is not well understood is how hypoxia affects the habitat requirements of different species or the resilience of an ecosystem. Pelagic species will experience habitat compression when hypoxia makes deeper, cooler water unavailable in the summer (*15*) or overlaps with nursery habitat (*9*). For example, the spawning success of cod in the central Baltic is hindered by hypoxic water at the halocline (70 to 80 m), the depth where salinity is high enough to provide buoyancy for cod eggs (*20*). Similar habitat compression occurs when sulphide is generated in sediments. In this case, as the redox potential discontinuity layer is compressed close to the sediment-water interface, deeper-dwelling species, including the key bioturbators that control pore-water chemistry (*21*), are eliminated. The presence of Fe^{3+} and Mn^{4+} in the sediment may buffer the system and reduce the formation of poisonous H_2S. Reduced bioturbation associated with hypoxia also alters sedimentary habitats by disrupting nitrification and denitrification. Hence, under hypoxic conditions, instead of nitrogen being removed as N_2 by denitrification, ammonia and ammonium together with phosphorus are the main fluxes out of reduced sediments (*8*, *22*) and may stimulate further primary production.

Habitat compression and the loss of fauna as a result of hypoxia have profound effects on ecosystem energetics and function as organisms die and are decomposed by microbes. Ecosystem models for the Neuse River estuary (*23*), Chesapeake Bay (*24*), and Kattegat (*25*) all show hypoxia-enhanced diversion of energy flows into microbial pathways to the detriment of higher trophic levels (Fig. 2). Only under certain circumstances will demersal fish predators be able to consume stressed benthic prey, because their tolerance to low oxygen concentration tends to be less (~3 to 4 ml of O_2/liter) than that of the benthic fauna. Thus, it is only within a narrow range of conditions that hypoxia facilitates upward trophic transfer. As the benthos die, microbial pathways quickly dominate energy flows. Ecologically important places, such as nursery and recruitment areas, suffer most from energy diversion into microbial pathways because hypoxia tends to occur in summer, when growth and predator energy demands are high.

Missing Biomass

Areas within ecosystems exposed to long periods of hypoxia have low annual secondary production and typically no benthic fauna. Estimates of the missing biomass in Baltic dead zones that are now persistently hypoxic are ~264,000 metric tons of carbon (MT C) annually (*7*) and represent ~30% of total Baltic secondary production (*26*). Similarly, estimates for the Chesapeake Bay indicate that ~10,000 MT C is lost because of hypoxia each year, representing ~5% of the Bay's total secondary production (*27*). If we estimate that ~40% of benthic energy should be passed up the food chain in the Baltic (*28*) and 60% in the Chesapeake Bay (*26*), when hypoxic conditions prevail, 106,000 MT C of potential food energy for fisheries is lost in the Baltic and 6,000 MT C in

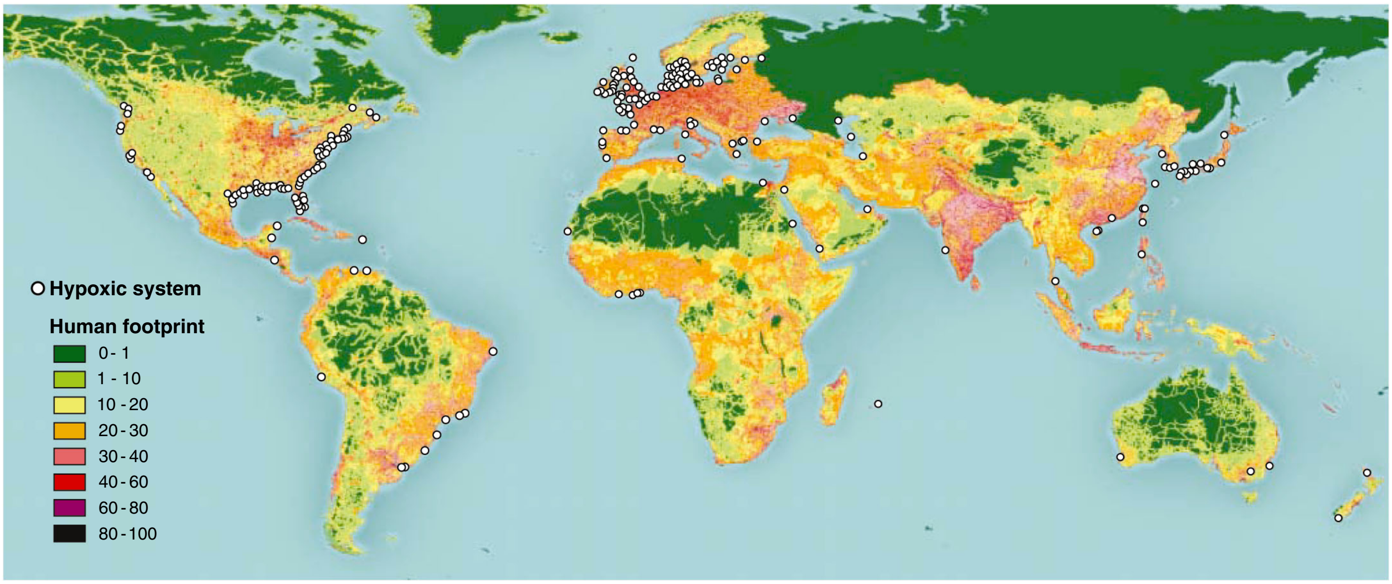

Fig. 1. Global distribution of 400-plus systems that have scientifically reported accounts of being eutrophication-associated dead zones. Their distribution matches the global human footprint [the normalized human influence is expressed as a percent (*41*)] in the Northern Hemisphere. For the Southern Hemisphere, the occurrence of dead zones is only recently being reported. Details on each system are in tables S1 and S2.

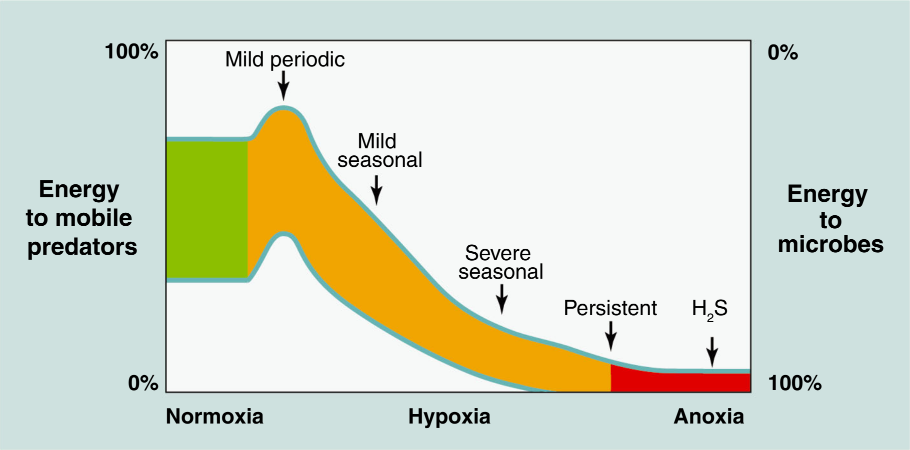

Fig. 2. Conceptual view of how hypoxia alters ecosystem energy flow. The green area indicates the range of energy transferred from the benthos to higher-level predators under normoxia, typically 25 to 75% of macrobenthic carbon. As a system experiences mild or periodic hypoxia, there can be a pulse of benthic energy to predators. This "windfall" is typically short-lived and does not always occur. With declining oxygen, higher-level predation is suspended, benthic predation may continue, and the proportion of benthic energy transferred to microbes rapidly increases (orange). Under persistent hypoxia, some energy is still processed by tolerant benthos. Microbes process all benthic energy as hydrogen sulphide, and anoxia develops (red).

the Chesapeake Bay, respectively. In areas of the Gulf of Mexico that experience severe seasonal hypoxia, benthic biomass is reduced by as much as 1.4 MT C/km^2 (*9*); assuming a 60% transfer efficiency, this is equivalent to approximately 17,000 MT C of lost prey to demersal fisheries.

Is the production lost during periodic hypoxia made up by the ecosystem during normal conditions, or partly compensated for by higher secondary production outside the dead zone? The latter seems to occur in the Baltic, where secondary production outside the dead zones has doubled as a result of eutrophication (*26*); but if the dead zones were eliminated, the Baltic would be more productive by at least a third to a half, assuming that organic matter was processed through benthos instead of by microbes. In Chesapeake Bay, because hypoxia dissipates after about 3 months, the entire area affected is returned to production by recruitment (*27*). Aerial estimates of missing biomass for about a third of the world's dead zones (table S1) indicate that as much as 343,000 to 734,000 MT C is displaced over a total area of 245,000 km^2 as a result of hypoxia.

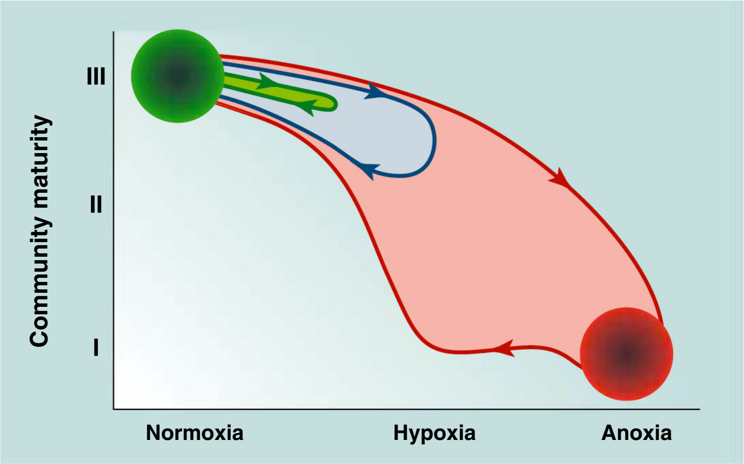

Fig. 3. Generalized pattern of benthic community response to hypoxia (*34*). As DO declines to <0.7 ml of O_2/liter and extends through time, mass mortality of both equilibrium (stage III) and opportunistic (stage I) species occurs (red). If anoxia is reached, benthos are eliminated. The recovery path from severe hypoxia is different than the decline path because of the hysteresis-like progression of successional dynamics. When exposed to mild hypoxia, mortality is moderate, and the recovery path is closer to the response path (blue) as fauna restart from midsuccessional stage II. When exposed to intermediate oxygen conditions, the response is minor (green) and not hysteresis-like.

The duration of seasonal hypoxia then becomes the primary factor affecting ecosystem energy flows. Within most systems that have strong seasonal cycles, increases in populations are related to recruitment events timed to take advantage of the input of new organic matter, usually a spring or autumn bloom; populations normally decline from a combination of resource depletion and predation (*29*). Thus, the shorter the interval between recruitment and the onset of hypoxia, the greater the negative effect on the upward flow of energy in the food chain. During persistent hypoxia, there is a drastic reduction in secondary production, and microbes remineralize virtually all organic matter.

Recovery

By the end of the 20th century, oxygen depletion of marine systems had become a major worldwide environmental problem, with only a small fraction (4%) of the 400-plus systems that had developed hypoxia exhibiting any signs of improvement (table S1). These improvements in DO were related to reductions in three factors: organic and nutrient loadings, stratification strength, and freshwater runoff.

From 1973 to 1990, the hypoxic zone on the northwestern continental shelf of the Black Sea had expanded to 40,000 km^2; however, since 1989, the loss of fertilizer subsidies from the former Soviet Union reduced nutrient loading by a factor of 2 to 4, with the result that, by 1995, the hypoxic zone had gone (*12*). As oxygen levels normalized, ecosystem function improved, and the benthic fauna started to recolonize but have not recovered to prehypoxic levels. In the Gulf of Finland, a decrease in water-column stratification occurred between 1987 and 1994, which improved DO conditions and facilitated the return of benthic fauna (*7*); however, with the return of stratification, conditions have again deteriorated.

In the northern Gulf of Mexico, the occurrence and extent of the dead zone are tightly coupled with freshwater discharge from the Mississippi River, which delivers large quantities of nutrients from U.S. agricultural activities. During years with low river flow, the area of hypoxia shrinks to <5000 km^2, only to increase to >15,000 km^2 when river flow is high (*30*).

The management of nutrients and carbon inputs has virtually eliminated dead zones from several systems, including the Hudson and East Rivers in the United States and the Mersey and Thames Estuaries in England (*31*, *32*). However, in other systems, such as the Chesapeake Bay, the management of nutrient input has not improved DO. Nevertheless, the management of sewage and pulp mill effluents has led to many small-scale reversals in hypoxia (table S1).

The key factors in determining the degree of ecosystem degradation are the duration of exposure and DO concentration. It may take years to recover from severe hypoxia and, moreover, the tolerance to oxygen depletion of mature community species may not mirror that of the opportunistic species that are the first colonizers. The benthos of many coastal areas may be reestablished by larval recruitment and succession, as described in the Pearson-Rosenberg model (*33*); however, the pattern of species that establish during recovery will not be the same as the pattern of species loss during DO deterioration, and consequently a hysteresis-like response will be observed (Fig. 3). A pronounced hysteresis-like response was documented in Gullmarsfjord, Sweden, which suffered hypoxia for about half a year, during which time the fauna was eliminated in deeper areas and diversity and abundance were reduced to less than one-third at medium depths (*34*). Within 2 years, the benthic community had recovered to the same community composition and density that had existed before the hypoxic event (Fig. 3). In this fjord, sedimentary redox conditions had not become intensely reducing, and rapid colonization occurred by larvae from benthic communities in adjacent undisturbed areas. Should hypoxia prevail for more than 5 years, recovery would be prolonged (*35*) and the hysteresis-like response exaggerated, as was recently observed in the Black Sea, where recovery of the benthos after hypoxia in 1994 was still not complete in 2004 (*36*).

Prospects for Change

Further expansion of dead zones will depend on how climate change affects water-column stratification and how nutrient runoff affects organic-matter production. General circulation models predict that climate change alone will deplete oceanic oxygen by increasing stratification and warming as well as by causing large changes in rainfall patterns (*37*), enhancing discharges of fresh water and agricultural nutrients to coastal ecosystems. For example, climate predictions for the Mississippi River basin indicate a 20% increase in river discharge, which will elevate nutrient loading and lead to a 50% increase in primary production, a 30 to 60% decrease in subpycnocline DO, and an expansion of the oxygen-depleted area (*38*). Conversely, if the climate becomes stormier and stratification decreases because of increased mixing, the risk of oxygen depletion will decline. Tropical storms and hurricanes influence the duration, distribution, and size of the Gulf of Mexico dead zone in a complex way. In 2005, four hurricanes (Cindy, Dennis, Katrina, and Rita) disrupted stratification and aerated bottom waters. After the first two storms, stratification was reestablished and hypoxia reoccurred, but the total area was a fourth less than predicted from spring nitrogen flux. The other two hurricanes occurred later in the season and dissipated hypoxia for the year (*30*).

Climate change also has the potential to expand naturally occurring OMZs into shallower coastal waters (*3*), damaging fisheries and affecting energy flows in the same way that eutrophication-driven hypoxia does. There is currently about 1,148,000 km^2 of seabed covered by OMZs (<0.5 ml of O_2/liter), and a small change in oceanographic processes could lead to a major expansion of these zones. Areas at greatest risk for expanding OMZs encompass the western continental shelves of South America, Africa, and the Indian subcontinent, where extensive OMZ and upwelling areas already exist. The development of dead zones along the western coast of other countries is highly likely if wind patterns shift and cause stronger upwelling. This effect might explain the recent development of a dead zone off the coast of Oregon (*39*). Furthermore, there is a possibility that increased loadings of terrestrial nutrients have contributed to an expansion of the OMZ on the western Indian continental shelf (*40*).

The weight of evidence indicates that in preindustrialized times, most coastal and offshore ecosystems never became hypoxic except in natural upwellings. However, measuring the effects of hypoxia on ecosystems is complicated by many factors, not least of which is the inadequate data on historic trends in DO concentrations and faunal populations, as well as the combined effects of multiple stressors, including fishing and habitat loss. It is the recurring nature of hypoxia that alters an ecosystem's state and prevents full recovery of function.

Currently, hypoxia and anoxia are among the most widespread deleterious anthropogenic influences on estuarine and marine environments, and now rank with overfishing, habitat loss, and harmful algal blooms as major global environmental problems. There is no other variable of such ecological importance to coastal marine ecosystems that has changed so drastically over such a short time as DO. We believe it would be unrealistic to return to preindustrial levels of nutrient input, but an appropriate management goal would be to reduce nutrient inputs to levels that occurred in the middle of the past century, before eutrophication began to spread dead zones globally.

References and Notes

1. N. N. Rabalais, R. E. Turner, W. J. Wiseman, *Annu. Rev. Ecol. Syst.* **33**, 235 (2002).
2. R. J. Diaz, R. Rosenberg, *Oceanogr. Mar. Biol. Annu. Rev.* **33**, 245 (1995).
3. J. J. Helly, L. A. Levin, *Deep Sea Res. Part I Oceanogr. Res. Pap.* **51**, 1159 (2004).
4. J. N. Galloway *et al.*, *Science* **320**, 889 (2008).
5. D. Justić, T. Legović, L. Rottini-Sandrini, *Estuar. Coast. Shelf Sci.* **25**, 435 (1987).
6. L. D. Mee, *Ambio* **21**, 278 (1992).
7. K. Karlson, R. Rosenberg, E. Bonsdorff, *Oceanogr. Mar. Biol. Annu. Rev.* **40**, 427 (2002).
8. W. M. Kemp *et al.*, *Mar. Ecol. Prog. Ser.* **303**, 1 (2005).
9. N. N. Rabalais, R. E. Turner, Eds., *Coastal Hypoxia: Consequences for Living Resources and Ecosystems* (American Geophysical Union, Washington, DC, 2001).
10. B. K. Sen Gupta, R. E. Turner, N. N. Rabalais, *Geology* **24**, 227 (1996).
11. R. Rosenberg, *Mar. Pollut. Bull.* **16**, 227 (1985).
12. L. Mee, *Sci. Am.* **295**, 78 (2006).
13. D. Tilman *et al.*, *Science* **292**, 281 (2001).
14. R. M. Tyler, T. E. Targett, *Mar. Ecol. Prog. Ser.* **333**, 257 (2007).
15. D. Breitburg, *Estuaries* **25**, 767 (2002).
16. E. V. Garlo, C. B. Milstein, A. E. Jahn, *Estuar. Coast. Mar. Sci.* **8**, 421 (1979).
17. R. E. Turner, N. N. Rabalais, D. Justić, *Environ. Sci. Technol.* **42**, 2323 (2008).
18. D. J. Conley *et al.*, *Ecol. Appl.* **17**, S165 (2007).
19. S. W. Nixon, B. A. Buckley, *Estuaries* **25**, 782 (2002).
20. M. Cardinale, J. Modin, *Fish. Res.* **41**, 285 (1999).
21. R. C. Aller, *Chem. Geol.* **114**, 331 (1994).
22. R. A. Duce *et al.*, *Science* **320**, 893 (2008).
23. D. Baird, R. R. Christian, C. H. Peterson, G. A. Johnson, *Ecol. Appl.* **14**, 805 (2004).
24. D. Baird, R. E. Ulanowicz, *Ecol. Monogr.* **59**, 329 (1989).
25. T. Pearson, R. Rosenberg, *Neth. J. Sea Res.* **28**, 317 (1992).
26. R. Elmgren, *Ambio* **18**, 326 (1989).
27. R. J. Diaz, L. C. Schaffner, in *Perspectives in the Chesapeake Bay: Advances in Estuarine Sciences*, M. Haire, E. C. Krome, Eds. (Chesapeake Research Consortium, Gloucester Point, VA, 1990), pp. 25–56.
28. P. Möller, L. Pihl, R. Rosenberg, *Mar. Ecol. Prog. Ser.* **27**, 109 (1985).
29. G. Graf, *Oceanogr. Mar. Biol. Annu. Rev.* **30**, 149 (1992).
30. N. N. Rabalais *et al.*, *Estuar. Coasts* **30**, 753 (2007).
31. C. A. Parker, J. E. O'Reilly, *Estuaries* **14**, 248 (1991).
32. P. D. Jones, *Mar. Pollut. Bull.* **53**, 144 (2006).
33. T. H. Pearson, R. Rosenberg, *Oceanogr. Mar. Biol. Annu. Rev.* **16**, 229 (1978).
34. R. Rosenberg, S. Agrenius, B. Hellman, H. C. Nilsson, K. Norling, *Mar. Ecol. Prog. Ser.* **234**, 43 (2002).
35. R. Rosenberg, *Oikos* **27**, 414 (1976).
36. L. D. Mee, J. Friedrich, M. T. Gomoiu, *Oceanography (Washington D.C.)* **18**, 100 (2005).
37. Intergovernmental Panel on Climate Change, *Climate Change 2007: the Physical Science Basis*, *Contribution of Working Group I to the Fourth Assessment Report of the Intergovernmental Panel on Climate Change* (Cambridge Univ. Press, New York, 2007).
38. D. Justić, N. N. Rabalais, R. E. Turner, *Limnol. Oceanogr.* **41**, 992 (1996).
39. F. Chan *et al.*, *Science* **319**, 920 (2008).
40. S. W. A. Naqvi *et al.*, *Nature* **408**, 346 (2000).
41. E. W. Sanderson *et al.*, *Bioscience* **52**, 891 (2002).
42. This work was supported in part by National Oceanic and Atmospheric Administration Coastal Hypoxia Research Program grant NA05NOS4781202 to R.J.D. We thank N. Rabalais and L. Schaffner for discussions and critical comments; A. Puente, K. Sturdivant, and S. Lake for helpful discussions; H. Burrell for artwork on the figures; and H. Berquist for producing the global map. This is contribution 2942 of the Virginia Institute of Marine Science.

Supporting Online Material

www.sciencemag.org/cgi/content/full/321/5891/926/DC1
Fig. S1
Tables S1 and S2
References

12 February 2008; accepted 2 June 2008
10.1126/science.1156401

Optical Negative Refraction in Bulk Metamaterials of Nanowires

Jie Yao,[1]* Zhaowei Liu,[1]* Yongmin Liu,[1]* Yuan Wang,[1] Cheng Sun,[1] Guy Bartal,[1] Angelica M. Stacy,[2] Xiang Zhang[1,3]†

Metamaterials are artificially designed subwavelength composites possessing extraordinary optical properties that do not exist in nature. They can alter the propagation of electromagnetic waves, resulting in negative refraction (*1*), subwavelength imaging (*2*), and cloaking (*3*). First reported at microwave frequencies by using metamaterials made of an array of split ring resonators and metallic wires (*4*), negative refraction has been observed in two-dimensional (2D) photonic crystals into the infrared (IR) region (*5*–*8*) and in surface plasmon waveguides at visible frequencies (*9*). In both cases, negative refraction is constrained in two dimensions and is limited to a narrow band of frequencies. An indirect observation of negative refraction in the mid-IR region was also reported in a semiconductor multilayer structure (*10*). Creating bulk metamaterials that exhibit negative refraction for visible light remains a major challenge because of substantial resonance losses and fabrication difficulties. Recent theoretical studies suggest that metamaterials consisting of metal wire arrays exhibit an optical response at frequencies far away from resonances (*11*, *12*), in which electromagnetic (EM) waves propagating along the nanowires exhibit negative refraction at a broad frequency band for all angles (*13*). Moreover, the material loss is much lower than traditional metamaterials with similar functionality.

We report observations of negative refraction in bulk metamaterials composed of silver nanowires with separation distance much smaller than the wavelength at optical frequencies (Fig. 1A). A porous alumina template was prepared by electrochemical anodization (*14*), into which silver nanowires were electrochemically deposited. A 1-μm-wide slit, etched through a 250-nm-thick silver film coated on the metamaterials, was illuminated by a collimated diode laser beam at different incident angles (see left side of Fig. 1A). The transmitted light was mapped by scanning a tapered optical fiber at the bottom surface of the metamaterial. The results are shown in Fig. 1, B and C, for incident light at wavelengths of 660 nm and 780 nm, respectively. When the incident angle is 30°, the transmitted beam is shifted to the left for transverse magnetic (TM)–polarized light, which corresponds to the negative refraction. The subwavelength composite forms an effective medium with opposite signs of electrical permittivities along and perpendicular to the wires (*9*). The hypobolic dispersion enables negative light refraction even though the phase velocity remains positive (*10*, *13*, *15*). Conversely, the transverse electric (TE)–polarized light undergoes positive refraction. Figure 1D shows the dependence of refraction angles on a range of incident angles at 780 nm. The group refractive indices of the metamaterial are shown to be –4.0 and 2.2 for TM and TE light, respectively. The phase refractive index of the metamaterial remains positive, in contrast to that of left-handed metamaterials (*1*, *4*). For normal incidence, the light intensity only decays ~ 0.43/μm in the medium at 780-nm wavelength, showing loss a few orders of magnitude lower than that of single-layer metamaterials reported at the same wavelength (*16*). Further calculations show that the negative refraction in this nanowire composite exists for longer wavelengths and also does not depend on the orientation of the nanowire lattice.

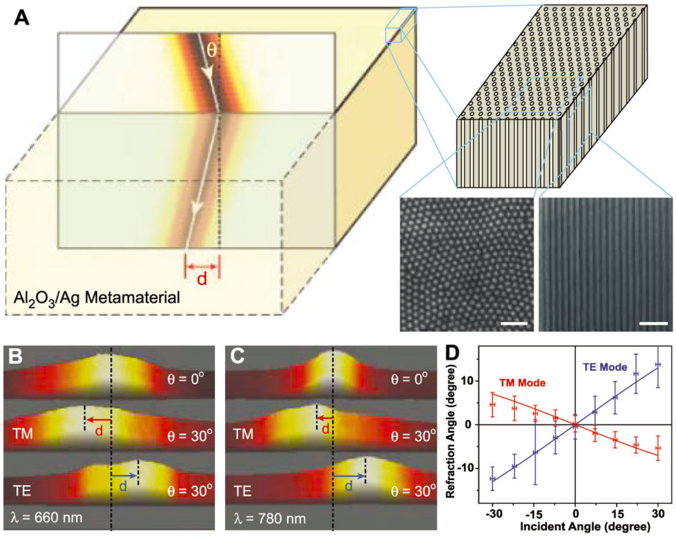

Fig. 1. Negative refraction in bulk metamaterial at visible frequencies. (**A**) (Left) Schematic of negative refraction from air into the silver nanowire metamaterials. (Right) Nanowires embedded in an alumina matrix, as well as scanning electron microscopy images showing the top and side view of the nanowires (60-nm wire diameter and 110-nm center-to-center distance). The scale bars indicate 500 nm. Measured beam intensity at the existing surface of the metamaterial slab at the wavelength of 660 nm (**B**) and 780 nm (**C**). The lateral displacement (d) of TM polarized light shows the negative refraction in the metamaterial at both wavelengths, whereas TE light undergoes positive refraction. The horizontal sizes of (B) and (C) are 5 μm and 12 μm, respectively. (**D**) The dependence of refraction angles on incident angles and polarizations at 780-nm wavelength. The negative refraction occurs for broad incident angles. The experiment data agree well with calculations (solid curves) using the effective medium theory. The sample thicknesses in (B) and (C) are 4.5 μm and 11 μm, respectively.

Because the dielectric response in this metamaterial does not require any resonance, the negative refraction has low loss and occurs in a broad spectral range, for all incident angles, making it an intrinsic optical response of the underlying metamaterials. Moreover, such bulk metamaterials can support propagating waves with large wave vectors that are evanescent in air or dielectrics, enabling manipulation of visible light at subwavelength scale. This can substantially affect applications such as waveguiding, imaging, and optical communication.

References and Notes

1. V. G. Veselago, *Sov. Phys. Usp.* **10**, 509 (1968).
2. J. B. Pendry, *Phys. Rev. Lett.* **85**, 3966 (2000).
3. J. B. Pendry, D. Schurig, D. R. Smith, *Science* **312**, 1780 (2006); published online 24 May 2006 (10.1126/science.1125907).
4. R. A. Shelby, D. R. Smith, S. Schultz, *Science* **292**, 77 (2001).
5. E. Cubukcu, K. Aydin, E. Ozbay, S. Foteinopoulou, C. M. Soukoulis, *Nature* **423**, 604 (2003).
6. P. V. Parimi, W. T. Lu, P. Vodo, S. Sridhar, *Nature* **426**, 404 (2003).
7. A. Berrier *et al.*, *Phys. Rev. Lett.* **93**, 073902 (2004).
8. E. Schonbrun *et al.*, *Appl. Phys. Lett.* **90**, 041113 (2007).
9. H. J. Lezec, J. A. Dionne, H. A. Atwater, *Science* **316**, 430 (2007); published online 21 March 2007 (10.1126/science.1139266).
10. A. J. Hoffman *et al.*, *Nat. Mater.* **6**, 946 (2007).
11. R. Wangberg, J. Elser, E. E. Narimanov, V. A. Podolskiy, *J. Opt. Soc. Am. B* **23**, 498 (2006).
12. M. G. Silveirinha, P. A. Belov, C. R. Simovski, *Phys. Rev. B* **75**, 035108 (2007).
13. More details are available as supporting material on *Science* Online.
14. H. Masuda, K. Fukuda, *Science* **268**, 1466 (1995).
15. D. R. Smith, D. Schurig, *Phys. Rev. Lett.* **90**, 077405 (2003).
16. G. Dolling, M. Wegener, C. M. Soukoulis, S. Linden, *Opt. Lett.* **32**, 53 (2007).
17. This work was supported by the Air Force Office of Scientific Research Multidisciplinary University Research Initiative Program (grant no. FA9550-04-1-0434) and NSF NSEC under award no. DMI-0327077. The authors thank E. Hajime for assistance in fabrication at the early stage of the work.

Supporting Online Material

www.sciencemag.org/cgi/content/full/321/5891/930/DC1
Materials and Methods
Fig. S1
References

10 March 2008; accepted 4 June 2008
10.1126/science.1157566

---

[1] National Science Foundation (NSF) Nanoscale Science and Engineering Center (NSEC), 5130 Etcheverry Hall, University of California, Berkeley, CA 94720–1740, USA. [2] Department of Chemistry, University of California, Berkeley, CA 94720, USA. [3] Materials Sciences Division, Lawrence Berkeley National Laboratory, 1 Cycletron Road, Berkeley, CA 94720, USA.

*These authors contributed equally to this work.

†To whom correspondence should be addressed. E-mail: xiang@berkeley.edu

Tail Reconnection Triggering Substorm Onset

Vassilis Angelopoulos,[1]* James P. McFadden,[2] Davin Larson,[2] Charles W. Carlson,[2] Stephen B. Mende,[2] Harald Frey,[2] Tai Phan,[2] David G. Sibeck,[3] Karl-Heinz Glassmeier,[4] Uli Auster,[4] Eric Donovan,[5] Ian R. Mann,[6] I. Jonathan Rae,[6] Christopher T. Russell,[1] Andrei Runov,[1] Xu-Zhi Zhou,[1] Larry Kepko[7]

Magnetospheric substorms explosively release solar wind energy previously stored in Earth's magnetotail, encompassing the entire magnetosphere and producing spectacular auroral displays. It has been unclear whether a substorm is triggered by a disruption of the electrical current flowing across the near-Earth magnetotail, at ~10 R_E (R_E: Earth radius, or 6374 kilometers), or by the process of magnetic reconnection typically seen farther out in the magnetotail, at ~20 to 30 R_E. We report on simultaneous measurements in the magnetotail at multiple distances, at the time of substorm onset. Reconnection was observed at 20 R_E, at least 1.5 minutes before auroral intensification, at least 2 minutes before substorm expansion, and about 3 minutes before near-Earth current disruption. These results demonstrate that substorms are likely initiated by tail reconnection.

Substorms are global reconfigurations of the magnetosphere involving storage of solar wind energy in Earth's magnetotail and its abrupt conversion to particle heating and kinetic energy (*1*, *2*). Because phenomena related to the onset of substorms are initially localized (within 1 to 2 R_E) in space but expand quickly to engulf a large portion of the magnetosphere (*3*, *4*), fortuitous (and thus unoptimized) conjunctions between single satellite missions have been unable to pinpoint the exact location of the substorm trigger in space. This has led to diverging theoretical efforts to explain the onset mechanism (*5*, *6*). The key question is whether substorm phenomena are triggered by a near-Earth dipolarization (current disruption) process, at ~10 R_E, or by the process of magnetic reconnection at ~20 to 30 R_E. Both processes operate during substorms, but attempts (*7*, *8*) to delineate the causal relation between them and substorm onset were limited due to temporal resolution, spatial propagation effects, and/or lack of simultaneous observations of the above key regions. The THEMIS mission (*9*, *10*) was designed to address this question. The mission uses five identical satellites (hereafter termed "probes") on orbits, enabling recurrent probe alignments parallel to the Sun-Earth line (probes within $\delta Y_{GSM} \pm 2$ R_E from each other; GSM, Geocentric Solar Magnetospheric coordinate system). The probes can thus monitor tail phenomena simultaneously at ~10 R_E and at ~20 to 30 R_E downtail, while mapping magnetically over a network of ground-based observatories (GBOs), which can determine the meridian and time of substorm onset on the ground (*11*). Here we present timing results from THEMIS for isolated substorms, which demonstrate that the substorm trigger mechanism is magnetic reconnection.

Substorm Signatures

The ground signatures of substorms consist of a rapid auroral intensification, a breakup of auroral forms into smaller filaments, and a poleward expansion and a westward surge of the most intense auroral arcs. Those are within 1 to 2 min of each other and have often been used synonymously with substorm onset. Ground magnetic signatures of currents associated with auroral arc intensification include abrupt increases in the auroral electrojet (AE) index (*12*) and irregular pulsations in the 40- to 150-s range called Pi2s (*13*), or at lower periods (*14*), observed at high-latitude (auroral) and mid-latitude (subauroral) magnetic stations. Such magnetic signatures are known to coincide with auroral intensification typically within 1 to 2 min (*15*) and are also used for substorm onset identification.

Before substorm onset, during the substorm growth phase, stable arcs intensify and move equatorward while the magnetotail plasma sheet thins and the cross-tail current increases (*16*–*19*). During the expansion phase, auroral arcs typically advance toward the poleward edge of the auroral oval and a current wedge develops in space, at ~10 R_E, composed of field-aligned currents into and out of the ionosphere (*17*). Current wedge formation is also referred to as dipolarization, because the field becomes more dipole-like, or as current disruption, because it is consistent with a disruption (reduction) of the duskward cross-

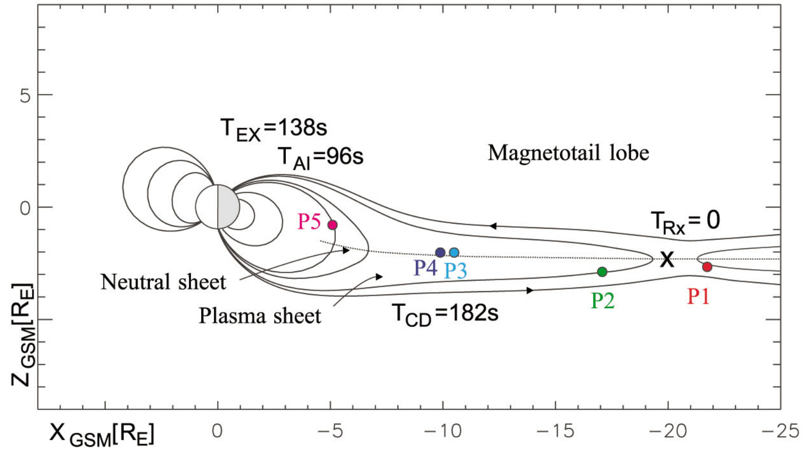

Satellite	Color	X	Y	Z	Neutral Sheet
THEMIS-A (P5)	🟪	-5.483	5.326	-0.623	0.6
THEMIS-B (P1)	🟥	-21.475	3.927	-2.806	-0.5
THEMIS-C (P2)	🟩	-17.165	4.573	-3.046	-0.8
THEMIS-D (P3)	🟦	-10.881	3.759	-2.086	0.2
THEMIS-E (P4)	🟦	-10.194	4.506	-1.913	0.2

Fig. 1. Projections of THEMIS probes in X-Z_{GSM} plane along with representative field lines and neutral sheet location in GSM coordinates at 04:45 UT on 26 February 2008. Times refer to the time delays in Table 1.

---

[1] Institute of Geophysics and Planetary Physics/ESS, University of California at Los Angeles, Los Angeles, CA 90095, USA. [2] Space Sciences Laboratory, University of California at Berkeley, CA 94720, USA. [3] Code 674, NASA/Goddard Space Flight Center, Greenbelt, MD 20771, USA. [4] TUBS, Braunschweig, D-38106, Germany. [5] Department of Physics and Astronomy, University of Calgary, Calgary, Alberta, Canada T2N 1N4. [6] Department of Physics, University of Alberta, Edmonton, Alberta, Canada T6G 2M7. [7] Space Science Center, University of New Hampshire, Durham, NH 03824, USA.

*To whom correspondence should be addressed. E-mail: vassilis@ucla.edu

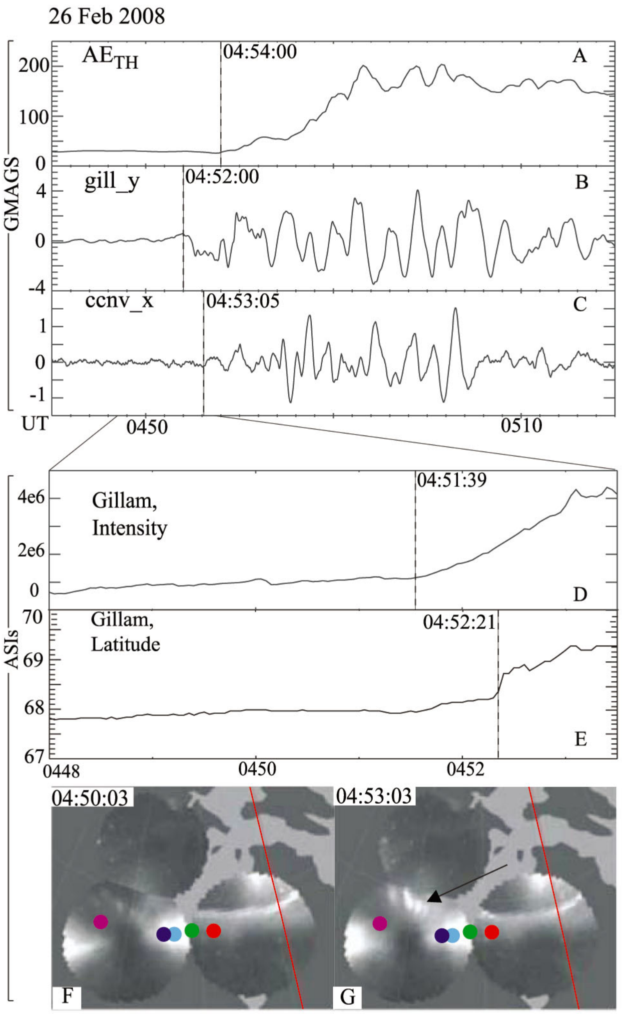

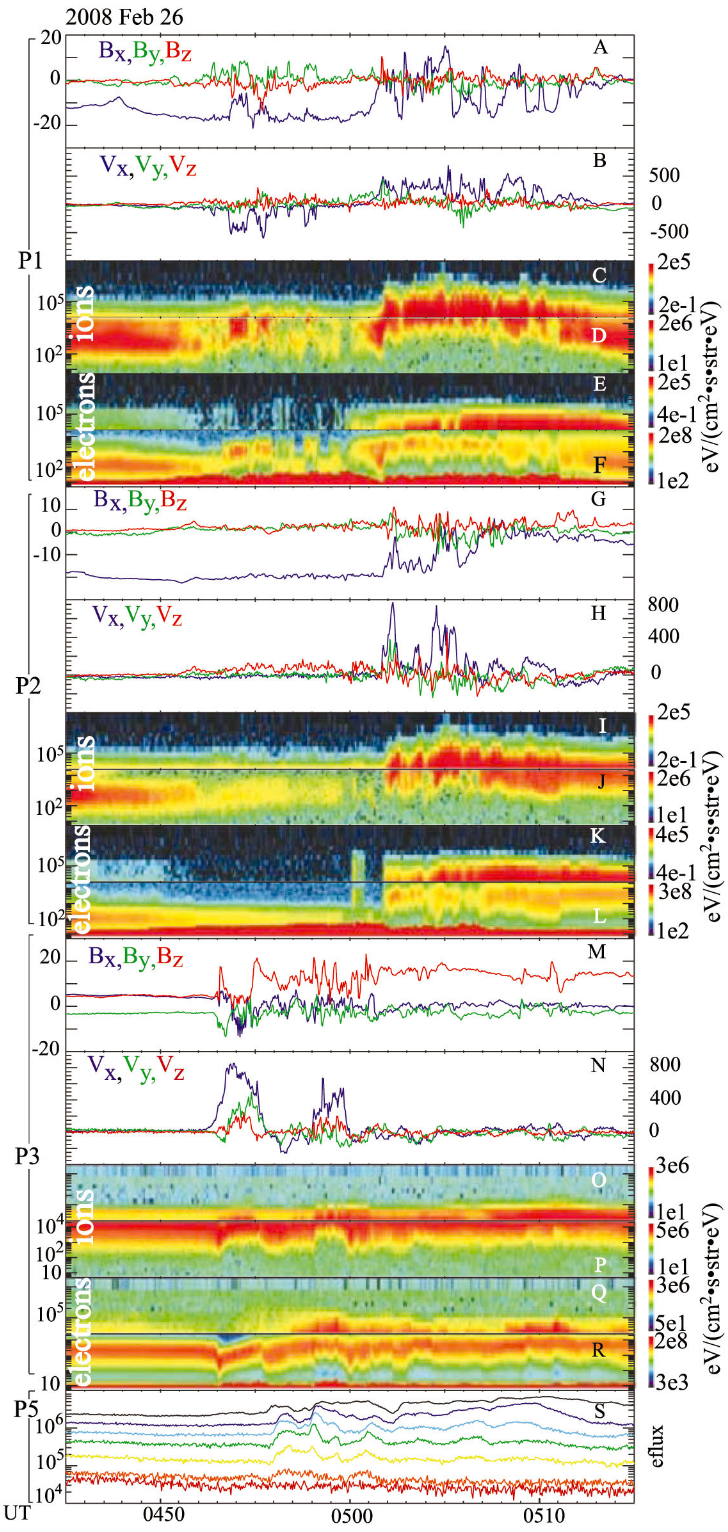

Fig. 2. **(left).** (**A**) THEMIS AE index, AE$_{TH}$, computed from THEMIS GBOs (*11*) and select CARISMA stations. (**B** and **C**) Band-pass–filtered (10 to 120 s) magnetograms from Gillam (east-west component; station magnetic coordinates: 66.5°N, 28.0°W) and Carson City, NV (north-south component; 45.1°N, 57.0°W), in nT. The filter includes the Pi2 band but extends to higher frequencies to reduce aliasing. (**D**) Integrated auroral intensity from the northern half of Gillam ASI's field of view (arbitrary units). (**E**) Latitude of poleward-most extent of auroral luminosity at station Gillam. (**F** and **G**) Composite images (mosaics) from THEMIS ASIs around the location of substorm onset, over a continental outline. Stations used in both stills are Gillam (bottom left), Rankin Inlet (top left; station magnetic coordinates: 72.7°N, 25.1°W), and Sanikiluaq (bottom right, 66.9°N, 3.5°W). Gillam had partially cloudy skies, reflecting the Moon from low in the horizon and obscuring the north-east and south-west views (the latter is reflection on the dome), though this does not affect our findings. The red line is the midnight meridian. Color circles indicate ionospheric footpoints of THEMIS probes (same symbols as in Fig. 1) based on the T96 mapping model (*24*). The arrow indicates optical onset location. **Fig. 3** **(right).** (**A** to **S**) Overview of magnetic field and particle data for 30 min, at 3-s resolution, around the 04:54:00 UT substorm. There are six panels per probe, arranged from top to bottom for probes P1, P2, and P3, plus one (bottom) panel showing only 30- to 200-keV ion spectra on P5, from the SST instrument. The six panels per probe are (from top to bottom) as follows: magnetic field measured by the FGM instrument (*35*); ion-flow velocity measured by the ESA instrument; energy spectra of 0.005- to 2000-keV ions from the SST and ESA instruments (next two panels); and energy spectra of 0.005- to 2000-keV electrons from the same instruments. All energy spectrograms show omnidirectional differential energy flux (eflux) in units of eV/(cm^2•s•str•eV). The abrupt change in eflux for each species exists because the data below 25 keV and above 30 keV were obtained by two instruments (ESA and SST, respectively) with different instrument geometric factors. Magnetic field and velocity are in GSM coordinates; *X*, *Y*, and *Z* components are shown in blue, green, and red, respectively.

tail current (*5*). Further downtail, fast tailward flows threaded by southward magnetic fields, or Earthward flows threaded by northward fields, are observed near substorm expansion onset and have been interpreted as evidence for magnetic reconnection (*20*, *21*). Substorm expansion is followed by substorm recovery, during which auroral forms remain active at the poleward boundary of the auroral oval for hours, until they eventually reduce in intensity and move equatorward, often starting another substorm sequence. Arc intensification alone does not necessarily constitute a substorm, even though it may involve the same underlying physics as substorms (*22*). The sequence of growth phase, expansion, and recovery of the aurora constitutes a bona fide substorm process. Due to the gradual intensification of auroral arcs at growth phase, it is typically easier to identify a substorm onset by its poleward expansion. The high cadence of the THEMIS ground measurements allows us to explicitly differentiate between the aforementioned observational determinations of onset, and we intentionally retain this differentiation as these phenomena manifest different magnetosphere-ionosphere coupling processes.

Substorm Timing on 26 February 2008

At 4:50 UT, the THEMIS probes were aligned along the Sun-Earth line, less than 1 R_{E} from the nominal neutral sheet (Fig. 1). A sudden increase of the THEMIS Auroral Electrojet Index ($\mathrm{AE_{TH}}$) to 200 nT was observed at 04:54:00 UT, indicating an isolated substorm onset (Fig. 2A). Auroral station Gillam and mid-latitude station Carson City recorded Pi2 pulsations (Fig. 2, B and C). The Pi2 pulsation onsets were determined as the times of the first increase in signal amplitude above background, at 04:52:00 UT and 04:53:05 UT, respectively. Observations from the THEMIS All-Sky Imagers (ASIs), seen in Fig. 2, F and G, and movies S1 and S2 (*23*), show that a relatively stable arc extended across the sky from Gillam to Sanikiluaq at 04:50:03 UT, and that by 04:53:03 UT the arc had intensified at Gillam (arrow in Fig. 2G). The auroral brightening region was initially ~100 km in width (the ASI field of view is ~800 km when mapped to 110-km altitude). Using the inflection point of the auroral intensity increase at Gillam (Fig. 2D), we determined that the auroral intensification onset was at 04:51:39 UT. The arc intensified at 67.8° geomagnetic latitude and expanded poleward of 68.2° at 04:52:21 UT [Fig. 2E and movie S2 (*23*)]; we denote the latter as the time of substorm expansion onset. These substorm onset times are summarized in Table 1.

For several minutes before the abrupt brightening at 04:51:39 UT, the arc developed small (50- to 100-km scale) filaments that moved along the arc and/or died down at these stations. Images from a NORSTAR imager at Rabbit Lake (just to the west of Gillam), seen in movie S3 (*23*), also captured these transient filaments, and in one instance (at 04:50 UT), the filaments were seen in conjunction with a localized transient enhancement in ultralow-frequency power at that station. Because auroral intensification onset was localized within the field of view of Gillam, but the filaments were developing for several minutes and over a 2-hour magnetic longitude range, we do not associate these filaments with the sought-after, abrupt substorm trigger. These filaments, however, may be related to preconditioning of the magnetosphere, leading up to substorm onset.

Using the T96 magnetospheric model (*24*), we projected the probe locations along magnetic field lines to the ionosphere. The probe footpoints lie near the west coast of Hudson Bay (i.e., near Gillam) and within 1 hour of Magnetic Local Time of the meridian of auroral intensification (the substorm meridian). A current wedge analysis of the mid-latitude magnetometer data confirms that the probe footpoints were within the substorm current wedge. Therefore, the probes were well positioned meridionally to examine the relative timing of substorm signatures on the ground and in space.

Table 1. Summary of timing results during the 26 Feb 2008 04:53:45 UT substorm onset, in order of time sequence. The last column is the time delay, assuming reconnection onset at 04:50:03 UT, at 20 R_{E}, which was arrived at based on our interpretation of data and an estimate of an average Alfvén speed in the plasma sheet of 500 km/s.

Event	Observed time (UT)	Inferred delay (seconds since 04:50:03 UT)
Reconnection onset	04:50:03 (inferred)	$T_{\mathrm{Rx}} = 0$
Reconnection effects at P1	04:50:28	25
Reconnection effects at P2	04:50:38	35
Auroral intensification	04:51:39	$T_{\mathrm{AI}} = 96$
High-latitude Pi2 onset	04:52:00	117
Substorm expansion onset	04:52:21	$T_{\mathrm{EX}} = 138$
Earthward flow onset at P3	04:52:27	144
Mid-latitude Pi2 onset	04:53:05	182
Dipolarization at P3	04:53:05	$T_{\mathrm{CD}} = 182$
Auroral electroject increase	04:54:00	237

Overview of tail signatures. Probes P1 and P2 recorded a decreasing magnitude of Earthward component, B_x, between 04:45 and 05:01 UT (Fig. 3, A and G), consistent with a decreasing current sheet thickness and an increasing current sheet density, as expected at substorm growth phase. The plasma sheet ion density and average energy, obtained from the data shown in Fig. 3, D and J, were about one particle per cubic centimeter and ~1 keV, respectively. These are attributes of a cold-dense plasma sheet after prolonged intervals of northward interplanetary field (*25*). Probe P1 observed at ~04:54 UT tailward flows ($V_x < 0$) accompanied by southward ($B_z < 0$) and duskward ($B_y > 0$) excursions of the magnetic field, followed at ~05:02 UT by Earthward flows and opposite-polarity magnetic field perturbations. Probe P2 observed Earthward flows of the same nature and at about the same time as P1 (05:02 UT). The flow and field signatures at P1 are expected from a reconnection site first located Earthward, then retreating (or reappearing) tailward of P1, starting at ~05:01 UT. The observed B_y-component variations ($B_y > 0$ tailward of the reconnection site; $B_y < 0$ Earthward of it) are also classical Hall signatures of reconnection (*26*–*28*).

Before the onset of the fast tailward flows, both probes observed two ion components: a 500-eV component, commensurate with the cold plasma sheet preceding the event, and a 10-keV component that appeared gradually. Both probes also observed relatively low-temperature electrons (100 to 200 eV) of decreasing flux. Despite the plasma sheet thinning, P1 and P2 remained within the plasma sheet. As the fast tailward flows were observed at P1, the average energy of the ions and electrons increased to 10 keV and 1 keV, respectively. After the tailward retreat of the reconnection site at 05:01 UT, both probes observed even hotter plasma (20-keV ions, 2-keV electrons) and crossed the neutral sheet as evidenced by the near-zero transitions of B_x at around 05:02 UT. This is evidence of plasma heating at the reconnection outflow and plasma sheet dipolarization at 05:02 UT at 22 R_{E}, the distance of P1.

If the flows are due to reconnection, the current sheet should resemble a slingshot-like, standing Aflvén wave (*27*, *28*). To evaluate the shear stress balance, we examined the correlation between the measured ion flows, $\Delta\mathbf{V_i}$, and the flows predicted from reconnection outflow, $\Delta\mathbf{V_A} \propto \pm\Delta\mathbf{B}\cdot N_{\mathrm{i}}^{-1/2}$, on P1 and P2 ($\mathbf{V_A}$: Alfvén speed, $\mathbf{B}$: magnetic field, N_{i}: the ion density). The correlation coefficients for the tailward and Earthward flows on P1 (04:53:30 to 04:58:30; 05:01:00 to 05:13:00) and for the Earthward flows on P2 (05:01:30 to 05:06:00) were 0.79, 0.61, and 0.86, whereas the slopes were –0.53, 0.32, and 0.51, respectively. The slopes are likely underestimates because of temporal variations in the reconnection process and because we have not yet included energetic particles in the velocity determination. Alternatively, the stress balance at the peak velocity near the center of the plasma sheet gives ratios: $|\Delta \mathbf{V}_\mathbf{i}|/|\Delta \mathbf{V}_\mathbf{A}| \sim 90\%$ ($\mathbf{V}_\mathbf{i}$, ion velocity), 67% and 88% for the tailward and Earthward flows on P1 (04:54:30 UT, 05:02:00 UT) and the Earthward flows on P2 (05:02:30 UT), respectively. Under the caveat of the need to include the superthermal ion corrections to the ion flow velocity, mostly required for the hotter, Earthward flows, the observations are consistent with the Alfvénic acceleration expected from reconnection.

P3 was near the neutral sheet. It observed fast (>400 km/s) Earthward flows starting at about 04:52:27 UT, followed by a transient increase in the northward component of the magnetic field (transient dipolarization) at 04:53:05 UT. The onset of fast flows was followed by a more permanent dipolarization at 04:54:40 UT, signifying the development of a substorm current wedge in near-Earth space. The transient dipolarization at ~04:53:05 UT is interpreted as the first indication of a substorm current wedge at P3.

P5, near geosynchronous altitude, saw an energy-dispersed ion injection of the 50- to 200-keV ions (Fig. 3S). The flux increase at the lowest-energy (highest-flux) channel is an exception, because it responds to the local plasma and is correlated with convective velocity changes measured at the same time. The energetic-particle dispersion (more energetic particles drifting faster than lower-energy particles) is consistent with a duskward drift of those particles to the location of P5 after an injection near midnight. Such dispersed injections are classical signatures of substorms observed by geosynchronous orbit satellites (*29*).

Observations around the time of onset. The fast tailward reconnection flows ($V_x < -100$ km/s) on P1 started at ~04:52:30 UT. They were preceded by a northward convective flow ($V_z > 50$ km/s) and an accompanying southward deflection of the magnetic field ($\delta B_z < 0$), which we interpret as evidence of onset of reconnection inflow toward the neutral sheet at 04:50:28 UT. Ion-velocity distributions (Fig. 4C) show two components: a relatively isotropic component below ~500 km/s and a duskward and tailward streaming component above 1000 km/s. These are the cold and hot ions seen earlier in the spectra of Fig. 3D. Similar behavior was found on probe P2. The anisotropy of the few-keV ions intensified by 04:51:14 UT (see distribution function in Fig. 4C); even 1-keV ions (~310 km/s) exhibited pronounced duskward drift. This is consistent with a diamagnetic ion current. The inferred gradient scale is approximately the gyroradius of a 1-keV proton in the local field (~20 nT), i.e., ~600 km. This is further evidence that the current sheet was thin and the current density high.

Electron velocity space distribution functions (Fig. 4D) exhibit a bidirectional anisotropy before 04:50:54 UT, which intensified in the ensuing minutes. As seen in Fig. 4E, 50- to 300-eV electrons were streaming toward the reconnection site (180° pitch angle, i.e., approximately Earthward), while 400- to 2000-eV electrons were streaming away from the reconnection site (0° pitch angle, i.e., ~tailward). Such electron streaming is a signature of reconnection due to the Hall current system (*21*), suggesting that reconnection had started near the location of P1 by 04:50:28 UT.

Probe P2 was farther away from the neutral sheet than P1, as evidenced by the enhanced magnetic field (Fig. 3G) and ion energy spectra (Fig. 3, I and J). No direct connection of field lines at P2 to the reconnection site was evident until after onset. However, similar to P1 at 04:50:28 UT, observations at P2 at 04:50:38 UT show the beginning of inflow toward the reconnection site ($V_z > 0$, Fig. 4G) and the start of a positive deflection of B_z along with a bipolar B_x. These are signatures of an Earthward flux transfer event (*30*, *31*), signifying tail reconnection somewhere tailward of P2. The simultaneous deflection of B_z northward at P1 and southward at P2 suggests that a reconnection topology was established at that time between the two probes, i.e., between 17 and 22 R_E (Fig. 1).

Probe P3 observed a slow ramp-up of the Earthward flow velocity ($V_x > 50$ km/s) at 04:52:27 UT (Figs. 3N and 4I), followed by a

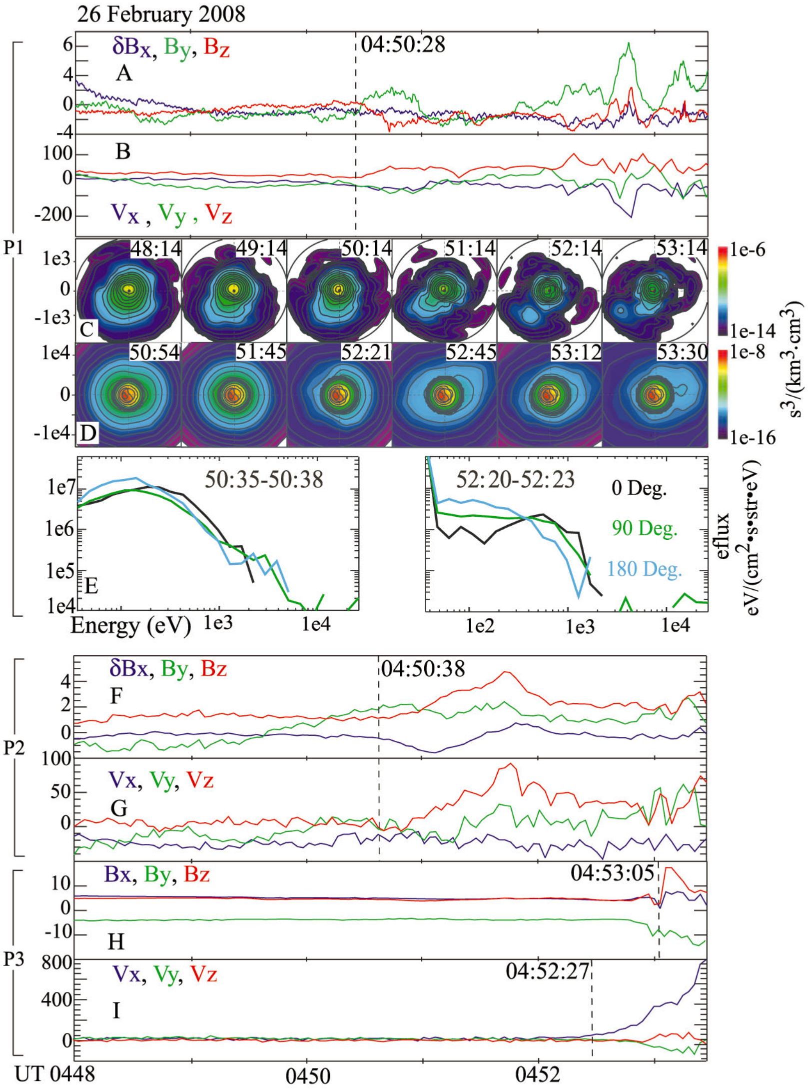

Fig. 4. Data from P1, P2, and P3 during the first few minutes before substorm onset. (**A**, **F**, and **H**) Magnetic field as in Figs. 2 and 3, except that on P1 the resolution is four samples per second. On P1 and P2 the X_GSM component (but not the others) was detrended (high-pass filtered) by subtracting a 6-min running average, to reveal details. (**B**, **G**, and **I**) Ion velocity as in Figs. 2 and 4. For dotted lines, see text. (**C** and **D**) Ion- and electron-velocity distribution functions near the spin plane in despun spacecraft coordinates (+*X* is Earthward and is to the right of the page; +*Y* is dawnward and is positive to the top of the page); units are in particles/(cm^3 km^3/s^3) and *X*, *Y* velocity planes are in km/s. (**E**) Energy flux spectra of electrons along (0°), opposite (18°), and perpendicular (90°) to the magnetic field for the times indicated.

deflection of B_z northward (dipolarization) and high-speed flows. The slow flows seen at P3 before the dipolarization did not necessarily emanate directly from the reconnection region; rather, they may have been nearby plasma that accelerated Earthward due to the forces from the establishment of a reconnection topology further downtail. The first signatures of dipolarization were timed at 04:53:05 UT.

Together, the observations at P1, P2, and P3 make a compelling case for onset of tail reconnection at or before t_1 = 04:50:28 UT, between P1 and P2 (Table 1). Approximating the Alfvén speed near the reconnection site as 500 km/s (based on a local density measurement of one particle per cubic centimeter and a magnetic field of 20 nT), we can infer the downtail location of the source, x_0, and the time of reconnection onset, t_0. Noting that the reconnection pulse can travel a distance of 5 R_{E} (the P1-P2 interprobe separation) in 60 s, we obtain $(t_1 - t_0) + (t_2 - t_0) = 60$ s, resulting in t_0 = 04:50:03 UT and $x_0 = 20\ R_{\mathrm{E}}$.

Time history of events. The inferred reconnection onset at 04:50:03 UT preceded the onset of auroral intensification by 96 s (Table 1). Arc intensification was followed by high-latitude Pi2 onset, 21 s later. The high-latitude Pi2 onset may signify the arrival of the field-aligned current pulse generated by the reconnection flows in the tail (*15*). It is unlikely that a shear Alfvén wave, starting at ~500 km/s, can travel from 20 R_{E} to the ionosphere in 96 s, due to both the high density in the plasma sheet and the large distance to the source. Conversely, kinetic Alfvén waves (*32*) of an ion acoustic gyroradius scale may exceed the local Alfvén speed by a factor of $\sqrt{2}$ and arrive faster. Those waves can also accelerate electrons (*33*), which may result in visible aurorae ahead of the wave. This would explain the observations of arc intensification 20 s earlier than the Pi2 onset and would be consistent with reported observations of Alfvénic aurorae (*34*).

Twenty-one seconds after the high-latitude Pi2 onset, the aurorae started to expand poleward. This expansion started 6 s before the arrival of an Earthward flow perturbation at P3 and about 40 s before the dipolarization at P3. Therefore, the initial poleward motion of the aurora cannot be caused by the near-Earth flux pile-up of reconnection flows. It is likely associated with the change in magnetic field mapping, because reconnection at 20 R_{E} results in the engulfment of higher magnetic latitude flux in the reconnection process. Flux pileup and current wedge formation may, however, be responsible for later stages of poleward arc expansion; careful modeling of the current wedge currents in realistic magnetotail fields is needed to properly address this question.

Across field lines, the reconnection process started to affect the inner magnetosphere at 11 R_{E} (P3's location) 144 s after onset. This time delay relative to reconnection onset is commensurate with the magnetosonic speed of the 1- to 4-keV plasma at the neutral sheet between P2 and P3, i.e., ~500 km/s. The first evidence of intense dipolarization, interpreted as the reconnected flux arrival at that same location, was seen 30 s after the first indication of Earthward flow and 3 min after reconnection onset at 20 R_{E}. The latter is also commensurate with the simultaneously observed plasma flow speed, ~400 km/s. The onset of mid-latitude Pi2 pulsations was observed simultaneously with the dipolarization at 11 R_{E}. Mid-latitude Pi2 onset has been interpreted previously as an integrated response to the field-aligned currents from the flows contributing to current wedge formation, but not necessarily due to the current disruption process in the near-Earth region (*15*). The observed Pi2 onset time at 04:53:05 UT is consistent with such an interpretation.

Other Substorm Events

In the aforementioned substorm event, the plasma sheet was atypically cold and dense, suggesting that the slower Alfvén and magnetosonic speeds may result in longer-than-usual communication times between the various regions within the plasma sheet, as well as between the tail and the ionosphere. This may have been responsible for the easy temporal differentiation of the substorm signatures on the ground and in space observed in this event. To demonstrate that our findings are typical of other events, we examined two additional isolated substorms on 16 and 22 February, both between 04:30 and 05:00 UT, and reached similar conclusions (*23*).

In the events analyzed, the earliest indication of substorm onset followed the first evidence of tail reconnection by <96 s and preceded the earliest indication of current disruption by >1 min. It is surprising how quickly the aurora intensifies in response to reconnection onset (<96 s). Electron acceleration by reconnection-generated kinetic Alfvén waves may explain this tight coupling between the ionosphere and the reconnecting plasma sheet. Our observations, however, raise another question: What growth-phase process preconditions and destabilizes tail reconnection during spontaneous and externally driven substorms? Because substorm arcs intensify gradually and the magnetotail thins slowly before onset (over several minutes), the entire magnetotail from geosynchronous altitude to 30 R_{E} would have enough time to partake in that process.

References and Notes

1. S.-I. Akasofu, *Planet. Space Sci.* **12**, 273 (1964).
2. W. I. Axford, *Phys. Chem. Earth* **23**, (C), 147 (1999).
3. S.-I. Ohtani *et al.*, *AGU Monogr. Ser.* **64**, 131 (1991).
4. V. Angelopoulos *et al.*, *Geophys. Res. Lett.* **24**, 2271 (1997).
5. A. T. Y. Lui, *J. Geophys. Res.* **101**, 13067 (1996).
6. D. N. Baker *et al.*, *J. Geophys. Res.* **101**, 12975 (1996).
7. K. Liou *et al.*, *J. Geophys. Res.* **107**, 1131 (2002).
8. V. A. Sergeev *et al.*, *J. Geophys. Res.* **100**, 19121 (1995).
9. V. Angelopoulos, *Space Sci. Rev.*, in press, www.springerlink.com/content/5334m68160740104/fulltext.pdf (2008).
10. D. G. Sibeck, V. Angelopoulos, *Space Sci. Rev.*, in press, www.springerlink.com/content/6132873114236203/fulltext.pdf (2008).
11. S. Mende *et al.*, *Space Sci. Rev.*, in press, www.springerlink.com/content/g1391t379r5g5495/fulltext.pdf (2008).
12. P. N. Maynaud, *Geophys. Monogr. 22* (American Geophysical Union, Washington, DC, 1980).
13. T. Saito, *Space Sci. Rev.* **10**, 319 (1969).
14. D. K. Milling *et al.*, *Geophys. Res. Lett.*, in press, www.agu.org/journals/pip/gl/2008GL033672-pip.pdf (2008).
15. L. Kepko *et al.*, *J. Geophys. Res.* **109**, A04203 (2004).
16. G. Rostoker *et al.*, *J. Geophys. Res.* **85**, 1663 (1980).
17. R. L. McPherron, *Rev. Geophys.* **17**, 657 (1979).
18. F. V. Coroniti, *J. Geophys. Res.* **90**, 7427 (1985).
19. J. Sanny *et al.*, *J. Geophys. Res.* **99**, 5805 (1994).
20. C. T. Russell, R. L. McPherron, *Space Sci. Rev.* **15**, 205 (1973).
21. T. Nagai *et al.*, *J. Geophys. Res.* **103**, 4419 (1998).
22. A. T. Aikio *et al.*, *J. Geophys. Res.* **104**, 12263 (1999).
23. Materials and methods are available as supporting material on *Science* Online.
24. N. A. Tsyganenko, *J. Geophys. Res.* **100**, 5599 (1995).
25. M. Fujimoto *et al.*, *Space Sci. Rev.* **80**, 325 (1997).
26. T. Nagai *et al.*, *J. Geophys. Res.* **106**, 25929 (2001).
27. M. Øieroset *et al.*, *Nature* **412**, 414 (2001).
28. A. Runov *et al.*, *Geophys. Res. Lett.* **30**, 1579 (2003).
29. J. Birn *et al.*, *J. Geophys. Res.* **102**, 2325 (1997).
30. V. S. Semenov *et al.*, *J. Geophys. Res.* **110**, A11217 (2005).
31. V. A. Sergeev *et al.*, *J. Geophys. Res.* **23**, 2183 (2005).
32. R. L. Lysak, W. Lotko, *J. Geophys. Res.* **101**, 5085 (1996).
33. C. C. Chaston *et al.*, *Geophys. Res. Lett.* **34**, L07101 (2007).
34. S. B. Mende *et al.*, *J. Geophys. Res.* **108**, 1344 (2003).
35. U. Auster *et al.*, *Space Sci. Rev.*, in press, www.springerlink.com/content/fr4u42m531431m34/fulltext.pdf (2008).

36. This work was supported by NASA contract NAS5-02099. The work of K.-H.G. was financially supported by the German Ministerium für Wirtschaft und Technologie and the German Zentrum für Luft- und Raumfahrt under grant 50QP0402. Logistical support for fielding and retrieval of the THEMIS-GBO and CARISMA (Canadian Array for Realtime Investigations of Magnetic Activity) data is provided by the Canadian Space Agency. CARISMA is operated by the University of Alberta. Special thanks to A. Prentice for careful editing of this paper.

Supporting Online Material

www.sciencemag.org/cgi/content/full/1160495/DC1
Materials and Methods
Figs. S1 and S2
Movies S1 to S7

14 May 2008; accepted 1 July 2008
Published online 24 July 2008;
10.1126/science.1160495
Include this information when citing this paper.

Density Multiplication and Improved Lithography by Directed Block Copolymer Assembly

Ricardo Ruiz,[1]* Huiman Kang,[2] François A. Detcheverry,[2] Elizabeth Dobisz,[1] Dan S. Kercher,[1] Thomas R. Albrecht,[1] Juan J. de Pablo,[2] Paul F. Nealey[2]*

Self-assembling materials spontaneously form structures at length scales of interest in nanotechnology. In the particular case of block copolymers, the thermodynamic driving forces for self-assembly are small, and low-energy defects can get easily trapped. We directed the assembly of defect-free arrays of isolated block copolymer domains at densities up to 1 terabit per square inch on chemically patterned surfaces. In comparing the assembled structures to the chemical pattern, the density is increased by a factor of four, the size is reduced by a factor of two, and the dimensional uniformity is vastly improved.

The use of self-assembling materials to define templates for patterning dense features at length scales of 25 nm and below may provide a means to continue to shrink the dimensions of electronic and storage devices as optical lithography, the engine of the semiconductor industry, reaches intrinsic technological and economical limits (*1*, *2*). For magnetic storage devices, the demands for diminishing feature size and spacing outpace those for integrated circuits, particularly as the industry considers introduction of patterned media (*3*, *4*) to extend densities beyond limitations imposed by the onset of the superparamagnetic effect in conventional continuous granular media (*5*). Self-assembling block copolymers form dense periodic arrays with dimensions and spacing of domains from ~3 to 50 nm (*6*, *7*). The domain structure of block copolymer thin films has already been used to create templates for defining nanoscale features in metals, semiconductors, and dielectrics for applications as varied as quantum dots and nanoporous membranes for creating insulating air gaps between wires in integrated circuits (*8*, *9*). One entry point for block copolymer thin films in fabrication thus capitalizes on inexpensive creation and processing of dense nanoscale features of roughly uniform dimensions. Although using the domain structure of thin copolymer films to pattern is termed block copolymer lithography, in the applications described above it has only a superficial relation to optical or electron-beam lithography used in the manufacture of high-performance devices. Lithography, as currently practiced for nanomanufacturing, requires essentially defect-free patterns, control over feature dimensions and shapes with molecular-level tolerances, and precise placement of each patterned feature with respect to the features in the same and underlying and overlying layers (*1*). In this context, for block copolymers to have an impact in lithography, they must demonstrate, as a minimum, the capability to define individual device elements with some advantage over established lithographic techniques.

Hexagonal arrays formed spontaneously by block copolymers may be applied directly for patterned media applications if adequate organization and dimensional uniformity can be achieved in thin-film templates. Methods to impart improved ordering in block copolymer films include chemical prepatterning (*10*, *11*), graphoepitaxy (*12*), solvent annealing (*13*), shear (*14*, *15*), electric fields (*16*), flow (*17*), thermal gradients (*18*, *19*), and internal fields (*20*). Whereas all these methods provide orientational ordering, only chemical prepatterning and graphoepitaxy provide additional control over translational ordering and feature registration (*9*). For patterned media applications, chemical prepatterning does not compromise storage area (as opposed to graphoepitaxy, where topographic features use valuable substrate area) and allows for guidance of the self-assembling system at a sufficient level to address stringent pattern quality requirements, including vanishingly small defect densities and control over feature shapes and dimensions. The prepatterning method (*10*), however, is disadvantageous in that it introduces a lithographic step, nominally at the same feature density as that achieved by the block copolymer. Even though the block copolymer assembly can perform a substantial pattern quality rectification with respect to the prepattern, creating a template where each and every feature is exposed by e-beam is challenging because of the long writing times required by large-area applications at high densities [defining of a master template for a 95-mm patterned media disk at 1 terabit per square inch (Tb/in^2) would take more than a month].

As a viable alternative, we developed a directed assembly method for feature density multiplication and pattern quality rectification. With density multiplication, not only is the resolution increased with respect to the prepattern but also the exposure time is reduced with the decrease in the number of written features. The constraints in defining the dimensions of individual features of the prepattern can be relaxed because of the rectification action by the block copolymer, enabling the use of faster resists and higher e-beam currents.

We use thin films of poly(styrene-*block*-methyl methacrylate) (PS-*b*-PMMA) to demonstrate both density multiplication and pattern quality rectification on substrates prepatterned by e-beam lithography. Two copolymers with different lattice constants, L_0, are used to generate hexagonal arrays of perpendicularly oriented PMMA cylinders in a PS matrix at two different densities: L_0 = 39 nm, and L_0 = 27 nm, as de-

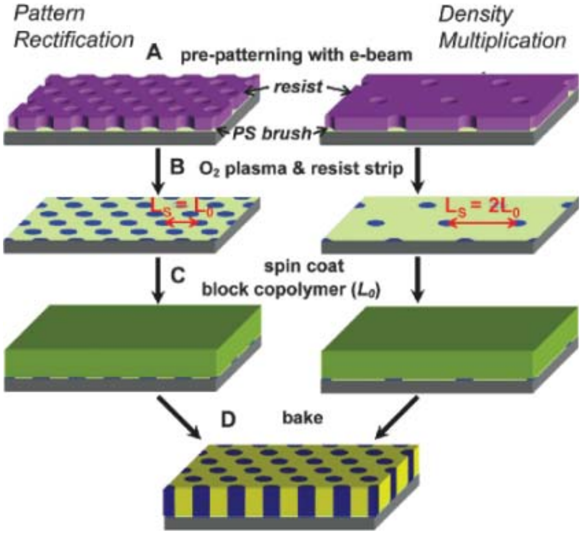

Fig. 1. Process to create lithographically defined chemically prepatterned surfaces and subsequent directed assembly. (**A**) Electron-beam lithography patterns at $L_s = L_0$ (left) and $L_s = 2L_0$ (right). (**B**) Chemical contrast on the substrate after O$_2$ plasma exposure on the e-beam–defined spots above. (**C**) Block copolymer thin film. (**D**) Guided self-assembly in registration with the underlying chemical pattern.

---

[1] Hitachi Global Storage Technologies, San Jose Research Center, 3403 Yerba Buena Road, San Jose, CA 95135, USA.
[2] Department of Chemical and Biological Engineering, University of Wisconsin, Madison, WI 53706, USA.

*To whom correspondence should be addressed. E-mail: Ricardo.Ruiz@hitachigst.com (R.R.); nealey@engr.wisc.edu (P.F.N.)

scribed in detail in the supporting online material (SOM). The assembly process is illustrated in Fig. 1. A brush of hydroxyl-terminated polystyrene (*21*, *22*) (M_n = 6 Kg/mol) is deposited on a SiO_x substrate. We then apply an e-beam resist layer and use an electron beam to write the closest possible match to a hexagonal pattern (*23*) with a lattice constant L_s, such that $L_s = nL_0$ with n = 1, 2 (Fig. 1A) over a total area of 100 μm by 100 μm (for L_s = 39 and 78 nm, we made additional patterns covering 3000 μm by 50 μm). Patterns with both n = 1 and n = 2 were written on the same sample. Samples for block copolymer assembly are then subjected to a brief dose of oxygen plasma to generate a chemical contrast on the substrate. We then remove the bulk of the resist (Fig. 1B), spin-coat a block copolymer film (Fig. 1C), and anneal it in vacuum as described in the SOM. The areas of the surface (arrays of spots) exposed to the oxygen plasma are preferentially wet by the PMMA block, and background areas are slightly preferential toward the PS block. (Perpendicular cylinders with defects including short sections of parallel cylinders are observed on areas of the sample adjacent to the patterned regions.) The PMMA domains are then selectively removed (*24*). We use scanning electron micrograph (SEM) images to quantify the feature size uniformity of both block copolymer and e-beam features (see SOM).

The improved quality of patterning afforded by directing the assembly of block copolymer films on lithographically defined chemically patterned surfaces in comparison to the lithographically defined patterns themselves is presented in Fig. 2. Figure 2, A to D, shows top-down SEM images of developed e-beam resist patterned at L_s = 39, 78, 27, and 54 nm, respectively. Figure 2, E to H, shows micrographs of the block copolymer films guided by the prepattern with the corresponding e-beam features above. The polymer pitch on the guided patterns (L_p) is 39, 39, 27, and 27 nm, respectively. In Fig. 2, I to L, we plot the dot size distributions of both the e-beam and the corresponding block copolymer patterns from at least 15,000 dots. For L_s = 39 and 27 nm, the e-beam patterns (Fig. 2, A and C) have a lower quality apparent in variations in distance between rows and dot size distribution. Both of these sources of noise are rectified by the block copolymer (Fig. 2, E and G). At L_s = 39 nm, the e-beam pattern shows an average dot size of A_s = 276 nm^2 with a standard deviation σ_s = 30 nm^2, whereas the block copolymer pattern had an average dot size A_p = 262 nm^2 with σ_p = 23 nm^2, rectifying the quality of the e-beam prepattern by narrowing the dot size distribution (Fig. 2I). The e-beam resist pattern at L_s = 27 nm does not have enough resolution (Fig. 2C) to define a useful lithographic mask, nor does it display the necessary statistics on dot size, shape, or placement required for the application. Nonetheless, the block copolymer film (Fig. 2G) maintains a uniform lattice constant and rectifies the dot size distribution of the e-beam prepattern from σ_s = 26 nm^2 down to σ_p = 11 nm^2 (Fig. 2K).

Directed assembly may be implemented not only to improve the quality but also to substantially augment the capabilities of the lithographic process beyond current resolution limits. Figure 2B shows the e-beam resist used to prepattern the substrate at $L_s = 2L_0$ = 78 nm. The block copolymer in Fig. 2F registers with the prepatterned sites and, because the lattice is nearly commensurate to the natural lattice of the block copolymer, the self-assembly interpolates the location of the PMMA cylinders in between the

Table 1. Standard deviation of dot placement errors along the *x* direction (σ_x) and the *y* direction (σ_y) on the e-beam–defined patterns and on the block copolymer patterns (in nm). At smaller dimensions, the block copolymer pattern has tighter distribution compared to the e-beam patterns, and the statistics are the same for the density multiplied and nonmultiplied patterns.

Pattern		σ_x		σ_y	
		E-beam	Copolymer	E-beam	Copolymer
L_s = 39	L_p = 39	2.2	1.6	2.1	0.4
L_s = 78	L_p = 39	1.4	1.6	0.9	0.4
L_s = 27	L_p = 27	3.1	1.9	1.9	1.0
L_s = 54	L_p = 27	2.3	1.8	1.1	1.0

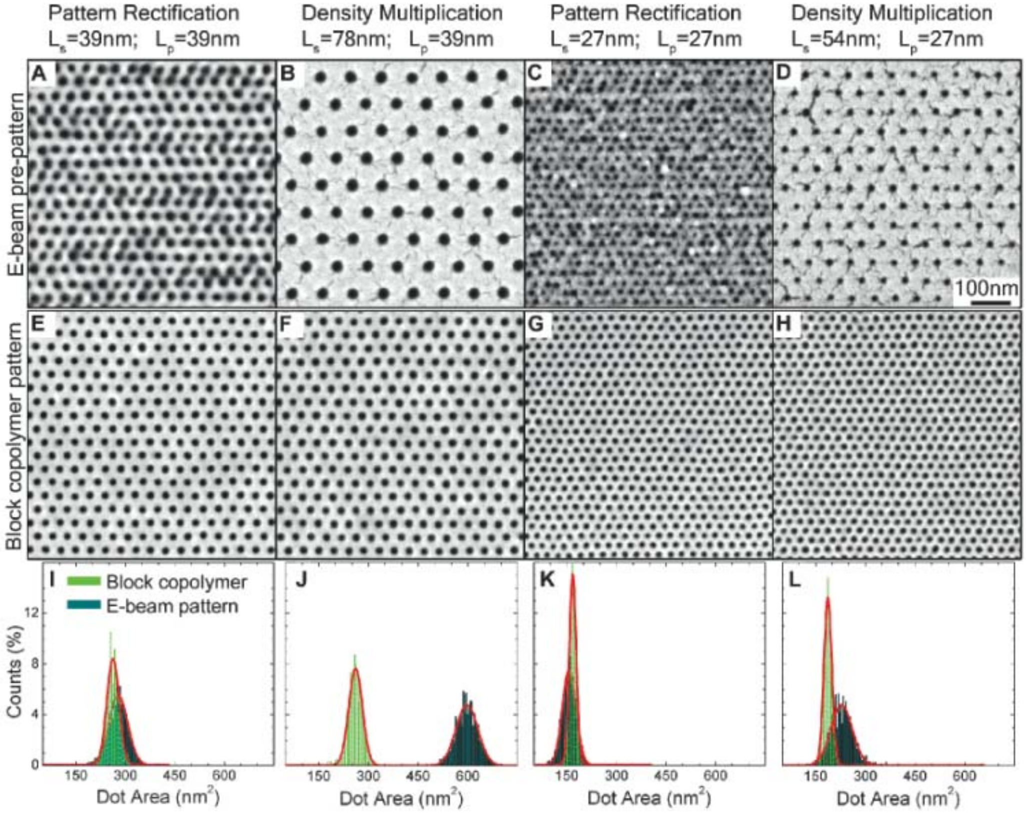

Fig. 2. (**A** to **D**) SEM images of developed e-beam resist with L_s = 39, 78, 27, and 54 nm, respectively. (**E** to **H**) SEM images of the block copolymer film on top of the prepattern defined by the corresponding e-beam pattern above. The lattice pitch on the block copolymer samples is L_p = 39, 39, 27, and 27 nm, respectively. (**I** to **L**) Dot size distribution of e-beam (dark teal) and guided block copolymer patterns (light green).

prepatterned dots, multiplying the density of features by a factor of four (two in each direction in analogy to heteroepitaxial thin films) in addition to maintaining a constant and uniform feature size. The commensurability tolerance is about $\pm 0.1L_0$ for the average lattice spacing. The e-beam prepattern at $L_s = 2L_0 = 78$ nm has an average area $A_s = 595$ nm^2 with $\sigma_s = 35$ nm^2. The block copolymer not only multiplies the feature density but also rectifies the dot area size by more than a factor of two to keep it constant at $A_p = 260$ nm^2 with $\sigma_p = 22$ nm^2 [basically with the same statistics when $L_s = 39$ nm (see Fig. 2, I to J)]. For $L_s = 2L_0 = 54$ nm, the polymer also multiplies the feature density to 1 Tdot/in^2 (27-nm pitch), as shown in Fig. 2, D and H, while rectifying the size distribution from $\sigma_s = 39$ nm^2 on the e-beam pattern down to $\sigma_p = 13$ nm^2 on the block copolymer (Fig. 2L).

Long-range order is preserved throughout the entire prepatterned area (100 by 100 μm^2 and 3000 by 50 μm^2 for some samples), with defect densities that are compatible with data storage requirements. High-resolution SEM image analysis was performed on a sampling set of images comprising ~15,000 to 20,000 dots total. Based on this sampling, we estimate a defect density $<10^{-4}$ for patterns with $L_s = 39$, 78, and 27 nm and $<10^{-3}$ for patterns with $L_s = 54$ nm. We project that defect tolerance in bit-patterned media will be on the order of 1 dot in 10^4 to 10^6, depending on the algorithms and countermeasures used. Long-range order is shown in larger area images (4 μm long) and even larger (tens of microns long) Moiré interference patterns in figs. S1 and S2, respectively.

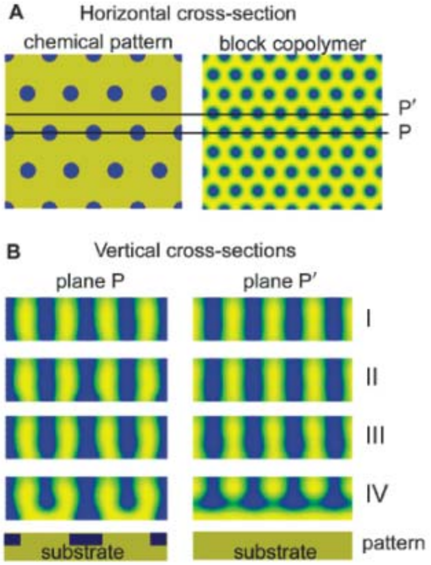

Fig. 3. Simulation of the directed assembly of block copolymer films for density multiplication. (**A**) The chemical pattern is shown on the left. On the right is a horizontal cross section of the simulated system taken at mid-height of the film. The color map gives the average local composition, with pure PS in yellow and pure PMMA in blue. Black lines correspond to the planes P and P' along which vertical cross sections are taken. (**B**) Vertical cross sections showing the average local composition for four different polymer-substrate interactions described in the text (cases I to IV)

The translational order of these patterns is assessed by looking at correlations in the *x* and *y* directions separately [as opposed to traditional Voronoi or Delaunay constructions (*25*), where all directions in the hexagonal lattice are equivalent] because our patterns are formed on rectangular and not hexagonal lattices as a result of e-beam limitations. We quantify placement accuracy by measuring the standard deviation of placement error along the *x* direction (σ_x) and the *y* direction (σ_y). The results are summarized in Table 1, and details can be found in the SOM. At smaller dimensions, the block copolymer patterns have tighter distributions and the statistics are preserved for the multiplied and nonmultiplied patterns. As a comparison, placement tolerances for patterned media are projected to be $\sigma \sim 1$ nm.

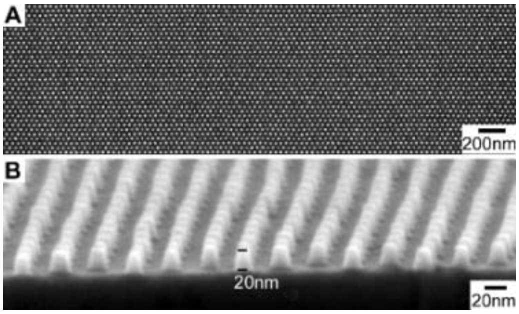

Fig. 4. Pattern transfer using a directed block copolymer template with density multiplication ($L_p = 39$ nm, $L_s = 78$ nm). (**A**) Cr dots after lift-off. (**B**) 20-nm-tall Si pillars etched using the Cr mask in (A).

Metrics of pattern quality that cannot be determined from top-down SEM images relate to the shapes and dimensions of features in the pattern transfer template. Of particular importance is the side-wall profile of the mask (*26*, *27*). Previous research suggests that the three-dimensional (3D) structure of the domains through the film thickness may be very different from plan-view images, or even bulk block copolymer morphologies, and are known to be strong functions of the geometry and strength of interactions between the polymer and the patterned substrate (*28*, *29*). We therefore explore the fundamental physics of assembly in the case of the interpolated structures by resorting to Monte Carlo simulations of a coarse-grain model of the block copolymer. Details of the simulation method can be found in reference (*30*). Parameters in the simulations were chosen to describe a PS-*b*-PMMA block copolymer with $L_0 = 39$ nm, a film thickness of $\sim 1.1L_0$, a spot pattern with $L_s = 2L_0$, and spot area equal to twice the natural cylinder area (Fig. 3A, left). A simulated system typically contains 60 cylinders. The PMMA block wets the spots and the PS block wets the background of the chemical pattern. The interactions between the patterned spots and the PMMA block (Λ_{PMMA}) and the patterned background and the PS block (Λ_{PS}) play a critical role with respect to the 3D structure of the assembled domains. The interfacial energies between the chemically patterned surface and the blocks of the copolymer are not known quantitatively, but Λ_{PMMA} is expected to be medium or strong and Λ_{PS} is expected to be weak. Four cases are considered to encompass these expectations and are presented in Fig. 3: (I) weak Λ_{PMMA} and weak Λ_{PS}, (II) strong Λ_{PMMA} and weak Λ_{PS}, (III) medium Λ_{PMMA} and medium Λ_{PS}, and (IV) strong Λ_{PMMA} and strong Λ_{PS}. In our model, the strength of interaction between the patterned substrate and a block is quantified by ΛN, where N is the number of beads per copolymer chain. Our weak, medium, and strong interactions correspond to $\Lambda N = 0.125$, 0.25, and 0.375, respectively. The nonpreferred block has an equal but repulsive interaction in all cases. Figure 3A (right) shows a representative cross section for all of the cases at half height in the plane of the film, showing the interpolation of cylindrical domains (with diameter comparable to the natural cylinder diameter) at four times the density with respect to the chemical pattern. Figure 3B shows vertical cross sections of the assembled domains through rows of cylinders on chemically patterned spots alternating with interpolated cylinders (left), and vertical cross sections of rows of interpolated cylinders (right). The cross sections represent a long-time simulation that averages over thermal fluctuations but highlight the effect of the pattern on the average cylinder shape. Cases I to III depict equilibrium scenarios for which a perpendicular orientation of the cylinders is achieved through the full thickness of the film, with case I being the most uniform. Medium Λ_{PMMA} causes the noninterpolated cylinders to adopt an undercut profile (case II). For even stronger Λ_{PMMA}, some of those cylinders actually break into two halves (not shown). If Λ_{PS} and Λ_{PMMA} are both increased (case III), then the interpolated cylinders exhibit a slight constriction at their base. Finally, in the limit of strong Λ_{PMMA} and strong Λ_{PS} (case IV), interpolated cylinders do not extend all the way to the substrate and form a complicated 3D network. They end at a distance of ~8 nm from the substrate and are connected to each other in the plane of the film, forming perimeters of hexagons centered around cylinders extending vertically away from each patterned spot. Interestingly, the pattern observed at the surface of the film is the same as in other cases, namely, a hexagonal array of spots. These simulated scenarios indicate that there is a window of tolerance for density multiplication to work successfully within a range of interaction values. The fact that there exists a window of tolerance suggests the possibility of added room for experimental optimization to generate lower defect densities or even higher orders of density multiplication. For instance, it should be possible to change the brush layer to optimize the brush interactions in density multiplied patterns with L_s = 54 nm in order to reduce the defect density below 10^{-4} (see Moiré patterns in fig. S2).

A technological benchmark for the quality of the patterns is garnered from transferring the pattern to the underlying substrate. The block copolymer film produced by density multiplication has a vertical side-wall profile suitable for pattern transfer. Using a lift-off technique, we fabricated 20-nm-tall Si pillars. We started with a block copolymer film like the one shown in Fig. 2F (L_s = 78 nm, L_p = 39 nm) after removing the PMMA cylinder and cleaned the pores with oxygen plasma. We deposited 7 nm of Cr by e-beam evaporation and removed the PS mask using a piranha solution leaving Cr dots on the surface (Fig. 4A). We used a CF_4 reactive ion etch to generate 20-nm Si pillars (Fig. 4B). The pillars were uniform over the entire sample (3 mm long) and otherwise identical to those formed in patterns where L_s = 39 nm. Taken together, molecular simulation and pattern transfer results demonstrate that the degree of perfection, registration, and vertical side-wall profiles of the enhanced-resolution templates provide a path based on e-beam patterning and directed assembly of block copolymers toward bit-patterned media at densities over 1 Tb/in^2.

We envision the role of directed assembly to enhance, augment, and advance the performance of lithographic processes rather than to attempt to develop replacement technology. The starting point is a chemical prepattern at or near the limit of current lithographic tools to provide strong thermodynamic driving forces for directed assembly of patterns with perfection, registration, resolution, and quality beyond those possible with traditional materials and processes. In this context, we anticipate that the experiments here with cylindrical-phase diblock copolymers could be extended to higher-density multiplication factors for patterned media and to other classes of block copolymers to achieve striped or more complex patterns such as those required by the semiconductor industry.

References and Notes

1. Semiconductor Industry Association, *International Technology Roadmap for Semiconductor, 2005 Edition* (Semiconductor Industry Association, San Jose, CA, 2005).
2. D. J. C. Herr, *Future Fab. Int.* **20**, 82 (2006).
3. B. D. Terris, T. Thomson, *J. Phys. D Appl. Phys.* **38**, R199 (2005).
4. C. Ross, *Annu. Rev. Mater. Res.* **31**, 203 (2001).
5. D. Weller, A. Moser, *IEEE Trans. Magn.* **35**, 4423 (1999).
6. F. S. Bates, G. H. Fredrickson, *Annu. Rev. Phys. Chem.* **41**, 525 (1990).
7. M. J. Park *et al.*, *Nano Lett.* **7**, 3547 (2007).
8. C. T. Black *et al.*, *IBM J. Res. Develop.* **51**, 605 (2007).
9. C. T. Black, *Acs Nano* **1**, 147 (2007).
10. S. O. Kim *et al.*, *Nature* **424**, 411 (2003).
11. M. P. Stoykovich *et al.*, *Science* **308**, 1442 (2005).
12. R. A. Segalman, H. Yokoyama, E. J. Kramer, *Adv. Mater.* **13**, 1152 (2001).
13. S. H. Kim, M. J. Misner, T. P. Russell, *Adv. Mater.* **16**, 2119 (2004).
14. G. Hadziioannou, A. Mathis, A. Skoulios, *Colloid Polym. Sci.* **257**, 136 (1979).
15. A. Keller, E. Pedemont, F. M. Willmout, *Nature* **225**, 538 (1970).
16. T. Thurn-Albrecht *et al.*, *Science* **290**, 2126 (2000).
17. T. Hashimoto *et al.*, *Polymer* **39**, 1573 (1998).
18. B. C. Berry, A. W. Bosse, J. F. Douglas, R. L. Jones, A. Karim, *Nano Lett.* **7**, 2789 (2007).
19. T. Hashimoto, J. Bodycomb, Y. Funaki, K. Kimishima, *Macromolecules* **32**, 952 (1999).
20. S. H. Kim *et al.*, *Macromolecules* **39**, 8473 (2006).
21. E. W. Edwards, M. F. Montague, H. H. Solak, C. J. Hawker, P. F. Nealey, *Adv. Mater.* **16**, 1315 (2004).
22. K. O. Stuen *et al.*, *J. Vac. Sci. Technol. B* **25**, 1958 (2007).
23. The chemical patterns are written on a rectangular lattice and not on a hexagonal lattice because the e-beam moves in an *x-y* grid with discrete steps along the *x* and *y* axis. The e-beam prepattern consists of a rectangular lattice with two dots in the unit cell that are the closest match to the natural hexagonal lattice of the block copolymer.
24. T. Thurn-Albrecht *et al.*, *Adv. Mater.* **12**, 787 (2000).
25. R. A. Segalman, A. Hexemer, E. J. Kramer, *Phys. Rev. Lett.* **91**, 196101 (2003).
26. K. C. Daoulas *et al.*, *Langmuir* **24**, 1284 (2008).
27. E. W. Edwards *et al.*, *Macromolecules* **40**, 90 (2007).
28. K. C. Daoulas *et al.*, *Phys. Rev. Lett.* **96**, 036104 (2006).
29. S. M. Park, G. S. W. Craig, Y. H. La, H. H. Solak, P. F. Nealey, *Macromolecules* **40**, 5084 (2007).
30. F. Detcheverry, H. Kang, K. C. Daoulas, M. Muller, P. F. Nealey, *Macromolecules* **41**, 4989 (2008).
31. We thank C. P. Henderson, B. Marchon (Hitachi GST), and H. Yoshida (Hitachi Ltd.) for insightful discussions. This research was supported by Hitachi Global Storage Technologies Inc., the Semiconductor Research Corporation, and the National Science Foundation through the University of Wisconsin Nanoscale Science and Engineering Center (MPS/DMR-0425880). Patent protection related to this work is pending.

Supporting Online Material
www.sciencemag.org/cgi/content/full/321/5891/936/DC1
Materials and Methods
Figs. S1 and S2
References

11 March 2008; accepted 27 June 2008
10.1126/science.1157626

Graphoepitaxy of Self-Assembled Block Copolymers on Two-Dimensional Periodic Patterned Templates

Ion Bita,[1]*† Joel K. W. Yang,[2]* Yeon Sik Jung,[1]* Caroline A. Ross,[1]‡
Edwin L. Thomas,[1]‡ Karl K. Berggren[2]‡

Self-assembling materials are the building blocks of bottom-up nanofabrication processes, but they need to be templated to impose long-range order and eliminate defects. In this work, the self-assembly of a thin film of a spherical-morphology block copolymer is templated using an array of nanoscale topographical elements that act as surrogates for the minority domains of the block copolymer. The orientation and periodicity of the resulting array of spherical microdomains are governed by the commensurability between the block copolymer period and the template period and is accurately described by a free-energy model. This method, which forms high-spatial-frequency arrays using a lower-spatial-frequency template, will be useful in nanolithography applications such as the formation of high-density microelectronic structures.

Self-assembly of nanometer-length-scale patterns in two dimensions (2D) is currently of interest as a method for improving throughput and resolution in nanolithography. Self-assembly in 2D has been studied widely in a range of systems, including self-assembled monolayers (*1*), quantum dots (*2*), and colloidal particles (*3*). Among these systems, the self-assembly of thin films of block copolymers (BCPs) has many attractive aspects resulting from the intrinsic ability of BCPs to generate uniform and periodic nanoscale structures in parallel over large areas by microphase separation (*4*). BCP thin films with spherical, cylindrical, or lamellar morphologies of different length scales may be created by adjusting the composition and molecular weight of the BCP. These morphologies can be employed for the fabrication of nanostructures: After selectively removing one of the blocks, the remaining pattern can be transferred into a functional material (*5*–*10*). However, the spontaneous process of microphase separation leads to the formation of “polycrystalline” BCP microdomain arrays consisting of randomly oriented ordered regions, or grains, which limits the potential applications. This issue has sparked the development of a host of techniques that attempt to control the ordering of thin-film BCP systems, that is, to template the positions of the microdomains and to form “single-crystal” structures

---

[1] Department of Materials Science and Engineering, Massachusetts Institute of Technology, 77 Massachusetts Avenue, Cambridge, MA 02139, USA. [2] Department of Electrical Engineering and Computer Science, Massachusetts Institute of Technology, 77 Massachusetts Avenue, Cambridge, MA 02139, USA.

*These authors contributed equally to this work.

†Present address: Qualcomm Micro Electro Mechanical Systems Technologies, 2581 Junction Avenue, San Jose, CA 95134, USA.

‡To whom correspondence should be addressed. E-mail: caross@mit.edu (C.A.R.), elt@mit.edu (E.L.T.), berggren@mit.edu (K.K.B.)

in which the locations and orientations of the microdomains are precisely determined (*11*–*13*). These techniques include the use of topographically (*14*–*16*) or chemically (*17*–*20*) patterned substrates as templates for the self-assembly process. Recent work has extended the chemical patterning technique such that templates with a period of up to four times that of the BCP could be used to produce large-area defect-free lamellar or cylindrical domain patterns (*21*, *22*).

We describe here a topographical graphoepitaxy technique for controlling the self-assembly of BCP thin films that produces 2D periodic nanostructures with a precisely determined orientation and long-range order. The surface of the substrate is patterned with a sparse 2D lattice of nanoscale posts designed to act as surrogate spherical or cylindrical domains of the minor component of the BCP. Each of these posts is designed to be chemically and physically nearly indistinguishable from the BCP entity (the microdomain and its associated corona) for which it substitutes. This approach differs from previous approaches, which used linear substrate steps or grooves (*12*, *16*), in that here the discrete posts are distributed over the substrate, providing a set of periodic constraints that interact both locally and globally with the array of BCP domains.

The BCP used in our experiments was spherical-morphology polystyrene-*b*-polydimethylsiloxane (PS-*b*-PDMS) with molecular weight = 51.5 kg/mol, minority block volume fraction f_{PDMS} = 16.5%, and polydispersity (PDI) = 1.04. This BCP was chosen because it has both a high Flory-Huggins χ-parameter, giving a large driving force for microphase segregation, and a high chemical selectivity between the two blocks for subsequent pattern transfer. The BCP was spin-coated to a thickness of ~50 nm and annealed at 200°C to obtain a monolayer of 20-nm-diameter PDMS spheres with a center-to-center spacing of 40 nm within a PS matrix [see supporting online material (SOM), section S1]. In this process, a surface layer of PDMS forms at the substrate-BCP and BCP-air interfaces due to the low surface energy of PDMS (*10*). By using CF_4 followed by oxygen reactive-ion etching (RIE), the PS matrix was selectively removed to reveal the oxidized PDMS spherical microdomains (*10*).

To template the BCP, we used a sparse 2D array of posts created by scanning-electron-beam lithography of a 40-nm-thick hydrogen silsesquioxane (HSQ) resist layer on a Si substrate. HSQ is a radiation-sensitive spin-on-glass that forms a silica-like material directly upon electron-beam exposure. Development reveals the exposed posts, without requiring further etching or

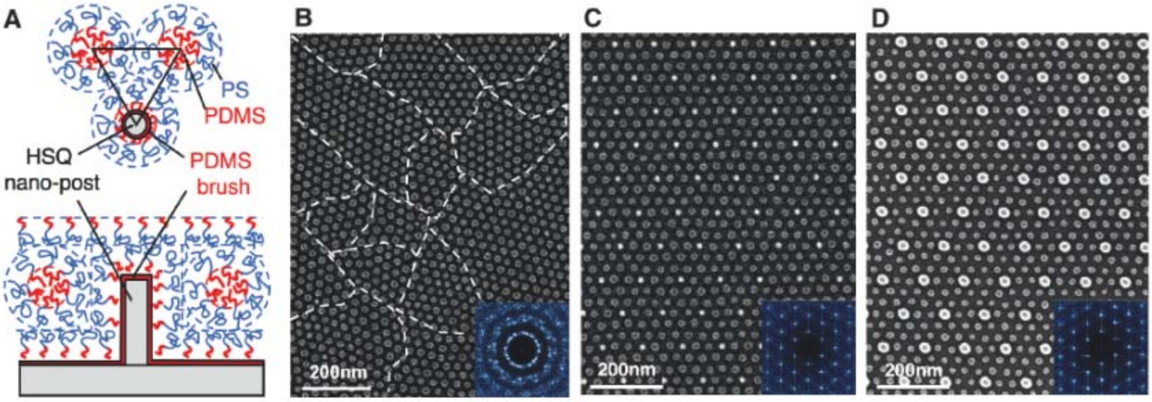

Fig. 1. (**A**) Top-down and side-view schematics showing the arrangement of PS-*b*-PDMS block copolymer molecules in the region surrounding a single post made from cross-linked HSQ resist. The post and substrate surfaces have been chemically functionalized by a monolayer of short-chain PDMS brush. (**B**) SEM images of a poorly ordered monolayer of BCP spherical domains formed on a flat surface, that is, without templating. The boundaries between different grain orientations are indicated with dashed lines. The inset is a 2D Fourier transform of the domain positions that shows the absence of long-range order. (**C** and **D**) SEM images of ordered BCP spheres formed within a sparse 2D lattice of HSQ posts (brighter dots). The substrate and post surfaces were functionalized with a PDMS brush layer in (C), which corresponds to the schematic in (A), and with a PS brush layer in (D). The insets show the 2D Fourier transforms in which the low-frequency components originate from the post lattice.

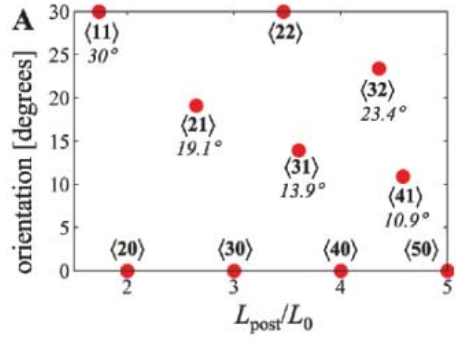

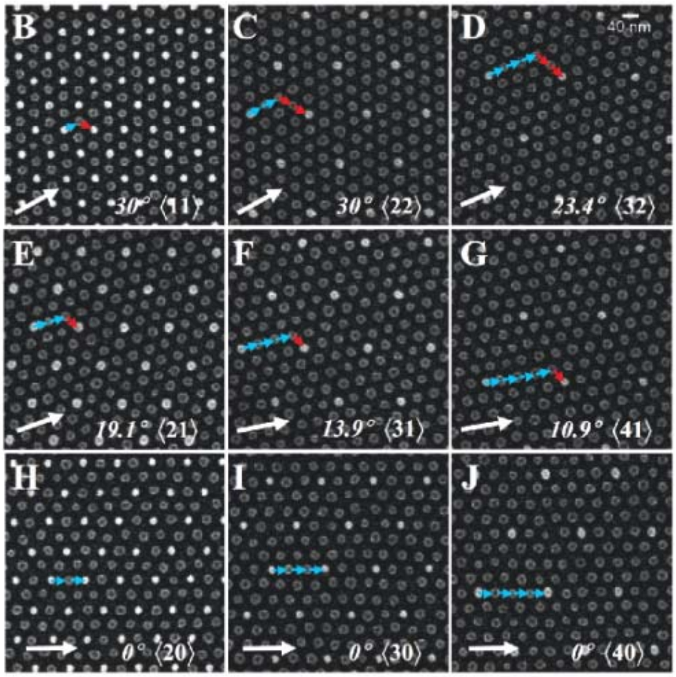

Fig. 2. (**A**) Calculated orientations at which the BCP microdomain lattice is commensurate with the post lattice, as a function of L_{post}/L_0. The BCP lattice is commensurate with the post lattice when the post lattice basis vectors of length L_{post} can be represented as integer multiples, <*ij*>, of the BCP lattice basis vectors of equilibrium length L_0. Because of the 6-fold symmetry of the BCP lattice, the angular span of 0° to 30° is sufficient to represent all possible nondegenerate orientations. (**B** to **J**) Plan-view SEM images of all the commensurate configurations found in (A) for the L_{post}/L_0 ratio range of 1.65 to 4.6. The white arrows show the orientation angle between the BCP microdomain lattice and the post lattice and are 120 nm long. The brighter dots are the oxidized HSQ posts, whereas the darker dots correspond to oxidized PDMS spherical domains. The blue and red arrows indicate the basis vectors of the BCP microdomain lattice and add up to form one horizontal basis vector of the post lattice.

processing. A key requirement for this process is for the surface of the posts to exhibit preferential affinity toward one of the domains of the BCP, which was established by chemical functionalization of the template surface using hydroxy-terminated homopolymer PS or PDMS brushes. Figure 1A illustrates the topographic and chemical design of the posts used in most of our experiments. The template was functionalized with a short PDMS homopolymer brush, and a post substitutes for a PDMS sphere in the close-packed array. The template can also be fabricated with an affinity toward the majority block by using a PS brush, which requires larger-diameter HSQ. PDMS brush-coated substrates provided better ordering of PS-*b*-PDMS microdomain arrays than PS-coated or uncoated substrates, which we attributed to higher surface diffusivity of the PDMS brush (*10*). The use of PDMS brush-coated posts, which required the ability to fabricate ~10-nm structures lithographically, was enabled by recent high-resolution development methods in electron-beam lithography (*23*).

Figure 1, C and D, shows that appropriately sized and functionalized posts could template the assembly of a BCP lattice. For comparison, Fig. 1B shows the results of untemplated assembly for the same BCP. The template in Fig. 1C consisted of ~12-nm-diameter HSQ posts functionalized with PDMS (5 kg/mol) of thickness ~2 nm, resulting in a post diameter of ~16 nm. Figure 1D shows results from 20-nm-diameter HSQ posts functionalized with PS (10 kg/mol) of ~5 nm thickness, resulting in a post diameter of 30 nm.

We next considered the more general problem of how a sparse template could be designed to ensure the formation of a single-grain BCP lattice of controlled period and orientation. For a close-packed template of period L_{post}, and a close-packed BCP microdomain array of period $L < L_{\mathrm{post}}$, the commensurability between the BCP lattice and the template lattices depends on the ratio L_{post}/L. In the simplest case, where L_{post}/L is an integer, the lattice vectors of the template and the BCP sphere array are parallel, as seen in the scanning electron micrograph (SEM) images of Fig. 1, where $L_{\mathrm{post}}/L = 3$, and θ, the angle between a post lattice basis vector and a BCP microdomain lattice basis vector, is zero. For noninteger values of L_{post}/L, however, a variety of commensurate BCP lattices with orientations $\theta \neq 0$ can occur. As shown in SOM section S2, when a basis vector of the post lattice is equal to the sum of integer multiples i and j of the two 60°-oriented basis vectors of the BCP microdomain lattice,

$$L_{\mathrm{post}}/L = \sqrt{i^2 + j^2 + ij} \qquad (1)$$

then the angle θ between the post lattice and BCP microdomain lattice is given by

$$\theta = \arccos\left(\frac{2i + j}{2\sqrt{i^2 + j^2 + ij}}\right) \qquad (2)$$

We use a notation of the form $\langle i\, j\rangle$ to describe the possible commensurate BCP lattice configurations that can form within a post lattice. For example, the structures shown in Fig. 1C and 1D would be labeled as $\langle 3\ 0\rangle$ under this notation, indicating that a post lattice basis vector is parallel to a BCP microdomain lattice vector and three times as long. Figure 2A presents a map of the mathematically possible commensurate lattice configurations in which the L_{post}/L ratio was varied continuously up to $L_{\mathrm{post}}/L = 5$. For each of these $\langle i\ j\rangle$ orientations, the number of microdomains templated by each post is given by $i^2 + j^2 + ij - 1$. For example, 8 BCP microdomains are templated per post for the $\langle 3\ 0\rangle$ lattice and 26 for the $\langle 3\ 3\rangle$ lattice. The post lattice is analogous to a coincident site lattice (CSL) of the BCP lattice, in which smaller $\langle i\ j\rangle$ values correspond to smaller CSL sigma values and a greater number of coincident post and BCP lattice sites. Figure 2, B to J, shows SEM images of all the commensurate orientations that we observed within the range $L_{\mathrm{post}}/L = 1.65$ to 4.6. These orientations agree with the predictions in Fig. 2A.

BCP arrays may develop a tensile or compressive strain to fit within a template, as observed in confined spherical, cylindrical, or lamellar arrays (*18*, *24*). Confined BCP arrays are capable of exhibiting strain, with tension being easier to accommodate than compression (*25*). This compliance enables a greater number of configurations to be experimentally accessed at particular values of L_{post}/L than the discrete results in Fig. 2A would suggest. The ability of the BCP microdomain lattice to deform elastically therefore enables multiple BCP arrangements to form on a given post lattice, each with a different lattice parameter and orientation θ.

To predict the configuration(s) that will form, we consider a simple free energy model for the BCP microdomain array as a function of L_{post}/L. Given an $\langle i\ j\rangle$ configuration and a post spacing L_{post} such that the commensurate sublattice period L differs from the equilibrium spacing of the BCP on a flat substrate, L_0, the templated BCP may either assume a strained spacing and fit inside the post lattice, or form local defects and relieve the long-range stress. The free-energy change for straining the BCP lattice can be approximated under an affine deformation model by considering the effect of strain on both the conformational entropy of a polymer chain and the interfacial energy between the BCP domains. The derivation of the free-energy expression is described in SOM section S3 and leads to

$$\Delta F_{\mathrm{chain}}/kT = \frac{2Mb}{L}\sqrt{\frac{\chi_{\mathrm{AB}}}{6}} + \frac{1}{2}\left(\frac{L^2}{4Mb^2} + \frac{4b\sqrt{M}}{L} - 3\right) \qquad (3)$$

where L is the strained BCP spacing required for the BCP lattice to be commensurate with the template for the considered $\langle i\ j\rangle$ configuration, M is the number of statistical segments of the BCP chain, b is the statistical segment length, χ_{AB} is the Flory-Huggins interaction parameter (*26*, *27*), k is Boltzmann's constant, $\Delta F_{\mathrm{chain}}$ is the free energy per BCP chain, and T is the temperature. The equilibrium spacing L_0 was obtained by minimizing the free energy with respect to L. $\Delta F_{\mathrm{chain}}/k\,T$ was then calculated for all the $\langle i\ j\rangle$ combinations by substituting $L = L_{\mathrm{post}}/\sqrt{i^2 + j^2 + ij}$. These energy curves are plotted in Fig. 3A as a function of L_{post}/L_0. Each distinct $\langle i\, j\rangle$ lattice has an energy well with a minimum corresponding to the value of L_{post}/L_0

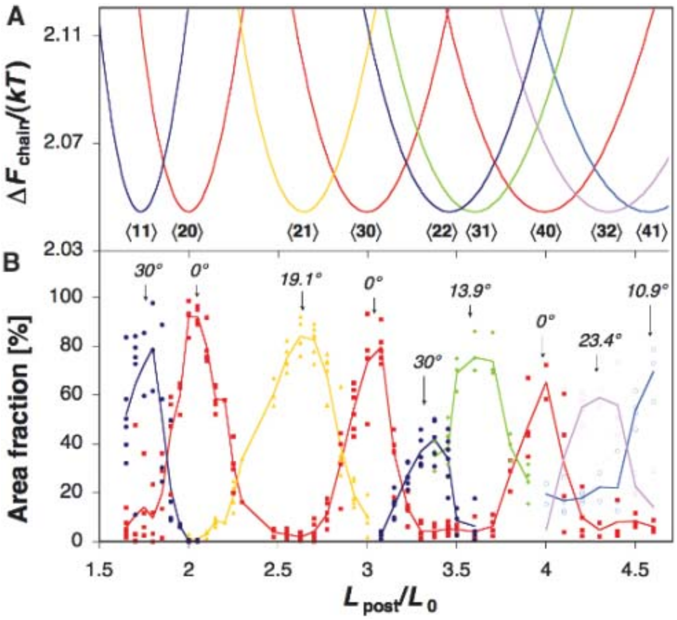

Fig. 3. (**A**) Theoretical prediction of free energy per BCP chain versus L_{post}/L_0 for each commensurate configuration. Free-energy minima occur at L_{post}/L_0 values where the commensurate condition is satisfied without straining the BCP microdomain array. (**B**) Experimental results showing the area fraction of each $\langle i\ j\rangle$ lattice versus L_{post}/L_0. Each filled circle is a data point obtained by image processing of an SEM image of a 1.3 μm by 1.3 μm square area of the templated region. This plot was generated from data collected from over 200 images of different post lattices on the same substrate. The solid lines connect the average values of the data points for a given L_{post}/L_0.

at which the post lattice is commensurate with an unstrained BCP microdomain lattice.

The predictions of this model were tested by preparing templates with the range of $L_{\mathrm{post}} = 66$ to 184 nm ($L_{\mathrm{post}}/L_0 \sim 1.65$ to 4.6) on a single substrate. Each template region consisted of posts covering a hexagonal area with a diameter of 4 μm. Having multiple templates on the same substrate ensured a uniform BCP film thickness (and hence the same L_0) across all templates with different L_{post} values. SEM images often showed more than one BCP microdomain lattice orientation within each post array. Image analysis was used to determine the (x, y) coordinates and Wigner-Seitz cells for each BCP lattice site. The area and orientation of each Wigner-Seitz cell were calculated to determine the area fraction of each BCP lattice (see SOM section S4). Figure 3B shows the area fraction of each lattice type as a function of the ratio L_{post}/L_0.

The experimental results and theoretical predictions in Fig. 3 agree closely. All the predicted lattice types, ⟨*1 1*⟩, ⟨*2 0*⟩, ⟨*2 1*⟩, ⟨*3 0*⟩, ⟨*2 2*⟩, ⟨*3 1*⟩, ⟨*4 0*⟩, ⟨*3 2*⟩, and ⟨*4 1*⟩, were observed as L_{post} varied. As expected, a particular lattice type dominated at the L_{post}/L_0 value for which the free-energy model predicted a minimum energy for that lattice type. We note that for the higher values of L_{post}/L_0, greater than ~3.5, there was no single BCP lattice orientation that completely filled the template, and all samples showed two or more different BCP lattice orientations. This effect can be understood as being due to the increasing width and number of the potential wells, such that the energy barriers separating different BCP orientations became smaller. A similar phenomenon was observed in previous work with BCP spheres packing in grooves, where N or $N + 1$ rows of spheres were observed to occur degenerately for wider grooves (*16*). For L_{post}/L_0 less than ~3.5, two lattice types also occurred simultaneously when L_{post}/L_0 was intermediate between values corresponding to energy minima.

Central to this work is the possibility of control of the final self-assembled lattice by design of the template parameters. The analysis above showed how a given BCP microdomain lattice ⟨*i j*⟩ could be selected by choice of L_{post}/L_0 and predicted what strain the BCP microdomain lattice experienced when fitting the post lattice. However, it did not address selection between degenerate lattice orientations. For example, two variants of lattice ⟨*2 1*⟩ could be formed when $L_{\mathrm{post}}/L_0 \sim 2.6$, with orientations of θ = +19° or –19°, as shown in Fig. 4A. For a 6-fold symmetric post lattice, no preference for either orientation was observed. However, a preference could be established by adding posts that occupied microdomain lattice sites of only one of the possible variants. Figure 4B shows a defect-free BCP microdomain lattice that was formed using a sparse post arrangement that selected for a unique BCP orientation. The template was formed by removing posts from the original periodic post lattice and adding posts that matched only the desired BCP ⟨*2 1*⟩ lattice variant, while maintaining the overall post areal density. Templates were also designed to reduce the incidence of one lattice type, for example ⟨*2 1*⟩, compared with a competing orientation such as ⟨*3 0*⟩, by changing the motif present at each post lattice site. Figure 4, C and D, shows how this was accomplished by a template whose motif consisted of pairs of posts. A template of single posts showed a gradual transition between ⟨*2 1*⟩ and ⟨*3 0*⟩ lattices as L_{post}/L_0 increases from 2.8 to 3.0. However, with the post pair motif, the ⟨*2 1*⟩ orientation was frustrated and occupied a smaller area fraction of the substrate, even at $L_{\mathrm{post}}/L_0 = 2.6$, where ⟨*2 1*⟩ gave the optimum lattice match with the template. Note also that the quality of the BCP microdomain lattice is relatively insensitive to the exact shape and size of the posts. Figure 4, E to G, shows well-ordered ⟨*3 0*⟩ lattices formed on three templates with identical period but differing post size and shape: 15-nm diameter, 25-nm diameter, and 45-nm × 25-nm ellipses. This tolerance is useful because it lowers the precision requirements on the template fabrication process.

In nontemplated films, the largest defect-free regions observed were on the order of 0.4 μm × 0.4 μm. On the other hand, in the templated case, defect-free arrays were observed over 2 μm or greater distances for $L_{\mathrm{post}}/L_0 < {\sim}3$. In cases where only one BCP lattice orientation existed, any defects that did occur did not disrupt the long-range orientation of the array, because the self-assembled structure remained in phase with the periodic boundary condition introduced by the template: Any point defect that occurred affected only the coordination number and spacing of nearby spherical domains. In the templated arrays, as the BCP microphase-separated, close-packed regions of domains are assumed to have nucleated around the posts, grown, and impinged; because the orientation of these small regions was fixed by the template, this locally registered nucleation of the lattice led to a macroscopically ordered BCP array, with some local regions having pairs of 5 and 7 coordinated spheres. This situation contrasts with the case of untemplated arrays, where such point defects would lead to a polycrystalline BCP microdomain lattice structure and a loss of long-range correlation. For larger L_{post}/L_0, we observed a slightly larger defect fraction, leading to coexistence of different BCP lattices and the presence of defects associated with their boundaries.

Although this work was performed using a spherical morphology PS-*b*-PDMS diblock copolymer, we expect the technique also to be appropriate for block copolymers with perpendicular cylindrical morphology, or lamellar structures. Indeed, the perpendicular cylinder morphology, which lacks the ability to adjust the positions of its domains along the direction normal to the

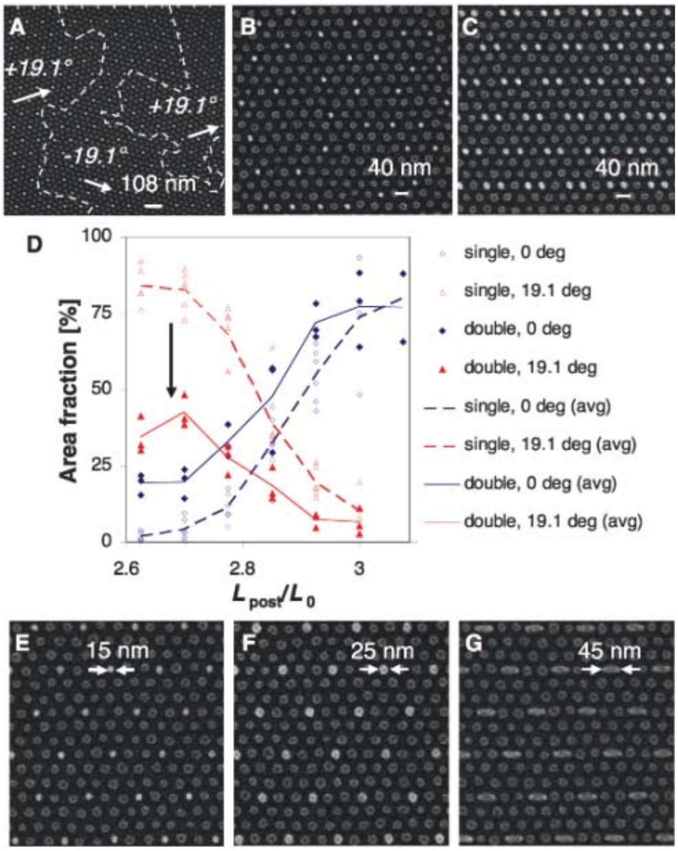

Fig. 4. (**A**) SEM image showing two degenerate ⟨*2 1*⟩ BCP microdomain lattice orientations (i.e., +19.1° and –19.1°) forming on one post lattice. The white dashed lines represent grain boundaries, and the arrows show the grain orientations. The periodic post lattice is commensurate with both orientations. (**B**) SEM image of a unique BCP microdomain lattice orientation obtained by breaking the periodicity of the post template. (**C**) A motif consisting of a pair of posts frustrates the formation of BCP lattice orientations other than the 0° ⟨*3 0*⟩ lattice. (**D**) A plot of area fraction versus L_{post}/L_0 for two template designs, single-post and double-post lattices. The double-post lattice template frustrates the 19.1° ⟨*2 1*⟩ orientation. (**E** to **G**) SEM images showing well-ordered BCP ⟨*3 0*⟩ arrays guided by pillars of different sizes [(E) and (F)] and shape (G) but with equal center-to-center spacing of 120 nm.

surface, may produce arrays with better placement accuracy than the accuracy demonstrated here, as well as higher aspect ratio features. Well-ordered block copolymer arrays may be useful as etch masks in a range of applications, such as patterned recording media, that require periodic nanoscale features covering large areas. This templating approach thus provides a method of combining top-down and bottom-up nanopatterning techniques, where information is placed on the substrate by writing a sparse lattice of posts, and the self-assembling material spontaneously populates the empty spaces on the template with a seamless nanostructured array of determined orientation and lattice spacing.

References and Notes

1. C. D. Bain *et al.*, *J. Am. Chem. Soc.* **111**, 321 (1989).
2. B. O. Dabbousi, C. B. Murray, M. F. Rubner, M. G. Bawendi, *Chem. Mater.* **6**, 216 (1994).
3. Y. Yin, Y. Xia, *Adv. Mater.* **13**, 267 (2001).
4. M. J. Fasolka, A. M. Mayes, *Annu. Rev. Mater. Res.* **31**, 323 (2001).
5. P. Mansky, P. Chaikin, E. L. Thomas, *J. Mater. Sci.* **30**, 1987 (1995).
6. M. Park, C. Harrison, P. M. Chaikin, R. A. Register, D. H. Adamson, *Science* **276**, 1401 (1997).
7. R. G. H. Lammertink *et al.*, *Adv. Mater.* **12**, 98 (2000).
8. T. Thurn-Albrecht *et al.*, *Science* **290**, 2126 (2000).
9. J. Y. Cheng *et al.*, *Adv. Mater.* **13**, 1174 (2001).
10. Y. S. Jung, C. A. Ross, *Nano Lett.* **7**, 2046 (2007).
11. C. Park, J. Yoon, E. L. Thomas, *Polymer* **44**, 6725 (2003).
12. R. A. Segalman, *Mater. Sci. Eng. Rep.* **48**, 191 (2005).
13. S. B. Darling, *Prog. Polym. Sci.* **32**, 1152 (2007).
14. R. A. Segalman, H. Yokoyama, E. J. Kramer, *Adv. Mater.* **13**, 1152 (2001).
15. J. Y. Cheng, C. A. Ross, E. L. Thomas, H. I. Smith, G. J. Vancso, *Appl. Phys. Lett.* **81**, 3657 (2002).
16. J. Y. Cheng, A. M. Mayes, C. A. Ross, *Nat. Mater.* **3**, 823 (2004).
17. L. Rockford *et al.*, *Phys. Rev. Lett.* **82**, 2602 (1999).
18. S. O. Kim *et al.*, *Nature* **424**, 411 (2003).
19. E. W. Edwards, M. F. Montague, H. H. Solak, C. J. Hawker, P. F. Nealey, *Adv. Mater.* **16**, 1315 (2004).
20. M. P. Stoykovich *et al.*, *Science* **308**, 1442 (2005).
21. J. Y. Cheng, C. T. Rettner, D. P. Sanders, H. C. Kim, W. D. Hinsberg, *Adv. Mater.*, published online 7 July 2008; 10.1002/adma.200800826.
22. R. Ruiz *et al.*, *Science* **321**, 936 (2008).
23. J. K. W. Yang, K. K. Berggren, *J. Vac. Sci. Technol. B* **25**, 2025 (2007).
24. G. J. Kellogg *et al.*, *Phys. Rev. Lett.* **76**, 2503 (1996).
25. D. J. Kinning, E. L. Thomas, *Macromolecules* **17**, 1712 (1984).
26. E. Helfand, *Acc. Chem. Res.* **8**, 295 (1975).
27. P. G. de Gennes, *Macromolecules* **13**, 1069 (1980).

28. The financial support of the National Science Foundation, the Semiconductor Research Corporation, the Nanoelectronics Research Initiative, King Abdullaziz City for Science and Technology and Alfaisal University, and the Singapore-MIT Alliance is appreciated. The Research Laboratory of Electronics Scanning-Electron-Beam Lithography Facility was used for this work. We thank M. Mondol and J. Daley for technical assistance. The authors declare no competing interests.

Supporting Online Material

www.sciencemag.org/cgi/content/full/321/5891/939/DC1
Materials and Methods
SOM Text
Figs. S1 and S2
Tables S1 and S2
References

21 April 2008; accepted 11 July 2008
10.1126/science.1159352

X-ray Diffraction and Computation Yield the Structure of Alkanethiols on Gold(111)

A. Cossaro,[1] R. Mazzarello,[2] R. Rousseau,[2]* L. Casalis,[3] A. Verdini,[1] A. Kohlmeyer,[4] L. Floreano,[1] S. Scandolo,[5] A. Morgante,[1,6]† M. L. Klein,[4] G. Scoles[2,3,7]

The structure of self-assembled monolayers (SAMs) of long-chain alkyl sulfides on gold(111) has been resolved by density functional theory–based molecular dynamics simulations and grazing incidence x-ray diffraction for hexanethiol and methylthiol. The analysis of molecular dynamics trajectories and the relative energies of possible SAM structures suggest a competition between SAM ordering, driven by the lateral van der Waals interaction between alkyl chains, and disordering of interfacial Au atoms, driven by the sulfur-gold interaction. We found that the sulfur atoms of the molecules bind at two distinct surface sites, and that the first gold surface layer contains gold atom vacancies (which are partially redistributed over different sites) as well as gold adatoms that are laterally bound to two sulfur atoms.

Self-assembled monolayers (SAMs) of alkyl sulfides on metal surfaces have many potential applications in molecular electronics, biosensors, and nanopatterning (*1*–*3*). In the high-coverage regime, the molecules are anchored to the metal substrate through their sulfur termination S, and the alkyl chains R [where R = $(CH_2)_nCH_3$] point away from the surface. Gold is the most commonly used substrate in sulfur-containing SAMs, in part because of the strong Au-S interaction.

However, despite many years of research on these systems, the nature of the Au-S interaction is still debated. Only recently has the role of the underlying Au substrate in the chemisorption of thiols been recognized, for both crystal and nanoparticle (NP) surfaces (*4*–*7*). For the short-chain limit (R = CH_3), the presence of adatoms and vacancies plays a crucial role in this process. Surface complexes wherein two S atoms are joined by an intermediate Au adatom (RS-Au-SR) have been observed experimentally at both low (*4*) and high coverage (*5*); this finding has been supported, and in certain cases predicted, by density functional theory (DFT) (*5*, *8*, *9*). Similar Au-SR motifs were recently identified at the surface of thiol-protected Au NPs (*10*).

It is natural to assume that these species are also present at the Au-SR interface of the long-chain SAMs (*11*). We now show that the energetics of the gold-SAM interface, in competition with the molecular packing forces arising from the alkyl chains at high coverage, lead to the formation of a commensurate superstructure, conventionally known as *c*(4×2) (*12*), in which the hydrocarbon chains tilt by about 30° from the surface normal. This structure yields the close packing that provides these SAMs with their technologically useful "passivating" properties (*2*, *13*–*15*).

Most of the structural models proposed so far for the *c*(4×2) superstructure have assumed that the Au(111) substrate remains flat and defect-free; they explain the superstructure in terms of nonequivalent chain torsion angles (*16*), sulfur dimerization (*15*), or differences in adsorption sites (*7*, *17*) [for a review, see (*18*)]. Only a few experimental investigations have been interpreted in terms of a more complex landscape at the interface. The alternatives included an Au atom rippling (*19*) and an increase in either the substrate roughness (*20*) or the density of defects (*21*). A recent theoretical study of intermediate-length alkyl sulfides on Au(111), which started from the results obtained in our previous work for CH_3S [methylthiol (MT)] SAMs (*5*), found that the RS-Au-SR motif is also energetically competitive for SAMs of the SC_nH_m moiety on Au(111) surfaces and is consistent with SAM corrugations seen in scanning tunneling microscopy (STM) images (*22*).

Here, we show that the existence of the RS-Au-SR structural motif for the case of longer alkanethiols is confirmed by a DFT-based theoretical simulation of the system that includes the lateral van der Waals interactions between the alkyl chains, as well as by a thorough analysis of extensive grazing incidence x-ray diffraction (GIXRD) experiments. Furthermore, DFT-based molecular dynamics (MD) simulations reveal the

---

[1] Istituto Nazionale per la Fisica della Materia–Consiglio Nazionale delle Ricerche (INFM-CNR) Laboratorio TASC, I-34012 Trieste, Italy. [2] International School for Advanced Studies, I-34014 Trieste, Italy. [3] Sincrotrone Trieste S.C.p.A., I-34012 Trieste, Italy. [4] Center for Molecular Modeling and Department of Chemistry, University of Pennsylvania, Philadelphia, PA 19104, USA. [5] Abdus Salam International Centre for Theoretical Physics and INFM/Democritos National Simulation Center, I-34014 Trieste, Italy. [6] Department of Physics, University of Trieste, I-34127 Trieste, Italy. [7] Department of Chemistry, Princeton University, Princeton, NJ 08544, USA.

*Present address: Pacific Northwest National Laboratory, Richland, WA 99352, USA.

†To whom correspondence should be addressed. E-mail: morgante@tasc.infm.it

presence at the buried interface of both Au adatoms and vacancies in the first layer, which provides, as in the case of CH_3S (*5*), a structural model that fits the x-ray data with great accuracy. We chose to focus on hexanethiol (HT) [R = $(CH_2)_5CH_3$], which is known to form a $c(4\times2)$ superstructure in coexistence with only minor amounts of the $(\sqrt{3}\times\sqrt{3})$ phase (*18*), because for shorter chains the equilibrium between the two structures has not been as clearly determined.

The nature of the potential energy landscape for SR adsorption can be understood by considering the adsorption energy E_{ad} for a variety of structures. In agreement with experiments (*23*), the E_{ad} values of HT are similar to those already reported for methylthiol (*5*, *22*, *24*). Without gold vacancies, the preferred configuration corresponds to the RS-Au-SR motif (Fig. 1), with E_{ad} = 2.0 eV (E_{ad} = 1.9 eV for MT). An on-top site is 0.5 eV higher in energy for both molecules, whereas the bridge site is 0.2 eV higher for MT but only 0.1 eV higher for HT. The energetic cost for the formation of a vacancy is about 0.5 eV for the passivated Au surface, which is more than compensated by an increase in the binding of the adsorbate. Thus, the bridge site becomes energetically competitive with that of the RS-Au-SR motif when vacancies are added; for example, one vacancy per thiol yields E_{ad} = 2.0 eV for HT and 1.8 eV for MT. Indeed, several models with both RS-bridge and RS-Au-SR motifs and one to three vacancies per $c(4\times2)$ cell are found to be energetically favorable (E_{ad} = 1.9 to 2.0 eV) (*22*). The existence of these almost isoenergetic adsorption species suggests that the potential energy surface for thiol adsorption is extremely flat; hence, both static and dynamic disorder are expected to play a key role at the Au(111) interface. It follows that, solely on the basis of $T = 0$ K calculations, DFT is unlikely to predict the difference of behavior between short- and long-chain thiols, nor to assign the structure to a single potential energy minimum.

To obtain a qualitative understanding of how the short- and long-chain species differ, we considered a series of DFT-based MD runs on HT and MT (*5*) SAMs. Small-cell MD simulations of four HT SAMs and two initial vacancies were performed at 300 and 500 K, starting from an on-top structure. The formation of an adatom added another vacancy, corresponding to a total 0.25 of an Au monolayer (ML). In these simulations, the alkyl chains hampered the dynamics; as a consequence, the amount of interconversion (Fig. 1E) between different structures was strongly reduced with respect to MT. The on-top site readily collapsed to a lower-energy structure for both MT and HT, but this process required 4 ps for HT at 500 K, versus <1 ps for MT at similar temperatures. At 300 K, the formation of RS-Au-SR species occurred for MT after 4 ps but was not observed with HT for the 10-ps duration of the simulation.

We also conducted 16-molecule simulations at 300 K starting from a repeated $(2\sqrt{3}\times3)$ superstructure consisting of eight bridges, four HT-Au-HT species, and eight vacancies. Here, bridge and HT-Au-HT configurations remained in equilibrium for the duration of the simulation. The slowing of dynamical processes can be seen in the probability plots of position distribution relative to an underlying $(\sqrt{3}\times\sqrt{3})$ cell in Fig. 1, A to D. Unimodal Au and S position distributions are found for HT, whereas those of MT are broader and often bimodal. All of the simulations show that HT chains retained a well-ordered hexagonal array with a tilt angle of about 30° with respect to the surface normal (Fig. 1F). This result is at variance with the MT case, where the surface was more dynamic and methyl groups did not show any short-range order.

Our DFT data suggest that several key aspects are needed to fit the $c(4\times2)$ structure: (i) Adatoms and vacancies should be present at the surface in similar concentrations, as found for MT (*5*), but more localized because of the hindered S-Au motion imposed by the longer alkyl chains; (ii) sulfur atoms should be located in either the bridge or RS-Au-SR configurations in roughly equal proportions; and (iii) the alkyl chains should retain a well-ordered hexagonal array with a height corrugation of about 0.6 Å.

The presence of vacancy and adatom defects on the gold surface is strongly supported by the GIXRD data. The similarities of some scans [(0, 0) and (4, –2); Fig. 2] with the equivalent ones taken on the $(\sqrt{3}\times\sqrt{3})$ MT phase (*5*) indicate that the two systems have common morphological and structural features. In particular, the drop in the x-ray reflectivity [the (0, 0) rod] of the two systems is similar and suggests analogous vacancy and adatom distribution probabilities (atomic roughness) at the molecule-gold interface.

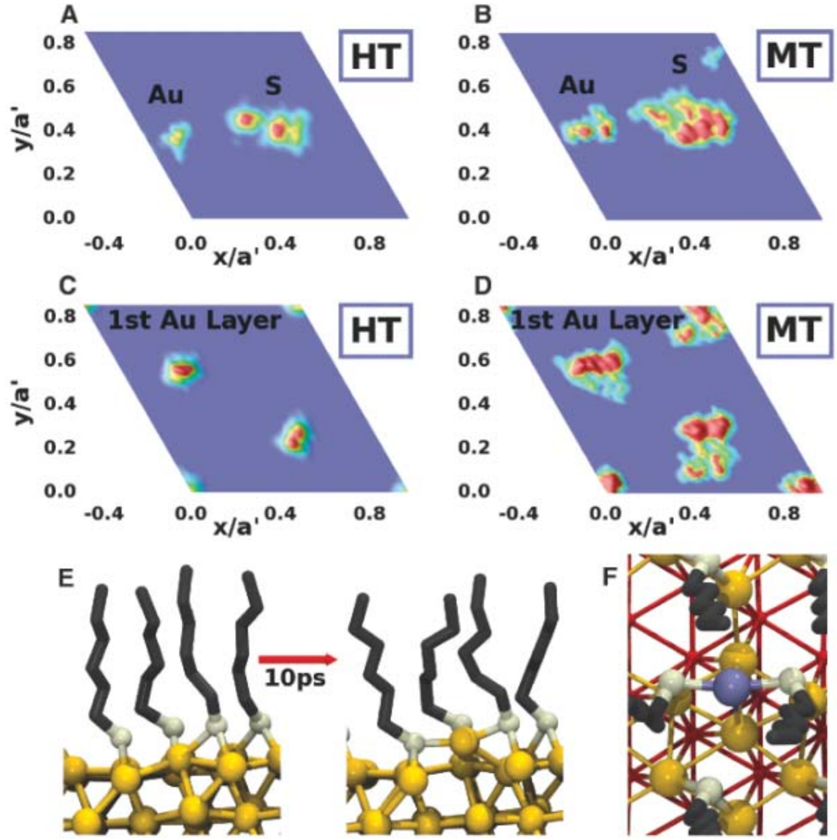

Fig. 1. Top view of the Au(111) surface and selected MD results. (**A** to **D**) Position density distributions, $P(x,y)$, for HT (16-molecule cell) and MT [from (*5*)] projected into the $(\sqrt{3}\times\sqrt{3})$ cell (a' = 4.99 Å). (A) Au adatom and S for HT, (B) Au adatom and S for MT; S shows two unimodal positions in (A) due to poor interconversion between bridge and RS-Au-SR configurations, whereas for MT (B) all positions are multimodal because of interconversion. (C) First Au layer for HT, (D) first Au layer for MT; all positions are unimodal and near the ideal lattice site for HT, but bimodal with large deviations from ideal lattice for MT. (**E**) MD snapshots separated by 10 ps at 500 K from 4-HT cell, showing formation of HT-Au-HT species (light yellow, S; black, C; dark yellow, Au); H atoms are not shown. (**F**) Average structure positions from 16-HT cell; colors are as in (E), except adatom labeled in blue and second Au layer marked in red. HT SAM exhibits hexagonal packing of the chains that are tilted off the normal by 30°, irrespective of the binding site. Au-S bond lengths are 2.45 Å for the bridge configuration, whereas lengths of 2.33 Å are found between the S and adatom in RS-Au-SR (compare with Table 1); S atoms display different heights of 2.0 Å and 2.6 Å above the surface for bridge and S-Au-S structures, respectively. This height corrugation is preserved in the height of chains.

The interface model found for the MT surface (*5*) was used as a starting point for the GIXRD analysis. As in that case, partially occupied atomic sites were adopted in the first Au layer to simulate the dynamical disorder induced by the interconversion between the two different thiol adsorption geometries plus vacancy migration. In agreement with our calculations, the fits yielded a model wherein adatoms and vacancies were delocalized over fewer sites than in the MT case. Best-fit conditions were found for a model where the topmost Au layer contained 2.8 vacancies per ($2\sqrt{3}\times 3$) unit cell (0.7 vacancies per HT), equivalent to 0.23 ML. The vacancy population was distributed over only two pairs of equivalent sites; that is, the vacancies were less delocalized than in the MT system, where we found 0.6 vacancies per ($\sqrt{3}\times\sqrt{3}$) unit cell (0.6 vacancies per MT), equivalent to 0.2 ML.

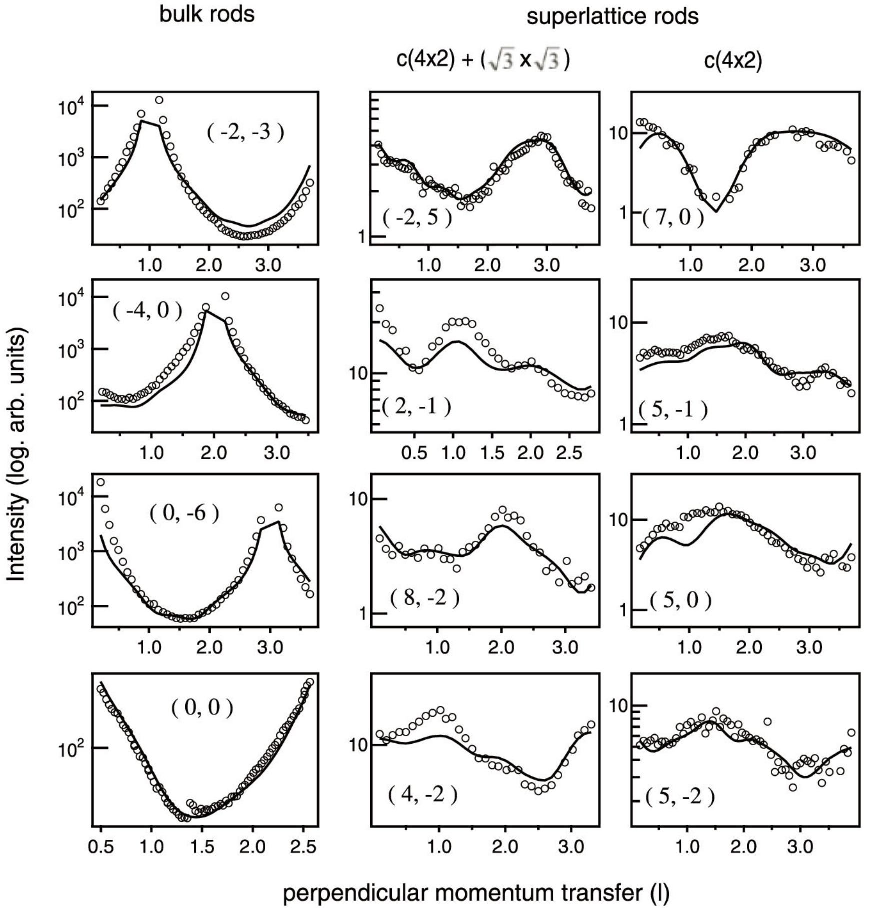

Fig. 2. X-ray diffraction rod data and fitting curves (solid lines) as a function of the perpendicular momentum transfer in l units [$l = 2\pi/c$, where c is the vector of the unit cell along the surface normal z (c = 7.06 Å)]. Bulk rods are reported in the left panel. Rods in the right panel refer to reciprocal lattice points that are common to both the $\sqrt{3}\times\sqrt{3}$ and $c(4\times 2)$ superlattices; rods at the far right refer to the $c(4\times 2)$ superlattice only. See supporting online material for further details.

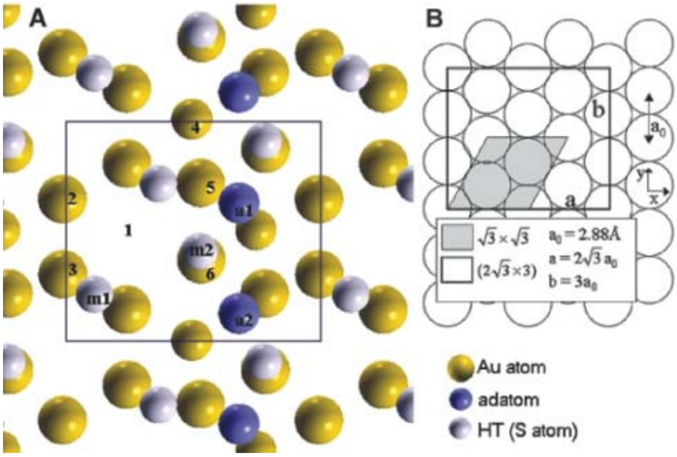

Fig. 3. (**A**) Top view of the model resulting from GIXRD fit. Only the topmost Au layer with adatoms and S atoms of molecules are indicated. (**B**) Top view of the Au(111) surface with indications of the unit cells mentioned in the text. The conventionally termed $c(4\times 2)$ corresponds to $c(2\sqrt{3}\times 4\sqrt{3})$, whose primitive cell is ($2\sqrt{3}\times 3$), as depicted in the model. Note that as a result of the zigzag geometrical constraint (see text for explanation), the two S atoms in bridge sites [labeled m1 in (A)] are inequivalent because they bridge two different Au pairs, namely the atom pairs 3-2 and 3-5. The average S-Au bond length results are 2.42 Å and 2.37 Å for RS in bridge and RS-Au-SR geometry, respectively.

The adatom was delocalized over only two symmetry-equivalent atomic sites (half a site per HT, versus one site per thiol in the case of MT), with the same 0.6 occupancy (0.3 adatoms per HT, i.e., adatom coverage of 0.1 ML), and was located in such a way that the average structure consisted of -S-Au-S-Au-S- one-dimensional zigzag chains aligned along the cell short axis (Fig. 3). Zigzag chains of this type are frequently observed in STM experiments on SAMs (*18*, *25*, *26*). With the caveat that the occupation of the adatom sites is here only partial because of dynamical fluctuations, such chains are nonetheless reminiscent of the "polymeric" zigzag motifs proposed for MT-Au(111) (*9*) and for MT on Au NPs (*6*). For the sake of clarity, only the topmost Au layer, the Au adatoms, and the S atoms are shown in Fig. 3. The second Au layer presents minor lateral ditortions, whereas the structure of the third and fourth layers is only slightly affected by the reconstruction.

The relative positions between Au adatoms and S atoms (i.e., molecules) derived by the GIXRD analysis are consistent with our theoretical model, wherein two molecules on the on-top site form the RS-Au-SR motif and the other two molecules adsorb on bridge sites. The coordinates of the first-layer Au atoms and molecules are reported in Table 1 (*27*). Although the fit of GIXRD is not very sensitive to the polar orientation of the molecular chains, the best fit yields an angle of 35° ± 10° with respect to the surface normal, in fair agreement with theory.

We note that in the common range of scanned reciprocal space, our GIXRD data are in good agreement with previous studies (*15*, *17*, *19*). With respect to previous interpretations, the model proposed here reconciles theoretical calculations and interpretation of experimental results. We found that the $c(4\times 2)$ superstructure of long-chain alkyl sulfides results from an approximate population of 2.8 vacancies and 1.2 adatoms per ($2\sqrt{3}\times 3$) cell and a limited interconversion between RS-Au-SR and RS-bridge structures. Although the SAM is ordered, the Au-S interface is affected by a dynamical disorder because of the partial delocalization of vacancies and adatoms. The constraint of the ordered SAM, driven by alkyl-chain packing, leads to a partial ordering at the interface and hence a superstructure of the ($\sqrt{3}\times\sqrt{3}$) lattice.

These findings strongly underscore the importance of the underlying Au-S interactions and support some recent single-molecule conductance measurements of the Au-dithiol system that have shown junctions differing in space and time because of both static and dynamic disorder (*28*).

Table 1. Atomic positions and occupations from GIXRD analysis. Au1 to Au6 are the Au atoms in the first Au surface layer, a1 and a2 are the Au adatoms, and m1 and m2 are the S atoms.

	Occupancy	x/a	y/b	z/c
	(±0.05)		(±0.008)	
Au1	0	—	—	—
Au2	1	−0.011	0.624	−0.045
Au3	1	−0.010	0.283	−0.025
Au4	0.6 (±0.1)	0.493	0.985	−0.022
Au5	1	0.527	0.697	+0.025
Au6	1	0.530	0.351	+0.033
a1	0.6 (±0.1)	0.678	0.610	0.294
a2	0.6 (±0.1)		a1 − b/2	
m1	—	0.113	0.193	0.265
m2	—	0.523	0.396	0.365

As a consequence of these findings, studies regarding the formation, growth, diffusion, and mechanical properties of these films may need to be revisited in order to properly account for the influence of Au-S interactions and the presence of the RS-Au-SR structural motifs. From a theoretical perspective, this gives paramount importance to the development of empirical potential models that include not only molecule-molecule interactions but explicitly the Au-SR interactions, which are often neglected. In addition, our findings indicate that the adatom structures will alter the local density of states at the Fermi energy (*18*) and will affect the interpretation of electronic and magnetic properties of these materials.

References and Notes

1. A. Ulman, *Chem. Rev.* **96**, 1533 (1996).
2. F. Schreiber, *Prog. Surf. Sci.* **65**, 151 (2000).
3. J. C. Love *et al.*, *Chem. Rev.* **105**, 1103 (2005).
4. P. Maksymovych *et al.*, *Phys. Rev. Lett.* **97**, 146103 (2006).
5. R. Mazzarello *et al.*, *Phys. Rev. Lett.* **98**, 016102 (2007).
6. H. Hakkinen *et al.*, *J. Phys. Chem. B* **110**, 9927 (2006).
7. M. Yu *et al.*, *Phys. Rev. Lett.* **97**, 166102 (2006).
8. A. Nagoya *et al.*, *J. Phys. Cond. Matter* **19**, 365245 (2007).
9. H. Grönbeck *et al.*, *J. Phys. Chem. B* **111**, 3325 (2007).
10. P. D. Jadzinsky *et al.*, *Science* **318**, 430 (2007).
11. R. L. Whetten, R. C. Price, *Science* **318**, 407 (2007).
12. The conventionally termed $c(4\times2)$ corresponds to a $c(2\sqrt{3}\times4\sqrt{3})$, whose primitive cell is $(2\sqrt{3}\times3)$.
13. R. G. Nuzzo *et al.*, *J. Chem. Phys.* **93**, 767 (1990).
14. N. Camillone *et al.*, *J. Chem. Phys.* **98**, 3503 (1993).
15. P. Fenter, A. Eberhardt, P. Eisenberger, *Science* **266**, 1216 (1994).
16. D. Anselmetti *et al.*, *Europhys. Lett.* **27**, 365 (1994).
17. X. Torrelles *et al.*, *J. Phys. Chem. B* **110**, 5586 (2006).
18. C. Vericat *et al.*, *J. Phys. Cond. Matter* **18**, R867 (2006).
19. X. Torrelles *et al.*, *Langmuir* **20**, 9396 (2004).
20. M. C. Gerstenberg *et al.*, *Phys. Rev. B* **61**, 7678 (2000).
21. M. Prato *et al.*, *J. Phys. Chem. C* **112**, 3899 (2008).
22. J. G. Wang *et al.*, *J. Phys. Chem. C* **111**, 12149 (2007).
23. D. J. Lavrich *et al.*, *J. Phys. Chem. B* **102**, 3456 (1998).
24. M. C. Vargas *et al.*, *J. Phys. Chem. B* **105**, 9509 (2001).
25. G. E. Poirier, *Langmuir* **15**, 1167 (1999).
26. A. Riposan *et al.*, *J. Phys. Chem. B* **110**, 23926 (2006).
27. In our structural determination, the distance of the Au adatoms from a Au(111) crystal plane is an integer multiple of the Au lattice constant, consistent with the Au coherent fraction of the x-ray standing wave measured in (*29*).
28. J. Ulrich *et al.*, *J. Phys. Chem. B* **110**, 2462 (2006).
29. P. Fenter *et al.*, *Surf. Sci.* **412–413**, 213 (1998).

30. We thank INFM's Parallel Computing Initiative and the San Diego Supercomputing Center (SDSC) for CPU time, and M. Tatineni at SDSC for help with getting early access to new TeraGrid resources. Supported by Ministero dell'Università e della Ricerca PRIN 2006020543 and FIRB NOMADE and by NSF grant CHE-0626354.

Supporting Online Material

www.sciencemag.org/cgi/content/full/321/5891/943/DC1
Materials and Methods
References

1 April 2008; accepted 8 July 2008
10.1126/science.1158532

Smoke Invigoration Versus Inhibition of Clouds over the Amazon

Ilan Koren,[1] J. Vanderlei Martins,[2,3] Lorraine A. Remer,[3] Hila Afargan[1]

The effect of anthropogenic aerosols on clouds is one of the most important and least understood aspects of human-induced climate change. Small changes in the amount of cloud coverage can produce a climate forcing equivalent in magnitude and opposite in sign to that caused by anthropogenic greenhouse gases, and changes in cloud height can shift the effect of clouds from cooling to warming. Focusing on the Amazon, we show a smooth transition between two opposing effects of aerosols on clouds: the microphysical and the radiative. We show how a feedback between the optical properties of aerosols and the cloud fraction can modify the aerosol forcing, changing the total radiative energy and redistributing it over the atmospheric column.

The effect of aerosols on clouds and precipitation contributes the largest uncertainty to the estimation of the anthropogenic contribution to climate change. There are two main pathways by which aerosols can change cloud properties: microphysical and radiative processes (*1*, *2*). Changes in aerosol particle concentration produce changes in the size distribution of the cloud droplets (because aerosols function as cloud condensation nuclei) and therefore affect condensation and evaporation rates, latent heat release, collision coalescence efficiency, and related cloud properties such as reflectance, lifetime, phase, size, and precipitation (*3*–*5*).

Additionally, the absorption of aerosols can change the atmospheric stability profile by heating the aerosol layer and cooling the layers below. This may stabilize shallow layers and reduce their relative humidity, suppress moisture and heat fluxes from the surface, and suppress shallow cloud formation inside or below the aerosol layer (*6*, *7*), while destabilizing the profile above the aerosol layer.

The microphysical and the radiative pathways of interaction initiate many feedbacks that add complexity to the system and have different sensitivities to the aerosol loading. Clouds are sensitive to the initial concentration and size distribution of the potential cloud condensation nuclei (CCN). For a given aerosol type (size distribution and chemistry), clouds have a logarithmic sensitivity to the amount of potential CCN (*8*–*10*). Small changes in the aerosol loading in clean environments (a low CCN concentration of ~100 CCN/cm^3) will potentially change the cloud properties (fraction, optical depth, and droplet size distribution) much more than similar changes when the cloud is polluted (a CCN concentration of ~1000 CCN/cm^3) and the effect approaches saturation. In contrast, the absorption of electromagnetic energy (mostly in the visible and near-infrared range) by aerosols has a completely different sensitivity to aerosol loading. The overall absorption of energy increases steadily with the aerosol loading, and the increasing rate depends on the diurnal cycle of solar flux (geometry), aerosol optical properties, surface albedo, and the depths of the aerosol layer (*11*).

In this paper, we develop a theoretical basis that ties together the two pathways and explores the relationships of cloud amount and vertical development to aerosol optical thickness (τ), a proxy for CCN and for the potential to absorb solar energy. We find a smooth transition between these two pathways in an observational data set obtained over the Amazon.

The (aerosol) absorption (cloud) fraction feedback (AFF) can be described as follows: Aerosol absorption of solar radiation heats the aerosol layer and cools the surface, stabilizing the temperature profile and reducing relative humidity and surface moisture fluxes (evapotranspiration). This effect reduces cloudiness. Reduced cloud coverage exposes greater areas of the aerosol layer to direct fluxes from the Sun and therefore produces more intense heating of the aerosol layer, further reducing cloudiness. This positive feedback will be balanced once the extra heating of the surface raises the surface temperature sufficiently to destabilize the profile again and to transfer the humidity concentrated

---

[1]Department of Environmental Sciences, Weizmann Institute, Rehovot 76100, Israel. [2]Department of Physics and Joint Center for Earth Systems Technology, University of Maryland Baltimore County, Baltimore, MD 21250, USA. [3]Laboratory for Atmospheres, NASA Goddard Space Flight Center, Greenbelt, MD 20771, USA.

near the surface to higher levels in the atmosphere, therefore promoting cloud formation.

If we assume that the surface temperature response is relatively slow compared to changes in the solar flux, a basic description of this system can be expressed analytically, assuming that the cloud fraction C_f depends linearly (*6*, *12*) on changes in the aerosol layer temperature T

$$C_f = C_{f0} - a(T - T_0) \qquad (1)$$

where C_{f0} and T_0 are the cloud fraction and the temperature for the pristine atmosphere and a (1/°C) is the proportionality constant that determines the sensitivity of cloud fraction to temperature changes.

For a given surface albedo and type of aerosol, the rate of change in the temperature of the aerosol layer dT/dt is proportional to the aerosol optical depth τ (*11*) and to the fraction of cloud-free sky $(1 - C_f)$ allowing direct interaction of the solar flux with aerosols

$$dT/dt = \tau Q(1 - C_f) \qquad (2)$$

where Q (°C/s) is a proportionality constant that depends on the aerosol optical properties and heat capacity of the layer.

Solving this system for T and C_f

$$T = T_0 - \frac{(1 - C_{f0})}{a}[1 - \exp(a\tau Qt)] \qquad (3)$$

and

$$C_f = 1 - (1 - C_{f0})\exp(a\tau Qt) \qquad (4)$$

yields an exponential dependence of the temperature T and the cloud fraction C_f in time. The cloud fraction depends on two components: the exponent that holds all the physical parameters (heat capacity, amount of aerosol absorption, and response of the clouds) multiplied by the initial fraction of clear sky $(1 - C_{f0})$. This shows that the radiative response of the system to a given environmental condition (a, τ, Q) in a given time depends on the initial cloud fraction C_{f0}. Smaller C_{f0} will yield a faster reduction in cloud fraction.

The logarithmic response of the cloud fraction to microphysical effects, shown in several observation and modeling studies (*8*–*10*, *13*–*16*), is simulated empirically by

$$C_{fm} = C_{fs}\left(1 - \exp\left(-\frac{1}{b}\tau\right)\right) \qquad (5)$$

where C_{fm} is the cloud fraction under the influence of the microphysical effect, C_{fs} is the saturation cloud fraction, and b is a parameter determining how fast the logarithmic effect saturates (*11*). The cloud fraction, represented empirically by Eq. 5, is the end result of all the aerosol effects and feedbacks on cloud microphysics.

Assuming the independence of the microphysical and radiative processes, and because the time response of the microphysical is much shorter than that of the radiative effects, the microphysical cloud fraction C_{fm} can approximate the initial cloud fraction C_{f0} of the radiative effect. Therefore, a superposition of the two effects yields

$$C_{ft} = 1 - (1 - C_{fm})\exp(a\tau Qt) \qquad (6)$$

The total cloud fraction C_{ft} (Eq. 6) can be approximated well by a superposition of two separate curves. One represents the microphysical effect (Eq. 5) and one the radiative effect (Eq. 4). The saturation cloud fraction from the microphysical process serves as the initial cloud fraction for the absorption processes ($C_0 = C_{fs}$). Figure 1 shows a conceptual scale analysis of the separated processes and the superposition of the two effects, as given by Eqs. 4 to 6. The equation constants were estimated by running a radiative transfer model with typical Amazonian profiles and smoke (*11*) and from previous studies (*6*, *10*, *15*, *16*). The absorption effect that appears almost linear in the plots is actually (slowly) exponentially decreasing, and the slopes that represent the reduction rate in cloud fraction due to absorption change as a function of the cloud fraction. For the same absorption properties and τ = 2, the maximum reduction in cloud fraction is 3% for $C_{f0} = 0.9$, 18% for $C_{f0} = 0.5$, and clouds have completely disappeared for $C_{f0} = 0.2$. With a smaller initial cloud fraction, the absorption effect begins to dominate at lower values of τ. The τ of maximum cloud fraction is 0.55 for $C_{f0} = 0.9$, 0.40 for $C_{f0} = 0.5$, and 0.3 for $C_{f0} = 0.2$.

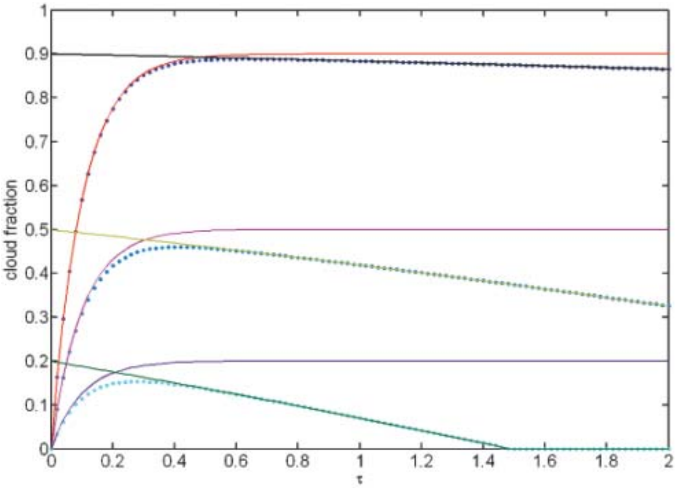

Fig. 1. Conceptual model of microphysics and absorption effects on cloud fraction for three saturation/initial cloud fractions C_{f0}. The absorption effect is simulated (Eq. 4) with characteristic time response t = 3 hours, a modest cloud fraction response to change in temperature $a = 0.05°\text{C}^{-1}$, and an atmospheric heating constant Q = 1°C per 3 hours per τ = 1.0. We ran this simulation for three cases of saturation cloud fraction C_{f0}. The overall effect is a superposition of the microphysics and absorption processes and was calculated with Eq. 6. Case 1 (red, blue, and black lines): $C_{f0} = 0.9$. The red line shows the cloud-fraction dependence on the microphysics, the black line shows the reduction due to absorption, and the dotted blue line is the overall effect. Case 2 (magenta, turquoise, and gold): $C_{f0} = 0.5$. The magenta line shows the cloud-fraction dependence on the microphysics, the gold line shows the reduction due to absorption, and the dotted turquoise line is the overall effect. Case 3 (purple, green, and light blue): $C_{f0} = 0.2$. The purple line shows the cloud-fraction dependence on the microphysics, the green line shows the reduction due to absorption, and the dotted light blue line is the overall effect.

To observe the effect of aerosol on cloud cover, we used Moderate Resolution Imaging Spectroradiometer retrievals of cloud and aerosol properties (*11*, *17*–*19*) over the Amazon in the dry season, when the region experiences consistent meteorological conditions (*11*, *20*). The cloud data, cloud fraction C_{ft}, and cloud-top pressure P (a measure proportional to the cloud vertical development) were sorted as a function of τ and averaged for each 50 samples, producing one τ, C_{ft}, and P value on the scatter plot (Fig. 2, upper row). Pixels with τ > 0.8 were removed to avoid a higher probability for misclassification of clouds and aerosols in high-τ regimes (*21*). Next, to show how the cloud fraction feedback changes the absorption rate, the same analysis was done on subsets of the data with cloud fraction <0.5 (Fig. 2, lower row).

Although the data for the pressure dependence on τ are scattered, the stronger absorption effect is noticeable for the smaller cloud fraction set with an absolute change of cloud fraction ΔC_{ft} of ~10% from the peak (maximum cloud fraction) to τ maximum, for the whole data set and ~15% for the lower cloud fraction. The relative change in cloud fraction defined as $\Delta C_{ft}/\max(C_{ft})$ is much larger for the lower fraction set (~0.47) as compared to the whole data set (~0.18). The τ at the curve maximum is shifted from ~0.3 for the whole set to ~0.2 for the lower cloud fraction set, as in the theoretical results (Fig. 1). Repetition of the same analysis on 2006 and 2007 data yielded almost identical results between 2007 and 2005. The 2006 results showed the same functional relationships but ~50% of the radiative effect at higher τ, which we attribute to very different burning and smoke conditions that year (*22*).

Cloud fraction correlates well with cloud-top height (vertical development) (Fig. 3, upper right). Therefore, by filtering out the pixels with the large C_{ft}, the data may be biased to lower, less-developed clouds. To see the combined effects of aerosols on clouds as a function of the cloud-top height, we did the following: First the data were sorted from clean to polluted by τ and divided into five equal sample subsets, from clean (blue) to most polluted (purple). Then each subset variable (τ and C_{ft}) was sorted by P and plotted, in Fig. 3, after application of a running average window of 100 samples (*10*). This processing was performed twice, once for the whole data set and once for the data filtered by $C_{\mathrm{ft}} < 0.5$.

The τ distribution versus P for the five groups is shown on the left side of Fig. 3. The polluted clouds reach higher levels of the atmosphere (*10*, *23*). We see on the C_{ft} distribution versus P for the whole data set (Fig. 3, upper right) that the boomerang shape of Fig. 2 (upper right) is apparent at most of the pressure levels, with a minimum C_{ft} for the clean case, a maximum for the medium pollution cases, and a moderate decrease in the C_{ft} for the most polluted (purple) set. For the shallowest clouds ($P > 850$ mb), the lowest C_{ft} occurs in the most polluted case.

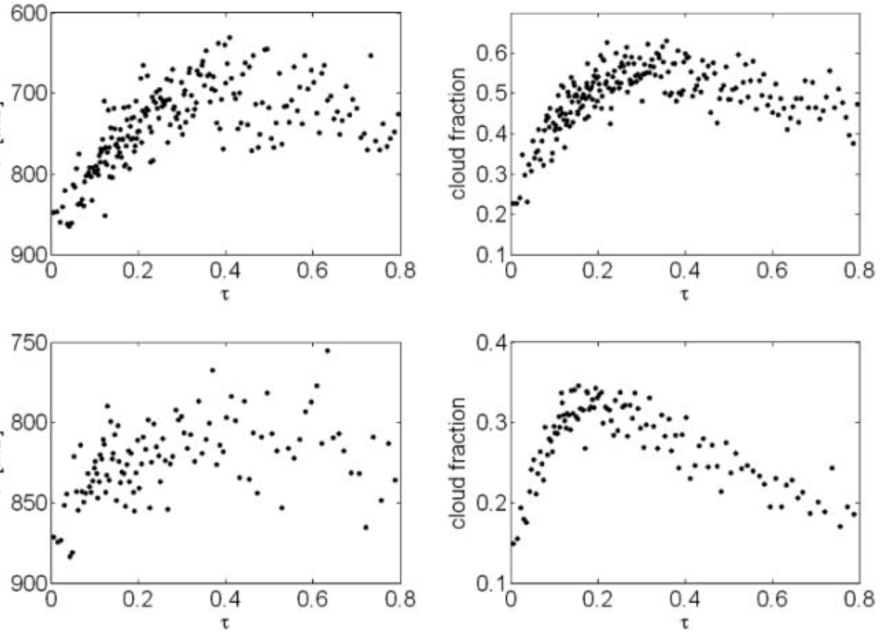

Fig. 2. Relationships between cloud properties and aerosol loading (estimated by τ). (**Left panels**) P versus τ. Lower P may indicate taller convective clouds that reach to higher levels of the atmosphere. (**Right panels**) Cloud fraction versus τ. The upper row shows all data and the lower row shows data restricted to a cloud fraction <0.5.

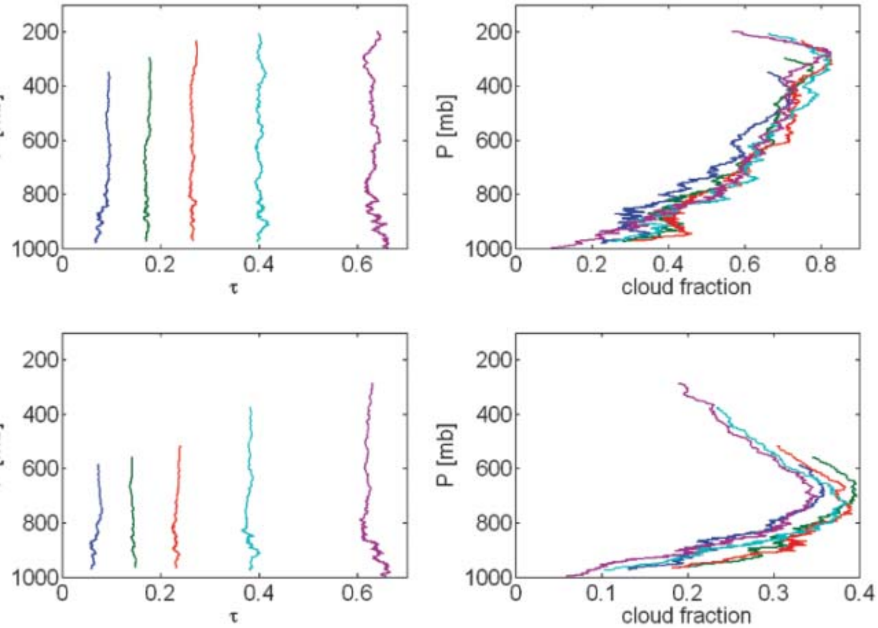

Fig. 3. Cloud fraction and τ divided into five subsets by τ, from the cleanest (blue) to the most polluted (purple) and plotted as a function of P. Results for the whole data set are plotted in the upper row; those for the subset of $C_{\mathrm{ft}} < 0.5$ are plotted in the lower row. (**Left**) The average aerosol optical depth of the five subsets versus the pressure. (**Right**) Cloud fraction for the five τ subsets versus P. The cloud fraction scale is stretched for the filtered data (lower right).

The AFF becomes apparent when results from the whole data set are compared to the subset of $C_{\mathrm{ft}} < 0.5$. By filtering out the data with large cloud fraction, we lose the higher clouds (the clean and medium cloud sets do not reach the same low pressure levels as before). A maximum in cloud fraction occurs in the middle atmosphere (700 mb), with a reduction in C_{ft} above it. The figure shows that at almost every level of the atmosphere, the most polluted set has the lowest cloud fraction. This corresponds to the deepening bend of the boomerang shape in Fig. 2 when cloud fraction is restricted by half. Additional analysis is shown in (*11*).

The theoretical construction predicts a smooth transition from a logarithmic microphysical effect dominating the trends in the lower τ values to the absorption effect that takes over as τ increases, creating a characteristic boomerang shape between cloud fraction and aerosol optical thickness. The theory predicts that the final cloud fraction is tied to the initial cloud fraction through the absorption effect of the aerosols (the AFF). Analysis of cloud data over the Amazon during the dry season of 2005 identified the same boomerang-shaped relationship between cloud fraction and aerosol optical thickness predicted by the analytical theory. In particular, we show that when the cloud fraction is restricted to less than 0.5, the absorption effect is stronger because of the larger interface between the direct solar radiation and the absorbing aerosols, as suggested by the AFF. The results are similar for higher clouds that are most likely above the smoke layer as well as clouds within the smoke layer, suggesting that over the Amazon, stabilizing the lower atmosphere and suppressing fluxes from the surface dominate the processes and can inhibit high and deep convective clouds even though the upper atmosphere can be less stable because of the smoke heating below.

The boomerang shape of C_{ft} (or P), increasing with τ until reaching a maximum and then decreasing as τ increases, makes the explanation of a superposition of the two effects—the internal (microphysical) and external (absorption)—robust. Other possible explanations such as meteorology driving both aerosol and clouds, artifacts of cloud and aerosol retrievals, or the existence of a smooth transition zone from clouds to aerosols (*24*, *25*) are not likely to produce such complicated relationships. In particular, a decrease in cloud fraction as τ increases cannot be explained by any identified retrieval artifacts or a continuum between aerosols and clouds. Furthermore, to reduce the likelihood of retrieval artifacts, the data were restricted to $\tau < 0.8$ to reduce aerosol misclassification as cloud.

The findings presented here have important implications for estimates of aerosol effects on climate forcing. Aerosols can either invigorate clouds, increasing cloud fraction and height (a result of the microphysical effects), or inhibit clouds, decreasing cloud fraction and height (a result of aerosol absorption). These two processes are superimposed, and affect clouds of varying vertical development differently. Small shallow clouds will be mostly inhibited throughout the range of τ, leading to net positive climate forcing (warming), whereas medium- and high-level clouds will be strongly invigorated in the low-τ range, leading to negative climate forcing (cooling) and the inhibition of higher aerosol loading, which again leads to warming.

Initial cloud fraction plays a critically important role in determining the balance between the two effects. Cloud fields with large cloud coverage will be affected mostly by microphysics (invigoration), whereas fields with low fraction will be inhibited strongly by aerosol absorption. This can further polarize the atmospheric regimes in such a way that the overcast mode will last longer with thicker clouds, whereas scattered cloud fields will be suppressed, resulting in smaller coverage of thinner clouds. Such redistribution of energy not only changes the climate radiative energy balance but also can change local and regional dynamics and precipitation patterns.

These results should help provide a better understanding of the processes involved in making estimates of climate forcing through cloud/aerosol interaction. Furthermore, these results will be useful in their current form for incorporation in or testing of cloud-resolving or climate models.

References and Notes

1. Y. J. Kaufman, I. Koren, *Science* **313**, 655 (2006).
2. H.-F. Graf, *Science* **203**, 1309 (2004).
3. S. Twomey, *J. Atmos. Sci.* **34**, 1149 (1977).
4. H. Jiang, G. Feingold, *J. Geophys. Res.* **111**, D01202 (2006).
5. D. Rosenfeld, *Science* **287**, 1793 (2000).
6. I. Koren, Y. J. Kaufman, L. A. Remer, J. V. Martins, *Science* **303**, 1342 (2004).
7. G. Feingold, H. Jiang, J. Y. Harrington, *Geophys. Res. Lett.* **32**, L02804 (2005).
8. G. Feingold, L. A. Remer, J. Ramaprasad, Y. J. Kaufman, *J. Geophys. Res.* **106**, 22907 (2001).
9. Y. J. Kaufman, I. Koren, L. A. Remer, D. Rosenfeld, Y. Rudich, *Proc. Natl. Acad. Sci. U.S.A.* **102**, 11207 (2005).
10. I. Koren, Y. J. Kaufman, L. A. Remer, D. Rosenfeld, Y. Rudich, *Geophys. Res. Lett.* **32**, 10.1029/2005GL023187 (2005).
11. See supporting data on *Science* Online.
12. A. S. Ackerman *et al.*, *Science* **288**, 1042 (2000).
13. Y. J. Kaufman, T. Nakajima, *J. Appl. Meteorol.* **32**, 729 (1993).
14. M. Wetzel, L. Stowe, *J. Geophys. Res.* **104**, 31287 (1999).
15. A. Khain, D. Rosenfeld, A. Pokrovsky, *Q. J. R. Meteorol. Soc.* **131**, 2639 (2005).
16. G. Myhre *et al.*, *Atmos. Chem. Phys.* **7**, 3081 (2007).
17. S. Platnick *et al.*, *IEEE Trans. Geosci. Remote Sens.* **41**, 459 (2003).
18. R. C. Levy, L. Remer, S. Mattoo, E. Vermote, Y. J. Kaufman, *J. Geophys. Res.* **112**, D13211 (2007).
19. M. D. King *et al.*, *IEEE Trans. Geosci. Rem. Sens.* **41**, 442 (2003).
20. C. A. Nobre, L. F. Mattos, C. P. Dereczynski, T. A. Tarasova, I. V. Trosnikov, *J. Geophys. Res.* **103**, 31809 (1998).
21. J. I. Brennan, Y. J. Kaufman, I. Koren, R.-R. Li, *IEEE Trans. Geosci. Remote Sens.* **43**, 911 (2005).
22. I. Koren, L. Remer, K. Longo, *Geophys. Res. Lett.* **34**, L20404 10.1029/2007GL031530 (2007).
23. M. O. Andreae *et al.*, *Science* **303**, 1337 (2004).
24. I. Koren, L. A. Remer, Y. J. Kaufman, Y. Rudich, J. V. Martins, *Geophys. Res. Lett.* **34**, L08805 (2007).
25. R. J. Charlson, A. S. Ackerman, F. A. Bender, T. L. Anderson, Z. Liu, *Tellus B Chem. Phys. Meterol.* **59**, 715 (2007).

26. This paper is dedicated to the memory of Yoram J. Kaufman, a dear friend and a brilliant scientist. This research was supported in part by the Israel Science Foundation (grant no. 1355/06), and NASA's Interdisciplinary Science Program under the direction of H. Maring. I.K. is the incumbent of the Benjamin H. Swig and Jack D. Weiler career development chair at the Weizmann Institute.

Supporting Online Material

www.sciencemag.org/cgi/content/full/321/5891/946/DC1
SOM Text
Figs. S1 to S5
References

16 April 2008; accepted 8 July 2008
10.1126/science.1159185

Ferruginous Conditions Dominated Later Neoproterozoic Deep-Water Chemistry

Donald E. Canfield,[1]* Simon W. Poulton,[2] Andrew H. Knoll,[3] Guy M. Narbonne,[4] Gerry Ross,[5] Tatiana Goldberg,[2] Harald Strauss[6]

Earth's surface chemical environment has evolved from an early anoxic condition to the oxic state we have today. Transitional between an earlier Proterozoic world with widespread deep-water anoxia and a Phanerozoic world with large oxygen-utilizing animals, the Neoproterozoic Era [1000 to 542 million years ago (Ma)] plays a key role in this history. The details of Neoproterozoic Earth surface oxygenation, however, remain unclear. We report that through much of the later Neoproterozoic (<742 ± 6 Ma), anoxia remained widespread beneath the mixed layer of the oceans; deeper water masses were sometimes sulfidic but were mainly Fe^{2+}-enriched. These ferruginous conditions marked a return to ocean chemistry not seen for more than one billion years of Earth history.

Early in Earth history, the deep oceans contained dissolved ferrous Fe, as documented by the widespread deposition of banded Fe formations (*1*). This condition expressed low atmospheric oxygen and low seawater sulfate concentrations in combination (*2*). The former limited the transport of oxygen into the deep ocean, whereas the latter limited rates of sulfide production by sulfate-reducing prokaryotes; without the low sulfate, the oceans would have been sulfidic, something like the modern Black Sea. Indeed, current models suggest that sulfidic deep-ocean conditions did become widespread around 1840 million years ago (Ma) as a result of increasing sulfate concentrations, and that this condition may have persisted through much of the Mesoproterozoic Era [1.6 to 1.0 billion years ago (Ga)] [(*3*–*6*); however, see (*7*) for another view].

The emergence of diverse animals by the end of the Neoproterozoic Era indicates a probable change to more oxic ocean and atmospheric conditions (*8*), but the course of this change is unclear. For example, despite a long-term increase in seawater oxygenation, iron formations recurred in association with globally extensive Neoproterozoic glaciations (*9*). An important pillar of the Snowball Earth hypothesis that maintains the Earth was completely covered in ice during significant periods of the Neoproterozoic, these iron formations are thought to represent the accumulation of Fe^{2+} in an ice-capped anoxic ocean (*10*, *11*). Ferruginous deep-ocean waters were also associated with the later Gaskiers ice age (580 Ma) (*12*), but deep-water oxygenation followed deglaciation, at least on the Avalon Peninsula, Newfoundland. Was this deep-water oxygenation, however, local or global, and was it the first time that oxygen pervaded deep waters during the Neoproterozoic era? Also, what is the relationship between short, ice age–associated intervals of iron deposition and the broader evolution of Neoproterozoic atmospheric and oceanic chemistry? Finally, and more broadly, how does Neoproterozoic ocean chemistry link the probable widespread occurrence of Mesoproterozoic sulfidic marine conditions with the predominantly oxic conditions of the Phanerozoic Eon (the past 542 Ma)? These outstanding issues invite further exploration of Neoproterozoic ocean chemistry.

We evaluated the redox chemistry of the marine water column by considering the speciation of Fe in well-preserved Neoproterozoic sedimentary rocks. With a calibrated Fe extraction proce-

---

[1]Nordic Center for Earth Evolution and Institute of Biology, Campusvej 55, University of Southern Denmark, 5230 Odense, Denmark. [2]School of Civil Engineering and Geosciences, Newcastle University, Drummond Building, Newcastle upon Tyne NE1 7RU, UK. [3]Botanical Museum, Harvard University, Cambridge, MA 02138, USA. [4]Department of Geological Sciences and Geological Engineering, Queen's University, Kingston, Ontario K7L 3N6, Canada. [5]Kupa'a Farm, Post Office Box 458, Kula, HI 96790, USA. [6]Geologisch-Paläontologisches Institute der Universität Münster, Corrensstrasse 24, Münster 48149, Germany.

*To whom correspondence should be addressed. E-mail: dec@biology.sdu.dk

dure (*13*), we separated Fe into forms that are biogeochemically highly reactive and those that are not. In modern marine sediments depositing under an oxic water column, highly reactive Fe (FeHR) constitutes a maximum of 38% of the total Fe pool (*14*). In contrast, sediments accumulating under an anoxic water column can have a much higher proportion of FeHR (*15*). Thus, when the ratio of FeHR to total Fe (FeHR/FeT) is greater than 0.38, deposition from an anoxic water body is indicated. In many instances, our samples come from surface outcrops (table S1), where some degree of post-exposure oxidation is difficult to discount. Most probably, however, even moderate surface weathering will have little influence on our final conclusions (*16*). Therefore, we used the principles outlined above to guide our interpretation of ancient seawater chemistry.

Fe speciation was determined for more than 700 individual samples from 34 different geologic formations, ranging in age from about 850 Ma in the middle Neoproterozoic to about 530 Ma in the Early Cambrian. Formation names, ages, an indication of depositional environment, and other notes are presented in Table 1. A complete discussion of chronology and depositional environment is presented in (*15*) and highlighted below where necessary. Speciation results, presented as FeHR/FeT, are plotted against time in Fig. 1A. We separated samples by depositional environment. Samples designated as "shallow shelf" were all deposited above the mean storm wave base. Those designated "outer shelf, shallow basin" were deposited in adjacent but deeper settings, below the mean storm wave base; these include samples deposited on the outer shelf and samples from epicontinental seas and rift basins where their position relative to the mean storm wave base had been influenced by changes in eustatic sea level. Our slope and deep basin samples are deep in an oceanographic sense, and most were deposited in passive margin settings with apparent open access to the global ocean (*15*).

Reactive Fe enrichments are common throughout the later Neoproterozoic (Fig. 1A), indicating frequent bottom-water anoxia in sediments deposited below the mean storm wave base. Reactive Fe enrichments are much less prevalent in shallow-shelf sediments, as would be expected; some of these are demonstrably oxic, such as the Bitter Springs Formation and the Quartzite and Multicolor Series from East Greenland, both associated with abundantly preserved cyanobacteria and stromatolites (*17*, *18*). Occasional high proportions of FeHR in shallow sediments could represent episodic anoxia in restricted environments such as lagoons or the preferential deposition of terrestrial Fe oxides in near-shore environments (*19*).

In some instances, in particular the Twitya Formation, western Canada, and the Tillite Group, East Greenland, our extraction results show little evidence of bottom-water anoxia (these sites are marked with asterisks on Fig. 1), but total Fe contents are greatly enriched as compared with average shale [4.7 weight percent (wt %) (*20*)]. In the Twitya Formation, FeT = 8.1 ± 2.1 wt %; in the Tillite Group, FeT = 7.23 ± 2.1 wt %. These iron concentrations generate Fe/Al ratios of 0.89 ± 0.19 in the Twitya Formation and 1.08 ± 0.18 in the Tillite Group, which are much higher than typically measured from oxic depositional settings [0.4 to 0.6 (*21*)] and, indeed, are comparable to those found in euxinic Black Sea sediments (*21*). Therefore, Fe/Al ratios in the Twitya Formation and Tillite Group provide independent evidence of Fe enrichment, and are fully consistent with enhanced Fe deposition from an anoxic water column (*21*). In these cases, high proportions of secondary silicate minerals such as chlorite indicate conversion (and thus loss) of unsulfidized FeHR during metamorphism (*21*).

As noted previously (*12*), clear evidence for the development of oxic deeper waters (represented by persistent FeHR/FeT ratios of well below 0.38) is seen at 580 Ma in the transition from the Gaskiers glaciation to the overlying Drook Formation on the Avalon Peninsula, Newfoundland. We identified similarly low FeHR/FeT in deep-water sediments from the Ediacaran upper Kaza Group, Caribou Mountains, western Canada. These sediments postdate the Marinoan glaciation, represented locally by the Old Fort Point Formation in the middle Kaza (*22*). About 1 km of stratigraphy separates our Upper Kaza samples from Old Fort rocks, and nearly 3 km more lie between the upper Kaza and basal Cambrian strata (*22*). Correlation of upper Kaza and post-Gaskiers successions is therefore possible but not certain. Nonetheless, upper Kaza data add to a growing body of evidence for widespread oxygenation of the global deep ocean around 580 to 560 Ma (*4*, *23*–*25*). Even so, oxygenation was not universal; our speciation results indicate that

Table 1. Formations, locations, and ages of the sections from this study. GC, Grand Canyon, United States; SA, South Australia; CM, Caribou Mountains, Canada; MM, Mackenzie Mountains, western Canada; YP, Yangtze Platform, South China; AP, Avalon Peninsula, Newfoundland; AB, Amadeus Basin, Australia; EG, East Greenland; SP, Spitzbergen, Svalbard; SS, Stuart Shelf, South Australia; SB, Siberia; DB, deep basin; OS, outer shelf and shallow basin, all below mean storm wave base; SS, shallow shelf, above mean storm wave base.

Formation	Location	Setting	Age range (Ma)*	Sample type
Kwangunt, Walcott Member	GC	OS	750–760	Core
Tapley Hill	SA	OS	665–697	Core
Apilla Tillite	SA	OS	698–700	Core
Brighton Limestone	SA	OS	663–665	Core
Kaza Group, Old Fort Point	CM	DB	608	Outcrop
Upper Kaza	CM	DB	580–573	Outcrop
Isaac	CM	DB	560–573	Outcrop
Twitya	MM	DB	650-697	Outcrop
Sheepbed	MM	DB	570–630	Outcrop
Doushantuo-a	YP	DB	570–631	Outcrop
Liuchapo-a	YP	DB	543–551	Outcrop
Niutitang-a	YP	DB	530–542	Outcrop
Niutitang (Xiaosi Member)	YP	DB	524–530	Outcrop
Mall Bay	AP	DB	581–583	Outcrop
Gaskiers	AP	DB	580–581	Outcrop
Drook	AP	DB	573–580	Outcrop
Briscal	AP	DB	569–570	Outcrop
Mistaken Point	AP	DB	564–567	Outcrop
Trepassey	AP	DB	562–564	Outcrop
Fermeuse	AP	DB	561–562	Outcrop
Bitter Springs	AB	SS	805	Outcrop
Quartzite Series	EG	SS	788–798	Outcrop
Multicolor Series	EG	SS	770–774	Outcrop
Limestone-Dolomite Series	EG	SS	750–755	Outcrop
Elbobreen	SP	OS	625–765	Outcrop
Dracoisen	SP	OS	620	Outcrop
Tillite Group	EG	OS	640–660	Outcrop
Canyon Formation	EG	OS	600	Outcrop
Woomera	SS	SS	625	Core
Arcoona ABC	SS	SS	620	Core
Elyuah	SS	OS	610	Core
Grants Bluff	SS	OS	590	Core
Upper Staraya	SB	SS	545	Outcrop
Kessyusa	SB	SS	540	Outcrop
Koftelv	EG	SS	530	Outcrop

*Not all sequences are well dated, so in many cases, age assignments are based on correlations with other sections, and in a few cases on educated guesses. See (*16*) for a full discussion of chronology.

parts of the deep ocean remained anoxic, even after this event.

What was the chemical nature of these anoxic deep waters? We addressed this by exploring further the speciation of FeHR. In particular, we evaluated the proportion of FeHR bound as sulfide phases (FeP/FeHR). Evidence from the Black Sea and other sulfidic (euxinic) basins shows that the ratio of FeP/FeHR commonly exceeds 0.8 under sulfidic water column conditions (*14*). When FeP/FeHR is less than this and the water column is anoxic, ferruginous water column conditions are indicated (*6*). FeP/FeHR ratios from samples in which FeHR/FeT suggests anoxia (when FeHR/FeT > 0.38) are plotted in Fig. 1. Typically, FeP/FeHR values fall well below 0.8, indicating ferruginous rather than sulfidic water-column conditions (*16*). Fe carbonates typically account for >20% of the reactive Fe pool in these samples (*15*), which rules out euxinic conditions, even in cases in which all of any original pyrite (FeS_2) was completely oxidized during weathering (*16*).

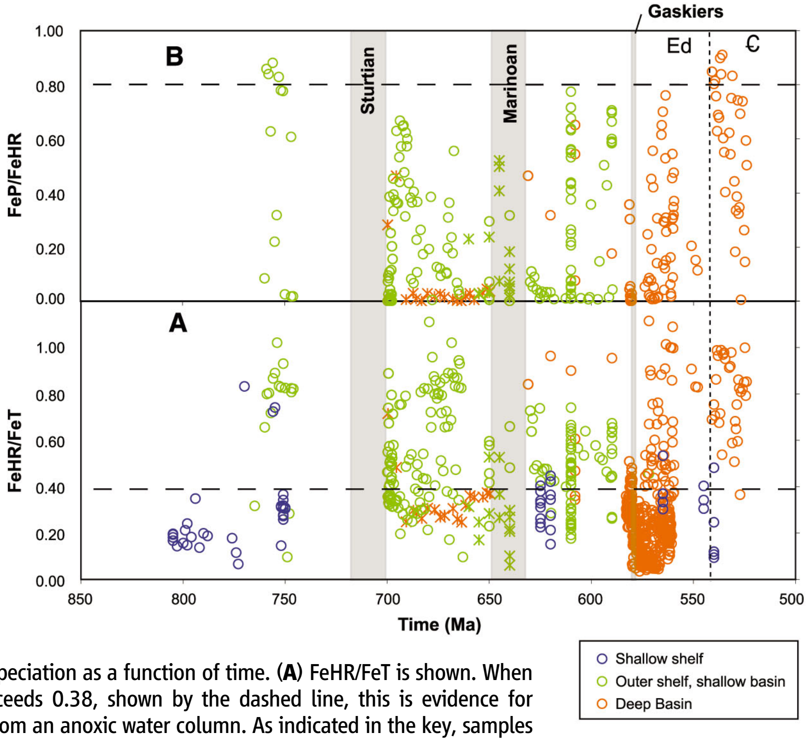

Fig. 1. Fe speciation as a function of time. (**A**) FeHR/FeT is shown. When the ratio exceeds 0.38, shown by the dashed line, this is evidence for deposition from an anoxic water column. As indicated in the key, samples are grouped into different depositional environments. Those samples designated with an asterisk have very high concentrations of total Fe and high ratios of total Fe to Al, which give independent evidence for anoxic deposition. These samples have probably lost FeHR during metamorphic conversion to unreactive Fe phases. The proportion of FeHR bound as FeS_2 is shown in (**B**). This proportion is given as FeP/FeHR. Only samples deposited below the mean storm wave base where anoxic deposition is indicated are plotted (FeHR/FeT $\geq$ 0.38). When this ratio exceeds 0.8, shown by the dashed line, deposition from a sulfidic water body is indicated, and ratios less than this are consistent with deposition from ferruginous waters. Only samples from the Chuar group and the Cambrian-Ediacaran boundary on the Yangtze Platform show evidence for sulfidic water column conditions [see SOM text for details and (*15*) for complete data]. The vertical dotted line indicates the Cambrian (Є)–Ediacaran (Ed) boundary.

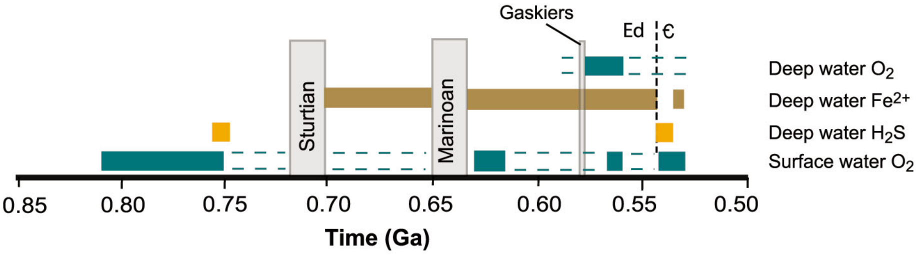

Fig. 2. A summary of our evidence of ocean-water chemical conditions through the last half of the Neoproterozoic and into the early Cambrian. Our results for deep-water chemistry do not necessarily reflect global trends but rather reflect the time course of our evidence for different deep-water chemical conditions. Deep water here means sediments deposited below the mean storm wave base. We extend evidence for deep-water oxygenation with dashed lines into pre-Gaskiers time, reflecting uncertainty in the age of the Upper Kaza Group, which shows evidence for oxic deep water. The dashed lines connecting our observations for the surface-water oxygenation reflect our belief that surface-water oxygenation was a continuous feature through the last half of the Neoproterozoic.

There are, however, two instances where sulfidic water-column conditions are clearly indicated: in parts of the Chuar Group, Grand Canyon, United States (~750 Ma), and the earliest Cambrian Niutitang Formation, Yangtze Platform, China (fig. S1). The Chuar Group deposited in a rift basin (*26*), but tidal influence is evident in shallow-water sequences (*26*), indicating, along with isotopic geochemistry and microfossil assemblages (*27*), probable open access to the global ocean. Our samples come mainly from distal black shales of the upper Walcott Member, which represents the deepest water of the Chuar Basin (*26*). As we have no other basinal samples contemporaneous with the Chuar, it is unresolved whether these sulfidic conditions represent a regional phenomenon or possible continuation of the deep marine sulfidic waters established during the Mesoproterozoic (*3*–*6*). Our finding of sulfidic bottom-water conditions at the Proterozoic-Cambrian boundary on the Yangtze platform reinforces previous studies of this region (*28*, *29*) and studies from Iran (*30*) and Oman (*31*), suggesting that sulfidic deep waters were widespread during the terminal Neoproterozoic and earliest Cambrian. Our data also show that on the Yangtze Platform, the sulfidic waters followed a long period of anoxic ferruginous conditions, and anoxic ferruginous conditions also followed this sulfidic interval (Fig. 1 and fig. S1).

A summary of our evidence for the development of Neoproterozoic ocean chemistry is given in Fig. 2. We have demonstrated that anoxic ferruginous conditions were common below the mean storm wave base in the latter half of the Neoproterozoic Era and, regionally at least, into the early Cambrian. Ferruginous waters formed in outer-shelf environments and shallow continental basins, as well as in deep basinal settings. Therefore, anoxic ferruginous marine deep waters were a general feature of later Neoproterozoic oceans, and not simply associated with Neoproterozoic glaciation, as previously thought. The ferruginous Neoproterozoic deep waters represent a return to the chemistry of much earlier, >1.8 Ga oceans (*1*).

Our new results reinforce previous work showing mid-Ediacaran (580 to 560 Ma) oxygenation of the deep ocean but show that this oxygenation was not universal and that anoxic conditions were also present. The spatial structure of this chemical mosaic is, however, unknown. We also show that, not surprisingly, shallow waters were typically well-oxygenated throughout the later Neoproterozoic and that, perhaps more surprisingly, sulfidic anoxic deep water was rare. Our sample set is large; nonetheless, it still provides only a series of geochemical snapshots in space and time. It is possible that ferruginous deep water first developed before the Sturtian ice age, that sulfidic conditions were more common, and that episodes of deep-water oxygenation preceded the Gaskiers or even earlier glaciations. Future work should resolve this.

In the modern world, and through much of the Phanerozoic Eon (*19*), marine anoxia produces sulfidic conditions. Why was this not generally true in the later Neoproterozoic? The persistence of Fe in anoxic deep waters requires that the molar flux of FeHR to the deep ocean be greater than half the flux of sulfide, the ratio needed to give excess Fe after the formation of FeS_2 (*3*). Therefore, to explain Neoproterozoic ferruginous deep-water chemistry, we must appeal to factors that either limited S input to the ocean or increased the input of Fe. Indeed, both may have been in play. Previous modeling has suggested that the surface inventory of S may have decreased in size through the Mesoproterozoic and into the Neoproterozoic because of the subduction of sedimentary sulfides deposited beneath sulfidic ocean waters (*32*). This would have made less S available for weathering and reduced the flux of sulfate to the ocean. Furthermore, Neoproterozoic sulfate concentrations were probably much less than today (*32*, *33*). Reduced sulfate levels change the redox balance during mid–ocean ridge hydrothermal circulation, resulting in an increased flux of Fe from hydrothermal fluids to the oceans (*34*). We propose that these processes, either singly or combined, produced the chemistry of later Neoproterozoic oceans.

References and Notes

1. H. D. Holland, *The Chemical Evolution of the Atmosphere and Oceans* (Princeton Univ. Press, Princeton, NJ, 1982).
2. D. E. Canfield, K. S. Habicht, B. Thamdrup, *Science* **288**, 658 (2000).
3. D. E. Canfield, *Nature* **396**, 450 (1998).
4. C. Scott *et al.*, *Nature* **452**, 456 (2008).
5. Y. Shen, A. H. Knoll, M. R. Walter, *Nature* **423**, 632 (2003).
6. S. W. Poulton, P. W. Fralick, D. E. Canfield, *Nature* **431**, 173 (2004).
7. H. D. Holland, *Philos. Trans. R. Soc. London Ser. B* **361**, 903 (2006).
8. A. H. Knoll, S. B. Carrol, *Science* **284**, 2129 (1999).
9. P. F. Hoffman, *S. Afr. J. Geol.* **108**, 557 (2005).
10. J. L. Kirschvink, *Am. Assoc. Pet. Geol. Bull.* **75**, 610 (1991).
11. P. F. Hoffman, A. J. Kaufman, G. P. Halverson, D. P. Schrag, *Science* **281**, 1342 (1998).
12. D. E. Canfield, S. W. Poulton, G. M. Narbonne, *Science* **315**, 92 (2007).
13. S. W. Poulton, D. E. Canfield, *Chem. Geol.* **214**, 209 (2005).
14. R. Raiswell, D. E. Canfield, *Am. J. Sci.* **298**, 219 (1998).
15. Materials and methods are available as supporting material on *Science* Online.
16. We have tried to avoid weathering by collecting in the field the freshest material possible, and furthermore, we have removed any further evidence of weathering when preparing samples for crushing, powdering, and eventual chemical extraction. Still, oxidative weathering is possible in some cases. The main influence of weathering will be to oxidize reduced-Fe phases such as FeS_2 and Fe carbonates to Fe oxides. In this way, the total reactive Fe content of the sample would be little affected, although the distribution of phases might be. For this reason, some of our FeS_2 and Fe carbonate contents may be underestimated. This is probably the worst for our Sheepbed samples, although all of these still retain FeS_2, sometimes in appreciable amounts (*15*). Nonetheless, even if we underestimate the FeS_2 and Fe carbonate contents of some samples because of weathering, our evaluation of the nature of ocean chemistry, and particularly the dominance of ferruginous conditions, is generally not affected. This is because although some Fe carbonate may have been lost, the Fe carbonate contents of most samples are high enough to preclude deposition in a sulfidic water column—even making the extreme (and probably incorrect) assumption that all Fe oxides represent oxidized FeS_2.
17. D. Z. Oehler, J. H. Oehler, A. J. Stewart, *Science* **205**, 388 (1979).
18. J. W. Green, A. H. Knoll, K. Swett, *Geol. Mag.* **126**, 567 (1989).
19. S. W. Poulton, R. Raiswell, *Am. J. Sci.* **302**, 774 (2002).
20. K. K. Turekian, K. H. Wedepohl, *Geol. Soc. Am. Bull.* **72**, 175 (1961).
21. T. W. Lyons, S. Severmann, *Geochim. Cosmochim. Acta* **70**, 5698 (2006).
22. G. M. Ross, J. D. Bloch, H. R. Krouse, *Precambrian Res.* **73**, 71 (1995).
23. D. A. Fike, J. P. Grotzinger, L. M. Pratt, R. E. Summons, *Nature* **444**, 744 (2006).
24. K. A. McFadden *et al.*, *Proc. Natl. Acad. Sci. U.S.A.* **105**, 3197 (2008).
25. Y. Shen, T. Zhang, P. F. Hoffman, *Proc. Natl. Acad. Sci. U.S.A.* **105**, 7376 (2008).
26. C. M. Dehler *et al.*, *Sediment. Geol.* **141**, 465 (2001).
27. K. E. Karlstrom *et al.*, *Geology* **28**, 619 (2000).
28. T. Goldberg, H. Strauss, Q. Guo, C. Liu, *Palaeogeogr. Palaeoclimatol. Palaeoecol.* **254**, 175 (2007).
29. B. Lehmann *et al.*, *Geology* **35**, 403 (2007).
30. H. Kimura, Y. Watanabe, *Geology* **29**, 995 (2001).
31. S. Schroder, J. P. Grotzinger, *J. Geol. Soc. London* **164**, 175 (2007).
32. D. E. Canfield, *Am. J. Sci.* **304**, 839 (2004).
33. L. C. Kah, T. W. Lyons, T. D. Frank, *Nature* **431**, 834 (2004).
34. L. R. Kump, W. E. Seyfried Jr., *Earth Planet. Sci. Lett.* **235**, 654 (2005).

35. For financial support, we thank Danmarks Grundforskningsfond, the Natural Environment Research Council (research fellowship to S.W.P.), NSF (Division of Earth Sciences grant 0420592 to A.H.K.), and the Natural Sciences and Engineering Research Council of Canada Discovery Grant, Northwest Territories Scientist's License. We acknowledge the help of N. P. James and T. K. Kyser; the insightful comments of D. Johnston; and the expert technical assistance of L. Salling, M. Andersen, and E. Hammarlund.

Supporting Online Material
www.sciencemag.org/cgi/content/full/1154499/DC1
Materials and Methods
Figs. S1 and S2
Table S1
References

21 December 2007; accepted 2 July 2008
Published online 17 July 2008;
10.1126/science.1154499
Include this information when citing this paper.

Plant Immunity Requires Conformational Charges of NPR1 via S-Nitrosylation and Thioredoxins

Yasuomi Tada,[1] Steven H. Spoel,[1] Karolina Pajerowska-Mukhtar,[1] Zhonglin Mou,[1]* Junqi Song,[1] Chun Wang,[2] Jianru Zuo,[2] Xinnian Dong[1]†

Changes in redox status have been observed during immune responses in different organisms, but the associated signaling mechanisms are poorly understood. In plants, these redox changes regulate the conformation of NPR1, a master regulator of salicylic acid (SA)–mediated defense genes. NPR1 is sequestered in the cytoplasm as an oligomer through intermolecular disulfide bonds. We report that S-nitrosylation of NPR1 by *S*-nitrosoglutathione (GSNO) at cysteine-156 facilitates its oligomerization, which maintains protein homeostasis upon SA induction. Conversely, the SA-induced NPR1 oligomer-to-monomer reaction is catalyzed by thioredoxins (TRXs). Mutations in both NPR1 cysteine-156 and TRX compromised NPR1-mediated disease resistance. Thus, the regulation of NPR1 is through the opposing action of GSNO and TRX. These findings suggest a link between pathogen-triggered redox changes and gene regulation in plant immunity.

Innate immune responses are evolutionarily conserved among plants and animals (*1*, *2*) and are often associated with changes in cellular oxidative and reductive states. In plants, these redox changes are sensed by the NPR1 protein, a master regulator of defense gene expression (*3*). In unchallenged plants, NPR1 resides in the cytoplasm as an oligomer maintained through redox-sensitive intermolecular disulfide bonds. Upon pathogen challenge, the plant defense signaling molecule salicylic acid (SA) increases and changes the cellular redox state, leading to reduction of the disulfide bonds in NPR1. Reduction of the NPR1 oligomer releases monomer that translocates to the nucleus where it activates the expression of a battery of *pathogenesis-related* (*PR*) genes (*4*). Mutations at residues Cys^{82} and Cys^{216} in NPR1 result in increased monomer accumulation, constitutive nuclear localization, and NPR1-mediated gene expression in the absence of pathogen challenge (*3*). On the basis of these results, it has been proposed that conformational changes in NPR1 (that is, oligomer-monomer exchange) regulate its nuclear translocation and activity (*3*).

Oligomerization of proteins through intermolecular disulfide bonds is unusual under reductive cytosolic conditions (*5*). However, treatment with SA not only induced NPR1 monomer release but also facilitated oligomerization in wild-type plants (fig. S1A). Similar results were obtained with biologically active NPR1 fused with green fluorescent protein (NPR1-GFP) (*4*) or with tandem affinity purification tag (NPR1-TAP) (fig.

S2), driven by the constitutive 35*S* promoter (Fig. 1A). On the basis of these observations, we hypothesized that a catalyst of cysteine thiol oxidation was involved in the formation of the NPR1 oligomer. To search for cellular oxidants facilitating NPR1 oligomerization, we established a cell-free assay in which total protein extract from *35S::NPR1-GFP* plants was treated with the reducing agent dithiothreitol (DTT) to partially convert the NPR1-GFP oligomer to monomer. Removal of DTT by dialysis allowed reformation of the oligomer as shown by a decrease in monomer, while the total protein amount remained constant (Fig. 1B). These data suggest that, depending on the cellular environment, NPR1 switches between the oligomeric and monomeric states.

Using the cell-free assay shown in Fig. 1B, we tested the effect of hydrogen peroxide (H_2O_2) as well as the nitric oxide (NO) donors sodium nitroprusside (SNP) and *S*-nitrosoglutathione (GSNO) on the NPR1 oligomer-monomer equilibrium, because these oxidants accumulate during innate immune responses (*6*, *7*). The treatment of protein extracts with H_2O_2 and SNP had no effect on NPR1 conformation (Fig. 1C). In contrast, GSNO, a natural NO donor, markedly facilitated oligomerization of NPR1 as shown by the disappearance of the monomer while total NPR1 levels remained unchanged (Fig. 1C). This is consistent with the finding that unlike SNP, the treatment of plant cell cultures with GSNO caused protein S-nitrosylation (*8*), a process in which NO is covalently attached to a reactive cysteine thiol to form an *S*-nitrosothiol (SNO) (*9*). To further confirm this specific effect of GSNO, NPR1 activity was monitored in the GSNO reductase knockout mutant *atgsnor1-3*, which displays increased S-nitrosylation activity (*7*). We found that SA-induced monomerization of the endogenous NPR1 (fig. S1B) and nuclear translocation of monomeric NPR1-GFP were inhibited (Fig. 1D). NPR1 oligomer accumulated to higher levels in the *atgsnor1-3* mutant as compared to the wild type (fig. S1B). Accordingly, SA-induced expression of the NPR1-dependent defense gene *PR-1* was also suppressed in *atgsnor1-3* plants (Fig. 1E). These data suggest that GSNO affects the conformation of NPR1 and consequently its activity in innate immunity.

In *Arabidopsis*, pathogen infection induces an increase in cellular SNO levels, and elevated SNO levels in *atgsnor1-3* are associated with enhanced susceptibility to disease (*7*). The effect of GSNO on NPR1 oligomerization, together with the fact that some of the cysteine residues in NPR1 are critical for oligomer formation (*3*), suggests that one or more NPR1 cysteine thiols are directly modified by GSNO. To test this, we examined whether NPR1 is S-nitrosylated in planta, using the biotin-switch method (*10*), which specifically detects S-nitrosylated proteins (*11*). Total protein was extracted from SA-treated wild-type and transgenic *35S::NPR1-GFP* plants and then incubated with or without ascorbate, which specifically reduces SNO groups (*10*). The resulting free thiols were then covalently coupled to biotin-HPDP (biotin–*N*-[6(biotinamido)hex1]-3′-(2′-pyridyldithio)propionamide) and immunoprecipitated with streptavidin beads. Immunoblot analysis revealed that both endogenous NPR1 and transgenic NPR1-GFP were pulled down only in ascorbate-treated samples, indicating that these proteins were specifically S-nitrosylated in vivo (Fig. 2A). Treatment with SA enhanced the S-nitrosylation of NPR1 (fig. S3A). We then applied the biotin-switch method to our cell-free assay and found that GSNO increased S-nitrosylation of NPR1, whereas SNP was ineffective in this respect (Fig. 2B). These results suggest that GSNO may facilitate NPR1 oligomerization directly through thiol S-nitrosylation.

Previously, we demonstrated that Cys^{82}, Cys^{150}, Cys^{155}, Cys^{160}, and Cys^{216} in and adjacent to the BTB/POZ domain of NPR1 (fig. S4) are important in the oligomer-monomer exchange (*3*). This suggests that the N-terminal half of NPR1 is sufficient for oligomerization. We purified recombinant protein containing the hexa-histidine (6xHis)–tagged N-terminal half of NPR1 (His6-NH, residues 1 to 246) and examined its oligomerization properties in response to NO donors. As compared with the control, treatment of purified His6-NH with GSNO resulted in increased S-nitrosylation and multimerization of His6-NH (Fig. 2C). Similar results were obtained with the NO donor diethylamine-NO (DEA/NO) (fig. S3, B and C), further supporting a role of SNO in stimulating NPR1 oligomerization. In contrast, SNP treatment failed to S-nitrosylate and multimerize His6-NH (Fig. 2C). Thus, at least one NO-sensitive cysteine lies within the 246 N-terminal

---

[1]Department of Biology, Post Office Box 90338, Duke University, Durham, NC 27708, USA. [2]Institute of Genetics and Developmental Biology, Chinese Academy of Sciences, Beijing 100101, China.

*Present address: Department of Microbiology and Cell Science, Post Office Box 110700, University of Florida, Gainesville, FL 32611, USA.

†To whom correspondence should be addressed. E-mail: xdong@duke.edu

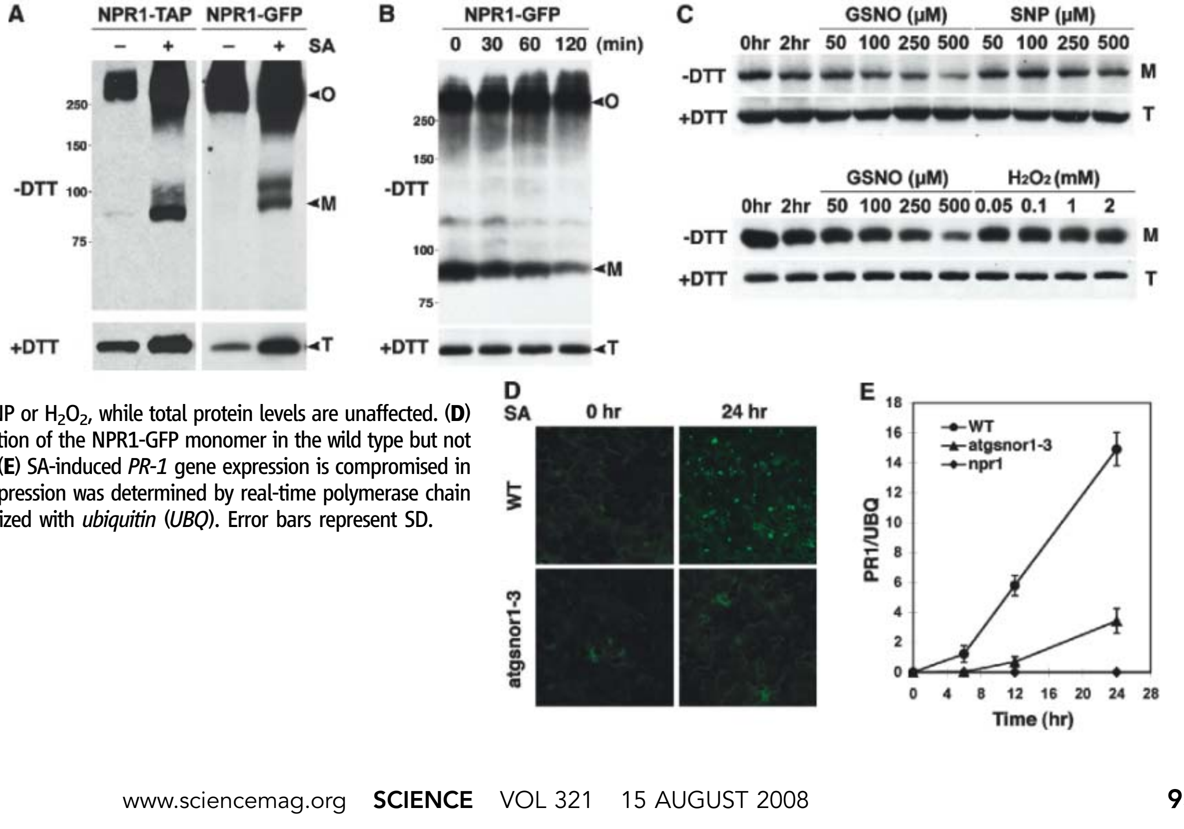

Fig. 1. GSNO facilitates the oligomerization of NPR1. (**A**) SA induces NPR1 monomer release as well as oligomerization. Nonreducing (–DTT) and reducing (+DTT) immunoblot analysis revealed oligomeric (O), monomeric (M), and total (T) NPR1. (**B**) Reoligomerization of monomeric NPR1-GFP in a cell-free assay. (**C**) NPR1 monomer disappears with an increasing concentration of GSNO but not of SNP or H_2O_2, while total protein levels are unaffected. (**D**) SA induces nuclear localization of the NPR1-GFP monomer in the wild type but not in the *atgsnor1-3* mutant. (**E**) SA-induced *PR-1* gene expression is compromised in *atgsnor1-3* plants. *PR-1* expression was determined by real-time polymerase chain reaction (PCR) and normalized with *ubiquitin* (*UBQ*). Error bars represent SD.

residues of NPR1. Indeed, mutation of Cys^{156} abolished both GSNO-triggered S-nitrosylation (Fig. 2D) and oligomerization (Fig. 2E). Taken together, these findings indicate that GSNO S-nitrosylates NPR1 at Cys^{156}. Similar to the SNO-mediated disulfide bond formation in myoglobulin (*12*, *13*), S-nitrosylation of Cys^{156} may directly facilitate disulfide linkage between NPR1 monomers. Computational modeling of the NPR1 BTB domain according to previously published BTB crystal structures (*14*, *15*) predicts that one or more disulifide bonds may form between Cys^{150}, Cys^{155}, Cys^{156}, and Cys^{160} in the NPR1 oligomer (fig. S5). Alternatively, S-nitrosylation of Cys^{156} may lead to conformational changes in NPR1 that favor oligomerization as reported for SNO-facilitated dynamin oligomerization (*16*).

Transformation of *35S::NPR1C156A-GFP* into mutant *npr1* plants consistently resulted in constitutive nuclear fluorescence relative to uninduced *35S::NPR1-GFP* plants (Fig. 3A), suggesting that the NPR1C156A-GFP (C156A, Cys^{156}→Asp^{156}) protein does not form oligomers as efficiently as wild-type protein. Although NPR1C156A-GFP protein still formed oligomers before induction, it lacked any SA-induced increase in oligomerization (Fig. 3B), indicating that Cys^{156} is required for SNO-facilitated oligomerization in vivo.

The effect of the *NPR1C156A* mutation on plant defense was demonstrated when plants were challenged by *Pseudomonas syringae* pv. *maculicola* ES4326 (*Psm* ES4326). Consistent with the nuclear accumulation of NPR1C156A-GFP (Fig. 3A) and its normal interaction with TGA transcription factors (fig. S6), untreated *35S::NPR1C156A-GFP* plants showed enhanced resistance to this pathogen as compared with *35S::NPR1-GFP* plants (Fig. 3C). However, unlike *35S::NPR1-GFP*, treatment with SA for 48 hours did not enhance resistance in *35S::NPR1C156A-GFP* plants. These findings indicate that SNO-Cys^{156}-mediated oligomerization is necessary to maintain NPR1 homeostasis upon SA activation. Immunoblot analysis (Fig. 3D) and GFP fluorescence (Fig. 3A) showed that the NPR1C156A protein was depleted 48 hours after SA treatment, explaining the compromised pathogen resistance.

To counter the effect of SNO-facilitated NPR1 oligomerization, reducing agents must be engaged upon SA induction to catalyze the NPR1 oligomer-to-monomer switch. To identify such agents, we performed pull-down assays with recombinant His6-NH protein and identified two thioredoxins (TRXs), TRX-h3 and TRX-h5 (Fig. 4A). Among the eight cytosolic *TRX-h* genes in *Arabidopsis*, *TRX-h5* is substantially up-regulated upon infection with *P. syringae* (*17*), whereas *TRX-h3* is the most highly constitutively expressed *TRX-h* (*18*) (fig. S7). In a reverse experiment, we covalently trapped NPR1 using mutant TRXs (TRX-h3M and TRX-h5M), in which the second catalytic cysteine was changed to serine to prevent the completion of substrate reduction (*19*) (fig. S8A). Pull-down experiments showed that the NPR1-binding affinity of TRX-h was inversely correlated with its enzymatic activity (fig. S8, B and C), suggesting that TRX-h is the enzyme catalyzing NPR1 oligomer reduction. The transient nature of this interaction made it difficult to examine the NPR1/TRX-h interaction in vivo. Therefore, we fixed the enzyme-substrate intermediate [see supporting online material (SOM) text] and coimmunoprecipitated TRX-5h with NPR1-TAP (Fig. 4B). Treatment with SA further increased the interaction. In vivo interaction of

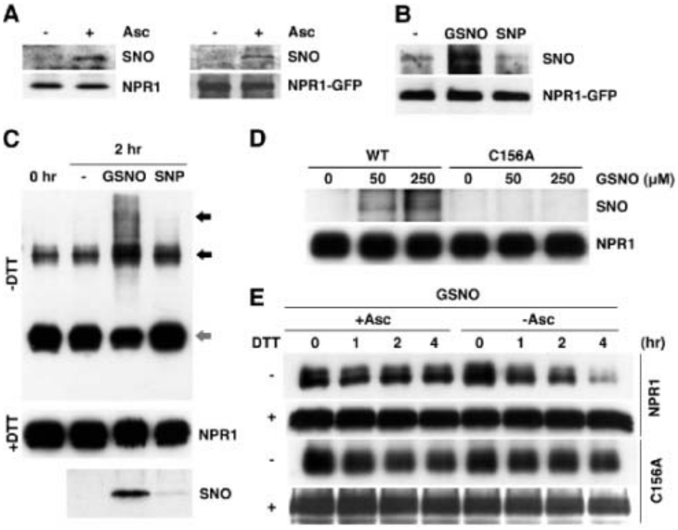

Fig. 2. S-nitrosylation of Cys^{156} facilitates the assembly of NPR1 oligomer. (**A**) SA induces S-nitrosylation of endogenous NPR1 and the NPR1-GFP proteins in vivo. Sodium ascorbate (Asc) was used to specifically detect S-nitrosylated (SNO) NPR1. Equal loading was verified with antibodies against NPR1 or NPR1-GFP. (**B**) GSNO, but not mock (–) or SNP treatment, induces S-nitrosylation of NPR1-GFP in plant extracts. S-nitrosylated NPR1-GFP was detected with the biotin-switch assay. An antibody against NPR1-GFP was used to verify equal loading. (**C**) GSNO, but not mock (–) or SNP treatment, induces S-nitrosylation and multimerization (black arrows) of recombinant His6-NH (NPR1 residues 1 to 246) monomer (gray arrow). Equal loading was verified with an antibody to NPR1. (**D**) Cys^{156} is the principal site of S-nitrosylation in NPR1. Recombinant His6-NH and His6-NH-C156A proteins were incubated with different GSNO concentrations, and S-nitrosylation was detected by the biotin-swich assay. Equal loading was verified with an antibody to NPR1. (**E**) The C156A mutation impairs GSNO-induced oligomerization. Recombinant His6-NH and His6-NH-C156A proteins were treated with GSNO and with (+) or without (–) sodium ascorbate. Subsequently, monomers were allowed to re-oligomerize for the indicated times. Monomeric (–DTT) and total (+DTT) proteins were detected with an antibody to NPR1.

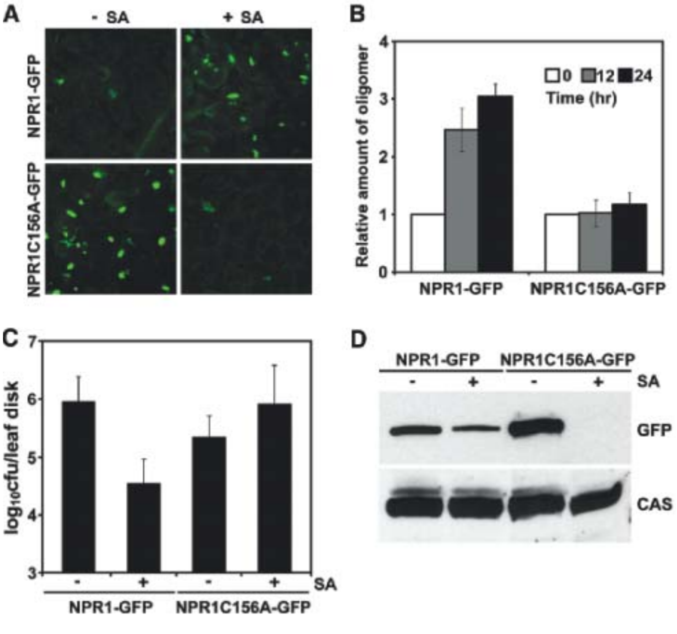

Fig. 3. S-nitrosylation of Cys^{156} is essential for NPR1 protein homeostasis and SA-induced disease resistance. (**A**) SA treatment reduces the constitutive nuclear fluorescence of NPR1C156A-GFP. (**B**) The C156A mutation impairs NPR1 oligomer formation in response to SA. *35S::NPR1-GFP* and *35S::NPR1C156A-GFP* plants were treated with SA. The relative amount of NPR1 oligomer was determined by calculating densitometric ratios between induced and uninduced samples and normalized against total NPR1 protein. Error bars represent SD (n = 3 measurements). (**C**) SA-induced resistance is compromised in NPR1C156A plants. Error bars represent 95% confidence limits (n = 8 xxxxx). cfu, colony-forming unit. (**D**) SA treatment decreases NPR1C156A protein levels. *35S::NPR1-GFP* and *35S::NPR1C156A-GFP* plants were treated with (+) or without (–) SA for 48 hours. NPR1-GFP protein was detected with an antibody to GFP, and equal loading was verified with an antibody against constitutively expressed Ca^{2+}-sensing receptor (CAS).

TRX-h5 with NPR1 suggests that it may be involved in catalysis of the NPR1 oligomer-to-monomer reaction during plant defense. We added recombinant TRX-h5 to cell lysates containing NPR1-GFP oligomer and showed that, compared to the control, the amount of NPR1-GFP monomer increased within 15 min of incubation (Fig. 4C).

TRX-h5 was required in vivo for SA-induced monomer release (Fig. 4D). Both *TRX-h3* and *TRX-h5* were required for full induction of *PR* genes (Fig. 4E). Additionally, in the *trx* mutants, NPR1-dependent systemic acquired resistance (SAR) against *Psm* ES4326, triggered after local inoculation of avirulent *Psm* ES4326/*avrRpt2*, was partially impaired (Fig. 4, F and G). Consistently, the TRX reductase knockout mutant *ntra* (*20*), which blocks the regeneration of cytosolic TRXs, showed a complete loss of SAR.

Our study provides a molecular mechanism to explain how cellular redox changes during pathogen challenge lead to transcriptional reprogramming and disease resistance (fig. S9). We propose that redox signals are conveyed through SNO and cytosolic TRXs, which directly catalyze the NPR1 oligomer-monomer exchange. Upon pathogen challenge, SA induces *TRX-5h* to catalyze the release of NPR1 monomer and possibly prevent oligomerization of some of the monomer. Induction also leads to S-nitrosylation of NPR1, which facilitates oligomerization to prevent protein depletion. SA-induced NPR1 oxidation and reduction may occur sequentially as the application of inducers of SAR results in transient oxidative and reductive fluctuations (*3*). To test this hypothesis, we treated plants with a combination of the translation inhibitor cycloheximide, the proteasome inhibitor MG115, and SA. In the absence of protein synthesis and degradation, SA-induced monomer accumulation was highest 12 hours after treatment. However, after 16 hours, NPR1 monomer re-oligomerized (fig. S10). The biological importance of controlling NPR1 homeostasis is demonstrated by the impaired immune responses of the *NPR1C156A* and *trx* mutants.

NO has long been proposed to be involved in responses to plant hormones, salt stress, ultraviolet light, and pathogens (*21*, *22*). However, our knowledge of NO direct targets and its molecular effects on gene expression is limited. Recently, S-nitrosylation of *Arabidopsis* peroxiredoxin II E was shown to cause the accumulation of peroxynitrite (ONOO$^-$) (*23*). Increased ONOO$^-$ levels induced tyrosine nitration of proteins, which might activate the plant defense mechanism known as the hypersensitive response. Even though the in vivo concentration and subcellular localization of GSNO have yet to be determined, genetic studies with *Arabidopsis atgsnor* mutants indicated that GSNO functions as an endogenous signal in plant defense responses (*7*). The identification of NPR1 as a direct target of S-nitrosylation may explain the phenotype of the *atgsnor* mutants. In mammals, NO functions as an anti-inflammatory signal by S-nitrosylating IκB kinase β (IKKβ) (*24*), the catalytic subunit of IKK, required for activation of the transcriptional immune regulator nuclear factor κB (NF-κB). S-nitrosylation of IKKβ inactivates IKK and retains NF-κB in the cytoplasm. This response is reminiscent of NPR1 oligomerization by S-nitrosylation, which prevents NPR1 from entering the nucleus (fig. S9). This suggests that redox-mediated transcription regulatory mechanisms are a common feature of immune responses in both plants and animals.

References and Notes

1. J. D. Jones, J. L. Dangl, *Nature* **444**, 323 (2006).
2. T. Nurnberger, F. Brunner, B. Kemmerling, L. Piater, *Immunol. Rev.* **198**, 249 (2004).
3. Z. Mou, W. Fan, X. Dong, *Cell* **113**, 935 (2003).
4. M. Kinkema, W. Fan, X. Dong, *Plant Cell* **12**, 2339 (2000).
5. K. J. Dietz, *Int. Rev. Cytol.* **228**, 141 (2003).
6. M. Delledonne, Y. Xia, R. Dixon, C. Lamb, *Nature* **394**, 585 (1998).
7. A. Feechan *et al.*, *Proc. Natl. Acad. Sci. U.S.A.* **102**, 8054 (2005).
8. C. Lindermayr, G. Saalbach, J. Durner, *Plant Physiol.* **137**, 921 (2005).
9. J. S. Stamler *et al.*, *Proc. Natl. Acad. Sci. U.S.A.* **89**, 444 (1992).
10. S. R. Jaffrey, H. Erdjument-Bromage, C. D. Ferris, P. Tempst, S. H. Snyder, *Nat. Cell Biol.* **3**, 193 (2001).
11. M. T. Forrester, M. W. Foster, J. S. Stamler, *J. Biol. Chem.* **282**, 13977 (2007).
12. D. T. Hess, A. Matsumoto, S. O. Kim, H. E. Marshall, J. S. Stamler, *Nat. Rev. Mol. Cell Biol.* **6**, 150 (2005).
13. D. R. Arnelle, J. S. Stamler, *Arch. Biochem. Biophys.* **318**, 279 (1995).
14. K. F. Ahmad *et al.*, *Mol. Cell* **12**, 1551 (2003).
15. X. Li *et al.*, *Cancer Res.* **59**, 5275 (1999).
16. G. Wang, N. H. Moniri, K. Ozawa, J. S. Stamler, Y. Daaka, *Proc. Natl. Acad. Sci. U.S.A.* **103**, 1295 (2006).
17. C. Laloi, D. Mestres-Ortega, Y. Marco, Y. Meyer, J. P. Reichheld, *Plant Physiol.* **134**, 1006 (2004).

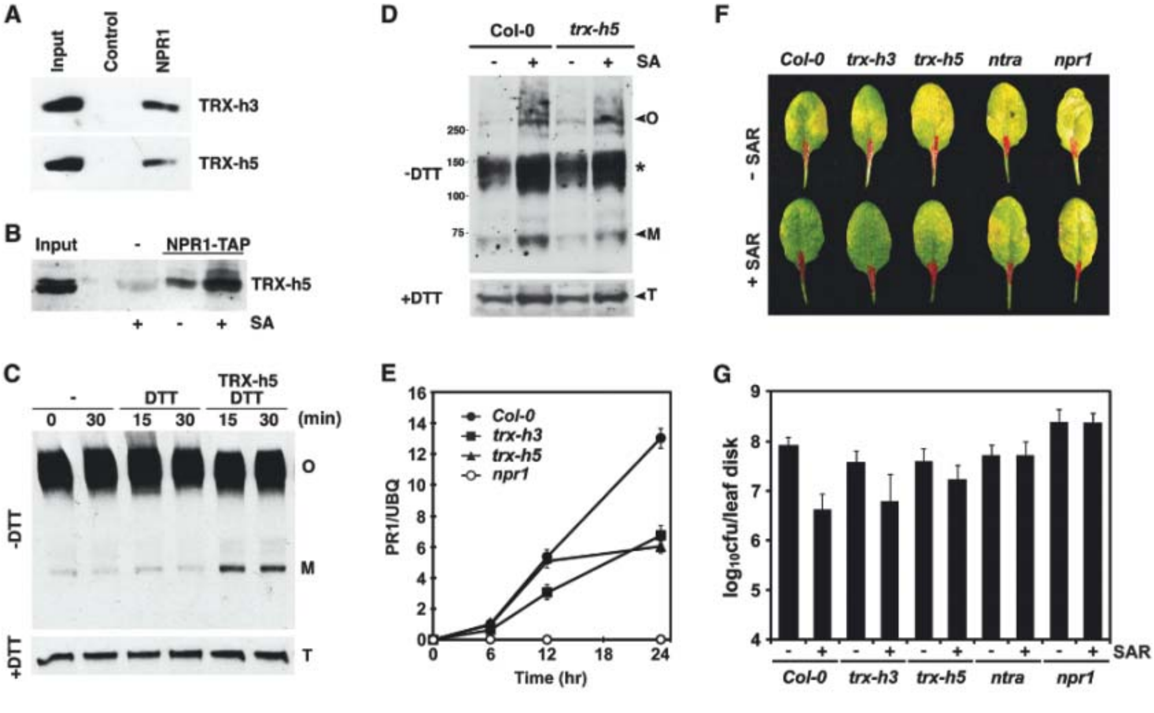

Fig. 4. TRX is a redox mediator of NPR1. (**A**) Immobilized His6-NH pulls down TRXs in vitro. TRXs were detected with protein-specific antibodies. (**B**) *35S::NPR1-TAP* transformed and untransformed plants were treated with or without SA. SA treatment enhanced coimmunoprecipitation of TRX-h5 with NPR1-TAP as detected by an antibody to TRX-h5. (**C**) NPR1-GFP oligomer (O) is reduced to monomer (M) by TRX-h5 in vitro. DTT (0.33 mM) was added to recycle TRX activity. Detection of total (T) NPR1-GFP verified equal loading. (**D**) In vivo reduction of NPR1 oligomer to monomer in Col-0 and *trx-h5* plants 12 hours after SA treatment. Nonreducing (–DTT) and reducing (+DTT) SDS-polyacrylamide gel electrophoresis were performed in parallel, and the endogenous NPR1 was detected with an antibody to NPR1. The asterisk indicates possible NPR1 dimer complexes. (**E**) SA-induced *PR-1* gene expression is compromised in *trx* mutants. *PR-1* expression was determined by real-time PCR and normalized with *ubiquitin* (*UBQ*). Error bars represent SD. (**F** and **G**) Induction of SAR significantly decreased disease symptoms and *Psm* ES4326 growth in Col-0 plants but not in the *trx*, *ntra*, and *npr1-1* mutants. Error bars represent 95% confidence limits (*n* = 8 samples).

18. J.-P. Reichheld, D. Mestres-Ortega, C. Laloi, Y. Meyer, *Plant Physiol. Biochem.* **40**, 685 (2002).
19. K. Motohashi, A. Kondoh, M. T. Stumpp, T. Hisabori, *Proc. Natl. Acad. Sci. U.S.A.* **98**, 11224 (2001).
20. J. P. Reichheld *et al.*, *Plant Cell* **19**, 1851 (2007).
21. A. Besson-Bard, A. Pugin, D. Wendehenne, *Annu. Rev. Plant Biol.* **59**, 21 (2008).
22. S. Grun, C. Lindermayr, S. Sell, J. Durner, *J. Exp. Bot.* **57**, 507 (2006).
23. M. C. Romero-Puertas *et al.*, *Plant Cell* **19**, 4120 (2007).
24. N. L. Reynaert *et al.*, *Proc. Natl. Acad. Sci. U.S.A.* **101**, 8945 (2004).
25. We thank M. Delledonne, J. Stamler, K. Murase, A. Matsumoto, K. Kojima, and K. Ozawa for discussion; G. Loake and N. Spivey for the *atgsnor1-3* mutant and microarray data on *TRXs*, respectively; J. Yoo for technical assistance; Y. Meyer and Z. Pei for TRX-h3/TRX-h5 and CAS antibodies, respectively; and J. Stamler, J. Siedow, Z. Pei, and N. Spivey for critiquing the manuscript. Supported by a grant from NIH (1R01-GM69594) to X.D.

Supporting Online Material
www.sciencemag.org/cgi/content/full/1156970/DC1
Materials and Methods
Figs. S1 to S10
References

25 February 2008; accepted 2 July 2008
Published online 17 July 2008;
10.1126/science.1156970
Include this information when citing this paper.

A Global View of Gene Activity and Alternative Splicing by Deep Sequencing of the Human Transcriptome

Marc Sultan,[1]* Marcel H. Schulz,[2,3]* Hugues Richard,[2]* Alon Magen,[1] Andreas Klingenhoff,[4] Matthias Scherf,[4] Martin Seifert,[4] Tatjana Borodina,[1] Aleksey Soldatov,[1] Dmitri Parkhomchuk,[1] Dominic Schmidt,[1] Sean O'Keeffe,[2] Stefan Haas,[2] Martin Vingron,[2] Hans Lehrach,[1] Marie-Laure Yaspo[1]†

The functional complexity of the human transcriptome is not yet fully elucidated. We report a high-throughput sequence of the human transcriptome from a human embryonic kidney and a B cell line. We used shotgun sequencing of transcripts to generate randomly distributed reads. Of these, 50% mapped to unique genomic locations, of which 80% corresponded to known exons. We found that 66% of the polyadenylated transcriptome mapped to known genes and 34% to nonannotated genomic regions. On the basis of known transcripts, RNA-Seq can detect 25% more genes than can microarrays. A global survey of messenger RNA splicing events identified 94,241 splice junctions (4096 of which were previously unidentified) and showed that exon skipping is the most prevalent form of alternative splicing.

Global analysis of gene expression has mostly relied on RNA hybridization on high-density arrays (*1*–*3*), allowing the profiling of many tissues (*4*, *5*) but detecting only specific sequences. Whole-genome tiling arrays theoretically allow the capture of much of the complexity of the transcriptome (*6*, *7*), but they ignore splice-junction information and are associated with high costs and difficulties in data analysis. Arrays that specifically detect alternative splicing (AS) events (*8*, *9*) have been hampered by issues of completeness and specificity.

Digital transcript-counting approaches overcome many of the inherent limitations of array-based systems and bypass problems inherent to analog measurements, including complex normalization procedures and limitations in detecting low-abundance transcripts. However, the expressed sequence tag (EST) approach, providing partial sequences of individual cDNA clones, is sensitive to cloning biases and has high costs. Serial analysis of gene expression (*10*) and massively parallel signature sequencing (*11*) are also costly and cannot be used for splicing events.

The potential of RNA-Seq (short-read high-throughput sequencing) was first demonstrated by the polony multiplex analysis of gene expression, allowing the detection of 0.3 RNA copies per cell (*12*). Illumina-based RNA-Seq technology has recently been applied to yeast and *Arabidopsis thaliana* (*13*–*15*), providing transcriptome surveys at single-nucleotide resolution.

We present here a snapshot of the human transcriptome at base-pair resolution via RNA-Seq (*16*). Briefly, poly(A) RNA was extracted from human embryonic kidney (HEK) 293T and Ramos B cells and used to generate double-stranded cDNA using random hexamers as primers. The double-stranded DNA was sheared by sonication for preparing the sequencing libraries according to the Illumina protocol (*16*). Illumina deep sequencing was used to generate 27–base pair (bp) reads from replicate samples for each cell line. Reads were mapped to the human genome (hg18, National Center of Biotechnology Information build 36.1) using the Eland software, allowing up to two mismatches (*16*). Of the total reads, 50% matched to unique genomic locations, 16 to 18% showed multiple matches, and 25% had no match to the genome (Table 1 and table S1). 6000 reads from HEK were adenovirus or SV40 sequences, reflecting the origin of this cell line. We mapped the unique reads to known genes based on both ENSEMBL (*17*) and RefSeq/ElDorado (Tables 1 and 2 and tables S1 and S2) (*16*): 80% of the unique reads mapped to known exons.

Digital expression levels were normalized (NE values) by taking into account the theoretical number of unique 27-mers (sequences that are 27 bases long) contained in each exon and the total number of reads generated in each experiment (table S2) (*16*).

To assess whether NE values were a reliable indicator of gene activity, we correlated these values with hypophosphorylated RNA polymerase II (PolIIa) occupancy, used as a landmark of transcription initiation (*18*). For HEK, we identified PolIIa islands by chromatin immunoprecipitation and sequencing (ChIP-Seq) (*16*). Figure 1 shows that the density of PolIIa reads correlates positively with gene expression levels. However, in contrast to a study reporting that 37% of the silent promoters contained PolII islands (*19*), we observed virtually no PolIIa near the promoters of silent genes. This apparent contradiction is most likely due to the higher sensitivity of RNA-Seq, detecting gene expression that would be scored silent with arrays (see below). The current model of the pre-recruitment of PolIIa at the promoter of silent genes (*20*) may be lacking sufficiently sensitive expression data. In Fig. 1, the peaks for low and moderately expressed genes exhibit a more pronounced shoulder than those for highly expressed genes. This might reflect the presence of a large preinitiation complex where PolIIa is parked upstream of the transcription start site (TSS) of the less active genes until activated, or the existence of alternative TSS. In clustering the reads specifying PolIIa-bound regions, we identified 9710 PolIIa-bound regions, of which 80% associated to known promoters (table S3) (*16*). Of the remaining 1936 PolIIa-bound regions, more than half were supported by Cap-analysis of gene expression (CAGE) tags (*21*), and 567 were either located within genes or less than 1 kb upstream of the next annotated transcript, representing putative alternative promoters.

In evaluating the dynamic range and sensitivity of RNA-Seq, we predicted the number of genes present within a cell type by applying a Poisson mixture statistical analysis on the number of reads mapped to genes (*16*, *22*). We showed that the performances achieved for each sample corresponded to a gene identification score of 83 to 92% for HEK and 70 to

---

[1] Department of Vertebrate Genomics, Max Planck Institute for Molecular Genetics, Ihnestrasse 73, 14195 Berlin, Germany. [2] Department of Computational Molecular Biology, Max Planck Institute for Molecular Genetics, Ihnestrasse 73, 14195 Berlin, Germany. [3] International Max Planck Research School for Computational Biology and Scientific Computing. [4] Genomatix Software Gmbh, Bayerstrasse 85a, 80335 Munich, Germany.

*These authors contributed equally to this work.

†To whom correspondence should be addressed. E-mail: yaspo@molgen.mpg.de

84% for B cells (fig. S1) (*16*). RNA-Seq was significantly more sensitive than microarrays on the same RNA source, detecting 25% more genes (Fig. 2, A and B) (*16*). Genes detected exclusively by RNA-Seq were in the lowest range of NE values, corresponding to rarely expressed genes (Fig. 2B). Between 100 and 200 transcripts were only detected on arrays (Fig. 2A), exhibiting intensity values close to the background and hence increasing the chance that those were artefacts, a known issue in array analysis (*23*, *24*).

We analyzed expression of all ENSEMBL genes expressed simultaneously on both platforms and in both cell lines (7043 genes) (*16*). Correlation between the two platforms was high [Pearson correlation coefficient (PCC) = 0.88], in spite of a compression effect resulting in smaller ratios in microarrays (Fig. 2C). This feature was reported previously and is partly due to the limited dynamic range of array experiments (*23*–*26*). Microarrays detected 3421 genes whose levels of expression were different between the two cell lines, whereas RNA-Seq detected 4376 such genes. The overlap between the two approaches was 2685 genes (table S4). For the latter, levels-of-expression differences between the two cell lines were highly concordant between the two approaches (PCC, 0.94; Kendall rank correlation coefficient, 0.75).

We carried out a functional analysis of differentially regulated and cell type–specific genes (table S5) (*16*). Among the 55 genes most over-

Table 1. Summary of genes, splice junctions, and previously unrecognized TUs identified by RNA-Seq; mapping of the read for the merged lanes.

Mapping summary	HEK 293	B cells
Total reads	8,638,919	7,682,230
Low-quality reads	234,160	194,999
Reads with multiple matches	1,546,361	1,324,770
Reads with unique matches	4,640,112	3,895,643
Reads mapping to annotated RNAs (ENSEMBL + Eldorado)	3,712,476	2,902,387
ENSEMBL genes with at least five reads	12,567	10,668
ENSEMBL genes with at least one read	14,963	13,739
Reads in intronic clusters	38,598	44,781
ENSEMBL genes with intronic read clusters	1445	1409
Introns with read clusters	1862	1847
Reads with no match to the genome	2,218,286	2,266,818
Reads aligned to splice junctions	307,904	229,453
Identified junctions	78,880	62,596
(expected)	(81,302)	(66,981)
Genes (at least five reads) with junctions	10,292	8655
Genes (at least one read) with junctions	10,558	8910
Genes (at least one read) with previously unknown junctions	2078	1732
Previously unknown junctions	2397	1965
Previously unknown junctions identified by less than one read	203	182

Table 2. Summary of genes, splice junctions, and previously unrecognized TUs identified by RNA-Seq; features associated to the 352 previously unknown intergenic TUs identified in HEK and B cells.

Features	Number of TUs
CAGE tags	253
CAGE tags + PolIIa-bound regions	22
PolIIa-bound regions (without CAGE)	2
Contain repeated elements	50
Match to human pseudogenes	9
Identity to human full-length cDNA	28
Similarity to nonhuman sequences	16
Similarity to known proteins	121
Exon-intron structure	24
Uniquely expressed in HEK293	134
Uniquely expressed in B cells	153
Expressed in both cell types	66

Fig. 1. Correlation of RNA PolIIa read density with TSS. The plot shows the number of RNA PolIIa reads relative to the TSS for all 12,567 ENSEMBL-expressed genes distributed in five groups: (i) high (4189 genes with 0.0889 < NE < 47.8; red); (ii) moderate (4189 genes with 0.0263 < NE < 0.0889; green); (iii) low (4189 genes with 0.0003 < NE < 0.0263; blue); (iv) uncertain (2396 genes with one to four reads; pink); and (v) silent (7333 genes with no read; black) expression. bps, base pairs.

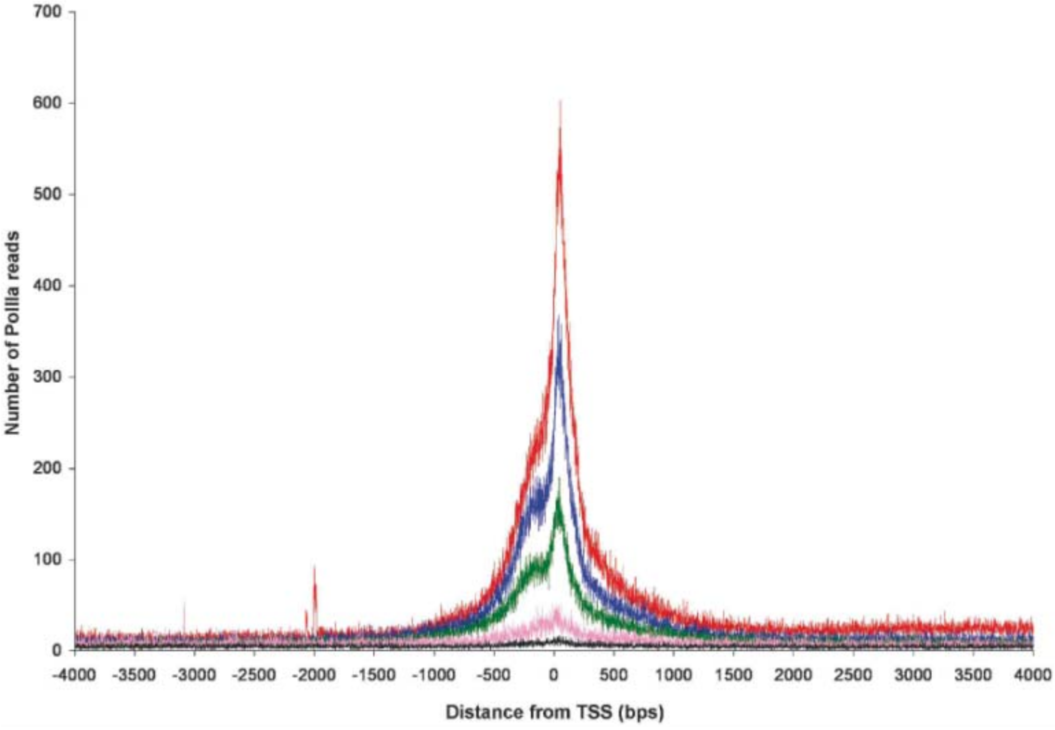

expressed in the lymphoma cells, we found an enrichment of factors involved in Ras protein signal transduction pathway and immune system processes. The 271 most active genes specific to B cells were significantly enriched for MHC class II receptors and factors belonging to the CD38, LCK (lymphocyte-specific protein tyrosine kinase), ZAP70 (zeta chain–associated protein kinase 70 kD), CD19, and BLK (B lymphoid tyrosine kinase) signaling pathways. Of the 2669 genes specific to HEK, the top 1000 were enriched for factors involved in DNA binding and for cytoskeletal proteins binding the extracellular matrix.

To more precisely define 5′ and 3′ gene boundaries and identify all transcribed regions, we analyzed reads in intronic and intergenic regions. We assessed noise levels by means of a Poisson model of the noncoding part of the genome; the probability to observe more than four random reads per 100-bp window was $<10^{-12}$ (*16*). We scanned the DNA regions 5 kb upstream and downstream of all transcripts, only considering read clusters that displayed a density similar to that of the neighboring exon. Approximately 500 genes were extended at the 5′ end by at least 50 bp (table S6), 300 of which were supported by CAGE tag(s) (*21*), and ~300 genes were extended at their 3′ end in each cell line. Only 15% of these were common to both cell types. Furthermore, we searched for read clusters in the 39% of the genome corresponding to intronic regions, using a stringent algorithm that required a minimum of five reads in 100-bp sliding windows (*16*). We identified 2751 and 2862 clusters (average length of 191 bp, totaling 38,598 and 44,781 reads) located within 1862 and 1847 introns of 1445 and 1409 genes in HEK and B cells, respectively (table S7). A large fraction (87%) of these clusters mapped to human ESTs (table S7). ESTs were used to infer previously unidentified exons of known genes when clusters and genes mapped to the same EST (e.g., 1500 and 1358 previously unknown exons were connected within 916 and 834 genes in HEK and B cells, respectively). Of these exons, 70% were unique to one cell type and likely to be differentially spliced. Remaining clusters could either represent rare exons not represented in ESTs or hallmarks of transcriptional activity in both the DNA strands.

Similarly, we scanned for transcriptional activity in the 58% of the human genome corresponding to intergenic regions (*16*). We identified 531 clusters totaling 13,805 reads distributed in 280 intergenic regions (table S8). Using inferences from EST mapping, 237 out of 531 (237/531) clusters collapsed within 58 transcribed units (TUs), whereas 294/531 clusters remained individual units, identifying altogether 352 TUs (size range: 92 to 182 bp) (table S8). An exon-intron structure was found in 24 TUs, based on a minimal distance of 1 kb between two clusters (*16*). Additional attributes supporting the importance of the previously unrecognized TUs—including CAGE tags, PolIIa-Bound regions, and similarities to known expressed sequences identified by BlastN and BlastX (*27*) analysis—are summarized in Table 2 (details in table S8).

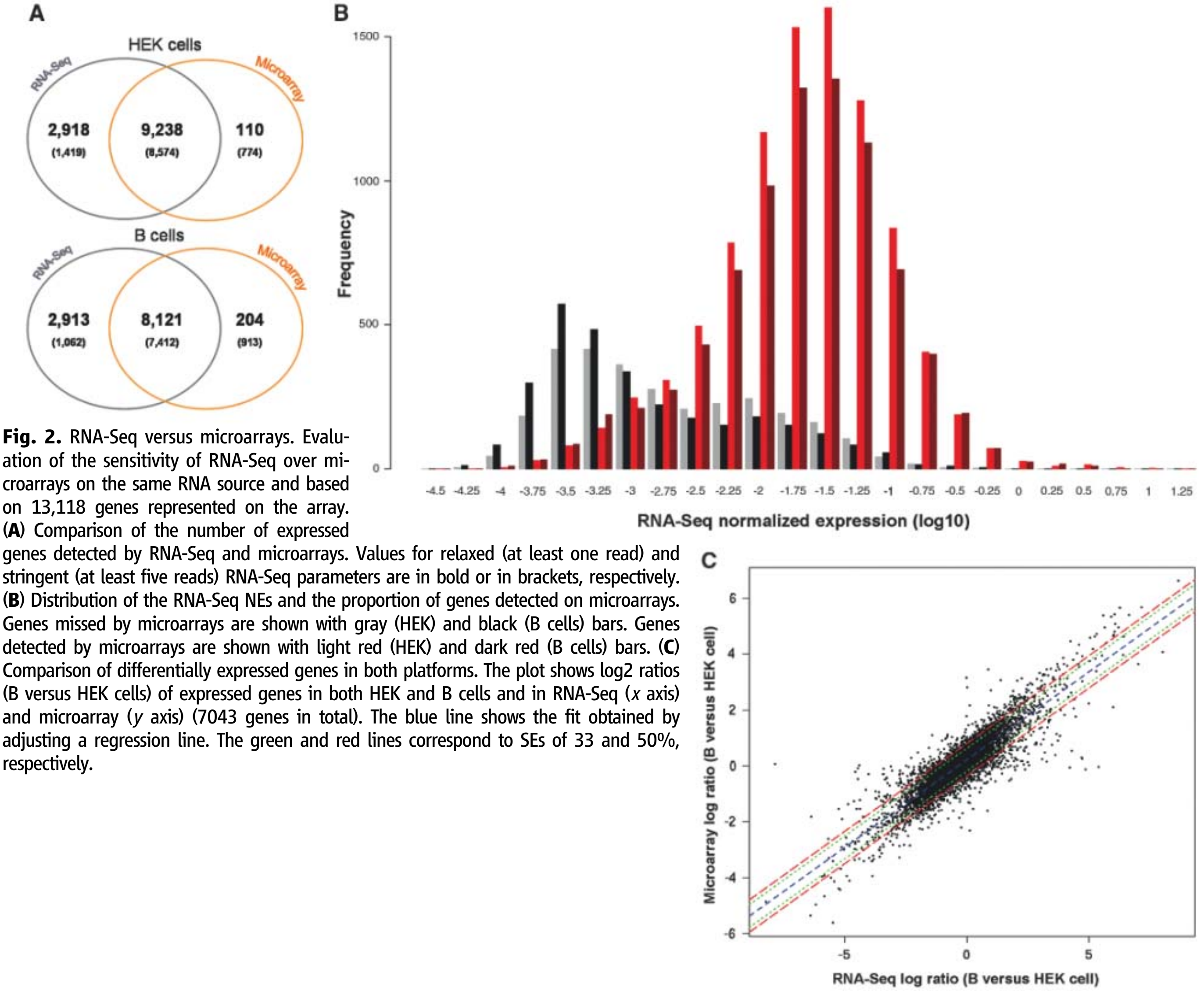

Fig. 2. RNA-Seq versus microarrays. Evaluation of the sensitivity of RNA-Seq over microarrays on the same RNA source and based on 13,118 genes represented on the array. (**A**) Comparison of the number of expressed genes detected by RNA-Seq and microarrays. Values for relaxed (at least one read) and stringent (at least five reads) RNA-Seq parameters are in bold or in brackets, respectively. (**B**) Distribution of the RNA-Seq NEs and the proportion of genes detected on microarrays. Genes missed by microarrays are shown with gray (HEK) and black (B cells) bars. Genes detected by microarrays are shown with light red (HEK) and dark red (B cells) bars. (**C**) Comparison of differentially expressed genes in both platforms. The plot shows log2 ratios (B versus HEK cells) of expressed genes in both HEK and B cells and in RNA-Seq (*x* axis) and microarray (*y* axis) (7043 genes in total). The blue line shows the fit obtained by adjusting a regression line. The green and red lines correspond to SEs of 33 and 50%, respectively.

More than 80% of the TUs were unique to one cell line. Similarities to known proteins were found in 121 TUs, although some contained a stop codon. In addition, Blast analysis grouped 13 TUs into six larger units (table S8). For instance, TU 33 and TU 34 defined a highly transcribed region spanning 190 kb on chromosome 2 (fig. S2). Overall, 7% of the orphan reads were clustered in potentially active regions. The bulk of orphan reads seems to reflect a moderate-to-low transcriptional activity more diffusely distributed in the genome. Relaxing the parameters to 3 reads per 400-bp window embedded 328,683 reads, roughly equally distributed between intronic and intergenic regions, covering a total of 27.5 Mb of DNA (0.9% of the human genome). Taking this figure, 66% of the polyadenylated transcriptome of the two cell lines mapped to known genes and 34% to nonannotated genomic regions.

Approximately 14% of the unmatched reads (Table 1) could be mapped to a set of synthetically computed splice junctions enumerating all theoretical constitutive and AS junctions within annotated transcripts Table 1 and table S9, A and B) (*16*). We observed, on average, 7.2 junctions per gene and a mean density of 3.8 reads

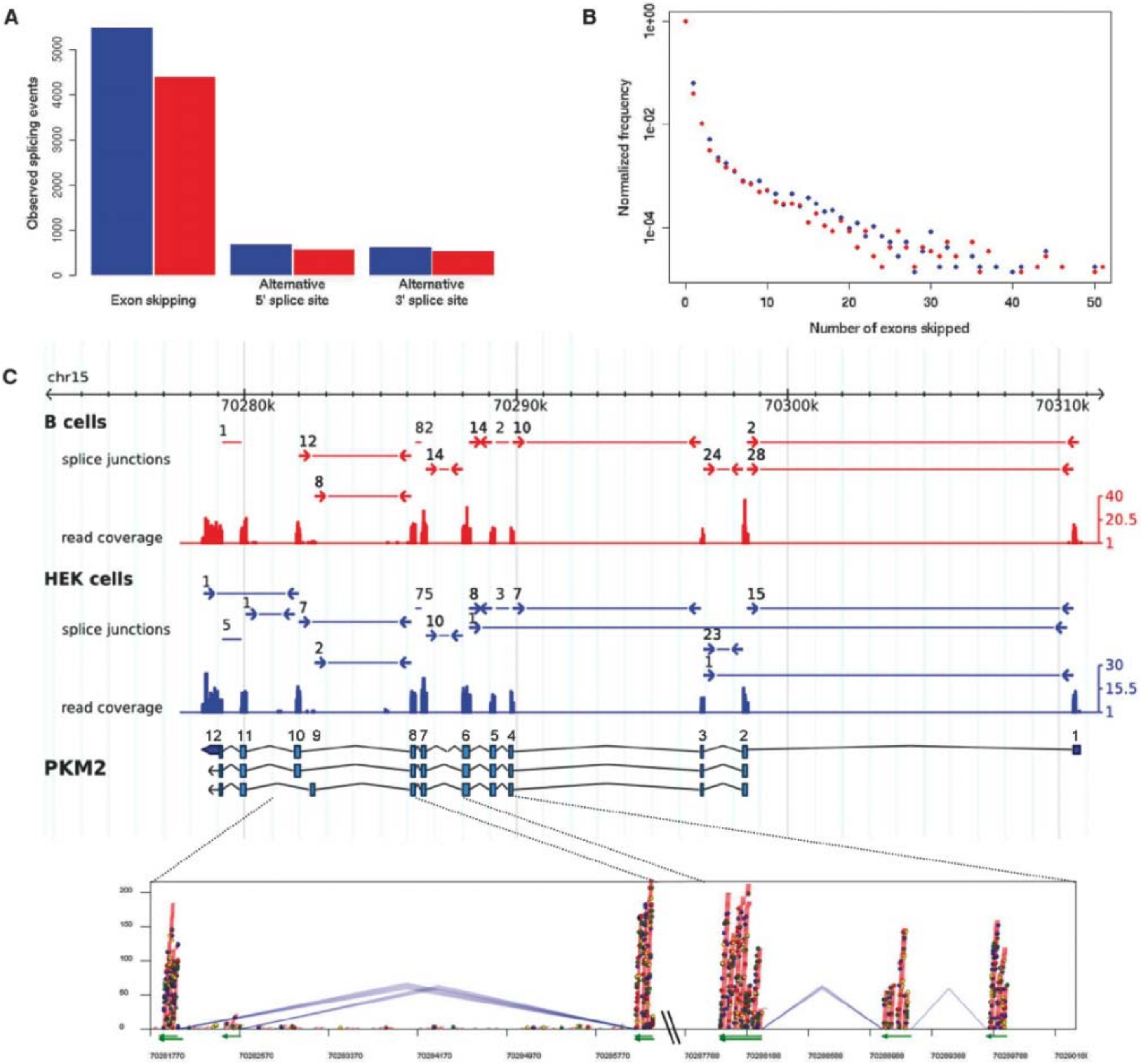

Fig. 3. AS events observed by junction reads. (**A**) Distribution of the three major types of AS: (i) cassette exons, (ii) alternative 5′ splice sites, and (iii) alternative 3′ splice sites. (**B**) Frequency of skipped exons normalized to the number of junctions that do not skip any exon in HEK (blue) and in B cells (red). (**C**) Example of AS in the PKM2 gene. Three isoforms annotated in ENSEMBL (ENST00000335181, ENST00000389092, ENST00000389091) are shown next to the gene name, and exons are numbered. The read coverage is shown for each exon (blue for HEK and red for B cells). Splice-junction reads are shown as arrows; the numbers above the arrows represent the number of reads at junctions. The bottom box shows base-pair resolution coverage in HEK cells of the gene's regions containing exons 8 to 10 (green arrows at left) and 4 to 6 (green arrows at right). The blue lines denote splice junctions. (Left) Two different sequenced junctions connecting either exon 9 or exon 10 and identifying alternative transcripts with mutually exclusive exons in HEK and in B cells. Colored dots represent sequence differences.

per junction. Although 29,689 junctions in HEK and 24,848 in B cells had only one read, those were considered highly notable, as we expect at most 23 reads hitting a junction by chance in the entire data set (*16*). Splice junctions were associated with 81% of the expressed genes. We also observed splice junctions for ~260 genes in each cell line that were not classified as expressed (Tables 1 and 2). Of those, 70% had between 1 and 4 reads and 30% were silent, suggesting a very low activity. The fact that 2275 expressed genes in HEK and 2013 in B cells had no splice-junction reads correlated with the fact that those genes contained fewer exons and a lower activity than the average, reducing the probability to hit a splice junction.

We observed 95% of the splicing events expected in this data set, given the current sequencing depth (Table 1) (*16*). We identified 4096 previously unknown splice junctions in 3106 genes, mostly called by single reads and unique to one cell type (Table 1). Many of these junctions were associated with actively transcribed genes exhibiting more exons than average, pointing to rare splicing events. Approximately 6% of all splice-junction reads identified AS events (6416 junctions in 3916 genes HEK and 5195 junctions in 3262 genes in B cells) (table S9). In a parallel study surveying the mouse transcriptome, AS forms were observed for 3462 genes in three tissues (*28*), but no attempts were made to search for previously unrecognized junctions. Within a cell type, junction reads identify AS in 30% of the expressed genes, where exon skipping was largely overrepresented (Fig. 3A). Skipping events affected mostly one or two exons, with a sharp decline between one and five exons (Fig. 3B). An illustrative example of AS is given for PKM2, also showing that the read density reflects the exon usage (Fig. 3C). Very complex patterns of AS could be detected. For instance, with the use of EIF4G1 coding for the eukaryotic translation initiation factor 4 gamma 1, we showed 12 AS junctions in B cells, of which five have not yet been identified (fig. S3). Although AS is known to regulate the expression of EIF4G1 (*29*, *30*), such a complex pattern had never been described before.

References and Notes

1. H. Lehrach *et al.*, in *Genome Analysis: Genetic and Physical Mapping*, vol. 1, K. Davies, Ed. (Cold Spring Harbor Laboratory Press, Cold Spring Harbor, NY, 1990), pp. 39–81.
2. G. G. Lennon, H. Lehrach, *Trends Genet.* **7**, 314 (1991).
3. E. M. Southern, *Curr. Opin. Genet. Dev.* **2**, 412 (1992).
4. G. M. Hampton, H. F. Frierson, *Trends Mol. Med.* **9**, 5 (2003).
5. T. R. Hughes *et al.*, *Cell* **102**, 109 (2000).
6. P. Bertone *et al.*, *Science* **306**, 2242 (2004), published online 11 November 2004; 10.1126/science.1103388.
7. J. Cheng *et al.*, *Science* **308**, 1149 (2005), published online 24 March 2005; 10.1126/science.1108625.
8. Q. Pan *et al.*, *Mol. Cell* **16**, 929 (2004).
9. J. A. Calarco, A. L. Saltzman, J. Y. Ip, B. J. Blencowe, *Adv. Exp. Med. Biol.* **623**, 64 (2007).
10. V. E. Velculescu, L. Zhang, B. Vogelstein, K. W. Kinzler, *Science* **270**, 484 (1995).
11. C. V. Jongeneel *et al.*, *Proc. Natl. Acad. Sci. U.S.A.* **100**, 4702 (2003).
12. J. B. Kim *et al.*, *Science* **316**, 1481 (2007).
13. U. Nagalakshmi *et al.*, *Science* **320**, 1344 (2008), published online 30 April 2008; 10.1126/science.1158441.
14. R. Lister *et al.*, *Cell* **133**, 523 (2008).
15. B. T. Wilhelm *et al.*, *Nature* **453**, 1239 (2008).
16. Materials and methods are available as supporting material on *Science* Online.
17. T. J. Hubbard *et al.*, *Nucleic Acids Res.* **35**, D610 (2007).
18. A. S. Brodsky *et al.*, *Genome Biol.* **6**, R64 (2005).
19. A. Barski *et al.*, *Cell* **129**, 823 (2007).
20. T. Margaritis, F. C. Holstege, *Cell* **133**, 581 (2008).
21. T. Shiraki *et al.*, *Proc. Natl. Acad. Sci. U.S.A.* **100**, 15776 (2003).
22. J.-P. Z. Wang, B. G. Lindsay, *J. Am. Stat. Assoc.* **100**, 942 (2005).
23. F. Liu *et al.*, *BMC Genomics* **8**, 153 (2007).
24. M. Barnes, J. Freudenberg, S. Thompson, B. Aronow, P. Pavlidis, *Nucleic Acids Res.* **33**, 5914 (2005).
25. C. V. Jongeneel *et al.*, *Genome Res.* **15**, 1007 (2005).
26. L. Shi *et al.*, *Nat. Biotechnol.* **24**, 1151 (2006).
27. S. F. Altschul, W. Gish, W. Miller, E. W. Myers, D. J. Lipman, *J. Mol. Biol.* **215**, 403 (1990).
28. A. Mortazavi, B. A. Williams, K. McCue, L. Schaeffer, B. Wold, *Nat. Methods* **5**, 621 (2008).
29. M. P. Byrd, M. Zamora, R. E. Lloyd, *J. Biol. Chem.* **280**, 18610 (2005).
30. M. J. Coldwell, S. J. Morley, *Mol. Cell. Biol.* **26**, 8448 (2006).
31. The Gene Expression Omnibus accession number for the microarrays and sequence data is GSE11892. Data are displayed in a public version of browser interfaces developed by the Max Planck Institute for Molecular Genetics (http://promotion.molgen.mpg.de/cgi-bin/gbrowse/Hs.Solexa) and Genomatix (www.genomatix.de/MPI). This work was supported in part by the Max Planck Society, the European Union [AnEUploidy (LSHG-CT-2006-037627) and BioSapiens (LHSG-CT-2003-503265)], the National Genome Research Network, and the Federal Ministry for Education and Research of Germany [BioChancePLUS-3 (0313724A) to A.K. and M.S.].

Supporting Online Material

www.sciencemag.org/cgi/content/full/1160342/DC1
Materials and Methods
Figs. S1 to S3
Tables S1 to S9
References

12 May 2008; accepted 27 June 2008
Published online 3 July 2008;
10.1126/science.1160342
Include this information when citing this paper.

Small CRISPR RNAs Guide Antiviral Defense in Prokaryotes

Stan J. J. Brouns,[1]* Matthijs M. Jore,[1]* Magnus Lundgren,[1] Edze R. Westra,[1]
Rik J. H. Slijkhuis,[1] Ambrosius P. L. Snijders,[2] Mark J. Dickman,[2] Kira S. Makarova,[3]
Eugene V. Koonin,[3] John van der Oost[1]†

Prokaryotes acquire virus resistance by integrating short fragments of viral nucleic acid into clusters of regularly interspaced short palindromic repeats (CRISPRs). Here we show how virus-derived sequences contained in CRISPRs are used by CRISPR-associated (Cas) proteins from the host to mediate an antiviral response that counteracts infection. After transcription of the CRISPR, a complex of Cas proteins termed Cascade cleaves a CRISPR RNA precursor in each repeat and retains the cleavage products containing the virus-derived sequence. Assisted by the helicase Cas3, these mature CRISPR RNAs then serve as small guide RNAs that enable Cascade to interfere with virus proliferation. Our results demonstrate that the formation of mature guide RNAs by the CRISPR RNA endonuclease subunit of Cascade is a mechanistic requirement for antiviral defense.

The clusters of regularly interspaced short palindromic repeat (CRISPR)–based defense system protects many bacteria and archaea against invading conjugative plasmids, transposable elements, and viruses (*1*–*8*). Resistance is acquired by incorporating short stretches of invading DNA sequences in genomic CRISPR loci (*1*, *9*, *10*). These integrated sequences are thought to function as a genetic memory that prevents the host from being infected by viruses containing this recognition sequence. A number of CRISPR-associated (*cas*) genes (*11*–*13*) has been reported to be essential for the phage-resistant phenotype (*1*). However, the molecular mechanism of this adaptive and inheritable defense system in prokaryotes has remained unknown.

The *Escherichia coli* K12 CRISPR/*cas* system comprises eight *cas* genes: *cas3* (predicted HD-nuclease fused to a DEAD-box helicase), five genes designated *casABCDE*, *cas1* (predicted integrase) (*13*), and the endoribonuclease gene *cas2* (*14*) (Fig. 1A and table S1). In separate experiments, each Cas protein was tagged at both the N and C terminus and produced along with the complete set of untagged Cas proteins (*15*). Affinity purification of the tagged component enabled the identification of a protein complex composed of five Cas proteins: CasA, CasB, CasC, CasD, and CasE (Fig. 1B). The

---

[1] Laboratory of Microbiology, Department of Agrotechnology and Food Sciences, Wageningen University, Dreijenplein 10, 6703 HB Wageningen, Netherlands. [2] Biological and Environmental Systems, Department of Chemical and Process Engineering, University of Sheffield, Mappin Street, Sheffield S1 3JD, UK. [3] National Center for Biotechnology Information, National Library of Medicine, NIH, Bethesda, MD 20894, USA.

*These authors contributed equally to this work.
†To whom correspondence should be addressed. E-mail: john.vanderoost@wur.nl

complex, denoted Cascade (CRISPR-associated complex for antiviral defense), could be isolated from *E. coli* lysates using any of the tagged subunits of the complex as bait, except for CasA.

The function of Cascade was studied by analyzing the effect of in-frame *cas* gene knockouts (*16*) on the formation of transcripts of the CRISPR region in *E. coli* K12 (Fig. 1A). Northern analysis of total RNA with single-stranded spacer sequences as a probe showed transcription of the CRISPR region in the direction downstream of the *cas2* gene (Figs. 1A and 2A) and no transcription in the opposite direction. Analysis of control strains (wild type and a non-*cas* gene knockout) revealed a small CRISPR-RNA (crRNA) product of ~57 nucleotides (Fig. 2A). The same product was present in much higher amounts in the *casA*, *casB*, and *casC* knockout strains but absent from strains lacking the overlapping genes *casD* and *casE* (Fig. 2A). The small crRNAs seem to be cleaved from a multi-unit crRNA precursor (pre-crRNA) (*7*, *17*, *18*), as is evident from the presence of two and three repeat-spacer units (~120 and ~180 nucleotides) that show up in the Δ*casA*, Δ*casB*, and Δ*casC* strains (Fig. 2A). The Δ*casE* strain contained a large pre-crRNA, suggesting that the disruption of this gene prevents pre-crRNA cleavage.

To study the accumulation and cleavage patterns of crRNAs in the *E. coli* K12 knockout strains in more detail and to rule out any effects of the gene disruptions on the expression of downstream or upstream *cas* genes, the five subunits of Cascade and the K12-type pre-crRNA were expressed in *E. coli* BL21(DE3), which lacks endogenous *cas* genes (*19*). Northern analysis showed that crRNAs of ~57 nucleotides were only produced in strains containing the Cascade complex (Fig. 2B). By omitting the individual subunits one by one, it became apparent that the small crRNA was absent only in the strain that lacked *casE* (Fig. 2B), indicating that this is the only Cascade subunit essential for pre-crRNA cleavage.

Activity assays with purified Cascade showed that the complex is capable of cleaving the *E. coli* K12 pre-crRNA into fragments of ~57 nucleotides in vitro (Fig. 2C). However, no cleavage was observed with either pre-crRNA from *E. coli* UTI89, which contains repeats with a different sequence (*20*), or a non-crRNA template (Fig. 2C). The RNA cleavage reaction proceeded in the absence of divalent metal ions and adenosine triphosphate and reached saturation level within 5 min. To investigate whether the CasE subunit is sufficient for pre-crRNA cleavage activity, it was overproduced as a fusion with the *E. coli* maltose binding protein (MalE). Like the complete Cascade, the CasE fusion protein cleaved only the K12-type pre-crRNA (Fig. 2D), showing that CasE is an unusual endoribonuclease that does not require the other Cascade subunits. We cannot rule out the possibility that pre-crRNA cleavage is an autocatalytic, ribozyme-like reaction, in which CasE is an essential RNA chaperone.

CasE belongs to one of the numerous families of repeat-associated mysterious proteins, the largest and most diverse class of Cas proteins (*12*, *13*). The crystal structure of a CasE homolog from *Thermus thermophilus* HB8 shows that the protein contains two domains with a ferredoxin-like fold, and displays overall structural similarity to a variety of RNA-binding proteins (*13*, *21*). On the basis of structure and amino acid conservation analysis of this protein family (fig. S1), the invariant residue His^{20} was mutated to Ala to analyze the effect on pre-crRNA cleavage. Northern blots indicated that crRNAs of ~57 nucleotides were no longer formed in the strain containing Cascade-CasE^{H20A} (Fig. 2E). Moreover, although the mutated CasE was still incorporated into Cascade, the pre-crRNA cleaving ability of purified Cascade was abolished (Fig. 2F), providing further support for the essential role of CasE in pre-crRNA cleavage and suggesting that the conserved His residue is involved in catalysis.

The crRNA cleavage sites were examined by simultaneous expression of K12-type pre-crRNA and Cascade. Under these conditions, the purification of Cascade yielded substantial amounts of copurified RNAs of ~57 nucleotides (Fig. 3A). Cloning and sequencing of this Cascade-bound RNA revealed that 85% of the clones [67 out of 79 clones (67/79)] were derived from crRNAs, of which 78% (52/67) started with the last eight bases of the repeat sequence (AUAAACCG) (Fig. 3B and fig. S2). This well-defined 5′ end

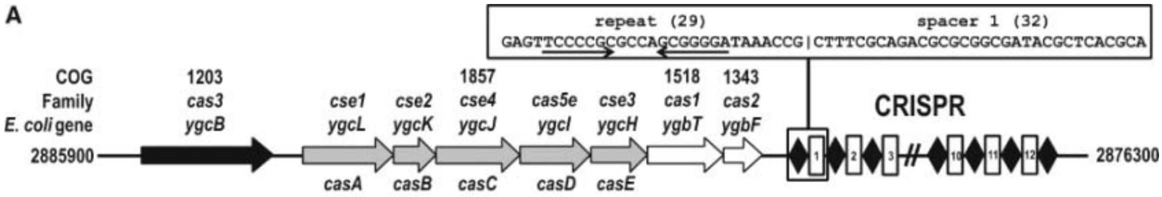

Fig. 1. The composition of the Cascade complex. (**A**) Schematic diagram of the CRISPR/*cas* gene cluster of *E. coli* K12 W3110. Repeats and spacers are indicated by diamonds and rectangles, respectively. A palindrome in the repeat is marked by convergently pointing arrows. Protein family nomenclature is as described in (*11*, *12*). (**B**) Coomassie blue–stained SDS-polyacrylamide gel of the affinity purified protein complex using either the N-terminal StrepII-tag (S) or C-terminal His-tag (H) of each of the subunits CasB, CasC, CasD, or CasE as bait. Asterisks indicate the 5.5 kD larger double-tagged subunits. Marker sizes in kilodaltons on the left; location of untagged subunits on the right.

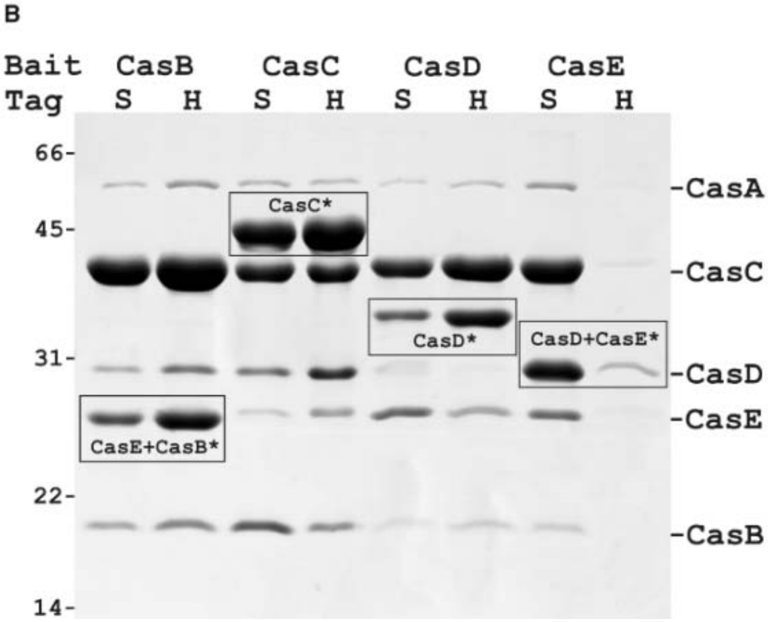

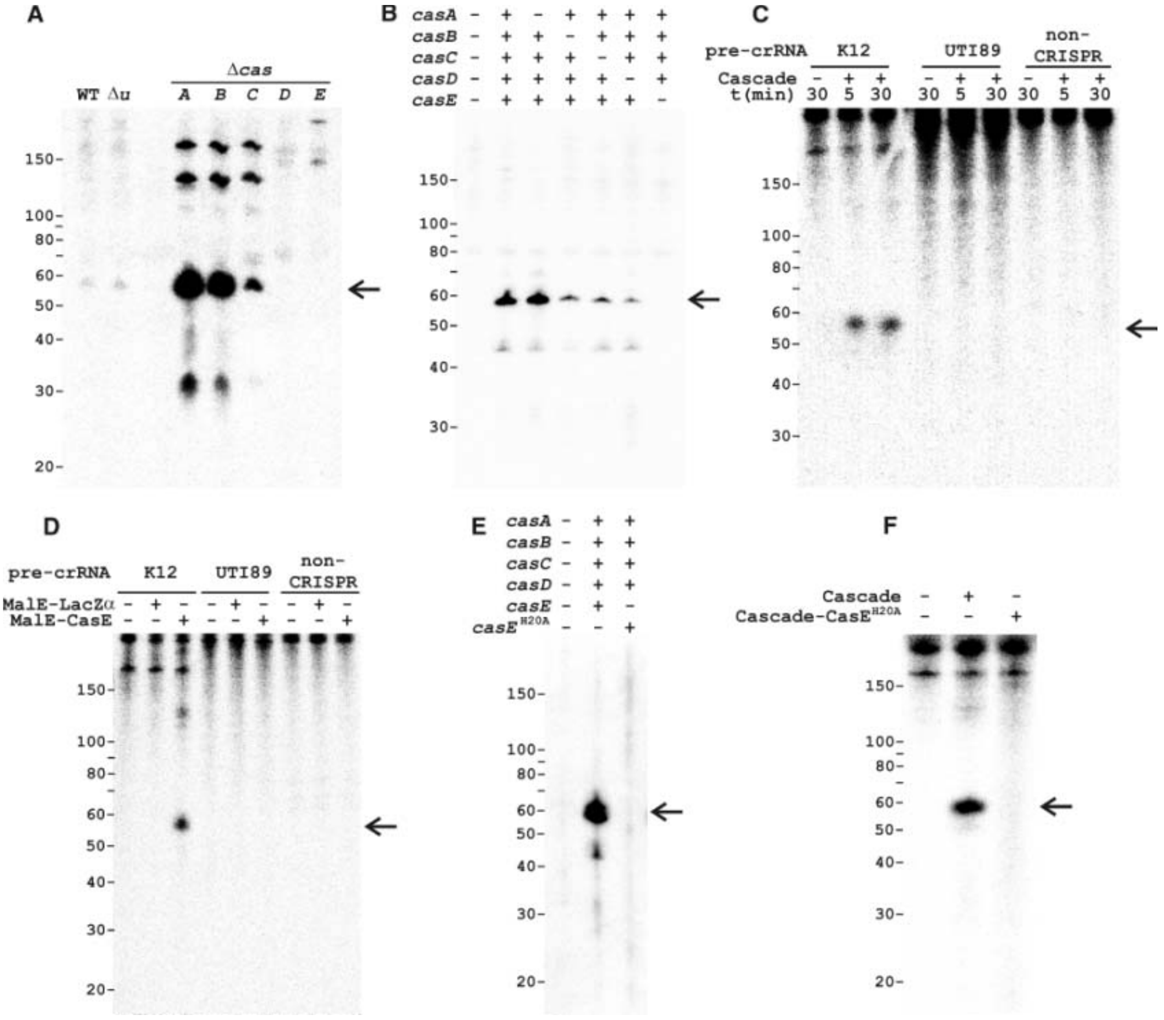

Fig. 2. Cascade cleaves CRISPR RNA precursors into small RNAs of ~57 nucleotides (marked by arrows). (**A**) Northern analysis of total RNA of WT *E. coli* K12 (WT), a non-*cas* gene knockout (Δ*u*, *uidA*, β-glucuronidase), and Cascade gene knockouts using the single-stranded spacer sequence BG2349 (table S2) as a probe. (**B**) Northern blot as in (A) of total RNA from *E. coli* BL21 (DE3) expressing the *E. coli* K12 pre-crRNA and either the complete or incomplete Cascade complex. (**C**) Activity assays with purified Cascade using in vitro transcribed α-^{32}P–uridine triphosphate–labeled pre-crRNA from *E. coli* K12 (repeat sequence: GAGUUCCCCGCCAGCGGGGAUAAACCG), *E. coli* UTI89 (repeat sequence: GUUCACUGCCGUACAGGCAGCUUAGAAA), and non-crRNA as substrates. (**D**) Activity assays as shown in (C) for 15 min with purified MalE-LacZα and MalE-CasE fusion proteins. (**E**) Northern blot as shown in (B) with Cascade or Cascade-CasE^{H20A}. (**F**) Activity assays as shown in (C) for 30 min with purified Cascade or Cascade-CasE^{H20A}.

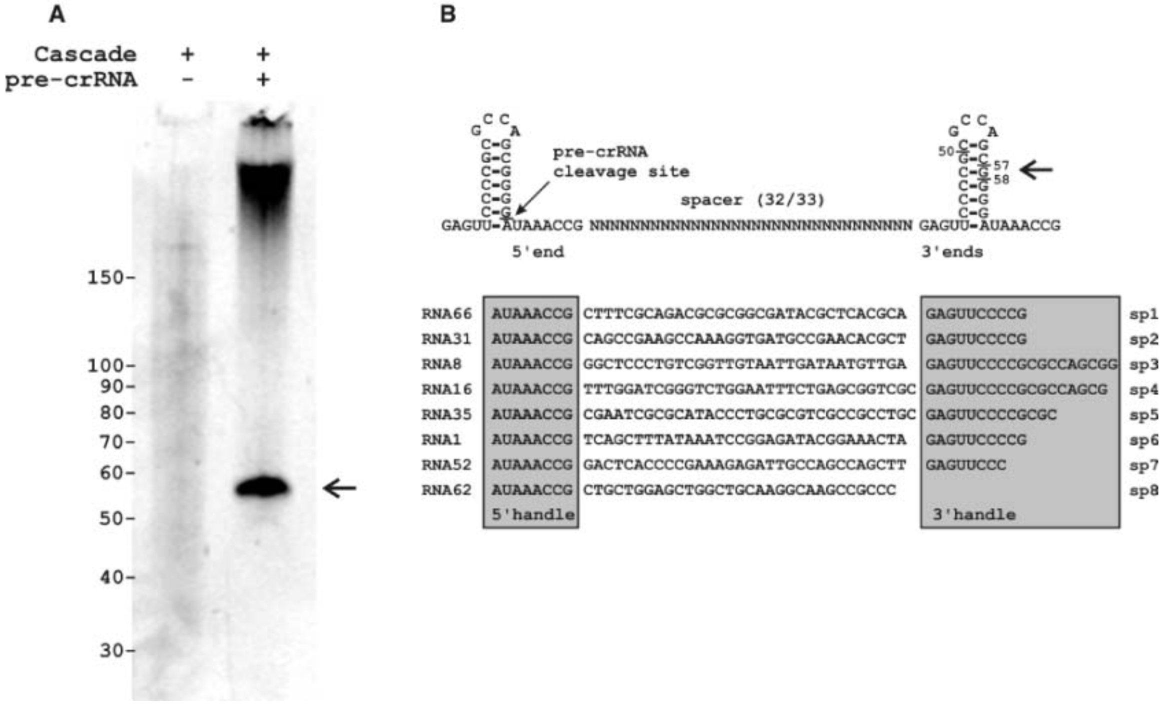

RNA66	AUAAACCG	CTTTCGCAGACGCGCGGCGATACGCTCACGCA	GAGUUCCCCG	sp1
RNA31	AUAAACCG	CAGCCGAAGCCAAAGGTGATGCCGAACACGCT	GAGUUCCCCG	sp2
RNA8	AUAAACCG	GGCTCCCTGTCGGTTGTAATTGATAATGTTGA	GAGUUCCCCGCGCCAGCGG	sp3
RNA16	AUAAACCG	TTTGGATCGGGTCTGGAATTTCTGAGCGGTCGC	GAGUUCCCCGCGCCAGCG	sp4
RNA35	AUAAACCG	CGAATCGCGCATACCCTGCGCGTCGCCGCCTGC	GAGUUCCCCGCGC	sp5
RNA1	AUAAACCG	TCAGCTTTATAAATCCGGAGATACGGAAACTA	GAGUUCCCCG	sp6
RNA52	AUAAACCG	GACTCACCCCGAAAGAGATTGCCAGCCAGCTT	GAGUUCCC	sp7
RNA62	AUAAACCG	CTGCTGGAGCTGGCTGCAAGGCAAGCCGCCC		sp8
	5'handle		3'handle	

Fig. 3. Cleaved crRNAs remain bound by Cascade. (**A**) Denaturing polyacrylamide gel showing the crRNA (marked by the arrow) isolated from purified Cascade in the absence and presence of co-expressed pre-crRNA. (**B**) Secondary structure of pre-crRNA repeats and example sequences of cloned crRNAs indicating the PCS and crRNA handles.

was followed by a complete spacer sequence and a less well-defined 3′ sequence ending in the next repeat region. A transcript of a single palindromic repeat can fold as a stable stem-loop of seven base pairs, which may facilitate recognition by RNA-binding Cas proteins (*8*, *20*), such as CasE. The pre-crRNA cleavage site (PCS) appeared to be located immediately upstream of the 3′ terminal base of the stem-loop formed by the repeat (Fig. 3B). The clone library did not contain crRNAs of 61 nucleotides, which would be the result of a single endonuclease cleavage event in each repeat, given the size of a repeat (29 nucleotides) and most spacers (32 nucleotides). Instead, in agreement with experimental observations (Figs. 2 and 3A), the crRNAs were truncated at the 3′ end by at least two guanosine bases from the endonuclease cleavage site, removing several stem-forming bases.

To test whether crRNA-loaded Cascade gives rise to phage resistance, two artificial CRISPRs were designed against phage Lambda (λ). Each of these CRISPRs targeted four essential λ genes (fig. S3). The coding CRISPR (C_{1-4}) produced crRNAs complementary to both the mRNA and the coding strand of these four genes, whereas the template CRISPR (T_{1-4}) targeted only the template strand of the same proto-spacer regions (fig. S3). A nontargeting CRISPR containing wild-type (WT) spacers with no similarity to the phage genome served as a control. Plaque assays with *E. coli* showed that the introduction of either one of these anti-λ phage CRISPRs in a strain expressing only Cascade did not result in reduced sensitivity of the host to a virulent Lambda phage (λ_{vir}) (Fig. 4A). However, strains that expressed Cascade and Cas3 were much less sensitive to phage infection. The template CRISPR rendered the strain insensitive to the phage at the highest phage titer tested ($>10^7$-fold less sensitive than the control strain), whereas the coding CRISPR reduced the sensitivity 10^2-fold (Fig. 4A) and produced plaques with a diameter ~1/10 of the standard λ plaque. The phage resistance phenotype was lost when Cascade was omitted (Fig. 4A), proving that both Cascade and Cas3 are required in this process. Moreover, strains containing Cas3 and Cascade-CasE^{H20A} displayed a sensitive phenotype, which shows that pre-crRNA cleavage is mechanistically required for phage resistance. The co-expression of Cas1 and Cas2 had no effect on the sensitivity profile of the strain (Fig. 4A), suggesting that these proteins are involved in other stages of the CRISPR/*cas* mechanism. Plaque assays with single anti-λ spacers (fig. S3) showed that the total reduction of sensitivity observed with the four anti-λ spacers (C_{1-4} and T_{1-4}) (Fig. 4A) results from a synergistic effect of the individual spacers (C_1 to T_4) (Fig. 4B).

Our results demonstrate that a complex of five Cas proteins is responsible for the maturation of pre-crRNA to small crRNAs that are critical for mediating an antiviral response. These mature crRNAs contain the antiviral spacer unit flanked by short RNA sequences derived from the repeat on either side termed the 5′ and 3′ handle, which may serve as conserved binding sites for Cascade subunits, as has been suggested previously (*20*). The Cascade-bound crRNA serves as a guide to direct the complex to viral nucleic acids to mediate an antiviral response. We hypothesize that crRNAs target virus DNA, because anti-λ CRISPRs of both polarities lead to a reduction of sensitivity to the phage. The model is supported by previous observations that virus-derived sequences are integrated into CRISPR loci, irrespective of their orientation in the virus genome (*1*–*4*, *7*, *9*, *10*, *13*). We conclude that the transcription of CRISPR regions—and the cleavage of pre-crRNA to mature crRNAs by Cas proteins—is the molecular basis of the antiviral defense stage of the CRISPR/*cas* system, which enables prokaryotes to effectively prevent phage predation.

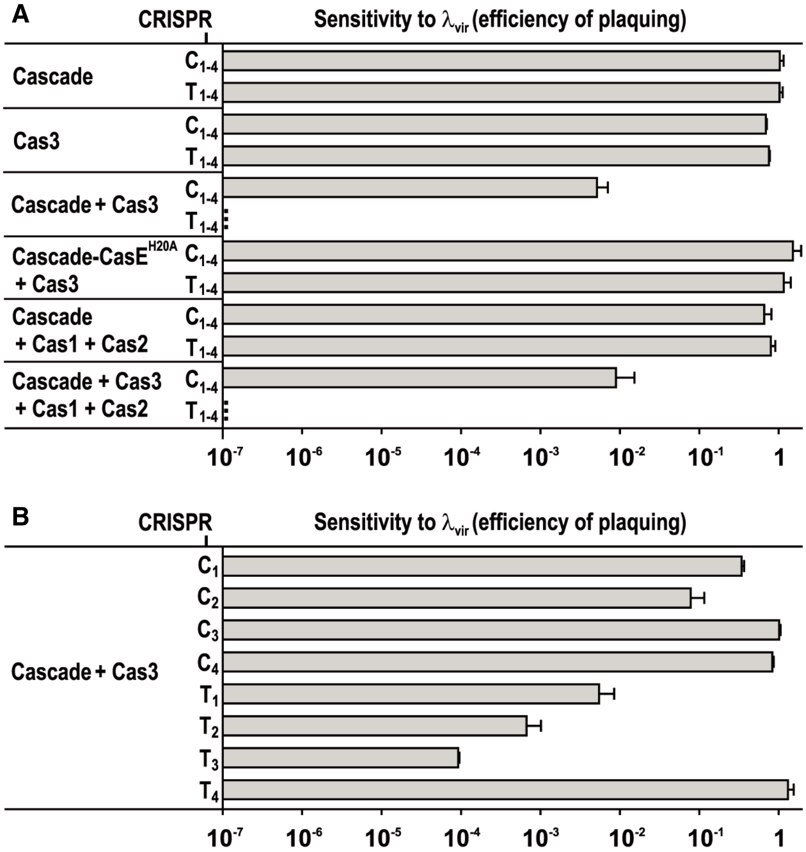

Fig. 4. Engineered CRISPRs confer resistance to λ in the presence of Cascade and Cas3. (**A**) Effect of the presence of different sets of *cas* genes on the sensitivity of *E. coli* to phage λ_{vir}. Cells were equipped with one of two engineered CRISPRs containing four anti-λ spacers each (fig. S3). The C_{1-4} CRISPR produces crRNA complementary to the coding strand and mRNA of λ_{vir}, and the T_{1-4} CRISPR targets only the template strand. The sensitivity of each strain to phage λ_{vir} is represented as a histogram of the efficiency of plaquing, which is the plaque count ratio of the anti-λ CRISPR to that of the nontargeting control CRISPR. (**B**) Effect of single anti-λ spacers (fig. S3) on the sensitivity of *E. coli* to λ_{vir}. Error bars indicate 1 SD.

References and Notes

1. R. Barrangou *et al.*, *Science* **315**, 1709 (2007).
2. F. J. Mojica, C. Diez-Villasenor, J. Garcia-Martinez, E. Soria, *J. Mol. Evol.* **60**, 174 (2005).
3. C. Pourcel, G. Salvignol, G. Vergnaud, *Microbiology* **151**, 653 (2005).
4. A. Bolotin, B. Quinquis, A. Sorokin, S. D. Ehrlich, *Microbiology* **151**, 2551 (2005).
5. J. S. Godde, A. Bickerton, *J. Mol. Evol.* **62**, 718 (2006).
6. G. W. Tyson, J. F. Banfield, *Environ. Microbiol.* **10**, 200 (2008).
7. R. K. Lillestøl, P. Redder, R. A. Garrett, K. Brügger, *Archaea* **2**, 59 (2006).
8. R. Sorek, V. Kunin, P. Hugenholtz, *Nat. Rev. Microbiol.* **6**, 181 (2008).
9. P. Horvath *et al.*, *J. Bacteriol.* **190**, 1401 (2008).
10. H. Deveau *et al.*, *J. Bacteriol.* **190**, 1390 (2008).
11. R. Jansen, J. D. Embden, W. Gaastra, L. M. Schouls, *Mol. Microbiol.* **43**, 1565 (2002).
12. D. H. Haft, J. Selengut, E. F. Mongodin, K. E. Nelson, *PLoS Comput. Biol.* **1**, e60 (2005).
13. K. S. Makarova, N. V. Grishin, S. A. Shabalina, Y. I. Wolf, E. V. Koonin, *Biol. Direct* **1**, 7 (2006).
14. N. Beloglazova *et al.*, *J. Biol. Chem.*, **283**, 20361 (2008).
15. Materials and methods are available as supporting material on *Science* Online.
16. T. Baba, H. Mori, *Methods Mol. Biol.* **416**, 171 (2008).
17. T. H. Tang *et al.*, *Proc. Natl. Acad. Sci. U.S.A.* **99**, 7536 (2002).
18. T. H. Tang *et al.*, *Mol. Microbiol.* **55**, 469 (2005).
19. J. F. Kim, H. Jeong, R. E. Lenski, personal communication.
20. V. Kunin, R. Sorek, P. Hugenholtz, *Genome Biol.* **8**, R61 (2007).
21. A. Ebihara *et al.*, *Protein Sci.* **15**, 1494 (2006).
22. We thank T. Verweij, C. G. J. van Houte, and M. R. Beijer for experimental contributions and T. Goosen (Hogeschool van Arnhem en Nijmegen BioCentre), M. J. Young (Montana State University), T. Bisseling, and W. M. de Vos

(Wageningen University) for helpful discussions. We are grateful for receiving strains from the KEIO collection distributed by National BioResource Project (National Institute of Genetics, Japan). We thank U. Dobrindt (University of Würzburg) for sending genomic material of *E. coli* UTI89. This work was financially supported by a Vici grant from the Dutch Organization for Scientific Research (Nederlandse Organisatie voor Wetenschappelijk Onderzoek) and a Marie Curie grant from the European Union. M.L. was supported by the Wenner-Gren Foundations.

Supporting Online Material
www.sciencemag.org/cgi/content/full/321/5891/960/DC1
Materials and Methods
Figs. S1 to S4
Tables S1 to S3
References

28 April 2008; accepted 1 July 2008
10.1126/science.1159689

Suppression of the MicroRNA Pathway by Bacterial Effector Proteins

Lionel Navarro,[1] Florence Jay,[1] Kinya Nomura,[2] Sheng Yang He,[2] Olivier Voinnet[1]*

Plants and animals sense pathogen-associated molecular patterns (PAMPs) and in turn differentially regulate a subset of microRNAs (miRNAs). However, the extent to which the miRNA pathway contributes to innate immunity remains unknown. Here, we show that miRNA-deficient mutants of *Arabidopsis* partly restore growth of a type III secretion-defective mutant of *Pseudomonas syringae*. These mutants also sustained growth of nonpathogenic *Pseudomonas fluorescens* and *Escherichia coli* strains, implicating miRNAs as key components of plant basal defense. Accordingly, we have identified *P. syringae* effectors that suppress transcriptional activation of some PAMP-responsive miRNAs or miRNA biogenesis, stability, or activity. These results provide evidence that, like viruses, bacteria have evolved to suppress RNA silencing to cause disease.

In RNA silencing, double-stranded RNA (dsRNA) is processed into small RNAs (sRNAs) through the action of RNase-III–like Dicer enzymes. The sRNAs guide Argonaute (AGO)–containing RNA-induced silencing complexes (RISCs) to inhibit gene expression at the transcriptional or posttranscriptional levels (*1*). In the *Arabidopsis thaliana* microRNA (miRNA) pathway, miRNA precursors (pre-miRNAs) are excised from noncoding primary transcripts (pri-miRNAs) and processed into mature miRNA duplexes by Dicer-like 1 (DCL1). Upon HEN1-catalyzed 2′-O-methylation (*2*), one miRNA strand incorporates an AGO1-containing RISC to direct endonucleolytic cleavage or translational repression of target transcripts (*1*). DCL4 and DCL2 perform major defensive functions by processing viral-derived dsRNA into small interfering RNAs (siRNAs), which, like miRNAs, are loaded into AGO1-RISC. As a counterdefensive strategy, viruses deploy viral suppressors of RNA silencing, or VSRs (*3*). RNA silencing also contributes to resistance against bacterial pathogens (*4*–*7*), which elicit an innate immune response upon perception of pathogen-associated molecular patterns (PAMPs) by host-encoded pattern recognition receptors (PRRs). For example, the *Arabidopsis* miR393 is PAMP-responsive (*4*, *8*) and contributes to resistance against virulent *Pseudomonas syringae* pv. *tomato* strain DC3000 (*Pto* DC3000) (*4*). Nonetheless, the full extent to which cellular sRNAs, including miRNAs, participate in PAMP-triggered immunity (PTI) in plants remains unknown.

To address this issue, *Arabidopsis* mutants defective for siRNA or miRNA accumulation were challenged with *Pto* DC3000 *hrcC*$^-$, a mutant that lacks a functional type III secretion system required for effector-protein delivery into host cells (*9*). This bacterium elicits but cannot suppress PTI and, consequently, multiplies poorly on wild-type Col-0– and La-*er*–inoculated leaves (Fig. 1A and fig. S1). However, *Pto* DC3000 *hrcC*$^-$ growth was specifically enhanced in the miRNA-deficient *dcl1-9* and *hen1-1* mutants (Fig. 1A), in which induction of the basal defense marker gene *WRKY30* was also compromised (fig. S2A) (*10*).

Because PTI is also a major component of nonhost resistance (*10*, *11*), we challenged *dcl1-9* and *hen1-1* mutants with *P. syringae* pv. *phaseolicola* (*Psp*) strain NPS3121, which infects beans but not *Arabidopsis*. Both *dcl1-9* and *hen1-1* mutants sustained *Psp* NPS3121 growth (Fig. 1B) and displayed compromised *WRKY30* induction (fig. S2B). Enhanced bacterial growth was also observed with the nonpathogenic *Pseudomonas fluorescens* Pf-5 and *Escherichia coli* W3110 strains (Fig. 1, C and D). Furthermore, the above nonvirulent bacteria all induced chlorosis and necrosis on miRNA-deficient mutants, resembling bacterial disease

---

[1] Institut de Biologie Moléculaire des Plantes, CNRS UPR 2353–Université Louis Pasteur, 12 Rue du Général Zimmer, 67084 Strasbourg Cedex, France. [2] Department of Energy Plant Research Laboratory, Michigan State University, East Lansing, MI 48824, USA.

*To whom correspondence should be addressed. E-mail: olivier.voinnet@ibmp-ulp.u-strasbg.fr

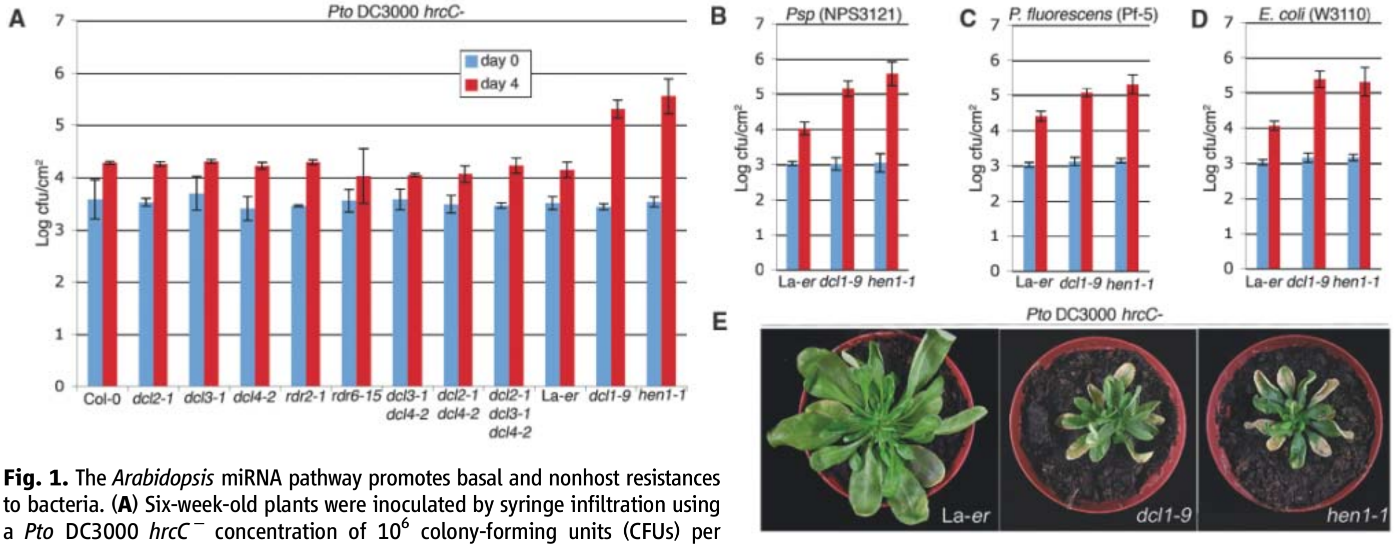

Fig. 1. The *Arabidopsis* miRNA pathway promotes basal and nonhost resistances to bacteria. (**A**) Six-week-old plants were inoculated by syringe infiltration using a *Pto* DC3000 *hrcC*$^-$ concentration of 10^6 colony-forming units (CFUs) per milliliter. Error bars indicate SE of log-transformed data from five independent samples. Similar results were obtained in three independent experiments. (**B** to **D**) Plants were inoculated as in (A) but with *Psp* NPS3121 (B), *P. fluorescens* Pf-5 (C), or *E. coli* W3110 (D). Similar results were obtained in two independent experiments. (**E**) Plants were inoculated as in (A) and pictures were taken at 6 days after inoculation.

symptoms triggered by virulent *Pto* DC3000 (Fig. 1E and fig. S3, A to D). However, we cannot exclude the participation of other endogenous sRNAs in this process (*6*, *7*), because the *hen1-1* mutant, which is additionally impaired in the accumulation of many types of sRNAs (*12*), consistently displayed more disease symptoms than the *dcl1-9* mutant did (fig. S3). Despite this possibility, our results indicate that the miRNA

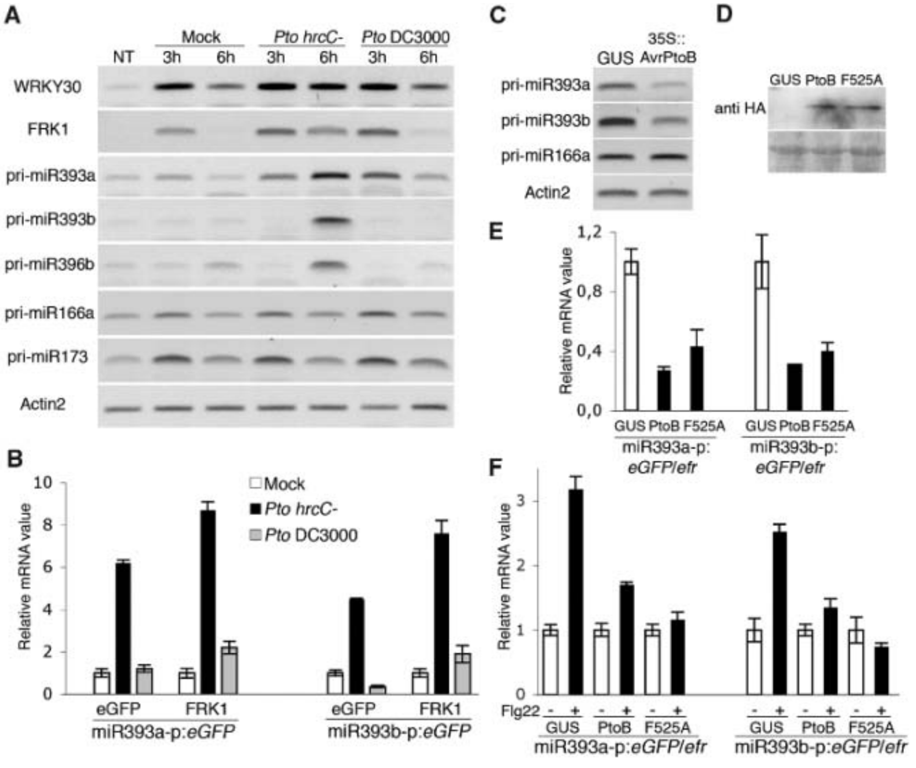

Fig. 2. Transcriptional repression of PAMP-responsive miRNAs by *Pto* DC3000 and AvrPtoB. (**A**) Five-week-old plants were syringe-infiltrated with a concentration of 2×10^7 CFU/ml of either *Pto* DC3000 or *Pto* DC3000 *hrcC*$^-$ and pri-miRNA expression was monitored by semiquantitative reverse transcription polymerase chain reaction (RT-PCR). NT, nontreated. Similar results were obtained in three independent experiments. (**B**) Five-week-old miR393a-p::eGFP and miR393b-p::eGFP transgenic lines were treated as in (A) for 6 hours. eGFP and FRK1 mRNA levels were analyzed by quantitative RT-PCR. Similar results were obtained in three independent experiments. (**C**) Semiquantitative RT-PCR analysis of pri-miRNAs. *Agrobacterium*-mediated transient expression was performed in 4-week-old *efr* leaves. Similar results were obtained in three independent experiments. GUS, β-glucuronidase. (**D**) Detection of AvrPtoB-3xHA and AvrPtoB$_{F525A}$-3xHA by Western analysis. In the bottom panel, Coomassie staining shows equal protein loading. Transient expression was performed as in (C). (**E**) Transient expression was performed in 4-week-old *At*-miR393a-p::eGFP/*efr* and *At*-miR393b-p::eGFP/*efr* lines as in (C). Expression of eGFP was monitored by quantitative RT-PCR. (**F**) As in (E), except that 3 days after *Agrobacterium*-infiltration, plants were challenged with 1 μM active or inactive flg22 for 6 hours.

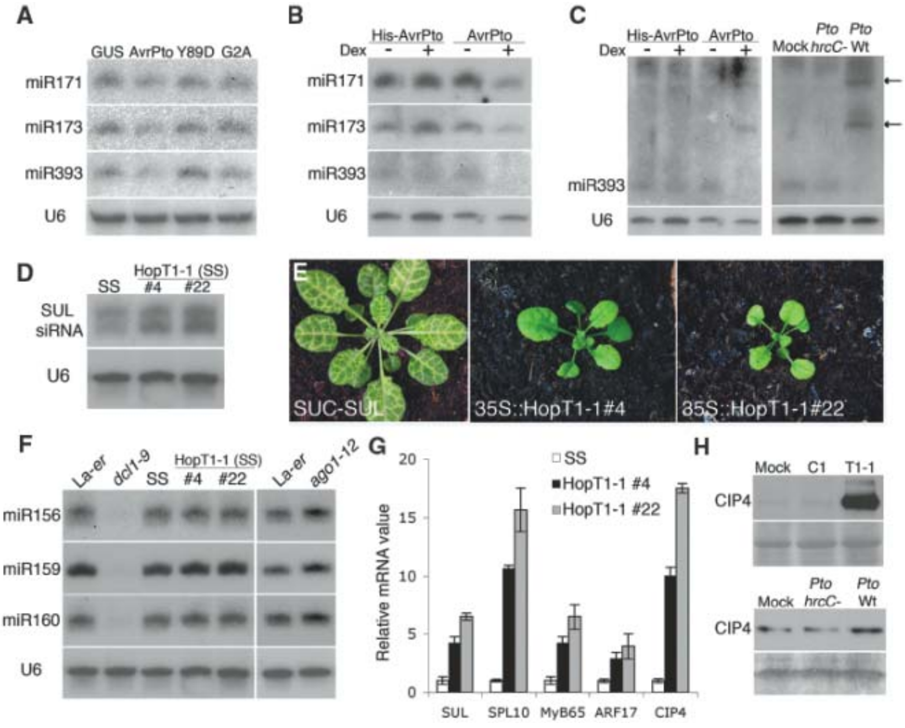

Fig. 3. Suppression of miRNA accumulation or activity by bacterial effectors. (**A**) Four-week-old *efr* plants were syringe-infiltrated with *A. tumefaciens* carrying AvrPto, AvrPto$_{Y89D}$, AvrPto$_{G2A}$, or GUS-intron constructs. Five days after infiltration, accumulation of miRNAs was assayed by Northern analysis. U6, the control, shows sRNA equal loading. Similar results were obtained in two independent experiments. (**B**) Same experiments as in (A) but in Dex::AvrPto and Dex::6xHis-AvrPto transgenic lines. miRNA accumulation was analyzed by Northern analysis 30 hours after dexamethasone (Dex) treatment (at a concentration of 30 μM). Similar results were obtained in two independent experiments. (**C**) Left panel shows the same experiment as in (B) but on miR393. Right panel shows miR393 levels 30 hours after inoculation with *Pto* DC3000 *hrcC*$^-$ or *Pto* DC3000 at 10^8 CFU/ml. Inoculation was performed by syringe infiltration on 5-week-old plants. Similar results were obtained in five independent experiments. Arrows: miR393 precursors stabilization (pre-miR393 stabilization was detected by 24 hours after inoculation). (**D**) Northern analysis of SUL siRNA levels in SS plants overexpressing HopT1-1. (**E**) Four-week-old SS plant (left) and HopT1-1 overexpressing (SS) plants (middle and right). (**F**) Northern analysis of canonical miRNA levels in HopT1-1–overexpressing (SS) plants. (**G**) Quantitative RT-PCR analysis of SUL and miRNA target transcript levels in HopT1-1–overexpressing SS plants. (**H**) HopT1-1 and *Pto* DC3000 elevate CIP4 protein levels. Upper panels show CIP4 protein levels upon transient delivery of HopT1-1 (T1) or HopC1 (C1) in 4-week-old *efr* leaves. Western analysis was performed using an antibody to CIP4. Ponceau staining shows equal protein loading. Bottom panels show CIP4 protein levels after inoculation with *Pto* DC3000 or *Pto* DC3000 *hrcC*$^-$ at 10^8 CFU/ml. Inoculation was performed by syringe infiltration on 5-week-old Col-0 plants. CIP4 protein levels were monitored 6 hours after inoculation by Western analysis. Coomassie staining shows equal protein loading. Similar results were obtained in two independent experiments.

pathway is probably an essential component of plant basal defense. As a corollary, some bacterial effectors must have evolved to suppress host-miRNA functions to enable disease.

In principle, suppression of the miRNA pathway could affect miRNA transcription, biogenesis, or activity. To test the first possibility, we challenged wild-type plants with *Pto* DC3000 or *Pto* DC3000 *hrcC*$^-$ and analyzed the levels of several pri-miRNAs. In virulent *Pto* DC3000–treated plants, induction of the PAMP-responsive pri-miR393a/b and pri-miR396b (*4*, *8*) was appreciably suppressed, as was induction of *WRKY30* and *Flagellin Receptor Kinase 1* (*FRK1*) (*13*), which were used as internal controls (Fig. 2A). In contrast, the PAMP-insensitive pri-miR166a and pri-miR173 remained unaffected. We then used the previously described *At*-miR393a-p::eGFP and *At*-miR393b-p::eGFP transgenic lines, which report *At-miR393a* and *At-miR393b* transcriptional activity (*4*). *Pto* DC3000 *hrcC*$^-$ caused an increase in enhanced green fluorescent protein (eGFP) mRNA levels in both transgenic lines, indicating the presence of PAMP-responsive elements upstream of *At-miR393a* and *At-miR393b* (Fig. 2B). However, this induction was compromised by *Pto* DC3000, as was induction of the *FRK1* control (Fig. 2B). These results suggest that some *Pto* DC3000 effectors suppress PAMP-triggered transcriptional activation of *At-miR393a* and *At-miR393b*.

To test this hypothesis, we engineered constructs to deliver distinct *Pto* DC3000 effectors into leaves of the *Arabidopsis efr* mutant, which sustains efficient *Agrobacterium*-mediated transient transformation (*14*) without affecting pri-miRNA, mature miRNA, or miRNA target levels (fig. S4). Bacterial effector expression was confirmed (fig. S5A), and pri-miRNA levels were subsequently monitored. AvrPtoB, an effector with E3-ubiquitin ligase activity (*15*), down-regulated pri-miR393a and pri-miR393b accumulation without affecting the PAMP-insensitive pri-miR166a (Fig. 2C). This effect occurs, at least in part, at the transcriptional level because AvrPtoB delivery into *At*-miR393a-p::eGFP/*efr* and *At*-miR393b-p::eGFP/*efr* leaves inhibited both basal expression and PAMP-triggered induction of *eGFP* (Fig. 2, E and F, and fig. S5B). Similar effects were obtained with AvrPtoB$_{F525A}$, a stable mutant in which the E3-ligase activity is abolished (Fig. 2, D to F, and fig. S5B). Therefore, AvrPtoB suppresses *At-miR393a* and *At-miR393b* transcription independently of its E3-ligase activity, as was previously shown for AvrPtoB-mediated suppression of PAMP-responsive *FRK1* (*16*).

To assay for interference with miRNA biogenesis or stability, levels of several PAMP-insensitive and -sensitive miRNAs were monitored upon transient effector delivery into *efr* leaves. Three bacterial effectors consistently reduced the accumulation of unrelated miRNAs (Fig. 3A and figs. S5, A to C, and S6), among which AvrPto is a well-characterized *Pto* DC3000 effector with demonstrated virulence function (fig. S9) (*17*). Further molecular analysis revealed that AvrPto-mediated reduction in miRNA accumulation may occur, at least in part, at the posttranscriptional level, because AvrPto did not alter pri-miRNA transcript levels (fig. S7A). Accordingly, conditional AvrPto expression in stable transgenic lines stabilizes miR393 precursors and concomitantly decreases accumulation of mature miR393, with no or little effects on pri-miR393 transcript levels (Fig. 3, B and C, and fig. S7B). Therefore, AvrPto possibly interferes with the processing of some miRNA precursors, a phenomenon also observed during *Pto* DC3000 infection (Fig. 3C and fig. S8).

AvrPto interacts with, and inhibits the kinase activity of, multiple transmembrane PRRs (*18*). Moreover, AvrPto strongly interacts with BAK1 (BRI1-associated receptor-kinase 1), a shared signaling partner of the brassinosteroid receptor BRI1 (brassinosteroid-insensitive 1) and the flagellin receptor FLS2 (flagellin sensing 2) (*19*–*21*). The AvrPto-BAK1 interaction compromises the ligand-dependent FLS2-BAK1 association resulting in suppression of PTI (*19*). Accordingly, AvrPto$_{Y89D}$, which is unable to interact with PRRs and BAK1 (*18*, *19*), displays compromised virulence function (*18*). Transient delivery of AvrPto$_{Y89D}$ did not alter miRNA accumulation, nor did delivery of AvrPto$_{G2A}$, carrying a mutated myristoylation site that disrupts AvrPto host plasma membrane localization (Fig. 3A and fig. S5C) (*16*, *22*). Conditional expression of an N-terminal histidine-tagged version of AvrPto (6xHis-AvrPto) displaying similarly compromised subcellular localization and virulence function gave comparable results (Fig. 3, B and C, and fig. S9). We conclude that AvrPto interferes with miRNA accumulation and that this interference is linked to its virulence function [supporting online material (SOM) text].

Finally, we tested whether *Pto* DC3000 effectors could also suppress miRNA activity. We used the SUC-*SUL* (SS) reporter line in which phloem-specific expression of an inverted-repeat transgene triggers non–cell-autonomous RNA interference (RNAi) of the endogenous SULPHUR (SUL) transcript, causing vein-centered chlorosis (*23*). Of the 21-nucleotide (nt) (DCL4-dependent) and 24-nt (DCL3-dependent) *SUL* siRNA species, only the former is required for RNAi in an AGO1-dependent manner (*23*). Stable transgenic lines

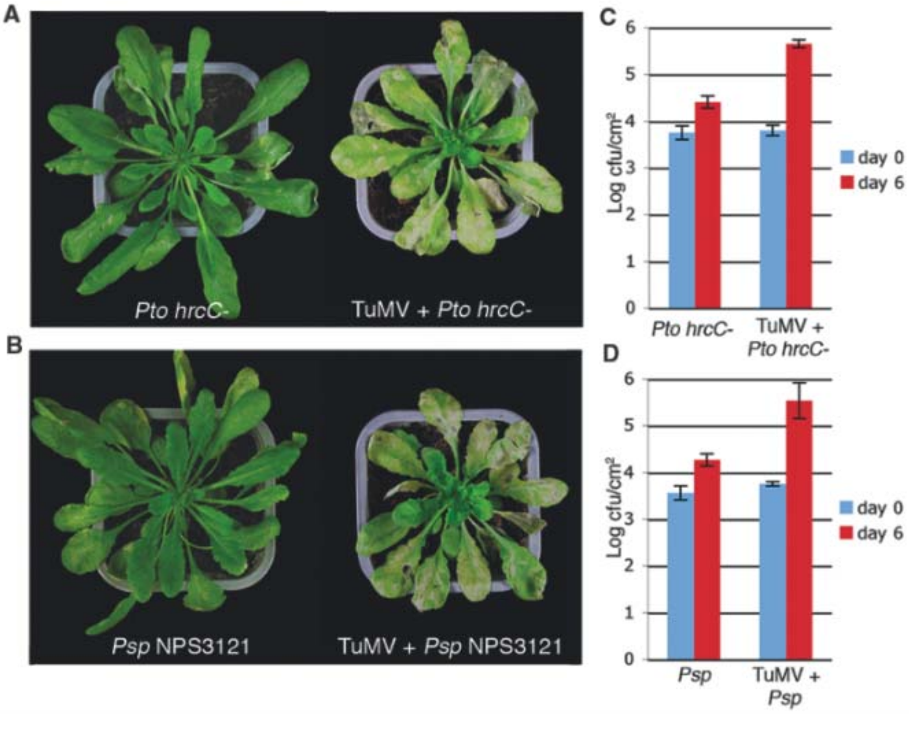

Fig. 4. TuMV infection enhances growth of and rescues symptoms induced by *Pto* DC3000 *hrcC*$^-$ and *Psp* NPS3121. (**A**) Five-week-old Col-0 plants were infected for 7 days with TuMV and further challenged with *Pto* DC3000 *hrcC*$^-$ at a concentration of 10^6 CFU/ml. The picture was taken 5 days after bacterial infiltration. (**B**) Same as in (A), but with *Psp* NPS3121. (**C**) Growth of *Pto* DC3000 *hrcC*$^-$ in mock-inoculated or TuMV-infected Col-0 plants 6 days after bacterial injection. Error bars indicate SE of log-transformed data from five independent samples. Similar results were obtained in two independent experiments. (**D**) Same as in (C), but with *Psp* NPS3121.

overexpressing HopT1-1 (fig. S10) exhibited attenuated chlorosis (Fig. 3E) and accumulated higher *SUL* mRNA levels (Fig. 3G). However, the *SUL* siRNA levels remained unchanged (Fig. 3D), mimicking the reported effects of the *ago1-12* mutation in SS (*23*). Also as in *ago1-12*, canonical miRNAs accumulated normally in HopT1-1–overexpressing lines, despite higher levels of miRNA target transcripts (Fig. 3, F and G, and fig. S11), suggesting that HopT1-1 probably suppresses slicing mediated by AGO1. Further transient overexpression of HopT1-1 in *efr* plants showed a dramatic increase in the protein, but not mRNA, levels of the miR834 target COP1-interacting protein 4 (CIP4) (Fig. 3H and fig. S12, A and B). Thus, HopT1-1 additionally, and perhaps predominantly, suppresses miRNA-directed translational inhibition, which is consistent with the involvement of AGO1 in this second process (*24*). Similarly, higher protein levels of CIP4 and of the copper/zinc superoxide dismutase 1 (CSD1-miR398 target) were detected in plants infected with virulent *Pto* DC3000 (Fig. 3H and fig. S12C), with no effect on CSD1, CIP4, and some other miRNA target transcript levels (fig. S13).

We show here that the miRNA pathway plays a major role in antibacterial basal defense and, accordingly, we have identified bacterial suppressors of RNA silencing, or BSRs. This finding provides a plausible explanation for the synergistic interactions observed in the field between some viral and bacterial phytopathogens. Consistent with this idea, we found that infection by *Turnip Mosaic Virus* (TuMV), which produces the P1-HcPro suppressor of siRNA and miRNA functions (*25*, *26*), reduces basal and nonhost resistances to promote growth and diseaselike symptoms from nonvirulent *Pto* DC3000 *hrcC*$^-$ and *Psp* NPS3121 bacteria (Fig. 4). It will now be important to elucidate how silencing factors are modified by VSRs and BSRs, and whether such modifications are sensed by specific resistance (R) proteins as postulated by the "guard hypothesis" (*27*).

The implication of the miRNA pathway in innate immunity is not specific to plants. For example, human *MiR146* is induced by several microbial components (*28*). Because type III secretion systems are widespread across Gram-negative bacteria (*29*), the intriguing possibility emerges that human pathogenic bacteria also have evolved to suppress RNA silencing to cause disease.

References and Notes

1. D. Baulcombe, *Nature* **431**, 356 (2004).
2. B. Yu *et al.*, *Science* **307**, 932 (2005).
3. S. W. Ding, O. Voinnet, *Cell* **130**, 413 (2007).
4. L. Navarro *et al.*, *Science* **312**, 436 (2006).
5. S. Katiyar-Agarwal *et al.*, *Proc. Natl. Acad. Sci. U.S.A.* **103**, 18002 (2006).
6. A. Agorio, P. Vera, *Plant Cell* **19**, 3778 (2007).
7. S. Katiyar-Agarwal, S. Gao, A. Vivian-Smith, H. Jin, *Genes Dev.* **21**, 3123 (2007).
8. N. Fahlgren *et al.*, *PLoS One* **2**, e219 (2007).
9. J. Yuan, S. Y. He, *J. Bacteriol.* **178**, 6399 (1996).
10. M. de Torres *et al.*, *Plant J.* **47**, 368 (2006).
11. X. Li *et al.*, *Proc. Natl. Acad. Sci. U.S.A.* **102**, 12990 (2005).
12. J. Li, Z. Yang, B. Yu, J. Liu, X. Chen, *Curr. Biol.* **15**, 1501 (2005).
13. T. Asai *et al.*, *Nature* **415**, 977 (2002).
14. C. Zipfel *et al.*, *Cell* **125**, 749 (2006).
15. R. Janjusevic, R. B. Abramovitch, G. B. Martin, C. E. Stebbins, *Science* **311**, 222 (2006).
16. P. He *et al.*, *Cell* **125**, 563 (2006).
17. P. Hauck, R. Thilmony, S. Y. He, *Proc. Natl. Acad. Sci. U.S.A.* **100**, 8577 (2003).
18. T. Xiang *et al.*, *Curr. Biol.* **18**, 74 (2008).
19. L. Shan *et al.*, *Cell Host Microbe* **4**, 17 (2008).
20. D. Chinchilla *et al.*, *Nature* **448**, 497 (2007).
21. J. Li *et al.*, *Cell* **110**, 213 (2002).
22. L. Shan, V. K. Thara, G. B. Martin, J. M. Zhou, X. Tang, *Plant Cell* **12**, 2323 (2000).
23. P. Dunoyer, C. Himber, V. Ruiz-Ferrer, A. Alioua, O. Voinnet, *Nat. Genet.* **39**, 848 (2007).
24. P. Brodersen *et al.*, *Science* **320**, 1185 (2008).
25. K. D. Kasschau, J. C. Carrington, *Cell* **95**, 461 (1998).
26. K. D. Kasschau *et al.*, *Dev. Cell* **4**, 205 (2003).
27. J. L. Dangl, J. D. Jones, *Nature* **411**, 826 (2001).
28. K. D. Taganov, M. P. Boldin, K. J. Chang, D. Baltimore, *Proc. Natl. Acad. Sci. U.S.A.* **103**, 12481 (2006).
29. L. J. Mota, G. R. Cornelis, *Ann. Med.* **37**, 234 (2005).
30. We thank Y. Yamamoto, A. Collmer, J. Alfano, G. Martin, C. Zipfel, E. Cascales, G. Preston, P. Hauck, and Y. B. Kwack for materials. This work was supported by a fellowship from the Federation of European Biochemical Societies (L.N.), an Action Thématique Incitative sur Programme grant from the CNRS, a grant from European Union–integrated project SIROCCO (Silencing RNAs: Organisers and Coordinators of Complexity in Eukaryotic Organisms) (LSHG-CT-2006-037900) to O.V., and U.S. NIH grant 5R01AI060761 (K.N. and S.Y.H.). Support from the Fondation Lilliane Bettencourt for Life Science to O.V.'s lab is also acknowledged.

Supporting Online Material

www.sciencemag.org/cgi/content/full/321/5891/964/DC1
Materials and Methods
SOM Text
Figs. S1 to S13
References

23 April 2008; accepted 15 July 2008
10.1126/science.1159505

Arsenic(III) Fuels Anoxygenic Photosynthesis in Hot Spring Biofilms from Mono Lake, California

T. R. Kulp,[1] S. E. Hoeft,[1] M. Asao,[2] M. T. Madigan,[2] J. T. Hollibaugh,[3] J. C. Fisher,[3]* J. F. Stolz,[4] C. W. Culbertson,[5] L. G. Miller,[1] R. S. Oremland[1]†

Phylogenetic analysis indicates that microbial arsenic metabolism is ancient and probably extends back to the primordial Earth. In microbial biofilms growing on the rock surfaces of anoxic brine pools fed by hot springs containing arsenite and sulfide at high concentrations, we discovered light-dependent oxidation of arsenite [As(III)] to arsenate [As(V)] occurring under anoxic conditions. The communities were composed primarily of *Ectothiorhodospira*-like purple bacteria or *Oscillatoria*-like cyanobacteria. A pure culture of a photosynthetic bacterium grew as a photoautotroph when As(III) was used as the sole photosynthetic electron donor. The strain contained genes encoding a putative As(V) reductase but no detectable homologs of the As(III) oxidase genes of aerobic chemolithotrophs, suggesting a reverse functionality for the reductase. Production of As(V) by anoxygenic photosynthesis probably opened niches for primordial Earth's first As(V)-respiring prokaryotes.

Anoxygenic photosynthesis, common to photosynthetic bacteria and certain cyanobacteria (e.g., *Oscillatoria*), harvests electrons from low–electrochemical potential donors and shunts them toward the reduction of CO$_2$ for incorporation into biomass. This mechanism of photoautotrophy typically uses hydrogen sulfide as an electron donor and a single photosystem as a catalyst, oxidizing sulfide to sulfur and sulfate to support the growth of phototrophs in anoxic sulfidic environments exposed to light, such as laminated microbial mats (*1*, *2*) and the pycnoclines of stratified lakes (*3*, *4*).

Oxygenic photosynthesis characteristic of plants, algae, and cyanobacteria uses two photosystems and harvests electrons from water, resulting in the evolution of molecular oxygen. Oxygenic photosynthesis changed Earth's atmosphere from reducing to oxidizing, a process that could have begun as early as 2.7 billion years ago (Ga) during the late Archean (3.8 to 2.5 Ga) based on the presence of cyanobacterial biomarkers in sedimentary rocks of this age (*5*). However, the key cyanobacterial biomarkers in ancient rocks, namely 2-methyl hopanes (*6*), also occur (as 2-methylhopane polyols) in photosynthetic bacteria (*7*); both cyanobacteria and photosynthetic bacteria appear to have formed the laminated mat structures found in ancient sedimentary rocks (*8*). Hence, anoxygenic photosynthesis may well have been widespread in the Archean (*9*). This conclusion is underscored by the discoveries that in addition to reduced sulfur compounds, Fe^{2+} (*10*, *11*) as well as NO$_2^-$ (*12*) serve as electron donors for anoxygenic photosynthesis carried out by photosynthetic bacteria.

---

[1] U.S. Geological Survey (USGS), Menlo Park, CA 94025, USA. [2] Department of Microbiology, Southern Illinois University, Carbondale, IL 62901, USA. [3] Department of Marine Sciences, University of Georgia, Athens, GA 30602, USA. [4] Department of Biological Sciences, Duquesne University, Pittsburgh, PA 15282, USA. [5] USGS Water Sciences Center, Augusta, ME 04330, USA.

*Present address: Division of Earth and Ecosystem Science, Desert Research Institute, Las Vegas, NV 89119, USA.
†To whom correspondence should be addressed. E-mail: roremlan@usgs.gov

Here, we supply evidence for As(III)-supported anoxygenic photosynthesis in naturally occurring microbial mats of cyanobacteria and photosynthetic bacteria from Mono Lake, California, hot springs and provide evidence of photoautotrophic growth of pure cultures of purple bacteria supported by As(III) oxidation to As(V). Because the only previously reported biogenic oxidation of As(III) was by chemolithotrophic (nonphototrophic) bacteria that require strong oxidants such as oxygen (*13*) or nitrate (*14*), it was assumed that dissimilatory arsenic reduction, a widely distributed microbial process that requires As(V) as an electron acceptor, arose only after the evolution of oxygenic photosynthesis (*15*). The ability of phototrophic prokaryotes to generate As(V) from As(III) under anoxic conditions (electrochemical potential = E_o' AsO_3^{3-}/AsO_4^{3-} = +139 mV) requires that the antiquity of prokaryotic arsenate respiration be reevaluated and has important implications for all aspects of the arsenic cycle.

We sampled two small hot spring–fed ponds, termed "green" and "red," located on the southeastern shore of Paoha Island in Mono Lake, California (37°59.633′ N, 119°01.376′ W), an area with numerous gaseous hydrocarbon seeps (*16*). Both habitats were alkaline, anoxic, and saline, and both contained arsenite and arsenate at high concentrations, as well as other dissolved reductants (methane, sulfide, and ammonia). The hot springs and ponds of Paoha Island lacked any visual evidence of Fe(III) oxides typical of acidic or circumneutral hot springs and also had low dissolved Fe(II) concentrations (≤0.7 μM). Although of similar chemistry (Table 1), the two ponds showed pronounced color differences due to the 1- to 2-mm-thick biofilms that completely covered their submerged rock cobble surfaces (Fig. 1). The green biofilm (67°C, Fig. 1A) was dominated by filamentous *Oscillatoria*-like cyanobacteria (Fig. 1B), whereas the red biofilm (43°C, Fig. 1C) contained mainly purple photosynthetic bacteria (Fig. 1 D). Obtaining smooth absorption spectra of the original mat material was complicated by the abundance of inorganic material present in the samples. However, small peaks at 850 and 795 nm, suggestive of bacteriochlorophyll a, were obtained from the red mat sample, and peaks at 664 and 638 nm, suggestive of chlorophyll a and phycocyanin, respectively, were obtained from the green mat sample.

Incubation of slurried biofilms showed As(III) oxidation linked to anoxygenic photosynthesis (*17*). Slurries from the green mat slowly oxidized As(III) to As(V) under anoxic conditions in the light but not in the dark (Fig. 2A) or in heat-killed controls incubated in the light (fig. S1A). Similarly, red mat material also oxidized As(III), and subsequent injected pulses of 1 mM and 5 mM As(III) were completely oxidized to As(V) (Fig. 2B). In contrast, a 0.25 mM As(III) addition was not oxidized by dark, anoxic controls or by killed controls incubated in the light (fig. S1, B and C). Red mat material incubated in an N_2 atmosphere oxidized ~1 mM As(III) completely to As(V) within 20 hours, with no corresponding oxidation occurring in the dark-incubated controls under N_2 (Fig. 2C). Similarly, oxidative loss of sulfide occurred under light/anoxic but not dark/anoxic conditions (Fig. 2D). Red mat material also demonstrated incorporation of ^{14}C-bicarbonate into cell material when incubated in the light under anoxic conditions with the following electron donors (percent radiotracer incorporated ± 1 SD, $n = 3$ slurries): none (0.29 ± 0.02), 100% methane headspace (0.28 ± 0.03), 2 mM As(III) (0.48 ± 0.04), and 2 mM sulfide (1.47 ± 0.23). In contrast, anoxic dark-incubated mat samples that were otherwise incubated as above all incorporated ≤0.007% (SD ≤ 0.002) of the added tracer. These results demonstrate that photoautotrophic CO_2 fixation can be linked to As(III) oxidation by cells in the red biofilm.

To obtain conclusive evidence for As(III)-linked anoxygenic photosynthesis, we isolated two axenic strains of a photosynthetic purple bacterium that displayed As(III)-dependent growth (*17*). One isolate, designated strain PHS-1 and studied in detail, oxidized As(III) and grew as a photoautotroph reaching high cell densities (Fig. 3, A and B). In contrast, strain PHS-1 did not grow in light-incubated control cultures lacking As(III), or in dark-incubated cultures that contained As(III) (Fig. 3B), in which no production of As(V) occurred (i.e., control arsenate concentrations remained at the carry-over levels of ~0.9 ± 0.1 mM throughout the 200 hours of incubation). Arsenite additions (2 or 4 mM) were made as a series of injections over the time course because high initial arsenite concentrations (~5 mM) were found to inhibit growth. In such experiments, a cumulative total of 12 mM injected As(III) was stoichiometrically converted to As(V) in phototrophic cultures (Fig. 3A). Growing cell suspensions of strain PHS-1 turned from light pink to the deep red color of natural populations (Fig. 1C), and absorption spectra confirmed that the cells contained bacteriochlorophyll a. Peaks near 800, 850, and 880 nm in the spectrum of intact cells of strain PHS-1, along with the major peak at 769 nm in methanol extracts of cells, are typical of purple bacteria containing bacteriochlorophyll a (fig. S2).

Cells of strain PHS-1 grown phototrophically on As(III) were motile and indistinguishable from

Table 1. Physical and chemical properties of the two Paoha Island hot spring–fed ponds compared with Mono Lake surface water.

Parameter	Red pond	Green pond	Mono Lake*
Temperature (°C)	43	67	20
Salinity (g/liter)	25	32	84
Dissolved O_2 (μM)	1.0	1.6	120
pH	9.4	9.3	9.8
Arsenite (μM)	92.0	68.4	0
Arsenate (μM)	9.7	65.1	200
Sulfide (mM)	5.8	5.0	0
Ammonia (mM)	1.2	1.4	0
Dissolved organic carbon (mM)	2.2	ND†	6.7
Methane (μM)	430	360	1.0
Ethane (μM)	4.0	4.0	0

*Mono Lake surface water data compiled from several sources (*17*). †ND, not determined.

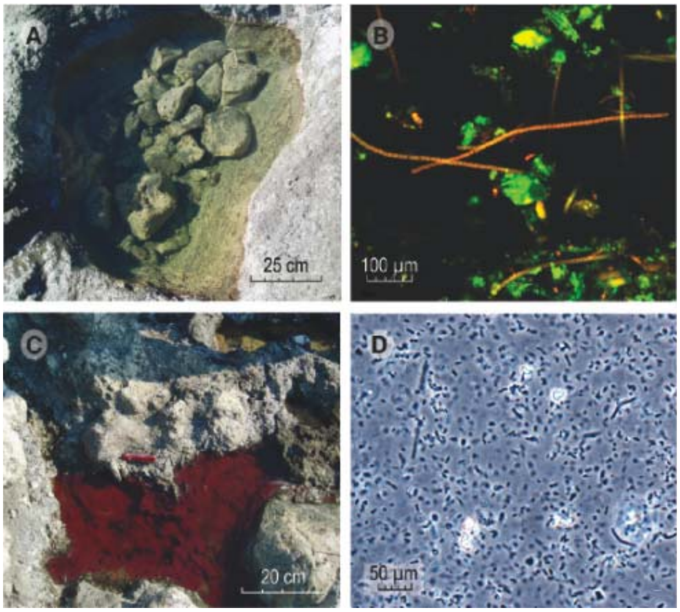

Fig. 1. Photographic and microscopic images of the hot spring–fed pools on Paoha Island. (**A**) Green pool. (**B**) Confocal microscopic image of green pool biofilm microbes showing a fluorescing *Oscillatoria*-like cyanobacterium. (**C**) Red pool. (**D**) Photomicrographic image of red pool biofilm material composed primarily of *Ectothiorhodospira*-like bacteria.

sulfide-grown cells (fig. S3). Phylogenetic analysis of 16*S* ribosomal RNA (rRNA) gene sequences indicated that strain PHS-1 is a member of the gamma-Proteobacteria genus *Ectothiorhodospira* and most closely related to the species *Ectothiorhodospira shaposhnikovii* (99.4% 16*S* rRNA gene sequence identity, Fig. 3C). The 16*S* rRNA gene sequence of strain PHS-1 was identical to that of strain MLP2, a second organism obtained from the red mat, but isolated with sulfide instead of As(III). Photoautotrophic growth of strain MLP2 was also stimulated by As(III), because growth yields in media containing 1 mM each of sulfide and As(III) were ~50% higher than controls containing sulfide alone. This suggests that the electron donor (sulfide versus arsenite) used for enrichment and isolation was not a factor in selecting for the As(III)-oxidizing phenotype. However, *Ectothiorhodospira* sp. strain ML Ecto, a purple bacterium previously isolated from an As(III)-oxidizing photosynthetic enrichment culture obtained from Mono Lake sediment (*18*), did not grow photoautotrophically on As(III).

Our experimental observations of the green mats (Fig. 2A) suggested that the *Oscillatoria*-type cyanobacteria that dominated the mat may also be capable of As(III)-supported anoxygenic photosynthesis. The pattern of light-dependent As(III) oxidation by the cyanobacterial mat was very similar to that of the red mat (Fig. 2, B and C), although the results with the green mat have not yet been confirmed with pure cultures in the

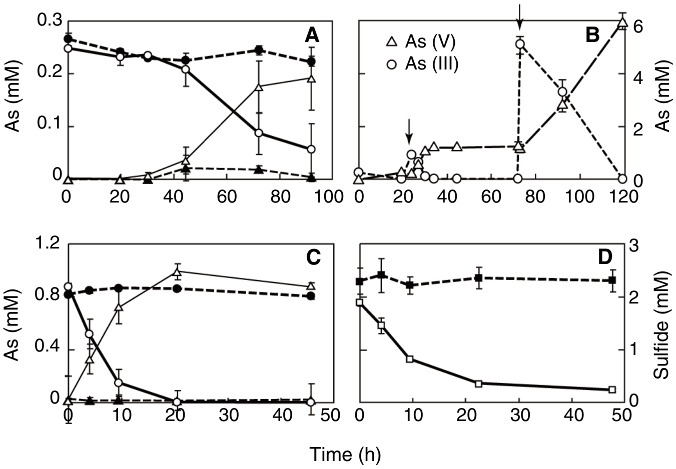

Fig. 2. Time-course incubations of slurried biofilm material incubated under anoxic conditions in the light (open symbols) or dark (closed symbols) at 45°C. Circles represent As(III), triangles represent As(V), and squares represent sulfide. Results represent the mean of three slurries, and bars indicate ±1 SD. (**A**) Oxidation of As(III) to As(V) by green pool biofilms. (**B**) Oxidation of As(III) to As(V) by red pool biofilms. Arrows indicate additions of As(III). (**C**) Short-term oxidation of As(III) to As(V) in light-incubated and dark-incubated red pool biofilms. (**D**) Oxidative loss of sulfide by red pool biofilms incubated in the light or dark.

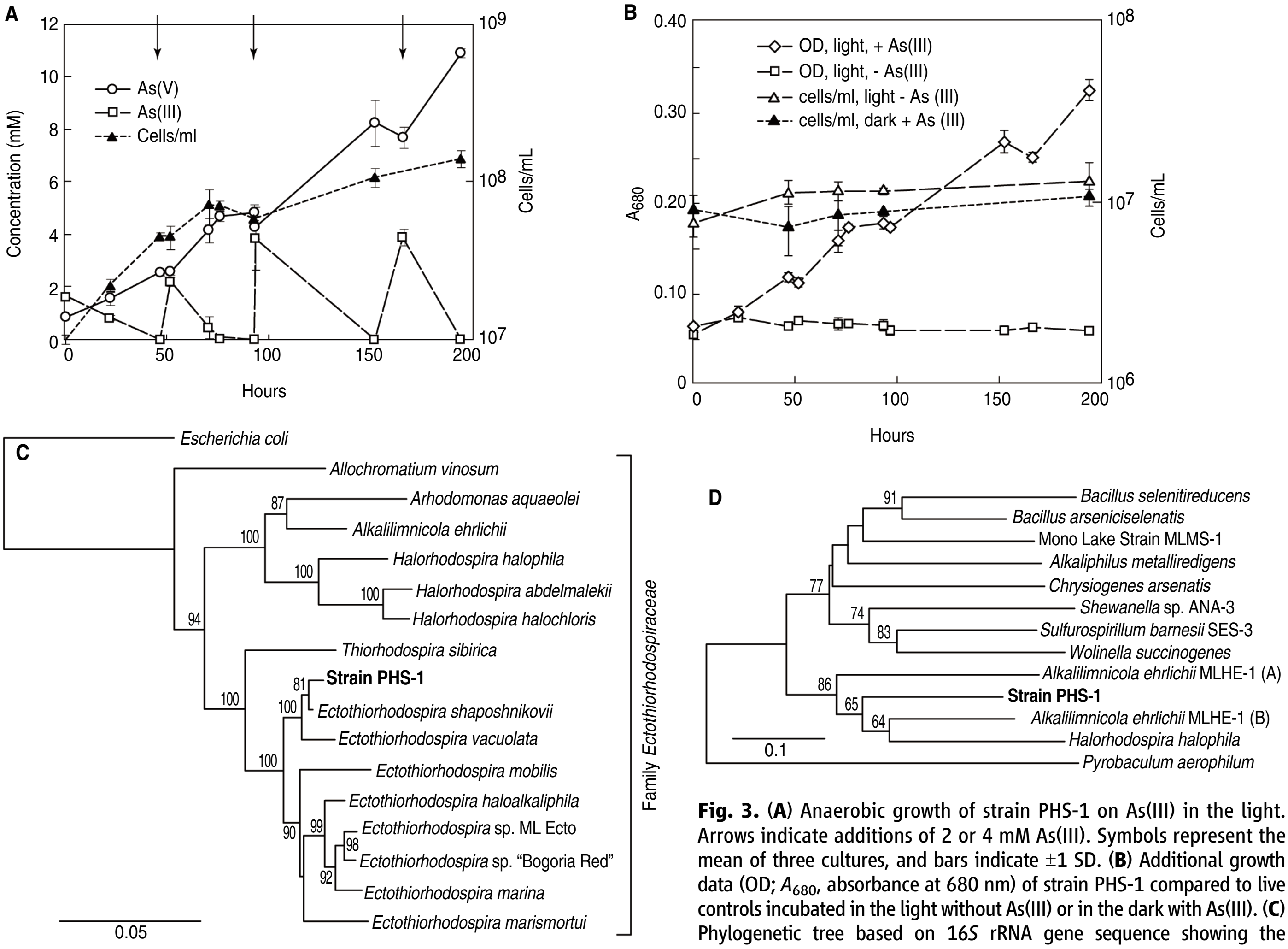

Fig. 3. (**A**) Anaerobic growth of strain PHS-1 on As(III) in the light. Arrows indicate additions of 2 or 4 mM As(III). Symbols represent the mean of three cultures, and bars indicate ±1 SD. (**B**) Additional growth data (OD; A_{680}, absorbance at 680 nm) of strain PHS-1 compared to live controls incubated in the light without As(III) or in the dark with As(III). (**C**) Phylogenetic tree based on 16*S* rRNA gene sequence showing the relationship of strain PHS-1 to other species of *Ectothiorhodospiraceae*. All sequences have been deposited in GenBank, and accession numbers are listed in the supporting online material (SOM). (**D**) Phylogenetic tree based on ArrA-like gene sequences showing the relationship between strain PHS-1 genes with others from the GenBank database. Accession numbers are given in the SOM.

laboratory as was done with strain PHS-1 (Fig. 3, A and B). Nevertheless, pure cultures of certain cyanobacteria (e.g., *Oscillatoria limnetica*) are known to use sulfide as an electron donor in anoxygenic photosynthesis (*19*). The oxidation of As(III) to As(V) by the Paoha cyanobacteria may be a second example of a two-electron transition—being analogous to the oxidation of H_2S to S^0 by *O. limnetica* (*19*). Phototrophic microorganisms may also contribute to As(III) oxidation in other environments, such as the chemically diverse hot springs of Yellowstone National Park, many of which contain arsenite (*20–22*), thereby broadening the ecological importance of the phenomenon described here.

Despite the clear evidence for arsenite oxidation by strain PHS-1, we were unable to obtain an amplicon for arsenite oxidase (*aoxB*) (*17*). This result was surprising because the gene is highly conserved across broad phylogenetic lineages (*23*) and primer sets have been successfully used for identifying *aoxB* in both pure cultures and environmental samples (*22*, *24*). An amplicon was obtained when primers for dissimilatory arsenate reductase designed for halophilic prokaryotes (*25*) were used. This occurred even though strain PHS-1 did not grow in the dark with 10 mM As(V) as the electron acceptor and 10 mM lactate, 10 mM acetate, or 4 mM sulfide as the electron donor [i.e., no loss of As(V) or production of As(III) and all optical densities (ODs) remained below 0.07 after 8 days of incubation]. The putative ArrA homolog for strain PHS-1 showed a high degree of sequence identity (~68%) to proteins from two other *Ectothiorhodospiraceae*, *Alkalilimnicola ehrlichii* and *Halorhodospira halophila* (Fig. 3D). *A. ehrlichii* is a nonphototrophic As(III)-oxidizing chemolithoautotroph that was isolated from the water column of Mono Lake (*14*). Analysis of its entire annotated genome revealed that it also lacks genes encoding an arsenite oxidase (e.g., *aoxAB*) but it does have two putative *arr* operons (*14*). Arsenic metabolism was not studied in *H. halophila* (*26*) although its genome contains a homolog of *arrA* (Fig. 3D) annotated as a "formate dehydrogenase." These results suggest that in the *Ectothiorhodospiraceae*, the Arr homolog is functioning in reverse or that an unknown mechanism for arsenite oxidation exists that carries out this process under anoxic conditions. Either way, it appears there are at least two distinct mechanisms for arsenite oxidation.

Over the past decade, several phylogenetically diverse microorganisms have been described that conserve energy from the oxidation or reduction of arsenic oxyanions and include deep lineages of both Bacteria and Archaea (*15*). In certain environments, a robust arsenic biogeochemical cycle supports a diverse microbial community (*25*, *27*). Our discovery of anaerobic photosynthetic oxidation of As(III) adds an important new dimension to the arsenic cycle and highlights a previously unsuspected mechanism that may have been essential for establishing and maintaining the arsenic cycle on the ancient anoxic Earth.

References and Notes

1. R. W. Castenholz, J. Bauld, B. B. Jørgensen, *FEMS Microbiol. Ecol.* **74**, 325 (1990).
2. D. J. Des Marais, *Adv. Microb. Ecol.* **14**, 251 (1995).
3. D. A. Culver, G. J. Brunskill, *Limnol. Oceanogr.* **14**, 862 (1969).
4. J. E. Cloern, B. E. Cole, R. S. Oremland, *Limnol. Oceanogr.* **28**, 1049 (1983).
5. J. J. Brocks, R. Buick, R. E. Summons, *Science* **285**, 1033 (1999).
6. R. E. Summons, L. L. Jahnke, J. M. Hope, G. A. Logan, *Nature* **400**, 554 (1999).
7. S. E. Rashby, A. L. Sessions, R. E. Summons, D. K. Newman, *Proc. Natl. Acad. Sci. U.S.A.* **104**, 15099 (2007).
8. T. Bosak, S. E. Greene, D. K. Newman, *Geobiology* **5**, 119 (2007).
9. M. M. Tice, D. R. Lowe, *Nature* **431**, 549 (2004).
10. F. Widdel, S. Schnell, S. A. Ehrenreich, B. Assmus, B. Schink, *Nature* **362**, 834 (1993).
11. A. Ehrenreich, F. Widdel, *Appl. Environ. Microbiol.* **60**, 4517 (1994).
12. B. M. Griffin, J. Schott, B. Schink, *Science* **316**, 1870 (2007).
13. J. M. Santini, L. I. Sly, R. D. Schnagl, J. M. Macy, *Appl. Environ. Microbiol.* **66**, 92 (2000).
14. S. E. Hoeft *et al.*, *Int. J. Syst. Evol. Microbiol.* **57**, 504 (2007).
15. R. S. Oremland, J. F. Stolz, *Science* **300**, 939 (2003).
16. R. S. Oremland, L.G. Miller, M. J. Whiticar, *Geochim. Cosmochim. Acta* **51**, 2915 (1987).
17. See supporting material on *Science* Online.
18. C. R. Budinoff, J. T. Hollibaugh, *ISME J.* **2**, 340 (2008).
19. Y. Cohen, E. Padan, M. Shilo, *J. Bacteriol.* **123**, 855 (1975).
20. C. R. Jackson, H. W. Langner, J. Donahoe-Christiansen, W. P. Inskeep, T. R. McDermott, *Environ. Microbiol.* **3**, 532 (2001).
21. S. D'Imperio, C. R. Lehr, M. Breary, T. R. McDermott, *Appl. Environ. Microbiol.* **73**, 7067 (2007).
22. W. P. Inskeep *et al.*, *Environ. Microbiol.* **9**, 934 (2007).
23. J. F. Stolz, P. Basu, J. M. Santini, R. S. Oremland, *Annu. Rev. Microbiol.* **60**, 107 (2006).
24. E. D. Rhine, N. Chadhain, G. J. Zylstra, L. Y. Young, *Biochem. Biophys. Res. Commun.* **354**, 662 (2007).
25. T. R. Kulp *et al.*, *Appl. Environ. Microbiol.* **72**, 6514 (2006).
26. J. C. Raymond, W. R. Sistrom, *Arch. Mikrobiol.* **69**, 121 (1969).
27. R. S. Oremland *et al.*, *Science* **308**, 1305 (2005).

28. We are grateful to the NASA Exobiology Program, the USGS, and NSF for providing research support. R. Jellison kindly made available his Mono Lake dataset to us. We thank J. Santini, D. K. Newman, J. E. Cloern, and C. Saltikov for constructive criticisms of earlier drafts of this manuscript and T. Crowe, S. Baesman, and T. Bennett for field assistance. The GenBank accession number for the arrA homolog is EU869183.

Supporting Online Material

www.sciencemag.org/cgi/content/full/321/5891/967/DC1
Methods
Figs. S1 to S3
References

21 May 2008; accepted 11 July 2008
10.1126/science.1160799

In Vivo Imaging Reveals an Essential Role for Neutrophils in Leishmaniasis Transmitted by Sand Flies

Nathan C. Peters,[1]* Jackson G. Egen,[2]*† Nagila Secundino,[1] Alain Debrabant,[3] Nicola Kimblin,[1] Shaden Kamhawi,[1] Phillip Lawyer,[1] Michael P. Fay,[4] Ronald N. Germain,[2]‡ David Sacks[1]†‡

Infection with the obligate intracellular protozoan *Leishmania* is thought to be initiated by direct parasitization of macrophages, but the early events following transmission to the skin by vector sand flies have been difficult to examine directly. Using dynamic intravital microscopy and flow cytometry, we observed a rapid and sustained neutrophilic infiltrate at localized sand fly bite sites. Invading neutrophils efficiently captured *Leishmania major* (*L.m.*) parasites early after sand fly transmission or needle inoculation, but phagocytosed *L.m.* remained viable and infected neutrophils efficiently initiated infection. Furthermore, neutrophil depletion reduced, rather than enhanced, the ability of parasites to establish productive infections. Thus, *L.m.* appears to have evolved to both evade and exploit the innate host response to sand fly bite in order to establish and promote disease.

Many parasitic diseases are transmitted by the bite of an infected arthropod, yet the dynamics of the host-parasite interaction in this context remain largely uncharacterized. Transmission of *Leishmania* by infected sand fly bite represents an attractive experimental system to study early inflammatory responses and relate these processes to the establishment of an infectious disease. Leishmaniasis is thought to be initiated by direct parasitization of macrophages after deposition into the skin (*1*). However, the ability of neutrophils to rapidly respond to and efficiently phagocytose a variety of pathogens suggests that they may also be an initial target of *Leishmania* infection (*2–4*). Indeed, after needle injection of *Leishmania major* (*L.m.*), infected neutrophils have been observed, and both host-protective and disease-promoting roles for these cells have been reported (*5–10*). How-

---

[1]Laboratory of Parasitic Diseases, National Institute of Allergy and Infectious Diseases, Bethesda, MD 20892, USA. [2]Laboratory of Immunology, National Institute of Allergy and Infectious Diseases, Bethesda, MD 20892, USA. [3]Laboratory of Bacterial, Parasitic, and Unconventional Agents, Division of Emerging and Transfusion Transmitted Diseases, Center for Biologics Evaluation and Research, U.S. Food and Drug Administration, Bethesda, MD 20892, USA. [4]Biostatistics Research Branch, National Institute of Allergy and Infectious Diseases, Bethesda, MD 20892, USA.

*These authors contributed equally to this work.
†To whom correspondence should be addressed. E-mail: dsacks@nih.gov (D.S.); jegen@niaid.nih.gov (J.G.E.)
‡These authors contributed equally to this work.

ever, the role of neutrophils has never been addressed in sand fly–transmitted *Leishmania* infections.

Sand fly biting involves wounding of the microvasculature to create a hemorrhagic pool from which to feed, a process that initiates a strong local inflammatory response (*11*–*13*). To further characterize the host response at the site of sand fly bite, we allowed uninfected or *L.m.*-infected *Phlebotomus duboscqi* sand flies, a natural vector of *L.m.*, to feed on the ears of C57BL/6 mice (*14*, *15*), which develop self-healing cutaneous lesions similar to the human disease. Flow cytometric analysis revealed a marked and sustained infiltration of neutrophils into the skin accompanied by a substantial recruitment of macrophages, regardless of the infectious status of the flies (Fig. 1, A and B). To visualize the bite site in vivo, we used a red fluorescent protein (RFP)–expressing strain of *L.m.* (*L.m.*-RFP) (*14*) (fig. S1, A to D) and mice expressing enhanced green fluorescent protein (eGFP) under the control of the endogenous lysozyme M promoter (LYS-eGFP mice) (*16*). eGFP^{hi} cells recovered from the skin of LYS-eGFP mice after *L.m.* infection are CD11b^{hi}Gr-1^{hi}F4/80$^-$MHCII$^-$ neutrophils, whereas eGFP^{lo} cells represent CD11b$^+$F4/80$^+$ MHCII$^{+/-}$Gr-1$^-$ monocyte/macrophage populations (fig. S1, E to G; see also fig. S1, H to K). Two hours after exposure of the ventral ear pinnae of LYS-eGFP mice to either uninfected or *L.m.*-RFP–infected sand flies, eGFP^{hi} neutrophils accumulated at sites of proboscis penetration through the skin (Fig. 1C).

Two-photon intravital microscopy (2P-IVM) revealed that as early as 40 min after exposure to sand flies, neutrophils had migrated into the skin and had begun to localize around apparent bite sites (Fig. 1D). Over the next hour, neutrophils rapidly accumulated in, and subsequently swarmed around, the vicinity of both infected and uninfected sand fly bites (Fig. 1D and movies S1 and S2), eventually forming an epidermal "plug" through sequential migration of neutrophils into the hole left by the sand fly proboscis (Fig. 1E, fig. S2, and movies S3 and S4). Parasite phagocytosis by neutrophils was readily observed during this recruitment process (movie S5), leading to the presence of large numbers of parasite-containing neutrophils at later time points (Fig. 1F and movie S6). In contrast to the rapid motility reported for mosquito-transmitted *Plasmodium* sporozoites, which appear to actively search for blood and lymphatic vessels (*17*, *18*), *L.m.* parasites appeared relatively immobile after sand fly delivery into the skin.

Because of the relatively low and variable number of parasites deposited by sand fly bite (*14*), we used intradermal needle inoculation of high numbers of infectious-stage *L.m.*-RFP metacyclic promastigotes to quantitatively analyze the fate of parasites post-infection (p.i.). The pattern of neutrophil recruitment at early time points was similar to sand fly bite, although comparatively short-lived (fig. S3). Two hours after injection of *L.m.*-RFP into the ear, analysis of all RFP$^+$ dermal cells revealed that the vast majority of the *L.m.*-RFP signal was associated with the CD11b^{hi}Gr-1^{hi}LYS-eGFP^{hi} neutrophil population (Fig. 2, A to D, and fig. S1N). These data are consistent with kinetic analyses of fixed tissue sections showing parasites initially interspersed between F4/80$^+$eGFP^{lo} macrophages and subsequently phagocytosed by newly arriving F4/80$^-$eGFP^{hi} neutrophils (Fig. 2, E and F).

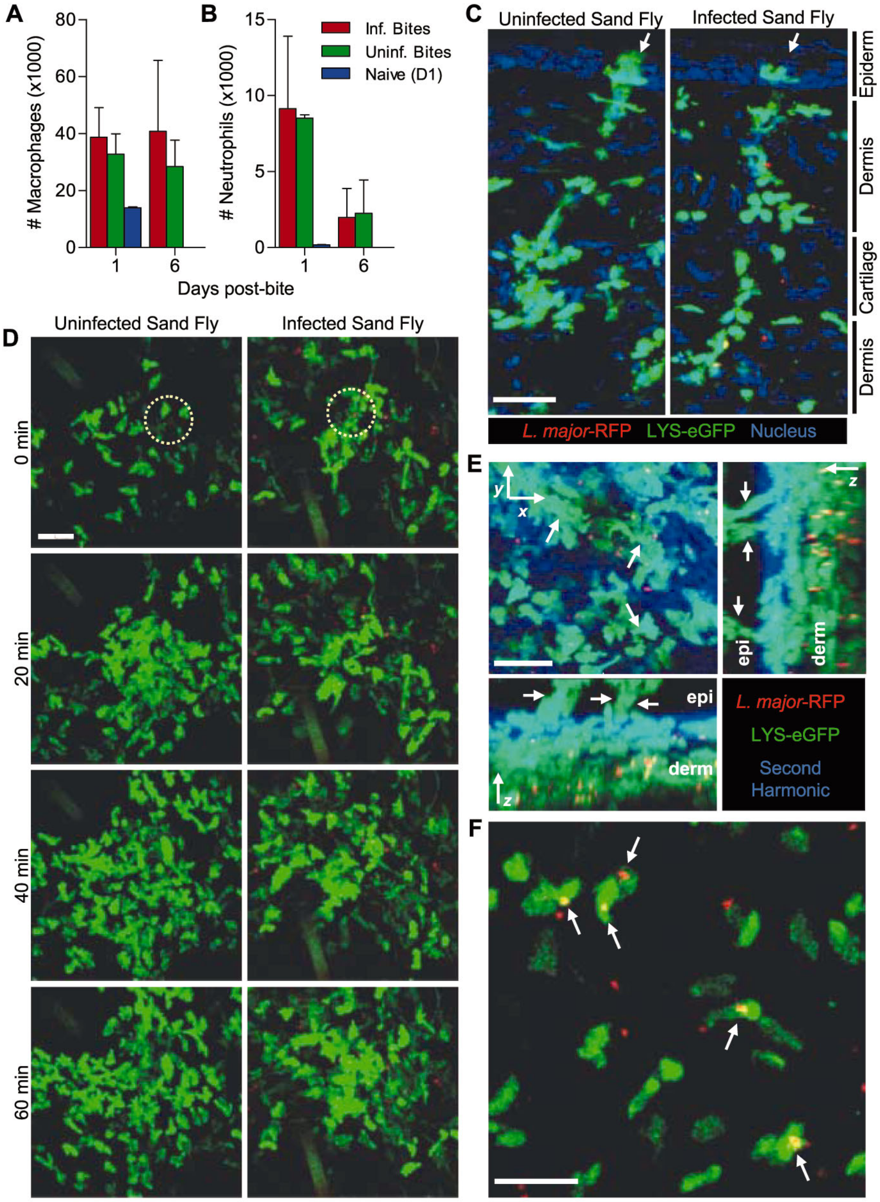

Fig. 1. Neutrophils are rapidly recruited to sites of sand fly bite, where they phagocytose *L. major* parasites. (**A** and **B**) Numbers of CD11b$^+$F4/80$^+$ macrophages/monocytes (A) and CD11b$^+$Gr-1$^+$7/4$^+$F4/80$^-$MHCII$^-$Ly6G$^+$ neutrophils (B) recruited into the ear (±SD; $n \geq 4$ ears per group per day) 1 or 6 days after being bitten by infected or uninfected sand flies. The number of cells in a naïve mouse ear is shown for day 1. (**C**) Ear sections from LYS-eGFP mice (green) bitten with uninfected sand flies (left) or *L.m.*-RFP–infected (red) sand flies (right) 2 hours before harvesting tissue. Arrows point to sites of proboscis penetration. See also movies S1 and S2. (**D**) 2P-IVM time-lapse images from the ears of LYS-eGFP mice (green) beginning 40 min after exposure to uninfected sand flies (left) or *L.m.*-RFP–infected (red) sand flies (right). Circles represent sites of sand fly proboscis penetration. (**E**) Maximum-intensity projection images across *x*, *y*, and *z* dimensions derived from 2P-IVM of the ear of a LYS-eGFP mouse (green) 2 hours after exposure to *L.m.*-RFP–infected (red) sand flies. Dermal and epidermal layers defined by the presence or absence of collagen (blue), respectively, are indicated. Arrows point to sites of proboscis penetration and neutrophil "plug" formation. See also movies S3 and S4. (**F**) Image obtained from a 2P-IVM time-lapse series of the ear of a LYS-eGFP mouse (green) 3 hours after exposure to *L.m.*-RFP–infected (red) sand flies. Arrows point to neutrophils with one or more intracellular parasites. See also movies S5 and S6. Scale bars, 30 μm [(C) to (E)], 20 μm (F).

Dynamic analysis of neutrophil recruitment and parasite uptake revealed the rapid accumulation of neutrophils inside blood vessels surrounding the infection site as early as 30 min p.i. and the subsequent diapedesis of these cells into the skin parenchyma (Fig. 2G and movie S7). Extravasating neutrophils were preferentially distributed to the side of the vessel facing parasite deposition and were characterized by an extremely elongated uropod (Fig. 2H and movie S8). Neutrophils then moved in a highly directed manner toward the inoculation site (Fig. 2, G to I), where they rapidly and efficiently phagocytosed individual parasites (Fig. 2J). Phagocytosis occurred concurrently with migrational arrest, as revealed by a decrease in neutrophil mean velocity after parasite uptake (Fig. 2K). Additional data acquired after needle inoculation in the absence of parasites suggest that the initial inflammatory response to sand fly bite or needle-induced tissue damage drives the robust neutrophilic recruitment observed in these studies, overriding the potential contribution of any parasite-specific signals (fig. S4 and movie S9).

Because macrophages are the definitive host cell for *Leishmania*, we explored their relationship with neutrophils. Mice expressing eGFP under the control of the endogenous major histocompatibility complex class II promoter (MHCII-eGFP) (*19*) (fig. S1, L and M) were inoculated with *L.m.*-RFP. Phenotypic analysis of RFP-gated dermal cells at 18 hours p.i. revealed that the RFP signal was primarily associated with CD11b^{hi}Gr-1^{hi}MHC-II-eGFP^{-} neutrophils and only small numbers of monocytes/macrophages or CD11c^{+} dendritic cells (DCs) (Fig. 3A and fig. S5). Strikingly, we observed an increase in the absolute number of RFP^{+} macrophages and a corresponding drop in the absolute number of RFP^{+} neutrophils over time (Fig. 3, C and D). By 6 to 7 days p.i., the RFP signal was found primarily in the macrophage/monocyte population and only sparsely in neutrophils and CD11c^{+} DCs (Fig. 3, B, D, and E). Although MHC-II-eGFP^{+}CD11c^{+} cells represented an extremely small proportion of infected cells at 1 day p.i., their increase in numbers by day 6 suggests that dermal DCs and/or Langerhans cells participate in the infectious process (*20*).

To determine the fate of *Leishmania* promastigotes after phagocytosis by neutrophils in vivo, we isolated infected and uninfected neutrophils from the ear dermis by cell sorting (Fig. 4, A to C). eGFP^{hi}RFP^{+} cells retained a normal cytoplasmic and nuclear appearance and contained intracellular *L.m.* parasites (Fig. 4D) (*21*). Limiting dilution analysis of sorted neutrophils revealed that 92% of RFP^{+} but only 1.2% of RFP^{-} neutrophils contained at least one viable parasite (Fig. 4E). Furthermore, naïve mice inoculated with 10^3 RFP^{+}GFP^{+} neutrophils or 10^3 cultured *L.m.*-RFP established equivalent infections (Fig. 4, F to H), which demonstrates that *L.m.* phagocytosed by neutrophils are viable and can contribute to the establishment and progression of disease.

The extremely dense clusters of eGFP-expressing neutrophils and macrophages/monocytes that formed several hours after parasite inoculation (Fig. 3E) made visualization of individual cell-cell interactions difficult. To overcome this problem, we injected sorted eGFP^{hi}RFP^{+} infected neutrophils into the ears of transgenic animals expressing eGFP under the control of the macrophage/monocyte-specific CSF1 receptor promoter (*22*). Recipient animals were preexposed to sand flies 12 hours before neutrophil transfer to induce an inflammatory environment at the infection site.

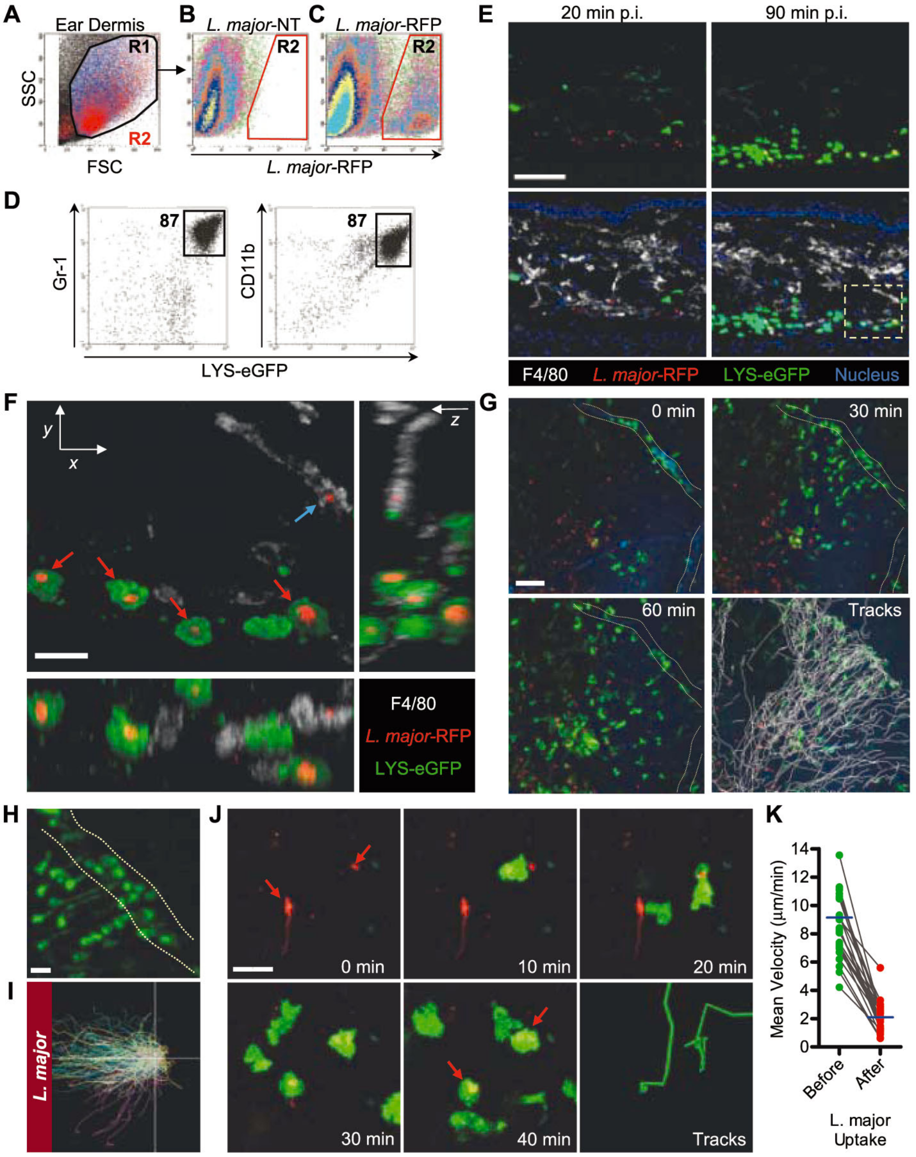

Fig. 2. Rapid recruitment and infection of neutrophils after intradermal inoculation of *L. major*. (**A**) Side scatter (SSC)/forward scatter (FSC) dot plot of ear-derived cells 16 hours p.i. with 10^6 *L.m.*-RFP. (**B** and **C**) SSC/RFP dot plots of R1-gated ear cells 16 hours p.i. with 10^6 *L.m.*–empty vector control (B) or *L.m.*-RFP (C). (**D**) GFP, Gr-1, and CD11b expression by RFP^{+} R2-gated cells from ears of LYS-eGFP mice 2 hours p.i. with 5×10^5 *L.m.*-RFP. (**E**) Ear sections from LYS-eGFP mice 20 min (left) or 90 min (right) p.i. with 10^4 *L.m.*-RFP stained with F4/80 (white) and a nuclear dye (blue). Top panels show GFP and RFP images; bottom panels show a merge of all channels. (**F**) Maximum-intensity projection images across *x*, *y*, and *z* dimensions from boxed region in (E). Red arrows indicate *L.m.*-RFP phagocytosed by neutrophils; blue arrow indicates a parasite captured by a macrophage. (**G** to **K**) LYS-eGFP animals were subjected to 2P-IVM 30 min p.i. with 10^4 *L.m.*-RFP. (G) Time-lapse images showing GFP^{+} (green) cells, *L.m.*-RFP (red), and blood vessels (blue). Panel labeled "Tracks" shows the paths followed by cells from the vessel to site of inoculation of parasites over 60 min. (H) Magnified view from (G) showing neutrophil extravasation from vasculature. See also movies S7 and S8. (I) Cell migration paths from three independent experiments (cyan, yellow, and purple tracks) were normalized for their origin and their position relative to the site of parasite deposition. (J) Time-lapse images showing neutrophil (green) migration before and after phagocytosis of *L.m.*-RFP (red, arrows). (K) Neutrophil mean velocity 10 min before and 10 min after parasite phagocytosis. Data points represent individual cells and were compiled from four separate experiments. Scale bars, 50 µm [(E) and (G)], 15 µm [(F), (H), and (J)].

Using 2P-IVM, we observed what appeared to be viable parasites [as indicated by their expression of RFP (fig. S1, A to D)] being released from apoptotic neutrophils in the vicinity of surrounding macrophages (fig. S6 and movies S10 to S12).

We next examined the functional role of neutrophils on the establishment and progression of sand fly–transmitted leishmaniasis. Mice treated

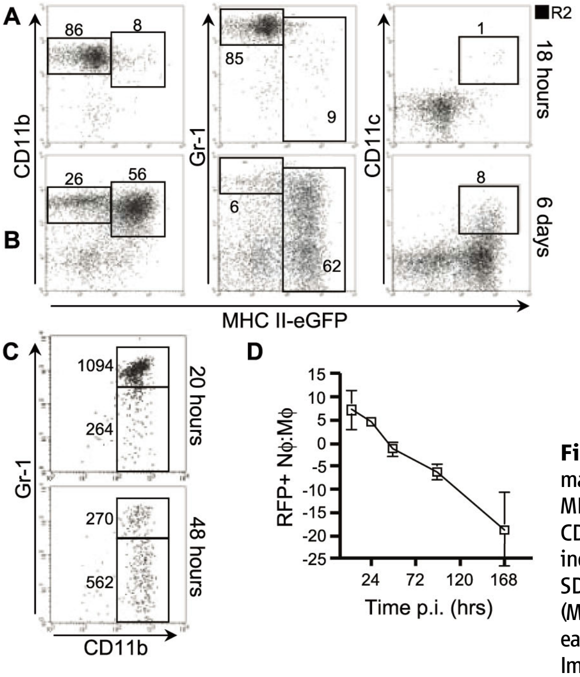

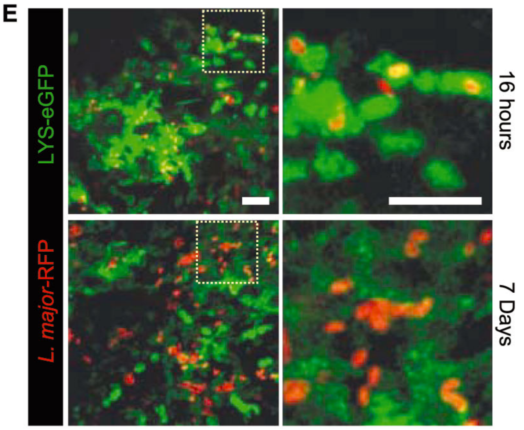

Fig. 3. *L. major* transitions from neutrophils to macrophages early after intradermal inoculation. (**A** and **B**) Dot plots gated on RFP$^+$ cells (R2 in Fig. 2C) from ears of MHC II-eGFP mice taken at 18 hours (A) or 6 days (B) p.i. with 10^6 *L.m.*-RFP. (**C**) CD11b and Gr-1 expression of RFP$^+$-gated cells at 20 and 48 hours p.i. Numbers indicate the absolute number of gated cells per sample. (**D**) Mean of the ratio ± SD of RFP$^+$ infected neutrophils (Nϕ) to RFP$^+$ infected macrophages/monocytes (Mϕ); n = 4 to 6 individual ears per time point. (**E**) 2P-IVM projection images from the ears of LYS-eGFP mice (green) at 16 hours or 7 days p.i. with 10^4 *L.m.*-RFP (red). Images at right are magnified views of the boxed regions. Scale bars, 20 μm.

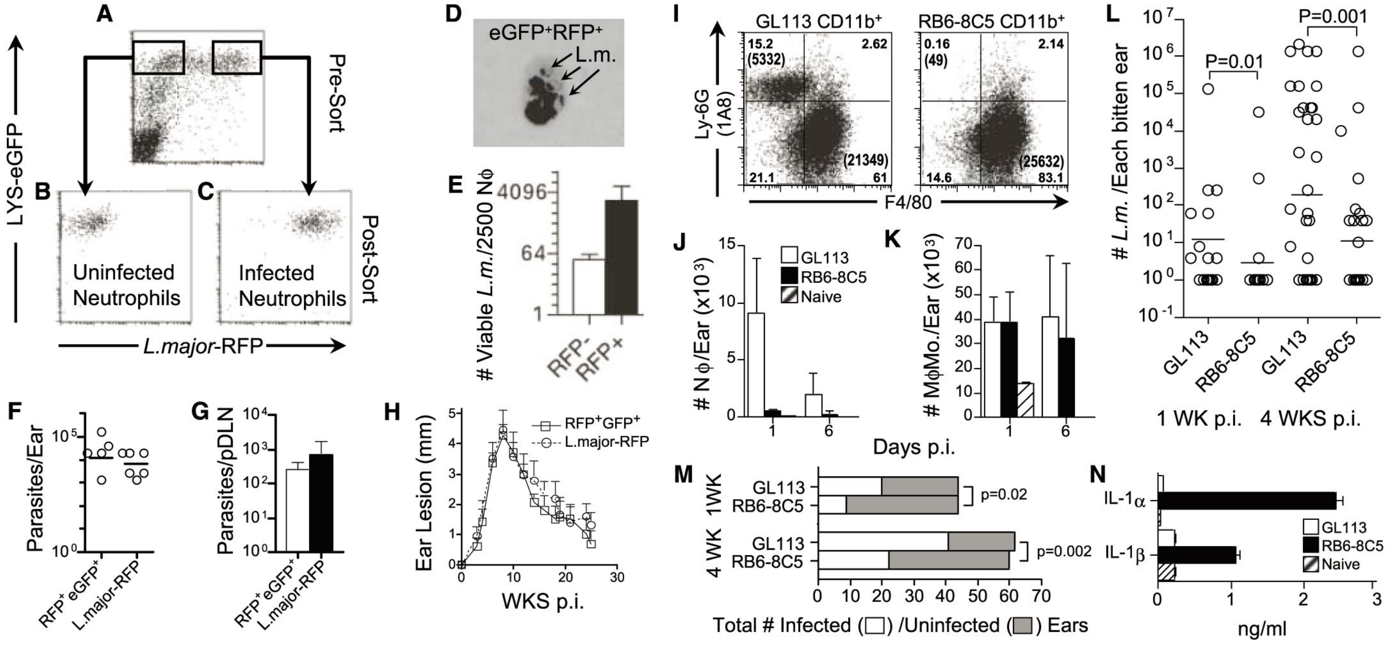

Fig. 4. Neutrophils harbor viable parasites and promote productive infections. (**A** to **D**) LYS-eGFP^{hi} neutrophils from the ear 12 hours p.i. with 2.5×10^6 *L.m.*-RFP were sorted into uninfected RFP$^-$ (B) or *L.m.*-infected RFP$^+$ [(C) and (D)] populations. [(B) and (C)] Post-sort. (D) Dif-Quick stain of the cytospun eGFP$^+$RFP$^+$ post-sort population. (**E**) Number of viable parasites per 2500 RFP$^-$ and RFP$^+$ neutrophils (±SD of triplicate samples). (**F** to **H**) Wild-type mice were injected in the ear with 10^3 culture-derived *L.m.*-RFP metacyclic promastigotes or 10^3 RFP$^+$eGFP^{hi} infected neutrophils. Twenty-one days after injection, mice were assessed for parasite load in individual ears (F), pooled draining lymph nodes (pDLNs) (G), and mean ± SEM (n = 8) ear lesion diameter over the course of infection (H). (**I** to **N**) Mice were treated with control (GL113) or neutrophil-depleting (RB6-8C5) monoclonal antibodies 16 hours before exposure to infected sand flies. (I) Representative dot plot of CD11b$^+$-gated Ly-6G$^+$F4/80$^-$ neutrophils and Ly6G$^-$F4/80$^+$ macrophages/monocytes on day 1 p.i. [(J) and (K)] Analysis of the total number of CD11b$^+$7/4$^+$F4/80$^-$MHCII$^-$Ly6G$^+$ neutrophils (J) and CD11b$^+$F4/80$^+$ macrophage/monocytes (K), per ear ± SD ($n \geq 4$ per group per day), on day 1 and day 6 p.i. (L) Parasite loads in individual ears at 1 and 4 weeks after exposure to infected sand flies in GL113-treated versus RB6-8C5–treated animals, as determined by limiting dilution analysis. Each open circle represents a single exposed ear in three (1 week) or four (4 weeks) pooled experiments. (M) Representation of the total incidence of infected versus uninfected ears in RB6-8C5– versus GL113-treated animals at 1 week [odds ratio = 0.299, 95% CI (0.097, 0.847), P = 0.020] and 4 weeks [odds ratio = 0.293, 95% CI (0.126, 0.658), P = 0.0017] after transmission, as determined by limiting dilution analysis. (N) Spontaneous release of interleukin-1α and 1β by ear derived cells, as determined by multiplex cytokine analysis at 1 week p.i.

with neutrophil-depleting antibody 16 hours before infected sand fly exposure had a specific and marked reduction of CD11b$^+$Ly-6G$^+$F4/80$^-$ neutrophils in the ear dermis 1 day after transmission (Fig. 4, I and J), whereas the CD11b$^+$Ly-6G$^-$F4/80$^+$ macrophage/monocyte population was unaffected (Fig. 4, I and K). In some but not all experiments, reduced numbers of neutrophils were also observed in ears 6 days after transmission (Fig. 4J). Neutrophil depletion significantly reduced the number of viable parasites detected per ear (Fig. 4L), as well as the incidence of ears with detectable parasites at 1 and 4 weeks after transmission (Fig. 4M). Thus, the early influx and persistence of neutrophils after sand fly transmission of *L.m.* appears critical for the development of cutaneous disease.

The data presented here are relevant to the "Trojan horse" model of *L.m.* infection (*2*), which postulates that uptake of infected neutrophils is a mechanism for "silent" entry of parasites into macrophages. Our observations indicate that neutrophils are the initial host cell for a substantial fraction of parasites after infection and that neutrophil depletion results in reduced disease at 1 week p.i. We found no evidence, however, for uptake of intact, infected neutrophils by macrophages. In addition, macrophages were efficiently recruited to sites of infection and were able to directly phagocytose parasites in neutrophil-depleted animals (fig. S7). Under these conditions, macrophages and DCs did not acquire more parasites relative to nondepleted animals containing competing neutrophils, which suggests that neutrophils may facilitate infection by rescuing parasites not accessible to other phagocytic cells from death in extracellular spaces. Alternatively, infected neutrophils may release transitional-stage parasites better adapted for macrophage uptake and survival, or macrophages may exhibit compromised microbicidal function in a setting in which they are heavily engaged in the anti-inflammatory process of clearing apoptotic neutrophils (*23*, *24*). This latter possibility is supported by an increase in the spontaneous release of the proinflammatory cytokines interleukin-1α and 1β by ear cells from neutrophil-depleted animals (Fig. 4N) (*25*).

The ability of phagocytic cells to rapidly localize to sites of tissue inflammation and subsequently capture and destroy pathogens is a hallmark of the innate immune response, highly conserved, and among the earliest observations in microbiology (*26*). We found that sand fly bites and needle inoculation induce an intense neutrophilic infiltrate into the skin, irrespective of parasite infection. These data are consistent with the finding that neutrophils are recruited to sites of sterile brain injury (*27*) and suggest that the predominance of *L.m.*-infected neutrophils at the site of parasite deposition is a by-product of a host response aimed at wound repair and sterilization. Thus, the neutrophilic host response to the wound inflicted by arthropod vectors appears to have been a driving force in pathogen evolution aimed at counteracting and even exploiting the presence of these innate effector cells.

References and Notes

1. N. Peters, D. Sacks, *Immunol. Rev.* **213**, 159 (2006).
2. G. van Zandbergen, W. Solbach, T. Laskay, *Autoimmunity* **40**, 349 (2007).
3. A. W. Segal, *Annu. Rev. Immunol.* **23**, 197 (2005).
4. W. M. Nauseef, *Immunol. Rev.* **219**, 88 (2007).
5. Y. Belkaid *et al.*, *J. Immunol.* **165**, 969 (2000).
6. F. L. Ribeiro-Gomes, M. T. Silva, G. A. Dosreis, *Parasitology* **132** (suppl.), S61 (2006).
7. M. Charmoy *et al.*, *J. Leukoc. Biol.* **82**, 288 (2007).
8. F. Tacchini-Cottier *et al.*, *J. Immunol.* **165**, 2628 (2000).
9. L. Chen *et al.*, *Parasitol. Int.* **54**, 109 (2005).
10. G. van Zandbergen *et al.*, *J. Immunol.* **173**, 6521 (2004).
11. C. R. Teixeira *et al.*, *J. Immunol.* **175**, 8346 (2005).
12. S. Kamhawi, Y. Belkaid, G. Modi, E. Rowton, D. Sacks, *Science* **290**, 1351 (2000).
13. Y. Belkaid *et al.*, *Proc. Natl. Acad. Sci. U.S.A.* **97**, 6704 (2000).
14. N. Kimblin *et al.*, *Proc. Natl. Acad. Sci. U.S.A.* **105**, 10125 (2008).
15. See supporting material on *Science* Online.
16. N. Faust, F. Varas, L. M. Kelly, S. Heck, T. Graf, *Blood* **96**, 719 (2000).
17. R. Amino *et al.*, *Nat. Med.* **12**, 220 (2006).
18. J. P. Vanderberg, U. Frevert, *Int. J. Parasitol.* **34**, 991 (2004).
19. M. Boes *et al.*, *Nature* **418**, 983 (2002).
20. L. Soong, *J. Immunol.* **180**, 4355 (2008).
21. E. Aga *et al.*, *J. Immunol.* **169**, 898 (2002).
22. S. H. Burnett *et al.*, *J. Leukoc. Biol.* **75**, 612 (2004).
23. D. V. Krysko, K. D'Herde, P. Vandenabeele, *Apoptosis* **11**, 1709 (2006).
24. C. D. Gregory, A. Devitt, *Immunology* **113**, 1 (2004).
25. C. Matte, M. Olivier, *J. Infect. Dis.* **185**, 673 (2002).
26. P. Martin, S. J. Leibovich, *Trends Cell Biol.* **15**, 599 (2005).
27. J. V. Kim, M. L. Dustin, *J. Immunol.* **177**, 5269 (2006).

28. We thank K. Beacht for technical assistance; H. Qi, M. Bajénoff, S. Nylén, and M. A. McDowell for discussions; T. Moyer and C. Henry for neutrophil sorting; and A. Rothfuchs for GL113 and RB6-8C5 monoclonal antibodies. Supported by the Intramural Research Program of the NIAID.

Supporting Online Material

www.sciencemag.org/cgi/content/full/321/5891/970/DC1
Materials and Methods
Figs. S1 to S7
Movies S1 to S12
References

16 April 2008; accepted 4 July 2008
10.1126/science.1159194

Tumor Regression in Cancer Patients by Very Low Doses of a T Cell–Engaging Antibody

Ralf Bargou,[1,2]* Eugen Leo,[3]*† Gerhard Zugmaier,[3] Matthias Klinger,[3] Mariele Goebeler,[1,2] Stefan Knop,[2] Richard Noppeney,[4] Andreas Viardot,[5] Georg Hess,[6] Martin Schuler,[7] Hermann Einsele,[2] Christian Brandl,[3] Andreas Wolf,[3] Petra Kirchinger,[3] Petra Klappers,[3] Margit Schmidt,[3] Gert Riethmüller,[8] Carsten Reinhardt,[3] Patrick A. Baeuerle,[3]‡ Peter Kufer[3]

Previous attempts have shown the potential of T cells in immunotherapy of cancer. Here, we report on the clinical activity of a bispecific antibody construct called blinatumomab, which has the potential to engage all cytotoxic T cells in patients for lysis of cancer cells. Doses as low as 0.005 milligrams per square meter per day in non–Hodgkin's lymphoma patients led to an elimination of target cells in blood. Partial and complete tumor regressions were first observed at a dose level of 0.015 milligrams, and all seven patients treated at a dose level of 0.06 milligrams experienced a tumor regression. Blinatumomab also led to clearance of tumor cells from bone marrow and liver. T cell–engaging antibodies appear to have therapeutic potential for the treatment of malignant diseases.

Substantial evidence suggests that cytotoxic T lymphocytes participate in controlling tumor growth and that they can be harnessed in immunotherapeutic settings. For example, their presence in colorectal tumors was shown to strongly predict clinical outcome (*1*), and adoptive transfer of ex vivo expanded tumor-derived lymphocytes (*2*) or of T cell receptor gene transfected T cells to melanoma patients (*3*) has been shown to lead to cancer regression. However, therapies aimed at inducing specific T cell responses against cancer cells, including vaccination (*4*) and CTLA-4–blocking antibodies (*5*), have been limited by relatively low response rates and relapses, presumably because of immune escape mechanisms of cancer cells (*6*, *7*).

An alternative approach to harness the high cytotoxic potential of T cells has been the use of T cell–engaging antibodies (*8*, *9*). Conventional antibodies are not able to directly recruit T cells because these cells lack Fcγ receptors. Well-studied antibody constructs for engaging T cells are bispecific T cell engagers (BiTE), which are based on single-chain antibodies (*10*, *11*). These molecules can transiently tether resting T cells to tumor cells, leading to concomitant T cell activation and serial lysis of tumor cells (*12*–*14*). To date, various mouse models have demonstrated high levels of activity of BiTE antibodies (*15*–*20*). The independence of this approach from peptide antigen presentation and tumor-specific T cell clones suggests that it can overcome major immune escape mechanisms.

We have investigated clinical activity and safety of increasing doses of BiTE antibody blinatumomab (also called MT103/MEDI-538) with dual specificity for CD19 and CD3 (*21*–*24*) in an ongoing study with non–Hodgkin's B cell lymphoma (NHL) patients relapsed to standard therapies. Demographics, staging, number of prior therapies, treatment details, and clinical outcome of all 38 patients from the currently completed dose levels are shown in table S1 (*25*). At dose levels of 0.005 mg/m^2 per day and higher, CD19$^+$ target cells rapidly vanished from peripheral blood of patients for the rest of the treatment period (table S1). Figure 1 shows representative pharmacodynamic data for patient 28, who had a complete and lasting tumor regression at a dose level of 0.03 mg/m^2 per day. The decline of CD19$^+$cells (Fig. 1A) was accompanied by expression of apoptosis marker annexin V (Fig. 1B), indicating lysis rather than extravasation of target cells. Peripheral T cells initially disappeared but then reappeared, with counts and kinetics showing a high interpatient variability (Fig. 1C and fig. S1). In this and several other patients treated at higher dose levels, peripheral T cell numbers increased severalfold over baseline, which coincided with expression of activation markers CD69, CD25, and HLA-DR by a significant proportion of CD8$^+$ T cells (Fig. 1D). During or after treatment, total T cell counts either contracted to baseline or remained at a higher level than before treatment (Fig. 1C). The increase in T cell counts under blinatumomab treatment was predominantly caused by an expansion of effector memory CD8$^+$ and CD4$^+$ T cells with CD45RA$^-$/CCR7$^-$ phenotype, whereas counts of CD8$^+$ T cells with phenotypes of naïve, central memory, and CD45RA$^+$ effector memory T cells remained more or less constant (Fig. 1E). The early disappearance of T cells may be explained by a transient increase in the adhesiveness of T cells to vessels and/or extravasation, whereas their expansion may be due to proliferation of effector memory T cells.

Among 38 patients receiving blinatumomab at doses from 0.0005 to 0.06 mg/m^2 per day, a total of 11 major responses have been observed (Table 1 and table S1), which were centrally confirmed according to defined criteria (*26*). All four complete (CR) and seven partial tumor regressions (PR) occurred at doses of 0.015 mg/m^2 per day and higher, indicating a dose response relationship (Table 1). All seven patients treated at the recently completed dose level of 0.06 mg/m^2 showed objective responses. Tumor regressions were observed in patients with follicular lymphoma, mantle cell lymphoma, and chronic lymphocytic leukemia. Examples of a complete tumor regression in the pelvic area of patient 16 (Fig. 2A) and of a partial regression in the chest area of patient 15 (Fig. 2B) are shown. In all responding patients, the majority of tumor shrinkage occurred within the first 4 weeks of treatment.

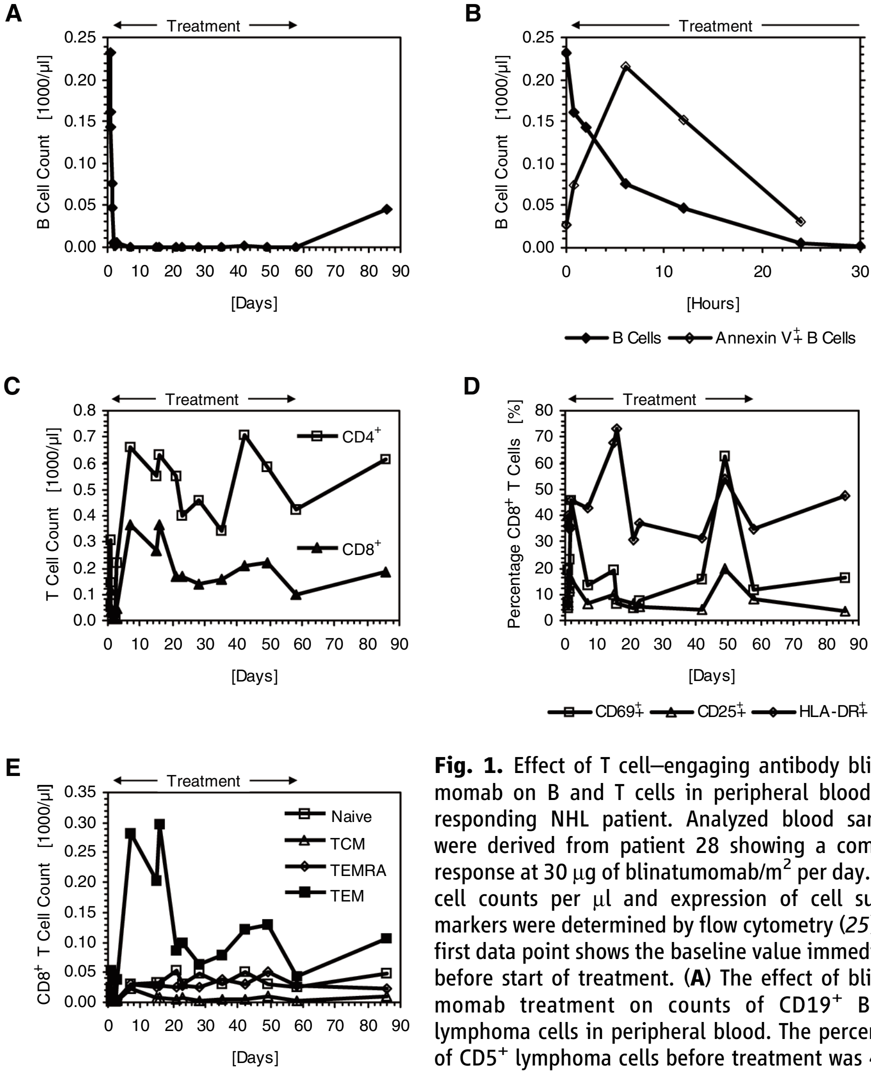

Fig. 1. Effect of T cell–engaging antibody blinatumomab on B and T cells in peripheral blood of a responding NHL patient. Analyzed blood samples were derived from patient 28 showing a complete response at 30 μg of blinatumomab/m^2 per day. Total cell counts per μl and expression of cell surface markers were determined by flow cytometry (*25*). The first data point shows the baseline value immediately before start of treatment. (**A**) The effect of blinatumomab treatment on counts of CD19$^+$ B and lymphoma cells in peripheral blood. The percentage of CD5$^+$ lymphoma cells before treatment was 44%. (**B**) The effect of blinatumomab treatment on surface expression of apoptosis marker annexin V during the decay phase of B cell counts. MFI indicates mean fluorescence intensity. (**C**) The effect of blinatumomab treatment on total counts of CD4$^+$ and CD8$^+$ T cells. (**D**) The effect of blinatumomab treatment on activation markers CD69, CD25, and HLA-DR expressed on peripheral CD8$^+$ T cells. (**E**) The effect of blinatumomab treatment on four distinct CD8$^+$ T cell subpopulations. TCM, central memory T cells; TEM, effector memory T cells; and TEMRA, CD45RA$^+$ effector memory T cells. For experimental details, see (*24*).

Table 1. Relationship between dose level and antitumor activity of BiTE antibody blinatumomab in relapsed NHL patients. Abbreviations used are FL, follicular lymphoma; MCL, mantle cell lymphoma; CLL, chronic lymphocytic leukaemia. For details of trial design, see (*25*).

Blinatumomab dose levels tested (mg/m^2 per day)	Patients	Tumor regression (percent)	Complete regression (disease)	Partial regression (disease)
0.0005, 0.0015, 0.005	12	0 (0)	0	0
0.015, 0.030	19	4 (21)	2 (MCL, FL)	2 (FL, CLL)
0.060	7	7 (100)	2 (MCL, FL)	5 (MCL, 4 FL)

---

[1]Interdisciplinary Phase I/II Unit of the University of Würzburg, Klinikstraße 6-8, 97070 Würzburg, Germany. [2]Universitätsklinikum Würzburg, Medizinische Klinik und Poliklinik II, Klinikstraße 6-8, 97070 Würzburg, Germany. [3]Micromet AG, Staffelseestraße 2, 81477 Munich, Germany; and Micromet, Incorporated, 6707 Democracy Boulevard, Bethesda, MD 20817, USA. [4]Universitätsklinikum Essen, Klinik für Hämatologie, Medizinische Klinik und Poliklinik, Hufelandstraße 55, 45147 Essen, Germany. [5]Universitätsklinikum Ulm, Innere Medizin III, Robert-Koch-Straße 8, 89081 Ulm, Germany. [6]Klinikum der Johannes-Gutenberg Universität III, Medizinische Klinik und Poliklinik, Langenbeckstraße 1, 55131 Mainz, Germany. [7]Universitätsklinikum Essen, Innere Klinik (Tumorforschung), Tumorforschung, Hufelandstraße 55, 45122 Essen, Germany. [8]Institute for Immunology, Ludwig-Maximilians-Universität, Goethestraße 31, 81333 Munich, Germany.

*These authors contributed equally to this work.

†Present address: Johnson and Johnson Pharmaceuticals, Turnhoutsebaan 30, 2340 Beerse, Belgium.

‡To whom correspondence should be addressed. E-mail: patrick.baeuerle@micromet-inc.com

Longest duration of a CR currently is 13 months in a patient with mantle cell lymphoma, and three more patients have ongoing regressions lasting for >6 months (table S1). No relapse has thus far been observed in responding patients treated with blinatumomab at dose levels of 0.03 and 0.06 mg/m^2 per day. Blinatumomab doses of 0.015 mg/m^2 per day and higher led to depletion of tumor cells not only in blood (Fig. 1A), lymph node lesions (Fig. 2, A and B), and spleen (Fig. 2C) but also in bone marrow (Fig. 2D) and, in one case, in infiltrated liver (Fig. 2E). In 9 of 11 cases of bone marrow infiltration, immunohistochemical and flow cytometric analysis of patient biopsies revealed either complete (6/11) or partial elimination of tumor cells from bone marrow (3/11) (table S1).

Adverse events thus far recorded in the trial up to the completed dose level of 0.06 mg/m^2 per day are listed by their incidence and grade in table S2 (any event occurring in ≥3 patients) and table S3 (grade 3 and 4 events occurring in ≥1 patient). Most frequent side effects included pyrexia, lympho- and leukopenia, chills, and increase of C reactive protein. The majority of adverse events occurred within the first week of treatment and usually normalized to grade 1 or lower during further treatment. Symptoms of the central nervous system—including disorientation, confusion, speech disorders, tremor, and convulsions—have been observed, all of which were fully reversible during or shortly after discontinuation of treatment. All adverse events that led to a discontinuation of treatment with blinatumomab are described in detail in (*25*). No clinically apparent cytokine-release syndrome was evident in any patient. Unlike with antibodies blocking CTLA-4, no autoimmune phenomena have thus far been observed in patients treated with blinatumomab. Antibodies binding or neutralizing blinatumomab have not yet been detected in patients.

First confirmed responses to blinatumomab as a single agent occurred in NHL patients at a serum level of 0.6 ng/ml (at 0.015 mg/m^2 per day). This is about 5 orders of magnitude below serum levels reported for the monoclonal antibody rituximab at a dose of 375 mg/m^2 per week, which likewise elicits objective responses as single agent in this disease (*27*). The enormous potency difference between BiTE antibody blinatumomab and a conventional antibody may relate to the high lytic potential of cytotoxic T cells, which are activated by engagement of only very few CD3 receptor subunits, can rapidly adopt a serial lysis mode, and proliferate at the site of their activation. An ongoing clinical phase II trial is investigating the activity of blinatumomab in patients with acute lymphoblastic leukaemia. It will also be interesting to investigate whether BiTE antibodies are active in solid tumor indications. A clinical trial with a BiTE antibody specific for EpCAM (*18*), a target antigen widely expressed on human adenocarcinoma (*28*) and on cancer stem cells (*29*), has recently been initiated.

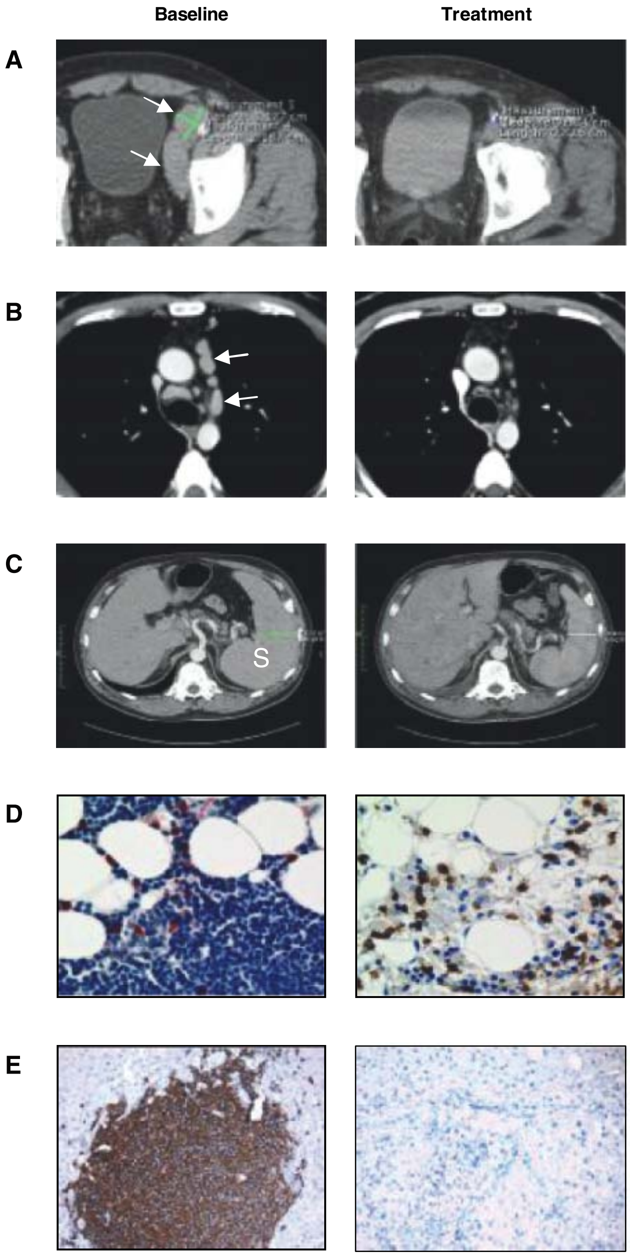

Fig. 2. Antitumor activities of T cell–engaging antibody blinatumomab. (**A**) Computer tomography (CT) images of patient 16 (0.015 mg of blinatumomab/m^2 per day) before and after 8 weeks of treatment. The response of this patient was rated as complete. Arrows indicate two lymph node tumors in the pelvic area. (**B**) CT scans of patient 15 (0.015 mg of blinatumomab/m^2 per day) before and 4 weeks after treatment. The response of this patient was rated partial. Arrows indicate lymph node tumors in the mediastinum. (**C**) CT scans of the abdomen of patient 16 (0.015 mg of blinatumomab/m^2 per day) before and 4 weeks after treatment. S denotes splenomegaly. (**D**) Micrographs of marrow biopsies of patient 13 at baseline and 15 days after start of treatment with 0.015 mg of blinatumomab/m^2 per day, Blue indicates tumor cells (hematoxylin staining); brown, T cells (CD3 staining). (**E**) Micrographs of liver biopsies from patient 33 (0.06 mg of blinatumomab/m^2 per day) stained for B cell antigen CD20 at baseline and after 4 weeks of treatment. Representative sections of biopsies are shown.

References and Notes

1. J. Galon *et al.*, *Science* **313**, 1960 (2006).
2. M. E. Dudley *et al.*, *J. Clin. Oncol.* **23**, 2346 (2005).
3. R. A. Morgan *et al.*, *Science* **314**, 126 (2006); published online 30 August 2006 (10.1126/science.1129003).
4. S. Gross, P. Walden, *Immunol. Lett.* **116**, 7 (2008).
5. L. F. Langer, M. F. Clay, M. A. Morse, *Expert Opin. Biol. Ther.* **7**, 1245 (2007).
6. G. A. Rabinovich, D. Gabrilovich, M. Sotomayor, *Annu. Rev. Immunol.* **25**, 267 (2007).
7. N. Meidenbauer *et al.*, *Cancer Res.* **64**, 6319 (2004).
8. U. D. Staerz, O. Kanagawa, M. J. Bevan, *Nature* **314**, 628 (1985).
9. D. Müller, R. E. Kontermann, *Curr. Opin. Mol. Ther.* **9**, 319 (2007).
10. M. Mack, G. Riethmueller, P. Kufer, *Proc. Natl. Acad. Sci. U.S.A.* **92**, 7021 (1995).
11. P. A. Baeuerle, C. Reinhardt, P. Kufer, *Drugs Future* **33**, 137 (2008).
12. P. Hoffmann *et al.*, *Int. J. Cancer* **115**, 98 (2005).
13. C. Brandl *et al.*, *Cancer Immunol. Immunother.* **56**, 1551 (2007).
14. K. Brischwein *et al.*, *J. Immunother.* **30**, 798 (2007).
15. T. Dreier *et al.*, *J. Immunol.* **170**, 4397 (2003).
16. B. Schlereth *et al.*, *Cancer Res.* **65**, 2882 (2005).
17. B. Schlereth *et al.*, *Cancer Immunol. Immunother.* **55**, 785 (2006).
18. K. Brischwein *et al.*, *Mol. Immunol.* **43**, 1129 (2006).
19. S. A. Hammond *et al.*, *Cancer Res.* **67**, 3927 (2007).
20. S. Offner *et al.*, *Mol. Immunol.* **43**, 763 (2006).
21. A. Löffler *et al.*, *Blood* **95**, 2098 (2000).
22. A. Löffler *et al.*, *Leukemia* **17**, 900 (2003).
23. T. Dreier *et al.*, *Int. J. Cancer* **100**, 690 (2002).
24. B. Schlereth *et al.*, *Cancer Immunol. Immunother.* **55**, 503 (2005).
25. Materials and methods and safety data are shown on *Science* Online.
26. B. D. Cheson, *Hematol. Oncol. Clin. North Am.* **21**, 841 (2007).
27. D. G. Maloney *et al.*, *J. Clin. Oncol.* **15**, 3266 (1997).
28. P. Went *et al.*, *Br. J. Cancer* **94**, 128 (2006).
29. P. Dalerba *et al.*, *Proc. Natl. Acad. Sci. U.S.A.* **104**, 10158 (2007).
30. We thank P. Meier, S. Wissing, F. Hanakam, T. Urbig, D. Nagorsen, and the team from Metronomia GmbH for highly professional support of this study. The study was

supported by the Interdisciplinary Center of Clinical Research (IZKF) of the University of Würzburg. G.R. is on the board of and consults for Micromet AG, a fully owned subsidiary of Micromet, Incorporated, a biopharmaceutical company that develops antibodies engaging cytotoxic T cells for cancer therapy. R.B. also consults for Micromet. R.B., P. Kufer, and G.R. are inventors of a patent covering CD19/CD3 bispecific antibodies. E.L., P. Kufer, and P.A.B. are inventors of a patent application covering a mode of BiTE treatment.

Supporting Online Material

www.sciencemag.org/cgi/content/full/321/5891/974/DC1
Materials and Methods
SOM Text
Fig. S1
Tables S1 to S3

1 April 2008; accepted 7 July 2008
10.1126/science.1158545

The Contribution of Single Synapses to Sensory Representation in Vivo

Alexander Arenz, R. Angus Silver, Andreas T. Schaefer, Troy W. Margrie*

The extent to which synaptic activity can signal a sensory stimulus limits the information available to a neuron. We determined the contribution of individual synapses to sensory representation by recording excitatory postsynaptic currents (EPSCs) in cerebellar granule cells during a time-varying, quantifiable vestibular stimulus. Vestibular-sensitive synapses faithfully reported direction and velocity, rather than position or acceleration of whole-body motion, via bidirectional modulation of EPSC frequency. The lack of short-term synaptic dynamics ensured a highly linear relationship between velocity and charge transfer, and as few as 100 synapses provided resolution approaching psychophysical limits. This indicates that highly accurate stimulus representation can be achieved by small networks and even within single neurons.

Sensory representation relies on the computational efficiency of individual neurons, which is limited by the amount of information available to a cell through its synaptic inputs. The quality of these synaptic signals will depend not only on presynaptic firing rates but also on the stochastic properties and the short-term dynamics of release, postsynaptic receptor activation, and desensitization. Although sensory representation has been studied in many cell types, poor control of sensory input parameters and uncertainty regarding the number of synapses involved in compound responses have hampered our understanding of unitary synaptic contribution. To overcome these problems, we studied granule cells (GCs) in the cerebellar flocculus (Fig. 1A), where the contribution of individual mossy fiber (MF) can be resolved (*1*, *2*). However, in contrast to previous studies (*2*, *3*) this preparation permits the use of a highly accurate and quantifiable vestibular stimulus over a large region of sensory space (*4*–*6*). Moreover, because several features of motion detection along the vestibular-cerebellar pathway have been elucidated by extracellular recordings (*4*–*7*), the synaptic information content can be placed in the broader context of cerebellar function.

In vivo whole-cell voltage clamp recordings (*8*) in ketamine- and xylazine-anesthetized mice (*9*) revealed the presence of spontaneously occurring EPSCs with a mean frequency of 13 ± 2.3 Hz (SEM, $n = 18$ cells) in the absence of a vestibular stimulus. During horizontal rotation (Fig. 1B), a bidirectional modulation of EPSC frequency was observed (range from 0 to 110 Hz, time bins = 100 ms) (Fig. 1C and movie S1). Plotting the EPSC frequency as a function of the stimulus parameters angular position (green), velocity (black), and acceleration (orange) revealed that EPSC rate was linearly related to velocity ($r^2 = 0.7 \pm 0.04$) but not to position ($r^2 = 0.05 \pm 0.02$) or acceleration [$r^2 = 0.03 \pm 0.01$; analysis of variance (ANOVA), $P < 10^{-20}$, $n = 18$ cells] (Fig. 1D). Synaptic responses to vestibular stimulation fell into one of two distinct classes (fig. S1): positive rate modulation in the ipsilateral direction and negative modulation in the contralateral direction (type 1, $n = 9$) or vice versa (type 2, $n = 9$) (*5*). The GC excitatory drive, as quantified from the change in total charge transferred, was also modulated in a manner similar to that of EPSC frequency (fig. S1). Both type 1 and type 2 cells showed a near-perfect correlation between EPSC frequency and velocity (type 1: $r = 0.94 \pm 0.09$, $n = 9$; type 2: $r = 0.97 \pm 0.01$, $n = 9$) (Fig. 1E). Although the slope (gain) of the relationship between EPSC frequency and velocity varied widely across cells (Fig. 1E, inset), the mean gain was also similar for type 1 and type 2 responses (type 1: 0.42 ± 0.11 Hz / (°/s), type 2: 0.36 ± 0.07 Hz / (°/s); $P = 0.68$). However, because inputs could be silenced at high velocities in the nonpreferred direction (mean decrease = 58 ± 9%, range from 0 to 100%, $n = 18$ cells) (Fig. 1F), the correlation between EPSC frequency and velocity deteriorated in the nonpreferred direction [$r_{\text{(pref. direct.)}} = 0.952$; $r_{\text{(nonpref. direct.)}} = 0.753$] (Fig. 1G).

MF-GC EPSCs have been shown to exhibit frequency-dependent depression (*10*, *11*) and glutamate-spillover-mediated AMPA receptor activation (*12*), suggesting that the excitatory charge in vivo could be a nonlinear function of velocity. We therefore assayed the synaptic excitatory drive by quantifying the amplitude and decay time course of spontaneous and motion-evoked EPSCs (Fig. 2A). In the majority of cases ($n = 13/18$ cells), we observed no significant difference ($P > 0.05$) in EPSC amplitude or EPSC-weighted decay between spontaneous EPSCs and those recorded during movement in the preferred direction (Fig. 2B). Moreover, there was no change in the EPSC amplitude distribution as the angular velocity was increased in the preferred direction (Fig. 2, C to E). The relationship between charge per unit time (calculated over 100-ms bins) and both EPSC frequency ($r = 0.78 \pm 0.05$, $n = 18$ cells) and motion velocity ($r = 0.73 \pm 0.06$, $n = 18$ cells) was linear (Fig. 2, F and G). This lack of short-term dynamics over these EPSC frequencies therefore allows angular velocity to be linearly represented both by EPSC frequency and excitatory charge at the postsynaptic membrane. Furthermore, the coefficient of variation of EPSCs observed in this class of responses ($cv = 0.55 \pm 0.03$, $n = 13$ cells) was similar to that for single MF inputs recorded in vitro (*12*), and the frequencies of both spontaneous and evoked EPSCs observed here are entirely consistent with recordings from individual MFs showing high action potential rates in vivo (*5*, *11*, *13*) (fig. S2).

Some GCs ($n = 5/18$ cells) (Fig. 2A, solid circles) did, however, exhibit a significant increase in EPSC amplitude in the preferred direction ($P < 0.05$) (Fig. 3, A and B) and a significantly higher cv (0.67 ± 0.04, $P < 0.05$). In these cells, the cumulative amplitude histogram changed shape during motion in the preferred direction, allowing in three out of five cells the separation of distinct inputs with use of an amplitude threshold criterion (–18 to –20 pA; $n = 3$ cells) (Fig. 3C) (*2*). We always observed that, although one population of EPSCs was insensitive to our stimulus, the other population was modulated by horizontal rotation (Fig. 3D). In two out of three cells, these two EPSC populations also showed significantly different decay time courses ($P < 0.05$), confirming that they arose from distinct synaptic inputs. In these cases, neither the nonmodulated (input 1) nor modulated (input 2) input showed frequency-dependent changes in EPSC amplitude (input 1: $P = 0.99$; input 2: $P = 0.07$, ANOVA) (Fig. 3E). Because the slow decay time (overall $wd_{\text{input 1}} = 3.97 \pm 1.24$ ms versus $wd_{\text{input 2}} = 3.28 \pm 1.07$ ms, $n = 3$ cells) (Fig. 3F) and high spontaneous frequency (>7 Hz, three cells) of the nonmodulated input are distinct from the low frequency, very fast decaying miniature events observed in vitro (*14*), the nonmodulated population consists predominantly of action potential–evoked events. Although we cannot distinguish intrinsic from extrinsic MF-evoked EPSCs, the overall similar decay time course ($P = 0.17$, $n = 3$ cells) of the nonmodulated EPSCs to the modulated EPSCs and those EPSCs evoked by stim-

---

Department of Neuroscience, Physiology, and Pharmacology, University College London, University Street, London WC1E 6JJ, UK.

*To whom correspondence should be addressed. E-mail: t.margrie@ucl.ac.uk

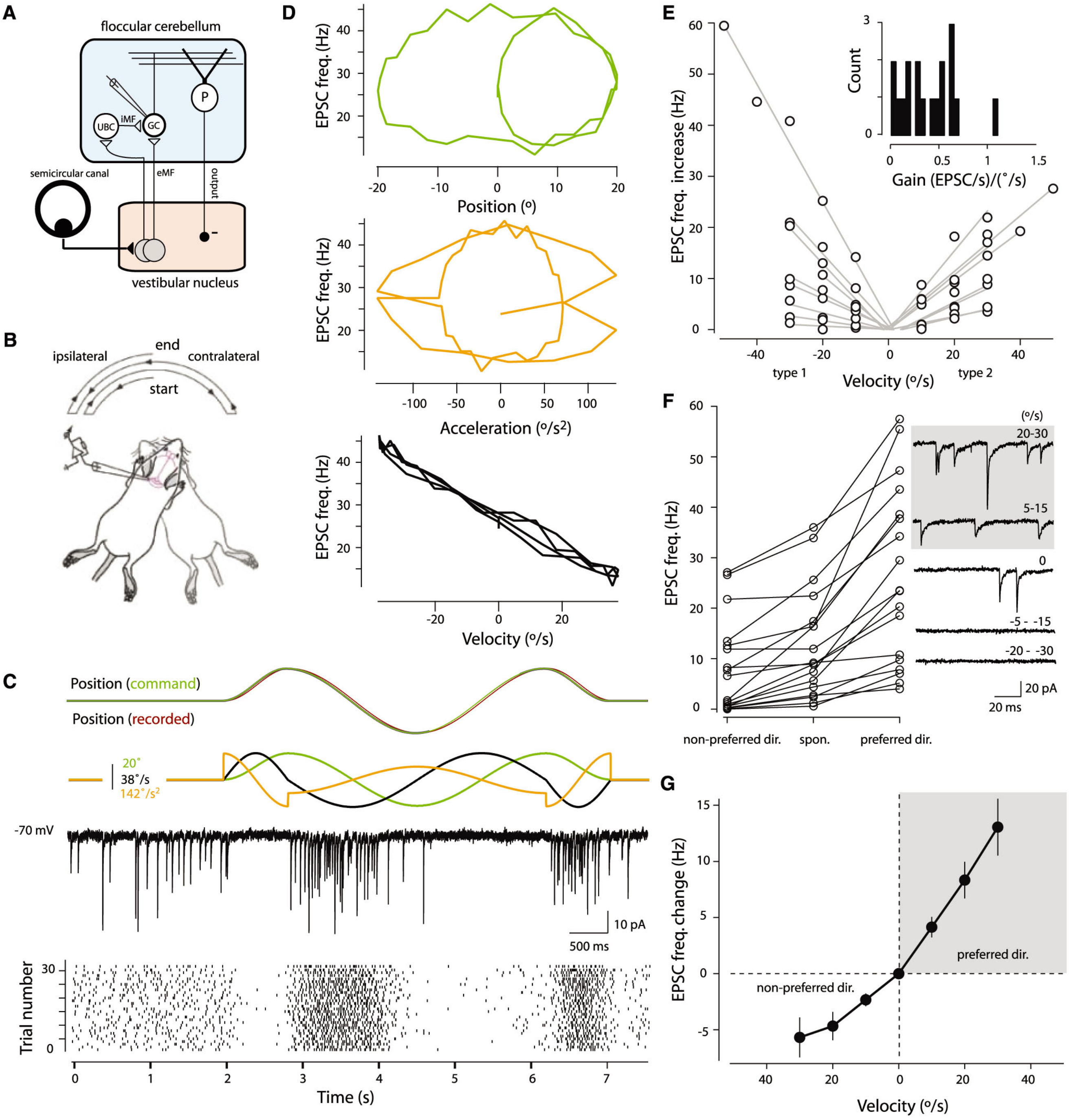

Fig. 1. Motion encoding at MF-GC synapses. (**A**) Simplified diagram of vestibular cerebellum with input from extrinsic MFs (eMF) or indirectly via intrinsic MFs (iMF) of local unipolar brush cells (UBC) (*1*, *26*). The GC–Purkinje cell (P) pathway provides an inhibitory feedback loop to the vestibular nucleus. (**B**) Stimulus used to produce horizontal motion. (**C**) (Top) The positional command signal (green) and the recorded position (brown). (Middle) The position (green), velocity (black), and acceleration profiles (orange) obtained by differentiating the command signal. (Bottom) An example current trace of recorded EPSCs and a raster plot of EPSC onset times for 30 consecutive trials. (**D**) Trajectory plots for an example cell showing EPSC rate during motion (per 100-ms time bins, *n* = 30 trials) plotted against position, acceleration, and velocity. (**E**) The evoked increase in EPSC frequency plotted against velocities recorded in the preferred direction for type 1 and type 2 responses. Linear fits through three to five average velocities (10° s^{-1} bins) are shown for each cell (*n* = 18). (Inset) A histogram of the slopes of each fit (gains). (**F**) Plot showing average EPSC frequencies recorded during baseline and for peak velocities in the preferred and nonpreferred direction (range 35.2 to 37.7° s^{-1}) for all cells. (Right) Example current traces showing asymmetry in EPSC frequency modulation. (**G**) Change in EPSC frequency from baseline rates plotted against velocity for all cells (*n* = 18). Error bars indicate SEM.

ulation of a single extrinsic MF in vitro (*12*) suggests that they arise from the same class of MFs.

Because it is necessary for individual and populations of synapses to reliably report stimulus information online during a sensory event, coherent representations in the cerebellum are likely to involve signals distributed over many MF-GC connections. We used a Bayesian reconstruction algorithm (*9*) (fig. S3) to quantify the ability of the MF-GC synapse to report our motion stimulus. Although activity through a single synapse could indicate the direction of

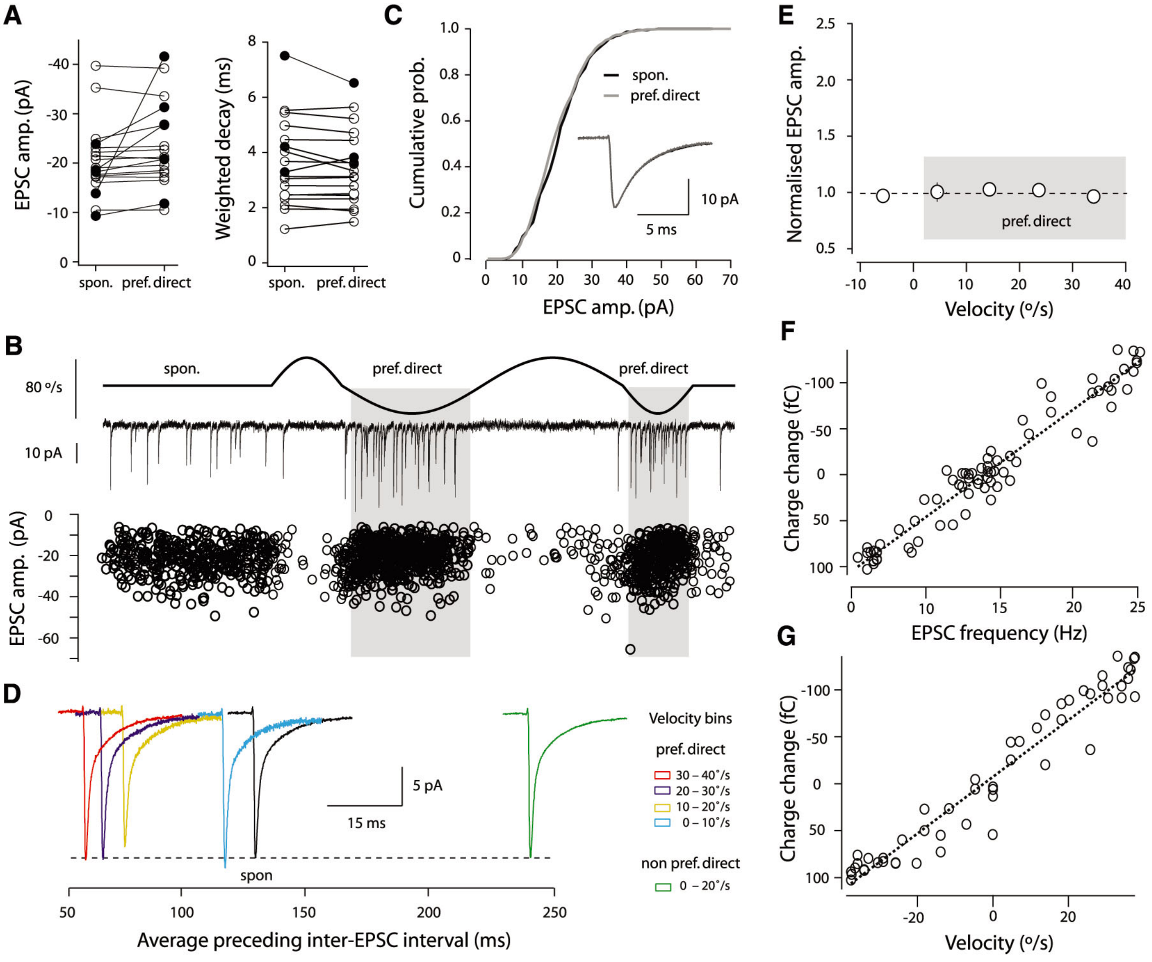

Fig. 2. Velocity is linearly represented by charge transfer. (**A**) Mean EPSC amplitude and weighted decays for EPSCs occurring during baseline and motion in the preferred direction (group 1: cells showing no change, $P > 0.05$, open circles, $n = 13$; group 2: showing a significant change, $P < 0.05$, solid circles; $n = 5$). (**B**) (Top to bottom) Velocity stimulus waveform, example current trace, and EPSC amplitudes recorded from a group 1 cell plotted over time (n = 31 trials, 1545 events). (**C**) Cumulative probability distributions for spontaneous and stimulus-evoked EPSC amplitudes recorded from the cell shown in (B). (Inset) The average EPSCs recorded during baseline (black) and motion in the preferred direction (gray). (**D**) Average EPSC traces for the same cell over 10° s^{-1} velocity bins, aligned on the time scale reporting the average preceding inter-EPSC interval for that velocity bin. Scale bar insert shows time scale for EPSC traces. (**E**) Population data for average EPSC amplitude recorded at different velocities (n = 13 cells). Data points reflect the mean values obtained from 10° s^{-1} velocity bins and are normalized to the average EPSC amplitude observed during baseline. Plot of change in charge transfer from baseline against EPSC frequency (**F**) and velocity (**G**) (all calculated over 100-ms bins) from a representative cell.

motion (Fig. 4A), its estimate of motion velocity (per time bin) suffered from significant errors but improved with increasing synapse number toward psychophysical estimates ($err_{1\ \mathrm{synapse}} = 15.6 \pm 1.3$ ° s^{-1} versus $err_{100\ \mathrm{synapses}} = 4.8 \pm 0.5$ ° s^{-1}, stimulus range from –37.7 to +37.7 ° s^{-1}, $P < 10^{-8}$) (Fig. 4, B and C). In parallel, the reliability (SD of error) of the velocity estimate significantly improved with the logarithm of synapse number ($r = -0.998$, $P < 0.01$) (Fig. 4, B and C). This indicates that activity through as few as 100 MF-GC synapses can reliably report the direction and velocity of our motion stimulus.

We recorded motion-evoked synaptic currents and found that velocity information is represented linearly via bidirectional modulation of EPSC frequency and charge around a tonically active vestibular input. By using differences in the EPSC waveform as a signature of distinct MF-GC synapses, we also found that floccular GCs receive inputs with unique receptive fields, which suggests that multiple vestibular, visual (*15*), and/or eye movement–related signals (*16*) may converge on individual GCs (*17*). In contrast to a single vestibular primary afferent, which can accurately report subtle changes in velocity over a single trial (*18*), about 100 MF-GC synapses were required to provide enough resolution to meet psychophysical predictions (*18*, *19*). This has two major implications for information processing in the cerebellum. MF-GC synapses do not simply relay peripheral spike rates (*2*, *11*, *18*, *20*) but appear to present vestibular information to be integrated with other stimulus features. Second, although the quality of velocity information may be diluted by the probabilistic nature of transmitter release and action potential firing along the sensory pathway (*21*), sensory information is preserved by a population synaptic signal arising from many MFs. Although the absolute number of MF-GC synapses required will depend on the time frame of cerebellar operation, it seems likely that reliable velocity information must be presented to downstream Purkinje cells as an orchestrated coincident GC signal (*22*, *23*).

The highly linear synaptic properties and broad gain distribution of vestibular inputs onto GCs provide a system well suited for cue combination tasks, where stimulus probability distributions are inferred from linear combinations of neural activity (*24*). The very limited number of inputs onto GCs has allowed us isolate and monitor stimulus-evoked EPSCs arising from distinct synaptic contacts (*2*). However, in more complex neurons such as Purkinje and pyramidal cells, nonlinear interactions between synaptic inputs within the dendritic tree may affect the processing of such information at the soma (*25*). In such cells, more reliable stimulus reconstruction and multimodal processing is likely to be achieved through the integration of large numbers of inputs with similar receptive fields.

References and Notes

1. J. C. Eccles, M. Ito, J. Szentagothai, *The Cerebellum as a Neuronal Machine* (Springer, Berlin, 1967).
2. H. Jörntell, C. F. Ekerot, *J. Neurosci.* **26**, 11786 (2006).
3. P. Chadderton, T. W. Margrie, M. Hausser, *Nature* **428**, 856 (2004).
4. C. Fernandez, J. M. Goldberg, *J. Neurophysiol.* **34**, 661 (1971).
5. S. G. Lisberger, A. F. Fuchs, *J. Neurophysiol.* **41**, 764 (1978).
6. D. E. Angelaki, A. G. Shaikh, A. M. Green, J. D. Dickman, *Nature* **430**, 560 (2004).
7. N. H. Barmack, V. Yakhnitsa, *J. Neurosci.* **28**, 1140 (2008).
8. T. W. Margrie, M. Brecht, B. Sakmann, *Pflüg. Arch. Eur. J. Physiol.* **444**, 491 (2002).
9. Materials and methods are provided on *Science* Online.
10. C. Saviane, R. A. Silver, *Nature* **439**, 983 (2006).
11. E. A. Rancz *et al.*, *Nature* **450**, 1245 (2007).

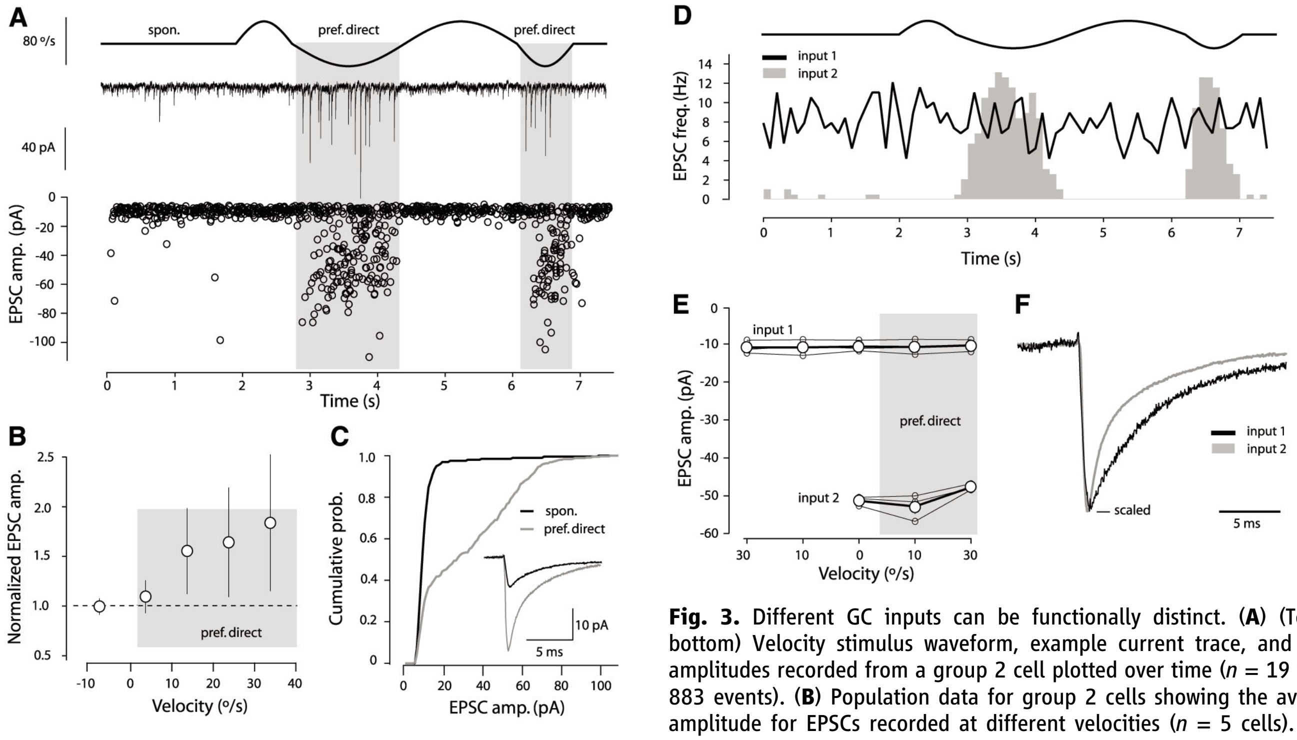

Fig. 3. Different GC inputs can be functionally distinct. (**A**) (Top to bottom) Velocity stimulus waveform, example current trace, and EPSC amplitudes recorded from a group 2 cell plotted over time ($n = 19$ trials, 883 events). (**B**) Population data for group 2 cells showing the average amplitude for EPSCs recorded at different velocities ($n = 5$ cells). Error bars indicate SEM. (**C**) Cumulative probability distributions for spontaneous and stimulus-evoked EPSC amplitudes recorded from the cell shown in (A). (**D**) Peristimulus time histogram for the cell shown in (A), for which two populations of EPSCs could be distinguished. (**E**) On the basis of their amplitude distributions, inputs were separated (3/5 cells), and the amplitude for each input was plotted over a range of velocities. Small circles correspond to individual cells. Large circles are population averages (SEMs are plotted). (**F**) Average traces from the nonmodulated (input 1) and modulated EPSC population (input 2) from the cell shown in (A), scaled to the same peak amplitude to highlight the distinct yet slow decay kinetics of both inputs.

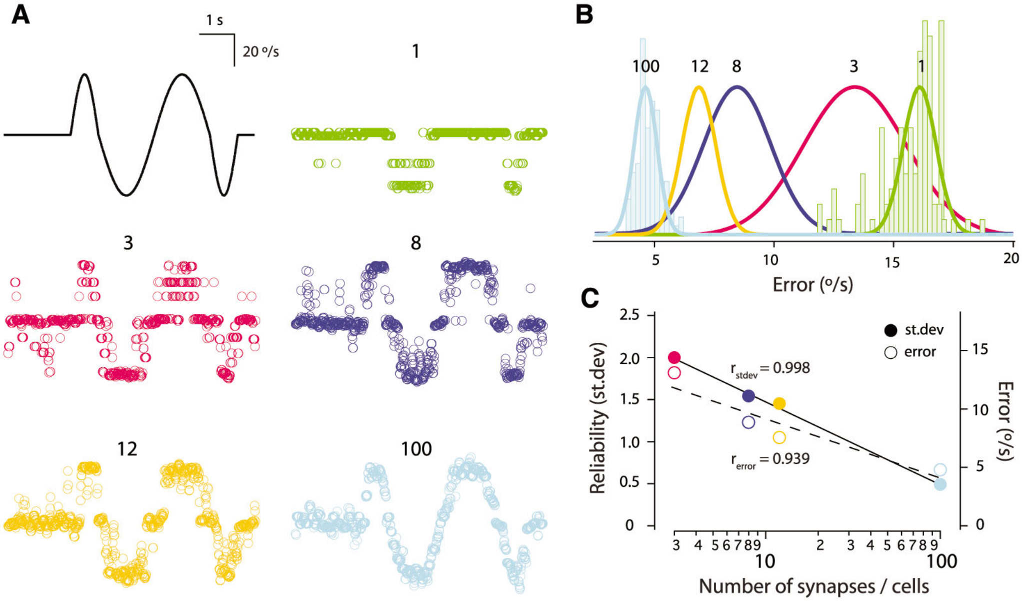

Fig. 4. Real-time velocity representation by MF-GC synapses. (**A**) Example stimulus estimates based on a single trial for 1, 3, 8, 12, and 100 synapses. (**B**) Distribution of mean error (average absolute deviation between reconstruction and applied stimulus) for 100 repetitions for the indicated number of synapses. Gaussian fits (scaled) for all distributions are shown. (**C**) The reliability (standard deviation of the error) and accuracy (mean error) plotted against the number of synapses used for stimulus reconstructions.

12. D. A. DiGregorio, Z. Nusser, R. A. Silver, *Neuron* **35**, 521 (2002).
13. P. L. van Kan, A. R. Gibson, J. C. Houk, *J. Neurophysiol.* **69**, 74 (1993).
14. L. Cathala, S. Brickley, S. Cull-Candy, M. Farrant, *J. Neurosci.* **23**, 6074 (2003).
15. H. Noda, *Ann. N. Y. Acad. Sci.* **374**, 465 (1981).
16. H. Noda, D. A. Suzuki, *J. Physiol.* **294**, 349 (1979).
17. D. Marr, *J. Physiol.* **202**, 437 (1969).
18. S. G. Sadeghi, M. J. Chacron, M. C. Taylor, K. E. Cullen, *J. Neurosci.* **27**, 771 (2007).
19. T. Mergner, F. Hlavacka, G. Schweigart, *J. Vestib. Res.* **3**, 41 (1993).
20. A. Yang, T. E. Hullar, *J. Neurophysiol.* **98**, 3197 (2007).
21. W. H. Calvin, C. F. Stevens, *Science* **155**, 842 (1967).
22. S. G. Lisberger, A. F. Fuchs, *J. Neurophysiol.* **41**, 733 (1978).
23. B. Barbour, *Neuron* **11**, 759 (1993).
24. W. J. Ma, J. M. Beck, P. E. Latham, A. Pouget, *Nat. Neurosci.* **9**, 1432 (2006).
25. M. London, M. Hausser, *Annu. Rev. Neurosci.* **28**, 503 (2005).
26. M. R. Dino, A. A. Perachio, E. Mugnaini, *Exp. Brain Res.* **140**, 162 (2001).

27. We thank R. Callister and A. Brichta for advice and helpful discussion and the members of the lab and T. Mrsic-Flögel for comments on the manuscript. This work was supported by the Wellcome Trust (A.A., R.A.S., and T.W.M.), the UK Biotechnology and Biological Sciences Research Council (A.T.S., R.A.S., and T.W.M.), and the Human Frontier Science Program (T.W.M.).

Supporting Online Material
www.sciencemag.org/cgi/content/full/321/5891/977/DC1
Materials and Methods
Figs. S1 to S3
References
Movie S1

28 March 2008; accepted 8 July 2008
10.1126/science.1158391

New Products Focus: Microarrays

Wash System

The Maui Wash System automates posthybridization wash protocols to provide clean, dry microarray slides. The system is suitable for mid throughput to high throughput laboratories that demand high-quality microarray data. The system accommodates many wash protocols, with user control of cycle times, reagent usage, temperature, slide agitation, and drying.

BioMicro Systems
For information 650-328-2580
www.biomicro.com

Cytogenetic Solution

Cytogenetic Solution, which combines the high-density SNP Array 6.0 with a simple assay and intuitive software, is designed to enable researchers to detect more copy-number abnormalities associated with congenital diseases. The microarray-based system provides cytogenetic researchers with an accurate method of detecting chromosomal abnormalities associated with congenital diseases such as autism and mental retardation. The copy number and loss of heterozygosity information it delivers enables scientists to identify uniparental disomies—genetic abnormalities that are frequent in many congenital diseases.

Affymetrix
For information 408-731-5791
www.affymetrix.com

Gene Expression BeadChip

The HumanHT-12 BeadChip is a 12-sample product designed to accelerate whole genome expression and expression-based quantitative trait loci (eQTL) studies. It includes more than 48,000 probes per sample. Along with the HumanWG-6, which offers high-quality, whole-genome expression data, the HumanHT-12 BeadChip provides gene expression researchers with a flexible and cost-effective screening tool.

Illumina
For information 858-332-4055
www.illumina.com

Chicken Microarray

The Oligonucleotide Array CGH (comparative genomic hybridization) chicken microarray contains 244,000 features. The 244K chicken CGH array enables users to analyze to what extent copy number variation contributes to phenotypic variation in chickens, a species of significant economic importance and an important developmental biology model. The product started as a custom array, but the manufacturer received enough demand to put it in its catalog.

Agilent Technologies
For information 408-553-7191
www.agilent.com

Microarray Scanners

Two new microarray scanners, the Axon GenePix 4300A and the Axon GenePix 4400A, improve the efficiency of research experiments, reduce the cost per data point, and offer broad applicability. The scanners provide customers with the ability to run the most advanced microarray applications, according to the manufacturer.

MDS Analytical Technologies
For information 888-637-7222
www.mdssciex.com

Silverquant Microarray Detection

The Silverquant microarray detection and scanning system provides four times higher sensitivity than fluorescence as well as signal stability. A new application note (No. 148) from Eppendorf Biochip Systems describes its features in detail and compares it with fluorescence in terms of sensitivity, dynamic range, reproducibility, and stability. According to the application note, the Silverquant detection technology offers higher resolution at low analyte concentrations, higher dynamic range, high reproducibility, and high signal stability with no photobleaching and no sensitivity to ozone. The Silverquant detection technology is reliable and robust with no moving optical parts. It features a 16-bit charge-coupled-device sensor, an integrated barcode reader, high resolution (up to 6 μm), fast scanning times (1 minute per slide at 12 μm). It scans standard microarray slides.

Eppendorf
For information +49-40-53801-1
www.eppendorf-biochip.com

Life Science Search Engine

A free version of the NextBio life science search engine is available. Using NextBio, a researcher or clinician can search the world's public life sciences data and literature, including more than 10,000 experiments, 16 million articles, and billions of data points. In addition, users can import their own experimental data into the NextBio search engine, share it with the community, and collaborate with others. With NextBio, researchers can find topics of interest quickly with an intelligent semantic auto-complete feature, make correlations across six species, perform searches to validate or generate novel hypotheses before investing in new experiments, and understand their own results by correlating them with the world's collective experimental data.

NextBio
For information 408-861-3610
www.nextbio.com

Electronically submit your new product description or product literature information! Go to **www.sciencemag.org/products/newproducts.dtl** for more information.

POSITIONS OPEN

ASSISTANT PROFESSOR
Molecular Biology

The Department of Molecular Biology at the University of Wyoming seeks an outstanding scientist for a tenure-track position at the Assistant Professor level. The successful candidate will be expected to establish an extramurally funded research program, participate in undergraduate teaching in the core molecular biology curriculum, and contribute to the Graduate Program in Molecular and Cellular Life Sciences **(website: http://www.uwyo.edu/mcls/).** Salary and startup package will be competitive. Candidates must have a Ph.D. degree or equivalent, postdoctoral research experience, and clear evidence of research productivity. Applications should be sent via **e-mail: molecularbiology@uwyo.edu** as a single PDF file (labeled with your last name) that includes a cover letter, curriculum vitae, research interests, and teaching interests and philosophy. In addition, three letters of recommendation should be sent to **e-mail: molecularbiology@uwyo.edu** or by regular mail to: **Search Committee Chair, Department of Molecular Biology, University of Wyoming, 1000 E. University Avenue, Department 3944, Laramie, WY 82071.** The Department of Molecular Biology consists of 15 faculty with diverse research interests and significant extramural support **(website: http://uwacadweb.uwyo.edu/UWmolecbio/).** The University of Wyoming enrolls about 12,000 students, including about 2,500 graduate students. Laramie is located in the Rocky Mountain region of southeastern Wyoming, about 120 miles from Denver. In addition to opportunities for academic excellence, the University of Wyoming offers a college-town environment, extraordinary outdoor recreation, and daily conveniences that contribute to our quality of life. Screening of applications will begin on October 15, 2008, and continue until a suitable candidate is identified.

The University of Wyoming is an Equal Opportunity/ Affirmative Action Employer.

FACULTY POSITION in IMMUNOLOGY
Department of Microbiology-Immunology and Interdepartmental Immunobiology Center
Northwestern University Feinberg School of Medicine

A tenure-track position is open for a full-time faculty researcher (Ph.D., M.D./Ph.D. or M.D.) in the areas of innate immunity, immune development, immune regulation, or immunobiology of autoimmune or infectious diseases. Rank is open, and salary is negotiable. All applicants should have substantial peer-reviewed publications that demonstrate research productivity and the ability to perform cutting-edge research. Candidates for an **ASSISTANT PROFESSOR** position should have postdoctoral research experience. Persons seeking appointment as **ASSOCIATE or FULL PROFESSOR** should have substantial, long-term research productivity, and a history of grant support and academic service. Candidates should also have an interest in teaching graduate and medical students. Starting date is negotiable after April 1, 2009. Application materials will be reviewed as received, but to receive full consideration, should be received by November 30, 2008. Please send complete curriculum vitae, a research statement, and the name and contact information of at least three references to **e-mail: immunology@northwestern.edu.**

Northwestern University is an Affirmative Action, Equal Opportunity Employer. Women and minorities are encouraged to apply. Hiring is contingent upon eligibility to work in the United States.

CAREER OPPORTUNITY

This unique program offers the candidate with an earned Doctorate in the life sciences the opportunity to obtain the Doctor of Optometry (OD) degree in 27 months (beginning in March of each year). Employment opportunities exist in research, education, industry, and private practice. Contact the **Admissions Office, telephone: 800-824-5526** at the **New England College of Optometry, 424 Beacon Street, Boston, MA 02115.** Additional information at **website: http://www.neco.edu, e-mail: admissions@neco.edu.**

POSITIONS OPEN

PARSONS

EXECUTIVE DIRECTOR
Institute for Advanced Energy Solutions

The National Energy Technology Laboratory (NETL) has partnered with three major regional universities (Carnegie Mellon University, the University of Pittsburgh, and West Virginia University) to establish the Institute for Advanced Energy Solutions (IAES). NETL's objective is to position the IAES as a prestigious and nationally recognized research organization that will address critical energy technology needs for the nation. Parsons, one of the managing site contractors, on behalf of NETL and the three universities, is seeking candidates for the position of Executive Director, IAES, which will be based in Pittsburgh, Pennsylvania. We are currently in search of candidates possessing the following qualifications: (1) Ph.D. in engineering or science, (2) successful record of scholarly research in fields relevant to energy technology, (3) experience in managing a technical or research organization, and (4) background in leading and growing a large research organization.

To view the full job description, please visit us at **website: http://www.parsonsjobs.com,** searching for identification #11344. For confidential consideration, please send your resume to **e-mail: lisa.kearney@parsons.com.** *Equal Opportunity Employer/Minorities/ Females/Persons with Disabilities/Veterans.*

FACULTY POSITION in MICROBIAL PATHOGENESIS
Department of Microbiology-Immunology
Northwestern University Feinberg School of Medicine

A tenure-track position is open for a full-time faculty researcher (Ph.D., M.D./Ph.D. or M.D.) in the areas of microbial pathogenesis (bacteria, parasites, and fungi), biodefense, immunobiology of microbial infections, normal microbial flora, or general microbiology. Rank is open, and salary is negotiable. All applicants should have substantial peer-reviewed publications that demonstrate research productivity and the ability to perform cutting-edge research. Candidates for an **ASSISTANT PROFESSOR** position should have postdoctoral research experience. Persons seeking appointment as **ASSOCIATE or FULL PROFESSOR** should have long-term research productivity and a history of grant support and academic service. Candidates should have an interest in teaching graduate and medical students. Starting date is negotiable after April 1, 2009. Application materials will be reviewed as received but, to receive full consideration, should be received by November 30, 2008. Please send complete curriculum vitae, statement of research interests, and the name and contact information of at least three references to **e-mail: nwumicroresearch@gmail.com.**

Northwestern University is an Affirmative Action, Equal Opportunity Employer. Women and minorities are encouraged to apply. Hiring is contingent upon eligibility to work in the United States.

ENVIRONMENTAL RESEARCH ANALYST. Conduct research and analyze commercial land for potential development with emphasis on environmental effects including physical and health hazards. Analyze data to interpret correlations between commercial property development and environmental effects. Prepare reports to present to city, state, and federal authorities for permits. Conduct feasibility studies for development of physical plants. Review plans, designs, layout, and physical requirements for commercial sites and buildings. Required: Master of Science in chemical engineering, chemistry, or forestry. Equivalent of 40 hours per week. Job/ interview site: Torrance, California. Send curriculum vitae to: **Person Realty Incorporated, 21641 S. Western Avenue, Suite C, Torrance, CA 90501.**

POSITIONS AVAILABLE:

NO Ph.D. REQUIRED?

Not sure a Ph.D. is the best route? Take heart: There are plenty of opportunities in science for those who have a B.S. or M.S. degree. **By Jacqueline Ruttimann**

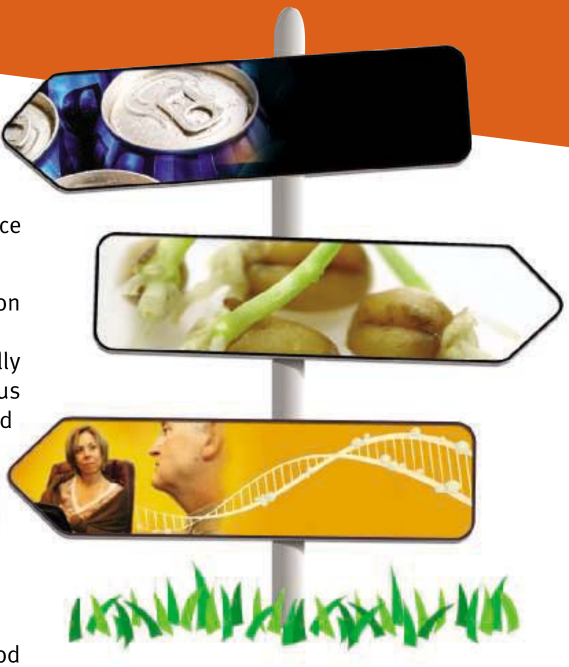

Upon completing college, many science undergraduates who don't want to go on to medical school think only one other option exists: pursuing a Ph.D.

A Ph.D, however, is not one-size-fits-all. While personally and financially rewarding in the end, those who choose this path should do so upon serious introspection. Long hours with low pay and dry spells in data are often the norm. Add to this the varied completion time which, depending on the program, ranges from four to eight years.

For those not sure of the life-style or time commitment involved, other fast-track options such as obtaining a Master's degree or entering a company exist. Many of these choices lie in not commonly considered industries or up-and-coming fields of study.

Food for Thought

A possible career may lie in the cereal you crunch or the soda you sip. Careers in the food industry are plentiful and in high demand, especially for budding scientists with either a Bachelor's or Master's degree.

"When most people think food science they think McDonald's and flipping burgers. Part of it is working on new types of beer, better packaging, and products that are environmentally friendly," explains **Martin Wiedmann,** director of graduate studies for the Department of Food Science at Cornell University, Ithaca, New York.

> "When most people think food science they think McDonald's and flipping burgers. Part of it is working on new types of beer, better packaging, and products that are environmentally friendly."

In technical terms, food science is the application of biological and physical sciences as well as engineering to the processing and manufacturing of foods in order to ensure their nutritive value, safety, and quality. To study the interactions of foods and food components, the field comprises several disciplines including chemistry, animal and plant biology, biochemistry, biotechnology, nutrition, physiology, microbiology, and engineering.

Professional food scientists also have the tall order of trying to increase the food supply to meet the demands of a rapidly growing population without straining the environment. "It's a great opportunity for people who like the application aspect of science and are looking to have a tremendous impact," says Wiedmann.

Alexandra Doronkin

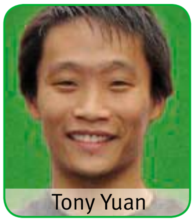

Tony Yuan

Sam Alcaine

Cornell's Food Science Program offers two types of Master's degree: a one and a half to two-year Master of Science (M.S.), for those relatively new to research, and a one-year Master of Professional Studies (M.P.S.), for those already in a professional career but wanting to upgrade their core set of skills and knowledge. While both degree programs require classes and research with department faculty members, only the M.S. students must submit a research-based thesis. Each program is tailored around the individual student, in which the class schedule is worked out in collaboration with an adviser. Students have a choice of classes such as general and international food science, food microbiology and engineering, enology, dairy science, sensory science, and food safety.

The students are in such high demand, says Wiedmann, that "most of our students have two to three job offers by the time they end their senior year." These offers range from governmental institutions such as the U.S. Food and Drug Administration and the U.S. Department of Agriculture to various food industries such as breweries and chocolatiers.

"The program is a great stepping stone between academia and industry," says current M.P.S. student **Yankai Liu.** "It provides the skills and expertise that are essential for a future career."

On scholarship from his native country Singapore, Liu plans to return there and serve in the Civil Service. Before then, however, he is working on a project with food process engineering professor Syed Rizvi on methods to improve mineral fortification of rice. The rewards of his efforts are plenty: if perfected, the rice could aid those suffering from malnourishment. continued »

UPCOMING FEATURES

Annual Postdoc Survey—August 29

Faculty Feature:
Enriching Your Academic Career—September 12

Focus on France —September 26

CREDIT: (TOP IMAGES): ISTOCKPHOTO.COM; (MIDDLE): MONSANTO COMPANY; (BOTTOM LEFT): MASTER OF BIOTECHNOLOGY PROGRAM PHOTO

Careers and Graduate Programs for B.S./M.S. Scientists

> "The global demand for grain and record commodity prices are driving up demand for faster delivery of new products with better technologies."
> –Dave Bubeck

CREDIT: PHOTO COURTESY OF PIONEER HI-BRED

Recipes for Success

"Lab work for the sake of lab work wasn't really interesting, and I didn't want to be in grad school that long," says **Sarah Kirk** who, after getting her biology degree from Hiram College, spent a couple of years as a lab tech in a microbiology lab at Case Western University, Cleveland, Ohio.

Cornell's program was a perfect fit. Kirk worked with food science professor Kathryn Boor on why flavored milk spoils faster than unflavored milk, and was hooked. Upon graduating, Kirk landed a job at M&M/Mars, where she specialized in confections and worked for five years on Starburst and helped launch mint Skittles. She is now at Kashi, where she works on whole grain and naturally healthy products ranging from cereals to snack bars. Although the food products differ, the extensive technical background from Cornell's program enabled her to easily make the switch.

"Only one or two companies prefer Ph.D.s," says Kirk. "A Master's degree was enough to get my foot in the door."

Alum **Sam Alcaine** has a job that most scientists who homebrew would crave: He works as a product developer at MillerCoors. While a senior majoring in cellular and molecular biology and genetics at the University of Maryland, College Park, brewing became a hobby to Alcaine. Wiedmann called and offered him an opportunity to combine his loves of genetics and yeast fermentation. "That basically sold me," he says. He worked on his M.S. in Wiedmann's lab on the transmission of antibiotic resistance genes among different *Salmonella* strains, and through the department's social network, landed his current job. "When looking for a Master's program, it doesn't always have to be your angle, but it does have to give you the tools," he advises.

Field of Dreams

Those not looking to go to graduate school right away and who would rather move straight into the work force could consider the agricultural biology industry. A not-too-distant cousin to food science, agrobio entails research and development of seed crops.

"The global demand for grain and record commodity prices are driving up demand for faster delivery of new products with better technologies," explains **Dave Bubeck,** North American research director at Pioneer Hi-Bred International, a leading global source of customized solutions for farmers, livestock producers, and grain and oilseed processors.

Plant breeding is a multidisciplinary field. Those who have entered it have had backgrounds in agronomy, agricultural engineering, plant sciences, entymology, botany, general biology, molecular biology, and genetics. As the field has become more computer based, it is not surprising to find even those with a mathematics or statistics degree. "There are excellent growth opportunities for those with a Bachelor's or Master's degree. The ratio in research and development groups in the seed industry of Ph.D.s to undergrads/Master's students is approximately 1:5," says Bubeck.

The timing for Bachelor's and Master's students, according to Bubeck, has never been better. Pioneer operates more than 90 worldwide research centers and has undergone a significant expansion in its R&D department. Nearly 300 new positions in this department were added in 2007, and the company plans to offer more than 300 additional positions this year—most of which will be non-Ph.D.

Similarly, over 70 percent of research associate positions at Monsanto are filled by those who have either a Bachelor's or Master's, says **Alexandra Doronkin,** the company's technology recruiting lead. Many who continue to work at Monsanto quickly climb the corporate ladder. "We go by contributions people make," she says. "We have many examples of people with Bachelor's or Master's degrees leading scientific project teams and managing key functions."

Bubeck offers the following piece of advice to future college graduates: "If you're not certain of pursuing a graduate degree after your Bachelor's, it may be more beneficial to get out into the work world first. If it leads you back to grad school, you are more committed to it."

Best of Both Worlds

Contemplating a career in either medicine or science? You may be able to find the best of both worlds in genetic counseling.

With the advent of next generation sequencing technologies, even more is being learned about our genetic makeup. However, there is a great need for this information to be translated to patients or relatives who are at risk of an inherited disorder. These people need to understand the disorder and its consequences, the probability of developing or transmitting disease, and the prevention options needed for personal health choices or family planning.

"It's part science, part counseling," explains **Angela Trepanier,** certified genetic counselor and president of the National Society of Genetic Counselors. "For somebody who really likes science but is not interested in becoming a physician or working on the bench as a Ph.D.—but is interested in working with people—this is a great profession to choose."

continued »

Featured Participants

American Board of Genetic Counseling
www.abgc.net

Cornell University
www.cornell.edu

Monsanto
www.monsanto.com

National Society of Genetic Counselors
www.nsgc.org

Northwestern University
www.northwestern.edu

Pfizer
www.pfizer.com

Pioneer Hi-Bred International Inc.
www.pioneer.com

University of Alabama-Birmingham
www.uab.edu

Wayne State University
wayne.edu


Jacqueline Gauthier


Tiara Johnson


Angela Trepanier

> "It's part science, part counseling. For somebody who really likes science but is not interested in becoming a physician or working on the bench—this is a great profession to choose."
>
> –Angela Trepanier

The profession is small but growing. Currently there are around 3,000 genetic counselors in the United States and numbers are growing worldwide. Those who enter the field go through Master's programs, of which there are 29 in the United States and three in Canada that are accredited by the American Board of Genetic Counseling. Typically those who enter have some sort of biology or psychology undergraduate degree. However, those in nursing, public health, and social work also apply.

At the Genetic Counseling Graduate program at Wayne State University School of Medicine, Detroit, Michigan, where Trepanier is program co-director, students take basic science, medical genetics, and counseling course work. In addition, they perform internships in a variety of clinical settings in which they first shadow and then perform the duties of a professional genetic counselor. Students also do a clinical research project based on some aspect of the career. Graduates, most of whom sit for a national certification examination, go on to various areas including clinical care, public health, industry, and nonprofit organizations.

Although genetic counseling first started with the detection of birth defects in prenatal and pediatric patients, "the profession has blossomed and grown," says Trepanier. Cancer genetics became a specialty in the 1990s, and now cardiovascular and psychiatric diseases are up-and-coming focuses.

"People who go into it tend to be into lifelong learning since the field is constantly changing," she says. Yet, says Trepanier, one can achieve work and life balance. "There's time to be a genetic counselor and still have a life."

For those who are interested, she suggests contacting and shadowing a genetic counselor for a day. She also advises getting some advocacy and counseling experience so prospective applicants can see whether they can work with people who are in crisis. Alternatively she advises contacting any of the graduate programs. "We want to talk to potential students. We're as interested in them as they are in us," she says.

Before entering the program, **Tiara Johnson** interned at a genetic counseling clinic and found her calling. "I really love the program. I've learned so much in such a short amount of time," says Johnson, now a second-year student. "Just knowing I could get done in another two years and be able to start a career that is highly recognized and respectable has meant a lot to me."

Like Johnson, recent graduate **Jacqueline Gauthier** feels secure in the future of her profession. "Genetics is very cutting edge and is going to change the face of medicine as we know it," says Gauthier, who now works at the Genetics Department at the University of Alabama-Birmingham and specializes in cancer and prenatal genetic counseling. "The positions are growing. Ten years from now, I don't have to make a total career shift."

A Scientist for All Seasons

Tony Yuan was at a career fork when he graduated from the University of Texas at Dallas with a biology B.S. He didn't know whether he should go on to medical school or work toward a Ph.D. When he received an e-mail about a Master's program at Northwestern University, he jumped at the chance. "I didn't want to spend that much time for a Ph.D. This program gives you a feel if you're a bench scientist or not."

The Master of Biotechnology program at Northwestern is a 15-month curriculum that stresses the interdisciplinary nature of the biotechnology industry and cross-trains former biology and engineering majors in each respective field for careers in the biotechnology or pharmaceutical industries. "Upon completion, these students are able to communicate across disciplines and are prepared for a wide variety of positions," assures program director **William Miller.**

The rigorous program combines coursework in bioprocess engineering and seminar classes in the ethical, legal, regulatory, communication, and business aspects of the biotechnology industry with over a thousand hours of research. In lieu of a thesis, written and oral research reports are required.

While the majority of course graduates go on to biotechnology and pharmaceutical industry companies such as Bristol-Myers Squibb, Amgen, Merck and Company, and Pfizer, about a quarter pursue further graduate education.

"The program gives you a gateway into industry," says recent alum **Kavi Mehta,** who now works in cell culture process development at Pfizer. "My earning potential went up almost three times and I'm working on more advanced projects."

Upon completing Northwestern's program, **Kanika Bhatia** discovered something about herself. "I'm not a sitting-in-the-lab type of person. I like my research a bit faster," she says. More interested in qualitative and regulatory research, she is now enrolled in the Quality Leadership Program at GE Healthcare, where she does rotations in these respective fields. She suggests that students who are not so sure about research "really think about what they want to do. Your heart has to be 100 percent in it."

Yuan concurs. "Look at all the options—especially if you're looking to get a Ph.D. or go on to medical school. There is not just one road you can take."

Jacqueline Ruttimann is a scientist turned freelance writer living in Chevy Chase, Maryland.

DOI: 10.1126/science.opms.r0800057

CREDIT: PHOTOS COURTESY OF WAYNE STATE UNIVERSITY SCHOOL OF MEDICINE

Weill Cornell Medical College

FACULTY POSITION
Pharmacology-Neuroscience

The C.V. Starr Laboratory in the Department of Anesthesiology of the Weill Cornell Medical College of Cornell University in New York City invites applications for a full-time, tenured/tenure-track faculty position for scientists or physician-scientists with research interests in pharmacology and/or neuroscience. Appointment to the rank of **ASSISTANT, ASSOCIATE, or FULL PROFESSOR** will be considered depending on qualifications. A joint appointment in an appropriate basic science department will be offered. The research area is broadly defined to include structural, biochemical, neurophysiological, cell biological, and molecular physiological approaches to fundamental problems of relevance to anesthesia including, but not limited to, synaptic transmission and plasticity, neuronal networks, ion channel physiology, pain, and mechanisms of anesthesia.

Applicants should forward electronic versions of (1) a covering letter; (2) curriculum vitae; (3) an overview of current and future research interests; and (4) the names and contact information of at least three references to **e-mail: neuropharmacology-search@med.cornell.edu.** Applications will be considered until the position(s) is filled.

Equal Opportunity Employer/Minorities/Females/Persons with Disabilities/Veterans.

DIRECTOR
Bard Center for Environmental Policy
Bard College

The Bard Center for Environmental Policy is seeking a Director who will provide dynamic intellectual and administrative leadership for the Center and its graduate program. The Center offers an M.S. degree and engages the community on regional, national, and international environmental policy issues. Responsibilities include fundraising and developing collaborations with regional environmental centers, nongovernment organizations, government agencies, and private sector firms. Ph.D. or terminal degree and distinguished record of scholarship required. Salary is competitive, and benefits are excellent.

Submit a letter of interest, curriculum vitae, and a list of at least three references to: **Bard Center for Environmental Policy Search, Human Resources-9006, Bard College, P.O. Box 5000, Annandale-on-Hudson, NY 12504-5000.** Additional information at **website: http://www.bard.edu/cep** or **e-mail: dgs@bard.edu.**

Affirmative Action/Equal Opportunity Employer.

ASSISTANT PROFESSOR
Benedictine University

Tenure-track position for fall 2009 semester. Teach freshman biology sequence and advanced coursework in organismal courses of your choice. Establish and participate in externally funded faculty/student research at the undergraduate level. Startup funds available. Priority given to applications received by Septemeber 20, 2008. Position open until filled.

Qualifications: Ph.D. required with research interest (pedagogical research included) involving undergraduate students; teaching and postdoctoral experience is preferred. *Must have permanent legal authorization to work in the United States.*

Application process: Submit cover letter, curriculum vitae, graduate and undergraduate transcripts, statement of teaching and research interests, and three letters of recommendation (one addressing teaching effectiveness) to: **Michelle Mosier, Coordinator, College of Science, Benedictine University, 5700 College Road, Lisle, IL 60532; fax: 630-829-6547.** *Equal Opportunity Employer.*

BIO-ORGANIC CHEMIST. The Williams College Chemistry Department invites application for a tenure-track position at the **ASSISTANT PROFESSOR** level for fall 2009. (Senior appointment possible in exceptional circumstances.) Initial teaching assignment, depending upon the successful candidate's subspecialty, will include two courses from: sophomore-level organic chemistry, enzyme kinetics and reaction mechanisms, biochemistry, and a course for nonscience majors. A semester teaching load normally includes complete responsibility for one course and two laboratory sections, and supervision of student research projects. Candidates should hold a Ph.D. or have completed their dissertation by September 2009 (postdoctoral experience is preferred). The successful candidate must have a strong commitment both to teaching at the undergraduate level and to developing a productive research program. Williams College is a highly selective, coeducational liberal arts institution of approximately 230 faculty and 2,000 undergraduates, located in northwestern Massachusetts. The Chemistry Department is composed of 12 faculty members, and graduates about 25 to 30 majors each year; the Department has excellent facilities for teaching and research. The College is actively working to increase the diversity of its science majors and seeks an individual who can help us meet these goals. Mail resume, undergraduate and graduate transcripts, descriptions of teaching philosophy and research projects for undergraduates, and three letters of recommendation to: **Prof. Enrique Peacock-López, Chair, Department of Chemistry, Williams College, Williamstown, MA 01267,** by October 1, 2008. Electronic applications will not be accepted. For additional information about the Chemistry Department, please visit our **website: http://www.williams.edu/Chemistry.** *Beyond meeting fully its legal obligations for nondiscrimination, Williams College is committed to building a diverse and inclusive community where members from all backgrounds can live, learn, and thrive.*

FACULTY POSITIONS in BIOLOGY

Hope College, a liberal arts college with a reputation of excellence in the natural and applied sciences, seeks applicants for two tenure-track positions at the **ASSISTANT PROFESSOR** level to begin August 2009. The successful candidates for each position will have a Ph.D. and be expected to develop vigorous, externally funded research programs with active participation by undergraduate students. (1) A broadly trained **PLANT SYSTEMATIST** who uses modern techniques to address evolutionary or ecological questions of fundamental significance. (2) A broadly trained **CELLULAR or DEVELOPMENTAL BIOLOGIST.** Applicants with more extensive teaching experience will be considered at the **ASSOCIATE PROFESSOR** level for this position. Additional information about the positions can be found on the **website: http://www.hope.edu/academic/biology/.** Application materials should be submitted prior to October 17, 2008.

POSTDOCTORAL POSITION available to study sphingolipid-mediated signaling in cancer (*Cell Cycle* **6:**522-7, 2007; *Trends Mol. Med.*. **13:**210-17, 2007; *Proc. Natl. Acad. Sci.* **103:**17384-9, 2006). Experience with expression arrays, real-time, quantitative PCR, molecular and cell biology, and tissue culture are required. Candidates must hold a Ph.D. or M.D. *and either* U.S. *citizenship or permanent resident status.* Please, submit curriculum vitae and three references to:

Julie D. Saba, M.D., Ph.D.
Scientist and Staff Physician
Children's Hospital Oakland Research Institute
5700 Martin Luther King Jr. Way
Oakland, CA 94609
Telephone: 510-450-7690
E-mail: jsaba@chori.org

POSTDOCTORAL POSITION is available at Indiana University School of Medicine (Indianapolis, Indiana) for a highly motivated **ELECTROPHYSIOLOGIST** to study cation channel function/properties. Experience in patch-clamp is required; additional experience in molecular biology and biochemistry is preferred. Send curriculum vitae to **Alexander G. Obukhov (e-mail: aobukhov@iupui.edu).**

RESEARCH ASSOCIATE positions are available in the integrative neuropharmacology laboratory for enthusiastic individuals with postdoctoral training and skills in proteomics, genomics, lipidomics, mass spectrometry, or gene expression analysis in neural tissues. Ongoing projects explore novel models, mechanisms, and molecular targets for addiction and depression. Desirable candidates should have excellent communication and supervisory skills, experience in proposal and manuscript writing, and readiness to work toward transitioning into a tenure-track position after two to three years. Salary offered will be competitive. To apply, please e-mail curriculum vitae and names of three references to: **Ashiwel Undieh (e-mail: ashiwel.undieh@jefferson.edu), Professor and Chair, Department of Pharmaceutical Sciences, Thomas Jefferson University, 130 S. 9th Street, Philadelphia, PA 19107.**


AAAS
Science
125 Questions:
What don't we know?
Science